

A SPECTROGRAPH FOR THE
RAPID ANALYSIS OF TRANSIENTS
AND
CLASSIFICATION OF SUPERNOVAE

Andrzej S. Piasek

A thesis submitted in partial fulfilment of the requirements of
Liverpool John Moores University
for the degree of
Doctor of Philosophy

September 2017

Declaration

The work presented in this thesis was carried out at the Astrophysics Research Institute, Liverpool John Moores University. Unless otherwise stated, it is the original work of the author.

While registered as a candidate for the degree of Doctor of Philosophy, for which submission is now made, the author has not been registered as a candidate for any other award. This thesis has not been submitted in whole, or in part, for any other degree.

Andrzej S. Piascik
Astrophysics Research Institute
Liverpool John Moores University
IC2, Liverpool Science Park
146, Brownlow Hill
Liverpool L3 5RF
United Kingdom

THURSDAY 28TH SEPTEMBER, 2017

I present an account of the development and application of SPRAT, a Spectrograph for the Rapid Analysis of Transients. SPRAT is designed to classify optical transients down to a visible magnitude, $m_V = 20$.

It is hosted on the fully robotic 2.0 metre Liverpool Telescope located on the Canary island of La Palma. The aim of high-throughput and a limited space-envelope constrained the design to be compact with a simple, efficient optical layout employing a volume phase holographic grating. It can operate in one of two modes to optimise the peak throughput wavelength. Peak red mode throughput is 0.35 at $\lambda = 6450 \text{ \AA}$. Peak blue mode throughput is 0.29 at $\lambda = 5250 \text{ \AA}$. It operates in the wavelength range $4020 - 8170 \text{ \AA}$ mid-range resolution $R \approx 300$ and the slit width is 1.9 arcsec.

A robotic telescope dictates that the instrument fully integrates into the existing system and is capable of automatically acquiring and observing an object. This was accomplished by having a linear optical path in both imaging and spectroscopic modes. When in imaging mode SPRAT automatically acquires a target onto the slit co-ordinates via world coordinate system fitting then switches into spectroscopic mode for observation.

The instrument was successfully commissioned on the Liverpool Telescope in September 2014 and has been in routine use since then. To characterise the calibration and optical stability of SPRAT an analysis of the long-term thermal and mechanical changes was undertaken. At the mid-range $\lambda = 6000 \text{ \AA}$ the thermal drift in resolution ΔR is 1 K^{-1} . The thermal drift in X and Y axes are $-0.029 \text{ arcsec K}^{-1}$ and $-0.018 \text{ arcsec K}^{-1}$ respectively. Superimposed on the X axis thermal drift is a bimodal shift of $+0.175 \text{ arcsec}$ which is assumed to be mechanical. Slit position stability during an observation is 0.031 arcsec . Focus is thermally and mechanically stable over an operating range $276 - 296 \text{ K}$.

I present 155 observations of supernovae obtained with SPRAT, drawn mainly from the Gaia and ASASS-SN transient surveys. These were used to explore the effects of

wavelength range, signal-to-noise ratio, redshift and l_{dip} on the True/False Positive Rates of supernova classification.

This led to the development of an automated classification pipeline which was applied to spectra of 26 potential electromagnetic counterparts of the LIGO sources GW150914, G194575 and GW151226. This observing programme included successful classification of objects down to magnitude $m \approx 20$, confirming that the key design aim of high-sensitivity instrument had been achieved.

The classification tool selected for observing programmes was the supernova identification tool, SNID (Blondin & Tonry, 2007). To examine and improve the classifications produced an automated script was created to explore the SNID parameter space.

This resulted in the development of an automated classification pipeline

In summary the feasibility of a system for fully automatic classification of transients is illustrated here. Such a systems will be essential in the future transient deluge anticipated by LSST, SKA and aLIGO+Virgo in the next decade.

Publications

In the course of completing the work presented in this thesis, the contents of parts of Chapter 3, parts of Chapter 6 and Appendix E have been submitted and accepted for publication in a refereed journal:

Piasek, A. S., Steele, I. A., Bates, S. D. Mottram, C. J., Smith, R. J., Barnsley, R. M., Bolton, B., Proceedings of the SPIE, Volume 9147, id. 91478H 16 pp. (2014). *SPRAT: Spectrograph for the Rapid Acquisition of Transients*

Piasek, A. S. and Steele, I. A., Proceedings of the SPIE, Volume 9908, id. 99083Z 9 pp. (2016) *Requirement analysis for a modular low resolution spectrograph*

Smith, R. J. and Piasek, A. S. and Steele, I. A., Barnsley, R. M., Proceedings of the SPIE, Volume 9913, id. 991317 20 pp. (2016) *Automated spectral reduction pipelines*

Copperwheat, C. M. and Steele, I. A. and Piasek, A. S. et al., Monthly Notices of the Royal Astronomical Society, Volume 462 3528-3536 pp. (2016) *Liverpool Telescope follow-up of candidate electromagnetic counterparts during the first run of Advanced LIGO*

Steele, I. A. and Copperwheat, C. M. and Piasek, A. S., IAU Symposium, Volume 324 283-286 pp. (2017) *Spectroscopy of candidate electromagnetic counterparts to gravitational wave sources*

Acknowledgements

Foremost to Prof. Iain Steele I offer my sincere thanks for all the help and insights that have illuminated the way and providing inspiration when it was needed. Thanks also to Stuart Bates for his practical advice and making parts fit when they didn't always want to. Many thanks to Robert Smith both for his encyclopedic knowledge of astronomy and attention to detail and to Chris Mottram for his adeptness in persuading recalcitrant software to work.

I am also hugely indebted to those very close friends who provided the most precious gifts of support and encouragement when it was needed most.

Last but not least I thank my lucky stars for the opportunity to contribute a little to the field of astronomy.

*“The inside of the atom is invisible, but there is a window in it,
a stained-glass window. The spectrum of the atom.”*

Dr. Jacob Bronowski

dla Krystyna
“for whome the stars danced”



is so grateful for all the variety and complexity of naturally occurring things, for which this life is too short to investigate.

Contents

Declaration	ii
Publications	v
Contents	ix
List of Tables	xv
List of Figures	xviii
1 Introduction	1
1.1 Overview	1
1.2 The Wavelength and Profile of Line Features in a Spectrum	2
1.2.1 Basic Elements of a Spectrograph	6
1.2.2 Aperture	9
1.2.3 Collimator Lens	10
1.2.4 Filter	10
1.2.5 Data Reduction	10
1.2.6 Transient Astronomy	17

1.2.7	The Liverpool Telescope and SPRAT	18
1.2.8	Thesis Aims	19
2	SPRAT Design and Laboratory Testing	21
2.1	Optical Design	21
2.1.1	Grating	22
2.1.2	CCD Selection	23
2.1.3	Anti-Reflection Coating Selection	26
2.1.4	Predicted Throughput	27
2.2	Experimental Layout	28
2.2.1	Optical Bench	28
2.2.2	Additional Equipment	32
2.2.3	Software	33
2.3	Instrument Testing	34
2.3.1	Nikon Camera Lens Transmittance	34
2.3.2	Monochromator Calibration	37
2.3.3	CCD Operating Temperature	39
2.3.4	Grism Rotation	40
2.3.5	Wavelength Calibration Lamp	41
2.3.6	Flat-Field Lamp	43
2.3.7	Reflections and Ghosting	44

2.3.8	Slit and Grating Alignment	48
2.3.9	Slit Width Calibration	48
2.3.10	Thermal Stability	49
2.4	Mechanical Design	50
2.4.1	Materials	50
2.4.2	Movable Components	51
2.4.3	Flexure	51
2.4.4	Plan View of Instrument	53
2.5	Summary	53
3	SPRAT Commissioning and On-Sky Characterisation	54
3.1	Preliminary Set-Up and Calibration	54
3.2	On-Site Electrical and Software Setup	61
3.3	Measured Instrument Parameters	64
3.4	Locating the Magic Pixel	69
3.5	Effect of Temperature and Orientation	71
3.5.1	Calibration Arc	73
3.6	Stability of Slit Position	80
3.7	Instrumental Zero Point	90
3.8	Measuring Bias that Varies Frame-to-Frame Without an Overscan	92
3.9	Data Pipeline	97

3.10	Conclusions	97
4	Classification of Supernovae with SPRAT	101
4.1	Supernovae	101
4.2	Other Transients	103
4.3	Supernovae Classification	104
4.3.1	Identifying Type I SNe	105
4.3.2	Identifying Type II SNe	108
4.4	Observing Programmes	108
4.5	Surveys and Alert Sources	110
4.5.1	Gaia Alerts	111
4.5.2	Other Alert Sources	116
4.6	Classification Tools	117
4.7	Science Case	119
4.8	Receiver Operating Characteristic (ROC) Metric for Tuning an Automated System	119
4.9	SNID Parameters	122
4.10	Methodology	122
4.11	Window Width	123
4.12	Classification of type Ia SNe	124
4.13	Classification of type Ibc SNe	125
4.14	Classification of type II SNe	127

4.15	Automated Classification Programme	128
4.16	Summary and Conclusions	135
5	Classification of Optical Counterparts for Gravitational Waves	138
5.1	Follow-up of aLIGO Alerts by the LT with SPRAT	138
5.2	Gravitational Wave Events	141
5.2.1	Follow-up of GW150914	141
5.2.2	Follow-up of G194575	143
5.2.3	Follow-up of GW151226	147
5.3	Automated Classification	151
5.4	Conclusions	156
6	Conclusions	158
6.1	Summary of SPRAT performance	158
6.2	Summary of Supernova Characterisation Results	159
6.3	Summary of GW results	161
6.4	Future Work	161
6.4.1	Observational Criteria	162
6.4.2	Design Implications	167
6.4.3	Summary and Conclusions	170
6.5	Final Conclusion	171
	Appendices	173

A	Observing Programme Spectra	174
B	Supplemental Observations	194
C	Gravity Wave Observations	198
D	Xe Arc Calibration Lines	202
E	Experiments with Flat Fielding Methods	204
E.1	Measuring Pixel to Pixel Variation Without the Slit and Dispersing Elements.	205
E.2	The Effect of Geometric Distortions	206
E.3	Use of the Lamp Flat	209
E.4	Use of the sky flat	214
E.5	An Alternative Approach - Correcting Image Distortion	216
E.6	Summary	220
F	List of Observations	221
	Bibliography	228

List of Tables

2.1	Estimated Photon Efficiency at $\lambda = 6000 \text{ \AA}$. Slit losses have been calculated assuming a 2.16 arcsecond slit and modelling the atmospheric seeing as a Gaussian profile with FWHM = 1.0 arcseconds.	27
3.1	Commands to control SPRAT using <code>send-command</code> . If no parameter is supplied to a command then the state is returned.	61
4.1	Transient Surveys - Overview	112
4.2	Transient Surveys - Optical Details	113
4.3	Comparison of redshift and alerting magnitudes	136

5.1	<p>Log of LT observations taken over the first aLIGO science run. For each object we provide the candidate ID and detection date, time and magnitude, as reported to the EM follow-up collaboration via the GRB Coordinates Network. The remaining columns give the date, time, instrument and exposure times of the LT classification observations. We provide references to the GRB Coordinates Network (GCN) circulars for both the transient discovery and the LT follow-up, and other relevant discovery papers, as follows: ¹Smartt et al. (2015), ²Steele et al. (2015a), ³Steele et al. (2015b), ⁴ Smartt et al. (2016), ⁵Singer et al. (2015a), ⁶Steele et al. (2015c), ⁷Steele et al. (2015d), ⁸Steele et al. (2015e), ⁹Cenko et al. (2015), ¹⁰Copperwheat & Steele (2015b), ¹¹Steele & Copperwheat (2015), ¹²Copperwheat & Steele (2015a), ¹³Palliyaguru & Corsi (2015), ¹⁴Copperwheat & Steele (2015c), ¹⁵Copperwheat et al. (2015a), ¹⁶Rabinowitz et al. (2015), ¹⁷Lipunov et al. (2015), ¹⁸Itoh et al. (2015), ¹⁹Palliyaguri et al. (2016, in prep.)</p>	142
5.2	<p>Classifications of transients candidates followed by the LT in response to event G194575. Where we obtain a secure supernova classification we provide a redshift, the time t since peak, and the percentage of matching templates in the SNID database which are consistent with the spectrum.</p>	145
5.3	<p>Classifications of transients candidates followed by the LT in response to event GW151226. Where we obtain a secure supernova classification we provide a redshift, the time t since peak, and the percentage of matching templates in the SNID database which are consistent with the spectrum.</p>	148

5.4	Comparison of SNID redshift and SN age estimation. σ_{zref} is the s.d. when compared against redshifts from 8 external reference sources. All Spectra columns, σ_z and σ_t , are the s.d. of the automated estimates of z and object age against those derived via manual classification. The final columns shows the improvement in age estimation when by eliminating spectra with $SNR < 5.0$	156
6.1	Summary of Transient Classification Programme	160
6.2	Summary of spectrograph requirements for the different science use cases considered. Note that for supernovae and AGN we assume we are observing sources with redshift $z < 0.1$. This is a reasonable reflection of the redshift distribution of supernovae observed to date with SPRAT.	171

List of Figures

1.1	Example low resolution visible spectra illustrating the different in the spectrum signature between type I (no hydrogen) and type II (hydrogen rich) supernovae. The SiII absorption feature in the upper spectrum allows further sub-classification as a type Ia SN. Spectra courtesy of the Weizemann Interactive Supernova Data Repository (Yaron & Gal-Yam, 2012)	4
1.2	The layout of optical elements in a basic spectroscope. The incoming beam is focused onto an aperture, usually a slit. Light from the aperture is formed into collimated beam prior to entering the disperser. The disperser is normally a prism or grating, which spreads the light into its component wavelengths, here shown as a grating operating in transmission. Finally the dispersed beam is focused onto a detector by the camera lens to form the image of a spectrum.	6
1.3	Deflection and dispersion by a prism with refractive index n and apex angle, α . A prism will both deflect and disperse light.	7
1.4	Here the grating line surface is profiled at a “blaze” angle, θ_B and d is the inter-line spacing. At the Littrow condition $\alpha = \beta = \theta_B$	8

1.5	The structure of a VPH grating assembly. The variation in shading within the dichromated gelatine layer indicates a periodic modulation of the refractive index that creates a dispersing grating.	9
1.6	Simulated data processing sequence to eliminate cosmic ray features for the case of 2 spectra. Both simulated spectra, S_1 and S_2 , have a peak and a trough produced by a cosmic ray impinging on the spectral data and adjacent sky respectively. The difference, $S_2 - S_1$, of the two input spectra is evaluated to separate the cosmic ray features from the spectra. Changes in the background sky brightness between the two exposures will introduce an offset. The median value is evaluate and cosmic rays are located by searching for features $> 5\sigma$ from the median. The offset is removed by subtracting the median to produce the correction values and regions not to be corrected are set to zero. The sign of the corrections are restored by comparing the value of S_1 and S_2 where the cosmic rays were detected. Where $S_1 - S_2 + offset > 0$ a correction is negative otherwise it is positive. The correction is subtracted from the sum of the spectra, $S_1 + S_2 - correction$, to produce the final spectrum.	15
1.7	The Liverpool Telescope at La Palma. The spectrograph was mounted on an instrument port on the white A&G box situated below the blue primary mirror cell (Image courtesy of R. J. Smith).	19
2.1	Quantum Efficiency for the BV (visible optimised) variant of the iDus CCD. The instrument operating wavelength range is shaded. Graph courtesy of Andor Technology.	24

2.2	The instrument layout showing the position of the optical elements. For clarity the camera lens is shown as a single doublet rather than the actual 6 elements of the AF Nikkor.	25
2.3	VIS-NIR (visible near IR) coating reflectance curve for light normally incident to a surface. Instrument operating range is shown shaded. (Courtesy of Edmund Optics)	26
2.4	The predicted total photon efficiency for normal operation is shown in red and is centered on 6000 Å with the beam normally incident onto the grism assembly. When the grism is rotated, the response becomes centered on ~5500 Å as shown by the blue plot.	28
2.5	Predicted SNRs at selected exposures for object of magnitude $M_v=14,16,18$ & 20 in normal operation.	29
2.6	Initial Optical Bench Layout. Measurements were taken with lights out and extraneous light from other equipment was excluded by enclosing the optical paths as shown. The CCD mount was an adjustable scissor type but exhibited excessive vertical and lateral play of several millimeters.	29

2.7	Final Optical Bench Layout. To allow instrument focusing and slit calibration by the telescope the Andor camera was removable and placed on top of the main optical bench (silver). Accurate camera re-positioning was achieved by fixed alignment plates and confirmed with a lateral displacement caliper. An additional small rectangular rotation plate and adjacent blue marks positioned the camera with a fixed rotation for viewing the 0 th order diffraction minimum. The other optical parts were mounted along a 4-bar optical cage secured to a large Melles Griot plate (black) bolted onto the main bench. The grism assembly was mounted on a front pivoting 4-bar mini-cage that could be rotated through -0.5 to $+6.0$ degrees via a micrometer acting on a sprung lever-arm. The lever geometry gave an angular rotation of 0.64° per mm. The slit opens symmetrically and the width was measured by directly using a dial-gauge.	30
2.8	The AF Nikkor f/1.8D camera lens internal layout showing the 6 air-gapped elements. The 12 curved surface interfaces present potential sources of light loss and internal reflections.	35
2.9	The Nikon Nikkor CCD camera lens transmission losses	36
2.10	Krypton bright emission lines in the visible. Courtesy of LOT-Oriel	38
2.11	The CCD cooling at a typical dark-room ambient temperature showing the cooling rate tail-off as ΔT increases. -60°C was the target temperature used for dark-room testing.	39
2.12	The variation of current variation with temperature for the BV variant of the iDus CCD. The tail-off at -80°C indicates that further cooling provides little further benefit in reducing electron noise. Graph courtesy of Andor Technology	40

2.13	The rotation of the grism illustrates the relative change in Kr emission line intensities. During testing, the instrument was optimised for green, 557 nm, which peaks at $\sim 1.75^\circ$. The blue 446 nm line peaks at $\sim 3.5^\circ$, more than double the intensity, suggesting that a selectable grating position would be of advantage.	41
2.14	Example of spectra taken during evaluation of wavelength calibration sources. Neon had a limited set of lines available for wavelength calibration in the visible. The slit width was reduced to $100\mu\text{m}$ to sharpen lines and exposure increased in an attempt to improve detection of fainter lines. Xenon provided the best set of calibration lines without saturating any prominent lines. Krypton shows the green, 556/557 nm and orange, 587 nm lines used when calibrating the monochromator. The prominent double at 758/760 nm is also evident and produced the ghost image on the left of the spectrum. To eliminate saturation of this line the image was take with a neutral density filter reducing the intensity of other lines.	42
2.15	Initial calibration arc lamp evaluation showed Ne as unsuitable because of its limited range of lines in the visible. Kr provided the widest range but produces a bright line at 7602 Å. All arcs showed a gap at centered around 5300 Å.	43
2.16	Calibration arc evaluation augmented with lines from NIST. Xenon now has the widest overall range and a reduced $\sim 5300\text{Å}$ gap so was selected as calibration source.	44

2.17	Wlamp is a generic 12V tungsten torch bulb. Two automotive lamps were evaluated. 233LB is tungsten with blue filter and Bosch434 a clear tungsten halide. Automotive lamps are designed to operate at 12.6V so were operated at 12.0V and at a small over voltage for comparison.	45
2.18	The effect of blue gel filters on the spectrum of the Bosch434 tungsten halide bulb was evaluated. Roscolux 3216 showed the least modulation and increased the relative intensity in the blue.	45
2.19	The effect of lateral mis-alignment of camera lens at 0.05 mm and 3.99 mm offsets from the optical axis. Not shown here but at a 0.50 mm offset the central reflection began to the first exhibit the ellipticity that is prominent in the right image. At 3.99 mm the additional ghosting extended beyond the field of view. Angular mis-alignment showed similar effects. The reflection arcs also show the unexpected displacement between the CCD chip center and the lens mount center.	46
2.20	This over-exposed Kr spectrum was made during ghost detection with a narrow 50 μ m slit. The bright 7602 Å line on the right is saturated and ghost lines extend into the lower masked region. Their intensity varies along the y-axis and can exhibit a ribbon like appearance. . . .	47
2.21	A mis-aligned grating is evident in this Kr spectrum where the upper and lower edges are not horizontal and was corrected by rotating the grating within the grism assembly. A very narrow slit width was used, \sim 5 μ m and dust contamination on the knife-edges produced streaks. The dust was removed using compressed gas optical cleaner.	48
2.22	Variable width slit calibration curve. The non-linear response is indicative that the knife-edge movement was not symmetric.	49

2.23	Pseudo optical bench sub-assembly.	50
2.24	1. Calibration mirror deployment, 2. Slit deployment, 3&4. Grism and rotation angle stop deployment	51
2.25	Telescope at zenith, A&G box rotated with instrument upright and horizontal, the maximum predicted deflection at the rear of the camera is 0.0017mm.	52
2.26	Telescope at horizon (worst case and not actually possible as minimum altitude angle is 25°), A&G box rotated with instrument on its side and horizontal, the maximum predicted displacement at the rear of the camera is 0.0022mm.	52
2.27	A plan view of the instrument identifying the optical elements. 1. Arc/Flat Calibration Angled Mirror (dark grey), 2. Slit (red), 3. Field Lens (blue), 4. Long-pass Filter (cyan), 5. Collimator Lens (blue), 6. 1 st Prism (green), 7. VPH Grating (yellow), 8. 2 nd Prism (green), 9. Camera Lens (cyan), 10. CCD (dark red)	53
3.1	View of SPRAT with auto-collimator fitted to entrance port. The auto collimator bolts onto the front plate and is centered on the entrance aperture. The optics were aligned prior to shipping and re-checked at site before the installation on the LT. This view shows the pneumatic valves and silver actuator pistons, and gray electrical junction box. . .	56
3.2	Fine focus setting using the slit image. A narrow slit was illuminated with an LED torch. The focus micrometer was moved through the visually estimated focus point at 6.80mm in 0.25mm increments. The minimum width of the slit image, and hence best focus, occurred at 7.00mm.	57

3.3	<p>Comparison of Kr arcs before and after the addition of baffling to exclude stray light entering from the front of the instrument. A thin slit width was set during alignment and testing. Contamination from stray light is evident in the centre of the spectrum in the upper pre-baffled image. The exposure was $t = 0.01$ ms to avoid saturation and highlights the bright band on the right of the region affected. The lower image was taken with $t = 1000$ ms, the longer exposure showing the improvement after the addition of 3 sets of baffles. Two baffles were across the full internal width, surrounding the order-blocking/field lens mount and around the slit. A third baffle was added to the slit front to block light by-passing the knife-edge support ring. The aperture masking on the slit front was later modified so the top of the spectrum was included.</p>	58
3.4	<p>The change in spectral response of a flat lamp image with grism rotation. The intensity change is the difference in counts relative to the average value. Grism rotation is expressed in mm displacement of the position stop. The maximum mean value is $\sim 12,000$ counts.</p>	60

3.5	The mounting of SPRAT on port 8 of the Liverpool Telescope. A demountable rear stand was attached to keep the instrument horizontal on scissor-lift table during installation. Gray cables carry electrical signals to the left side square junction box. Below it is a white block housing the pneumatic valves controlling the actuators. The black feed pipes have in-line regulators to set the maximum applied force and lead to the actuator cylinders. On the extreme left is the vertically mounted control panel containing the Arduino and power supply. The photo was taken mid-installation without the top cover fitted to allow actuator operation to be verified. Still to be fitted are the umbilical cables from the control panel and the Andor PSU, shutter control box and calibration arc power supply. The USB fibre extender (not shown) was installed next to A&G port 1, immediately to the right of the instrument. . . .	63
3.6	Xe emission arc in red (upper) and blue (lower) mode. The arc lamp manufacturer list of identifiable lines (Oriol-Instruments, 2008) was supplemented with bright lines from the NIST online database (physics.nist.gov, 2013). The intensity is derived from count and normalised to the brightest observed line.	65
3.7	The error between individual emission line wavelengths and a 4 th order polynomial fit. The overall RMS error is 0.30 Å in both modes. . . .	66
3.8	The deviation from linear wavelength to pixel mapping of the image of a spectrum image in red and blue modes. A 4 th order polynomial fitted to identified Xe emission lines has an RMS error of 0.30 Å in both modes. Rotating the grism produces a horizontal shift of 4 pixels in the spectrum image between red and blue modes. The order blocking filter cut-off clips the spectrum below ~4020 Å X=129 in blue and X=133 in red mode.	66

3.9	Comparison of Xe arc and 1H0323+342 emission lines widths. The width was determined at FWHM (Full Width at Half Maximum). The arc line widths are approximately constant across wavelengths while those of 1H0323+342 are on average narrower. A point source does not fill the slit width resulting in a higher resolving power.	69
3.10	Measured optical throughput in red and blue modes.	69
3.11	Sequence to observe standard star BD+40 4032 in blue mode taken during commissioning. 1) Acquisition mode showing target on magic pixel prior to slit deployment. 2) Slit deployed to confirm target star centered within slit. 3) Normal long-slit spectrum in blue mode. 4) Slit-less spectrum in blue mode. 5) Slit, grism and calibration mirror deployed for wavelength calibration using the built-in Xe arc lamp.	72
3.12	The emission line X-axis shift relative to datum spectra taken on MJD=57474 of a standard star BD+33 2642. The displacement between red and blue is a result of grism rotation shifting the optical beam when switching modes. The initial peak at MJD=57100 is prior to testing an alternative camera lens which disturbed the optical alignment. Post MJD=57200 the SPRAT optical system remained unmodified. A seasonal variation is evident in the 1 year interval between maxima. Gaps in the data are associated with engineering work and hardware outages.	75

- 3.13 The variation in the X-axis position of the Xe calibration emission lines. There is a correlation between X-axis shift and instrument internal temperature in both red and blue modes. Red and blue were analysed separately to remove any shifts caused by grism rotation when changing peak colour sensitivity modes. The bimodal distribution of data into two groups with a separation of ~ 0.4 pixel was unexpected. The points are colour coded by MJD date to show seasonal change which is evident in the grouping of yellow and blue points. 76
- 3.14 The variation in Y-axis shift with temperature was measured using dust lines as pseudo-absorption lines. The Y-axis shift shows a significant temperature correlation. The bimodal distribution that was shown in the X-axis data is much weaker and is largely absent from the blue mode data. The data points are colour coded by MJD date to highlight seasonal changes. The spread of coloured date coded points is evidence of a long term change, ~ 0.5 pixel year⁻¹. 77
- 3.15 The variation in Y-axis shift over time of 5 isotherms in the range $T = 279 - 284$ K. The most populated temperature intervals in red mode were selected resulting in a preferential clustering of dates centered around Spring 2015 and Spring 2016. The drift is 0.0014 pixel day⁻¹ which equates to an annual rate of ~ 0.5 pixel year⁻¹. 78

3.16	X- and Y-axis shifts with change in Cassegrain rotator angle. The sample is heavily biased to 11 degrees as this aligns the slit with the parallactic angle. The X-axis shift shows no correlation with Cassegrain angle with high values of $P > 0.8$. For Y-axis shift Spearman's rank correlation is ambiguous, $P_{\text{red}} = 0.061$, too low a confidence yet $P_{\text{blue}} = 0.001$. A change in gravity vector would be expected to have a common effect on both modes. Around the 11 degree point the data has a large scatter with mean red/blue s.d. = 0.47 pixels. Together with the large sampling bias means that the correlation is inconclusive.	79
3.17	Variation of X-axis shift with altitude angle at temperature $T = 281$ K. Temperature effects were minimised by selecting a reduced data set with $\Delta T = 1$ K. There is no indication of a correlation with temperature. Both blue and red data is poorly sampled above altitude angle 70 degrees with only data 3 points.	80
3.18	Variation in X-axis shift with altitude angle corrected for temperature. Compensating for thermal effects and the larger data sample shows a correlation between instrument orientation and X-axis shift.	80
3.19	Xe calibration arc X- and Y-axes shifts were not expected to correlate to azimuth position. The clustering of observation points is from arcs taken for standard stars and long term monitoring of 1H0323+342. Both X- and Y-axis shifts show no correlation with telescope azimuth angle.	81
3.20	A stacked spectrum of Seyfert galaxy 1H0323+342. This is the combined spectrum from 111 observations taken between MJD 56998 and 57714.	82

- 3.21 The relative X-axis displacement of the slit image relative to a datum image taken a temperature $T = 286$ K. The shift was determined with FIGARO `scross` and `peak` utilities sampling 21 pixel long sections of the slit above and below the target over the two Y co-ordinate ranges shown. The different sampling methods and regions produce consistent results. There is a clear correlation with temperature with the mean X-shift coefficient value -0.039 pixels K^{-1} 83
- 3.22 The X-axis thermal stability of the slit obtained by measuring the apparent width using `peak`, which returns the FWHM width. A temperature dependence of the slit width was expected and the mean X-axis coefficient was -0.018 pixel K^{-1} . The difference between the upper and lower width measurement indicates the slit width is not uniform and narrows by 0.0016 X-pixel per Y-pixel. Shortcomings of this method are that it measures the apparent FWHM width and includes any widening caused by a focus change. 84
- 3.23 A method to decouple the effect of defocus when measuring the slit width. Upper plot is the X-axis cross-section of an ideal slit image (left) and the effect of defocussing (right). The profile of a de-focused edge approximates to a Gaussian curve with the gradient maximum at the mid-point of the curve. The middle plot is the derivatives of the corresponding upper cross-sections. The distance between maxima of the peaks in the derivative remains constant for both an ideal and de-focused image. The FIGARO `idiff` utility does not preserve the sign of a detected edge and returns the positive absolute value of the gradient (lower plot). A change in the width of an edge peak indicates the focus has altered. 85

3.24	The stability of X-axis width with change in temperature obtained using the derivative of the image to detect edges. This method eliminates defocussing effects when measuring the apparent slit width on a raw image and shows a thermal coefficient $-0.011 \text{ pixel K}^{-1}$	86
3.25	The stability of the slit X-axis position during an observation. The position of the slit edges was taken pre- and post-observation and compared to a datum observation taken at temperature, $T = 285 \text{ K}$. The mean of the standard deviation for left and right edge X-axis shift is s.d. 0.07 pixels, showing that generally there is little movement during an observation. However there are 3 observation with a large shift of $\sim 0.3 \text{ pixel}$ occurred.	87
3.26	Change in the estimated seeing, ESTSEE, viewed at the slit (upper plot) and RCS seeing from the IO:O imager (lower plot) with temperature.	88
3.27	The difference between SPRAT slit and RCS reported seeing measured by optical imager IO:O. The atmospheric seeing was derived from the target object size. Both SPRAT and IO:O estimation of seeing show a temperature dependence. To de-couple common-mode thermal effects the RCS reported seeing was subtracted from the SPRAT seeing taken on the same observing night. The resulting plot shows no correlation with the instrument internal temperature and hence no detectable change in image size caused by a thermally induced defocus.	89

3.28	Variation in focus with temperature using slit-edge image sharpness. The <code>idiff</code> derivative of the slit image was first taken to detect slit edges. The offset between the left and right edges was attributed to differences in their edge sharpness and surface reflectivity. The width of the detected edges was measured with <code>peak</code> over the sample range $Y=100-120$. The lack of correlation shows that focus remains stable over the an internal temperature range of 25K.	89
3.29	Variation in focus with altitude angle using slit-edge image sharpness. The focus does small correlation with telescope altitude angle with a mean coefficient of $0.0035 \text{ pixel degree}^{-1}$	90
3.30	The distribution in the X- and Y-axis acquisition position of object 1H0323+342. The offsets are with respect to the magic pixel coordinate at $X = 479, Y = 179$	91
3.31	The instrumental zero-point Z derived from the observation of photometric standard BD+33 2642. Z was derived from L2 pipeline spectrum which performs 2x pixel binning and should be proportionally scaled for photometry at different levels of binning.	92
3.32	short caption	93
3.33	short caption	95

4.1	Supernova classification uses spectroscopic and photometric features to differentiate the object classes. Progenitors are thought to arise from two population, either Chandrasekhar limit white dwarf stars or late stage massive stars undergoing core collapse. The lack of H and He features in core collapse SNe is thought to be the result of loss of outer layers stripped by a close binary companion or by stellar wind loss in a Wolf-Rayet progenitor. (Image adapted from the original by Stephane Blondin)	106
4.2	Bolometric light curves for type Ia SNe illustrating the correlation between sharpness of the peak and luminosity. 1991bg and 1999by exhibit normal light curves but are under-luminous and 1991T is over-luminous. The remaining SNe are normal type Ia.	107
4.3	Accurate sub-type classification requires photometric data to complement initial spectroscopic observation. (Image from Wiki-commons) .	109
4.4	Gaia Photometric Survey alerting magnitudes. Spectroscopic observation were scheduled for alert objects brighter than 18.5 magnitude. It was noted that at day 74 of the validation phase alerts were limited <19.0 although this selection was removed post-hiatus.	114
4.5	The number of alerts generated per 0.5 magnitude interval. The first 8 points show a linear relationship for all 3 sample sets and the dotted lines are fitted to these points. Fainter than magnitude 19.0 and the LogN/LogS relationship breaks down indicating the data is incomplete.	115

4.6	Gaia Photometric Survey object declination. The declination observing limit was set to -30° . Some objects above the limit were not observable because of RA. The initial validation phase exhibited a northern hemisphere bias with few objects below -30°	116
4.7	The delay between detection and publication of Gaia alerts often exhibited an episodic pattern even post hiatus. The accumulation of detections is shown by a linear decrease in delay (purple) preceding a vertical set of published alerts points (green). The alert list only began providing both the detection and publish dates after 2014-11-07 (day 104). Delays >50 days are not shown.	117
4.8	The mean publishing delay over a 7 day interval shows a significant decreased with time. The shortest delays, with a mean value of 1.8 days, occurring in the interval between day 570 – 595	118
4.9	An ROC graph plots TPR against FPR for different version of a test. It is desirable for points to occupy the upper left sector. Point A is the perfect test result with all classifications correct and no mis-identifications. Points B and C are more typical, point B having a lower proportion of false identifications at the cost of fewer sought after types identified than point C. For points on the line $TPR = FPR$ such as D, the result is no better than random choice. For points below the line, E, the test is worse than random and the test result should be inverted to move the point above the line. Youden’s J statistic is the distance of a point above random choice and provides a single evaluation metric, However J can have more than one maximum, e.g. both J_B and $J_C = 0.5$ for two different versions of a test.	121

4.10	The change in TPR (left) and FPR (right) after forcing the redshift z , where known, for all spectra with SNR >0 . Applying a known z was expected to improve both TPR and FPR in all cases but the FPR increased for type II SNe for window size $>3500 \text{ \AA}$	125
4.11	Type Ia SN ROC for classification using different SNID template sets. The left column are without z the right column shows the improvement in classification when z is known. For a particular window size the SNR limit of the sampled set is progressively increased from >0 to >15 in increments of 5. SNR increases right to left along each line.	126
4.12	Type Ibc SN ROC for classification using different SNID template sets. For a particular window size the SNR limit of the sampled set is progressively increased from >0 to >15 in increments of 5. SNR increases right to left along each line.	129
4.13	Type II SN ROC for classification using different SNID template sets. For a particular window size the SNR limit of the sampled set is progressively increased from >0 to >15 in increments of 5. SNR increases right to left along each line.	130
4.14	All SN ROC for classification using different SNID template sets. For a particular window size the SNR of the sampled set is progressively changed from >0 to >15 in increments of 5.	131
4.15	AT2016coi is example of a SNID template mis-match. In red is best type match as suggested by SNID ($rlap=0.625$, $rlap=5.7$), blue shows the closest match ($lap=0.685$, $rlap=5.7$) obtained by visual selection from other suggested templates.	132

4.16	To capture the earliest phase in the evolution of a transient, the delay between the initial detection and the classification should be a minimum. The delays for the 4 principal sources of transient surveys used in the observing programme are shown here. The lack of data points centered around 57300 MJD were a result of engineering work on the telescope.	133
4.17	This shows the correlation between SNID estimated redshifts and those derived from host galaxies for particular SN types. The solid black line is the linear fit for all SN types and the dashed black the ideal fit. The correlation including all types except Ic is shown in black and has gradient 1.11	134
4.18	The distribution of redshift, magnitude and classification from the 3 main alert sources used. Gaia and ASAS-SN are surveys whereas TNS aggregates alerts from many sources. Oth denotes other non-SN objects. Unk indicates an unknown classification indicating an ambiguous or failed observation.	135
5.1	Spectrum of PS15ccx obtained during the follow-up campaign of event GW150914. We also plot the best supernova Type Ia (red, dashed) and supernova Type Ic (green, dotted) template fits.	141
5.2	Spectra obtained during the follow-up campaign of event G194575. We omit candidates for which our observations showed no evidence of a transient. For objects where a supernova identification is obtained via SNID, we overplot the best template fit (red line, dashed).	144

5.3	Spectra obtained during the follow-up campaign of event GW151226. We omit candidates for which our observations showed no evidence of a transient. For objects where a supernova identification is obtained via SNID, we overplot the best template fit (red line, dashed).	147
5.4	The SNR for GW targets for which a classification was obtained. For spectra with SNR <5, reducing the wavelength range to 3500 Å the mean improvement was +0.59. For spectra with SNR >the mean increase was +4.44. Despite a low SNR, 5 of 9 noisy spectra with SNR <5, produced automatic classification which matched manual identification. The large improvement in the SNR of iPTF15dkk was due to the removal of single broad cosmic ray signal at ~ 7800 Å.	152
5.5	Initial classification was done using SNID and selecting the closest matching full 4000 Å width spectrum by manual comparison. This is compared with automated classification which used the closest match as determined by the SNID <code>r_{lap}</code> parameter. Automated classification was performed with both the full 4000 Å and a symmetrically reduced 3500 Å wavelength range. The spectrum of PS15ccx could match either Ia or Ic so the classification is shown as Fail.	153
5.6	The SNID estimated redshift for manually classified objects compared with automated classification at full 4000 Å and reduced 3500 Å wavelength range. All reference redshifts, blue circles, were derived either from nearest host galaxy z , or NED and SIMBAD databases with the exception of iPTF15fel which as obtained from ATel # 8498.	155

5.7	The SNID estimated ages relative to day of maximum luminosity are compared between manual and automated classification. Compared with the automated 4000 Å the 3500 Å range over-estimates age by an average of 4.7 days.	156
6.1	The possible spectral range in the optical from which a sub-range can be selected for a final instrument. The upper (violet) lines are from the SDSS reference list which includes H, He and metals. The center (red) are lines and features significant for differentiating supernovae types. The lower (blue) lines show cometary molecular species which predominate towards the blue/UV.	163
6.2	Angular separation between for 112 SN observed using SPRAT showing that >50% of SN were within 4 arcsec of the host galaxy. The largest observed separation being 44 arcsec, less than half the slit length limit set by the requirements for observation of comet coma.	166
6.3	The average number of stars above a visible magnitude within a fixed radius of a central star. This is an all sky mean and does not take account of the higher density of stars in the galactic plane.	167
6.4	Angular displacement from a central wavelength of 5000 Å caused by atmospheric refraction.	170

Chapter 1

Introduction

This thesis describes the design, construction and evaluation of a Spectrograph for the Rapid Analysis of Transients (SPRAT) and its application to the observation and classification of transient astrophysical sources.

1.1 Overview

An astronomical spectrograph is a scientific instrument to analyze light from a celestial object by dispersing light into component wavelengths. By examining the position and relative intensity of distinct features in the spectrum we can gain knowledge about the velocity relative to the observer, the chemical composition and material dynamics.

The analysis of light from an object was first formally described in Opticks (Newton, 1704) where Newton elegantly showed that a narrow shaft of sunlight could be spread into a continuous spectrum by passing through a prism. This separation of the component wavelengths of light by passing through a dispersive element remains the fundamental principle of operation in all optical spectroscopic instruments.

Later it was discovered that the solar spectrum contain discontinuities in the form of

discrete dark lines, firstly by William Hyde Woolaston in 1704 and again by Joseph von Fraunhofer in 1714. Robert Bunsen and Gustave Kirchhoff independently established that positions of some of the dark lines coincided with the bright emission lines of known terrestrial elements and were caused by absorption of light by those elements. Kirchhoff went on to use this as a method to observe differences in the composition between the Sun and bright stars thus establishing stellar spectroscopy. The analytical utility of spectroscopy was further shown in 1898 when the yellow line in the solar spectrum at 5876 \AA was attributed to a new element, Helium, by Norman Lockyer and Jules Janssen. Detailed spectroscopic analysis remains a time efficient method of extracting information about a celestial object from a single observation.

1.2 The Wavelength and Profile of Line Features in a Spectrum

Many physical processes result in the emission, absorption of a photon or cause an apparent change in its wavelength or polarisation. The relative intensities along the wavelength domain of a spectrum provide a signature that can identify the source, for example to differentiate between type I & II SNe (Figure 1.1). The position and shape of individual features provide further information about the originating physical process. Interpretation of a spectrum entails disentangling which physical process created each feature to gain the information such as:

Relative Velocity: An apparent wavelength change, $\Delta\lambda$, of an identifiable feature with known rest wavelength, λ_0 , indicates relative motion. The velocity, v , of the source relative to the observer is then given by the Doppler equation

$$\frac{v}{c} = \frac{\Delta\lambda}{\lambda_0} \quad (1.1)$$

where c is the speed of light.

Chemical Composition: The electrons of an atom can only be bound at discrete energy levels that are dependent on the electrostatic potential, and hence atomic number, Z , of the nucleus. The transition of an electron between energy levels either requires energy absorption or energy emission. The energy is normally in the form of a single photon. Accurate measurement of the wavelength of the photon provides an indirect method of determining which transition generated it and hence the atomic number of the originating element. Similarly, photons from electron transition during ionisation processes in a molecule can identify the radical involved. This set of possible photon energies allow chemical composition and relative abundance to be inferred from the observed line wavelengths and strengths.

For transitions in simple hydrogen-like (single electron) atoms and ions the wavelengths are given by the Rydberg equation,

$$\frac{1}{\lambda} = RZ^2 \left(\frac{1}{n_f^2} - \frac{1}{n_i^2} \right) \quad (1.2)$$

Where n_i and n_f are the initial and final energy levels, given by the principal quantum numbers and the Rydberg constant, $R = 10.974 \times 10^6 \text{ m}^{-1}$. The Balmer series of transitions ($n_f = 2$) predominantly produce lines in the visible including the principal hydrogen lines with wavelengths in air of $H_\alpha = 6562.72 \text{ \AA}$, $H_\beta = 4861.35 \text{ \AA}$ and $H_\gamma = 4340.47 \text{ \AA}$ (physics.nist.gov, 2013) and are within the range of the instrument.

A primary role of the instrument is supernova classification. Differentiation between type Ia, Ib, Ic and type II supernovae is based on the relative abundance of hydrogen, helium and silicon and the instrument wavelength range includes the HeI, SiI and SiII lines, Figure 1.1. Finer sub-classification is possible using late-time emissions from CaII and OI lines. NaI, MgII and FeII lines fall within range providing spectral infor-

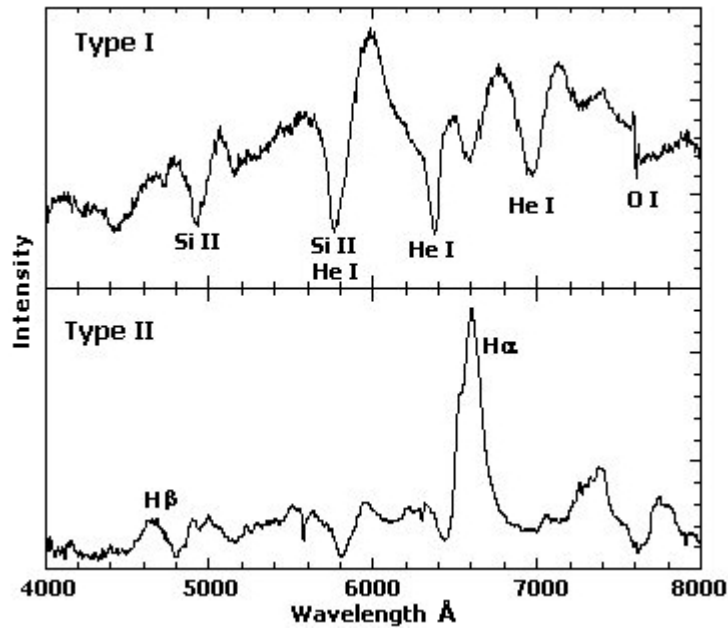


Figure 1.1: Example low resolution visible spectra illustrating the different in the spectrum signature between type I (no hydrogen) and type II (hydrogen rich) supernovae. The SiII absorption feature in the upper spectrum allows further sub-classification as a type Ia SN. Spectra courtesy of the Weizmann Interactive Supernova Data Repository (Yaron & Gal-Yam, 2012)

mation for other types of object.

Temperature and Pressure: An incandescent stellar source approximates to a black body with a continuous spectrum and a temperature can be obtained using Plank's law,

$$I_{\lambda}(T) = \frac{2hc^2}{\lambda^5 (e^{\frac{hc}{\lambda kT}} - 1)} \text{ Wsr}^{-1}\text{m}^{-3} \quad (1.3)$$

The peak wavelength value λ_{peak} at absolute temperature T can be derived by differentiation and solving to obtain Wien's displacement law,

$$T = \frac{b}{\lambda_{peak}} \text{ K} \quad (1.4)$$

where Wien's constant, $b = 2.8978 \times 10^{-3}$ mK.

Temperature can also be obtained by analysis of lines that have been Doppler broad-

ened. An emission line has an intrinsic broadening ($\Delta\lambda_i$) resulting from the uncertainty principle and is a function of the wavelength and lifetimes (t_i and t_f) of the electron in the initial and final excited energy levels,

$$\Delta\lambda_i \approx \frac{\lambda^2}{2\pi c} \left(\frac{1}{t_i} + \frac{1}{t_f} \right) \quad (1.5)$$

$$\approx 4.57 \times 10^{-4} \text{ \AA} \quad (\text{for H}_\alpha) \quad (1.6)$$

The speeds of unbound atoms of mass m follows a Maxwell-Boltzmann distribution and the wavelength of emitted or absorbed light is Doppler shifted resulting in line broadening ($\Delta\lambda_d$) with a Gaussian profile,

$$\Delta\lambda_d = \frac{2\lambda}{c} \sqrt{\frac{2kT}{m}} \quad (1.7)$$

$$\approx 0.430 \text{ \AA} \quad (\text{H}_\alpha \text{ at } 6000\text{K}) \quad (1.8)$$

This is ≈ 3 orders of magnitude greater than the intrinsic broadening in Equation (1.6).

Collisions with neutral particles and ions with in gas or plasma perturbs atomic energy levels and produces a line broadening ($\Delta\lambda_p$) that depends on the mean time between encounters. This collision frequency depends on the number density n , which is proportional to pressure. Pressure broadening produces a Lorentzian line profile given by,

$$\Delta\lambda_p \approx \frac{\lambda^2 n \sigma}{c\pi} \sqrt{\frac{2kT}{m}} \quad (1.9)$$

$$\approx 2.35 \times 10^{-4} \text{ \AA} \quad (\text{e.g. at the solar surface}) \quad (1.10)$$

where σ is the collision cross-section for particles of mass, m at temperature T . This is of the same order of magnitude as the intrinsic broadening.

1.2.1 Basic Elements of a Spectrograph

As in Newton's original experiment, the core optical component common to all spectrographs is a dispersive element. The two types of dispersive element that may be used to form a spectrum and/or deflect light are the prism and the diffraction grating. The other optical components usually found in a modern spectrograph are an aperture slit onto which the image is focused, followed by a collimator lens to produce a parallel beam into the disperser. The final dispersed beam is focused by an imaging lens onto a detector array (Figure 1.2). A single grating produces overlapping diffraction orders so the wavelength range is normally limited by the addition of a filter.

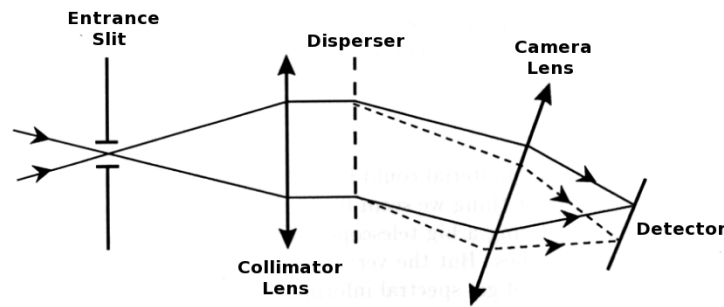


Figure 1.2: The layout of optical elements in a basic spectroscope. The incoming beam is focused onto an aperture, usually a slit. Light from the aperture is formed into collimated beam prior to entering the disperser. The disperser is normally a prism or grating, which spreads the light into its component wavelengths, here shown as a grating operating in transmission. Finally the dispersed beam is focused onto a detector by the camera lens to form the image of a spectrum.

Prism as Dispersive Element

The deflection, θ , of a plane wavefront passing through a prism depends on the difference between the refractive indices of air and glass and on the apex angle, α , as shown in figure 1.3. For small α ,

$$\theta \approx (n_{\text{glass}} - n_{\text{air}})\alpha \quad (1.11)$$

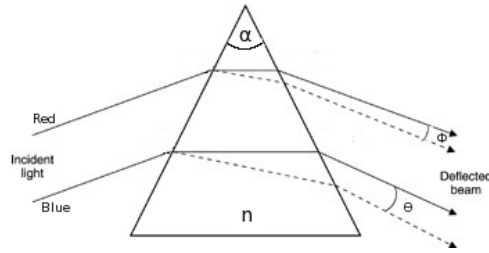


Figure 1.3: Deflection and dispersion by a prism with refractive index n and apex angle, α . A prism will both deflect and disperse light.

The refractive index varies with wavelength so that for polychromatic light θ will also vary thus spreading the input beam into a spectrum. For transparent materials the variance of refractive index with wavelength is characterised by the Abbe number, V ,

$$V = \frac{n_d - 1}{n_F - n_C} \quad (1.12)$$

Derived from the refractive indexes n_d , n_F , n_C at the wavelength of the Fraunhofer spectral lines D- (5893 Å), F- (4861 Å) and C- (6563 Å) respectively. Low values of V indicate high dispersion.

Grating as Dispersive Element

For a grating with lines set d distance apart, light of wavelength λ striking at an incident angle θ_i from the normal will be deflected by an angle θ_m as given by the grating equation,

$$d(\sin(\theta_m) + \sin(\theta_i)) = m\lambda \quad (1.13)$$

where m is the diffraction order $\pm m = (1, 2, 3, \dots)$.

Solving for maximum, the deflection angle, θ_m of the m^{th} order diffraction for a wavelength, λ , is given by,

$$\theta_m = \sin^{-1} \left(\frac{m\lambda}{d} - \sin(\theta_i) \right) \quad (1.14)$$

For the simple case of light normally incident to the plane of the grating, $\theta_i = 0$ and the 1st order diffraction this simplifies to:

$$\theta = \sin^{-1} \left(\frac{\lambda}{d} \right) \quad (1.15)$$

A grating may be optimised (“blazed”) for a particular diffraction order by adjusting the profile of the ruled lines such that the incident angle to the surface of a ruled line equals the diffraction angle, the Littrow condition (Figure 1.4). This also applies to transmission gratings.

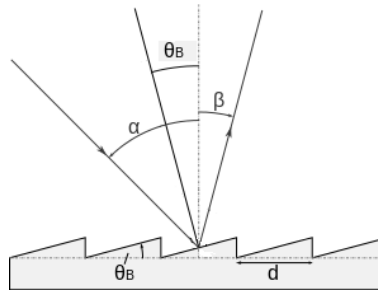


Figure 1.4: Here the grating line surface is profiled at a “blaze” angle, θ_B and d is the inter-line spacing. At the Littrow condition $\alpha = \beta = \theta_B$.

The equation for the resolving power, R , of a grating spectrograph operating in first order at wavelength λ with a collimated beam width W and on sky slit width χ arcseconds on a telescope with a primary mirror of diameter D is given by Equation 1.16.

$$R = \frac{\rho \lambda W}{\chi D} \quad (1.16)$$

where ρ is the grating line density in lines per metre.

Derivation of equations above (1.11 to 1.16) are not given here as they are available in standard reference texts (Born & Wolf (1999) and Brown (1965)) and also in spectrograph design literature (Eversberg & Vollmann, 2015).

Volume Phase Holographic (VPH) Grating

VPH gratings provides a low cost, high transmission efficiency (up to $\sim 80\%$) alternative to conventionally surface ruled gratings and exhibit low levels of ghosting/scattering (Barden et al., 1998). VPH gratings employ a thin photographically sensitive dichromated gelatine layer encapsulated in optical adhesive between anti-reflective (AR) coated glass (Figure 1.5). The gelatine layer has a periodic, sinusoidally modulated reflective index imposed upon it using a holographic process to create a dispersive element. The modulation runs across the plane containing the layer, analogous to the ruled lines of a conventional grating. The low cost and high transmission of VPH gratings makes them an attractive alternative to conventional ruled gratings and so were selected as the primary dispersive element for this instrument.

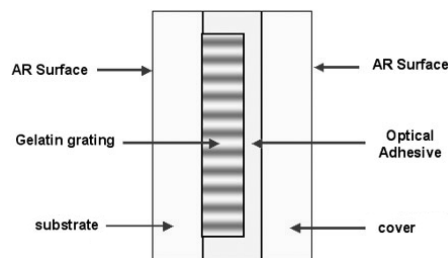


Figure 1.5: The structure of a VPH grating assembly. The variation in shading within the dichromated gelatine layer indicates a periodic modulation of the refractive index that creates a dispersing grating.

1.2.2 Aperture

For point sources entrance aperture coincident with the focal plane excludes light for adjacent objects. It normally takes the form a fixed width slit with the long axis perpendicular to the dispersion direction. The resulting spectrum is formed from wavelength dispersed images of an aperture. Hence resolving power, R , depends on the slit width. A slit can produce diffraction and obscuration losses and so a target must be accurately positioned centrally to maximise the flux throughput. Light from targets away from the

zenith undergoes atmospheric dispersion which elongates the object image. To maximise the light received a spectrograph is usually orientated such that the direction of sky dispersion lies along the slit.

With slitless spectroscopy it is possible to eliminate slit/obscuration losses. Contamination by overlapping spectra from the sky or nearby objects makes this method suitable for bright, isolated point sources.

1.2.3 Collimator Lens

The beam emerging from the focal plane diverges so does not present a parallel wavefront and results in a varying incidence angle θ_i across the disperser. A parallel wavefront is a requirement for a grating (the far field approximation). To correct for this a converging collimator lens is placed at its focal distance following the aperture.

1.2.4 Filter

For a simple grating spectrograph the 1st order dispersed beam is imaged to produce the final spectrum. To prevent light from higher diffraction orders from overlapping onto the 1st order a filter is used.

1.2.5 Data Reduction

Noise Sources

There are several sources which contribute to the overall noise within the final spectrum. Intrinsic noise within a CCD and electrons causes generates a signal even when no light is present. External sources of noise are present within the light from a source itself.

Statistical Noise Photons are discrete particles and their arrival at the detector is stochastic and show a Poisson distribution. The noise contribution depends on the number of incident photons, N_p , and is proportional to $\sqrt{N_p}$. Both the photons from the source and sky background contribute Poisson noise.

Thermal electrons The random thermal vibration of atoms within the CCD can be sufficiently energetic to free bound electrons into the conduction band and generate a “dark current” even in the absence of light. The average number of electrons N_e produced follows a Boltzmann distribution and is a function of absolute temperature T

$$N_e \propto e^{-\left(\frac{E_b}{kT}\right)} \quad (1.17)$$

where E_b is the energy band-gap for the CCD material and k is Boltzmann’s constant. A multi-stage Peltier is cost effective in cooling a CCD to 30-100° C below ambient and thus reduce the dark current.

Read-Out Noise On completion of an exposure, the electrons generated must be transferred from a CCD pixel array to an analogue-to-digital converter to produce a signal count. The electronics used to perform these processes further introduce noise into final signal count. Resonance effects and cross-talk within the electronics can be reduced by careful selection of read-out rate. The total contribution from the read-out electronics for a particular read-out is specified by the chip manufacturer.

Instrument Signature Removal

Bias and Dark Frame Correction With a zero exposure time the output from a CCD will produce an apparent signal value for each pixel, p_{bias} . These result from leakage currents within the CCD transfer electronics or ghosting resulting from residual elec-

trons from a previous bright exposure. Correction of this inherent offset is done by subtracting zero exposure time bias frames from observation images. The offset value can change with time so reference bias frames are updated periodically.

With no light falling on a pixel a signal p_{dark} also accumulates over time because of leakage currents within the pixel. This is a time dependent bias and can be compensated for by taking timed exposures with the shutter closed (dark frames) to evaluate the magnitude of the offset. The offset cannot be assumed to vary linearly with time as charge accumulation within a pixel will affect the leakage current.

Flat Field Correction. Sensitivity to light between pixels will vary because of non-uniformities created during manufacture. Dust or vignetting can introduce additional variation across the CCD field. The response can be corrected by using a reference pixel values p_{flat} from a source of uniform flux free of emission lines and applying the correction (1.18) to each raw pixel value, p_{raw} to evaluate the corrected value p_{corr} .

$$p_{corr} = \frac{(p_{raw} - p_{dark}) \times (p_{flat} - p_{dark})}{p_{flat} - p_{dark}} \quad (1.18)$$

Although a de-focused image of the inner surface of the telescope enclosure is often used (dome flat), for this instrument a built-in source will be used instead. This allows the illumination source spectrum to be more closely matched to the instrument's wavelength range and permit flats to be taken at any time. A more detailed analysis of the problem was undertaken and is presented in Appendix F.

Cosmic Ray Removal. Cosmic rays are high energy ($> 1 \text{ GeV}$) extra-solar particles which interact with the upper atmosphere resulting in a cascade of particles, many of which reach ground level. The particles have sufficient energy to liberate electrons in a directional cascade within a CCD causing a false signal. The cosmic ray flux at sea

level is $1.44 \times 10^{-2} \text{ cm}^{-2} \text{ s}^{-1}$ (Allkofer et al., 1975) and the CDD an area of 1.76 cm^2 giving a mean interval of ~ 40 s. The interval will be even shorter at 2400 m elevation as flux increases with altitude. Unless the incident particle is normal to the plane of the CCD the false signal will appear as bright, isolated, linear features in an image. Software tools exist to identify and remove cosmic ray features from 2-D images, for example IRAF `xzap` and FIGARO `bclean`. The `bclean` was found to be effective at removing cosmic rays from 2-D images from single raw observations but cannot be applied to the 1-D reduced spectrum produced by the data pipeline.

The nature of spurious feature superimposed on the final sky-subtracted spectrum depends on the orientation and location of the cosmic ray track on the CCD image. A cosmic ray track within the region containing a spectrum produces an artificial peak in the data. Tracks in a region adjacent immediately to a spectrum causes a local increase in the apparent sky brightness. The background sky brightness is sampled by the L1 pipeline either side of the spectrum to remove the effects of sky emission and absorption. Subtracting a cosmic ray contaminated region over-compensates the sky brightness and produces a trough feature. As the spurious spectral features produced by cosmic rays are not automatically removed by the SPRAT data pipeline, 3 alternative methods were employed depending on the number of raw exposure images.

- **Exposures = 1:** The result of a cosmic track crossing a spectrum often produces an easily identifiable feature, typically 1-3 pixels wide and with sharp change in amplitude. In cases where only a single exposure was taken and a cosmic ray was suspected the original raw image was visually inspected. A cosmic ray track crossing a spectrum in a raw image produces a positive peak in the L1 reduced data. A cosmic ray track adjacent to a spectrum in the region used for background sky subtraction by the L1 pipeline a negative peak is produced. If a cosmic ray was found near the location of a suspect feature the spectrum data was interpolated as the mean of the adjacent points.

- **Exposures = 2:** Follow-up observations of gravity wave candidates (Chapter 5) were normally taken with only 2 exposures. The target objects were faint, typically $m = 18 - 20$, requiring long individual exposure times, typically 800s. The resultant spectra were contaminated with spurious cosmic rays features. A low noise method to detect and eliminate comics ray features for the case of only 2 reduced spectra being available is illustrated (1.6).

1. The difference of the two spectra, $(S1 - S2)$, is evaluated to separate cosmic ray features from the spectra. Since cosmic rays can produce peaks and troughs in either spectrum, sign information whether feature should be corrected by addition or subtraction is lost by this step and must be recovered later.
2. A change in the sky brightness between the two raw exposures will introduce an offset after subtraction. The median of the $(S1 - S2)$ spectrum is taken and cosmic rays features are found by searching for pixel values $> V = 3\sigma$ from the median. The value of V is selectable and can be increased for noisy spectra.
3. The median is subtracted from a detected cosmic ray pixel value to remove the offset and giving the magnitude of the correction but which may have the incorrect sign.
4. The sign of the correction is determined at each pixel location associated with a feature wherever,

$$S1 - S2 + Offset > 0 \quad (1.19)$$

the correction is subtracted otherwise it is added.

- **Exposures > 2:** If 3 or more exposure frames are available the FIGARO cosmic ray rejection utility, `cosrej`, was used with a cutoff sigma value of 5.

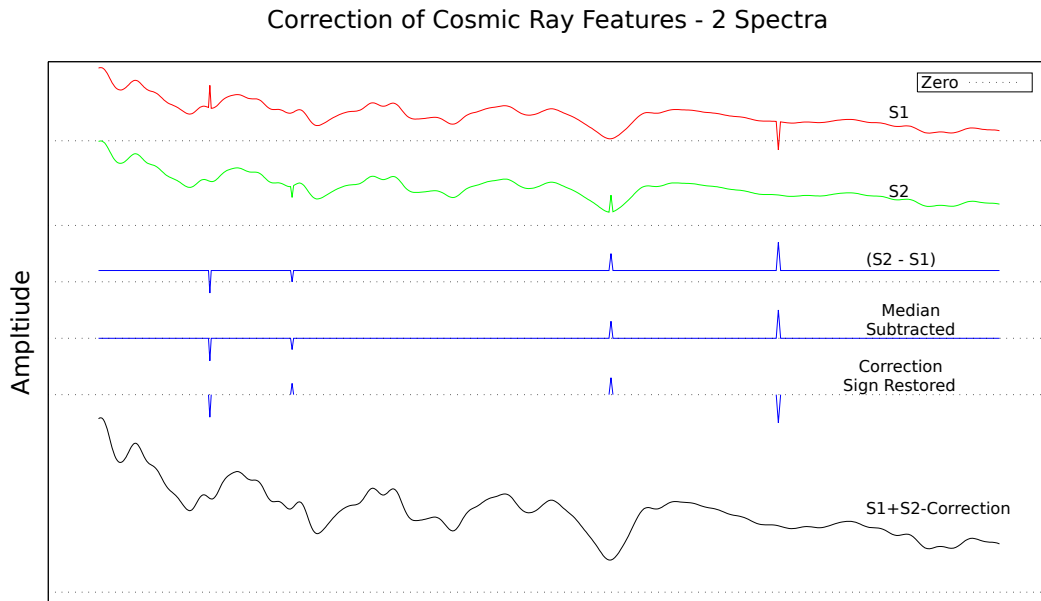


Figure 1.6: Simulated data processing sequence to eliminate cosmic ray features for the case of 2 spectra. Both simulated spectra, $S1$ and $S2$, have a peak and a trough produced by a cosmic ray impinging on the spectral data and adjacent sky respectively. The difference, $S2 - S1$, of the two input spectra is evaluated to separate the cosmic ray features from the spectra. Changes in the background sky brightness between the two exposures will introduce an offset. The median value is evaluated and cosmic rays are located by searching for features $> 5\sigma$ from the median. The offset is removed by subtracting the median to produce the correction values and regions not to be corrected are set to zero. The sign of the corrections are restored by comparing the value of $S1$ and $S2$ where the cosmic rays were detected. Where $S1 - S2 + offset > 0$ a correction is negative otherwise it is positive. The correction is subtracted from the sum of the spectra, $S1 + S2 - correction$, to produce the final spectrum.

Spectral Extraction. Lenses introduce a radially symmetric distortion of the imaged slit on the CCD, and becomes significant towards the edge of the image. This results in a “barrel distortion” which is corrected by applying a spherical transformation.

The spectrum on the CCD is a 2-dimensional image of the slit spread across wavelength space. Summing the flux along the direction of the slit improves the signal-to-noise ratio so the 2-D image is collapsed to 1-D as an initial step in the data pipeline. For a point source, the point-spread function approximates to a Gaussian function and the sub-section of the 2-D image containing the target object can be optimally ex-

tracted using algorithms (Horne (1986) & Marsh (1989)) and implemented using the IRAF EXTRACT and by the FIGARO `profile` and `optextract` tools.

Telluric and Spectral Response Corrections. Skyglow is a background flux generated by light from celestial sources such as the moon, stars and zodiacal light, and from atmospheric dust, thin cloud and aurora. Man-made light sources also contribute and the total flux varies both daily and seasonally. Compensation for skyglow is achieved by subtracting the flux from empty region of sky adjacent to the target, $S(\lambda)$, taken during the exposure.

Light is selectively absorbed and re-emitted by molecules within the atmosphere. Pressure and Doppler broadening increases the width of the emission lines adding time and temperature dependent variations. Hence the intrinsic spectrum of a target object, $I(\lambda)$, results in a modified spectrum arriving at the detector, $D(\lambda)$.

This telluric contamination is reduced by observing a standard photometric star with a known spectrum to create a correction function, $F(\lambda)$, which can be applied to recreate the original spectrum.

The conversion of photons to counts within a pixel wavelength dependent as is shown by quantum efficiency graph of a CCD (Figure 2.1). This is used to derive a spectral response function, $R(\lambda)$ to correct for the difference in conversion efficiency at different wavelengths.

Applying both corrections restores the intrinsic spectrum of the target object.

$$I(\lambda) = (D(\lambda) - S(\lambda)) \cdot F(\lambda) \cdot R(\lambda) \quad (1.20)$$

Wavelength Calibration. Variation of wavelength with pixel position along the X-axis (dispersion) of the CCD is not linear. A noble gas arc lamp with accurately known

emission lines was used to create a polynomial fitting function to map pixel position to wavelength

$$\lambda(x) = a_0 + a_1x + a_2x^2 + \dots + a_nx^n \quad (1.21)$$

selecting the polynomial order n such that the RMS error is a minimum. Arc lamp selection and calibration is described in Section 2.3.5.

1.2.6 Transient Astronomy

A topic of emerging importance in time domain astrophysics is the rapid characterisation of transient phenomena. Optical transient astronomy is concerned with the observation and study of objects which exhibit changes over short time scales ranging from minutes to months. Known object types includes cataclysmic variables (CVs), novae, SNe, active galactic nuclei (AGN), comets, gravitational lensing and eclipsing exoplanets. The exciting discovery of gravity waves (GWs) in black-hole black-hole (BH-BH) mergers (Abbott et al., 2016c) holds the prospect of detecting optical counterparts for black-hole neutron-star (BH-NS), and neutron-star neutron-star (NS-NS) mergers.

Potential transients are identified in photometric surveys such as Gaia (Prusti, 2012), the All-Sky Automated Survey for Supernovae (ASAS-SN) (Shappee et al., 2014), Pan-STARRS (Jewitt, 2003) together with several others sources (Table 4.1). The number of transients requiring classification will grow in the future as the number of satellite and ground based automated surveys increases both in number and detection efficiency. For example the Large Synoptic Survey Telescope (LSST) (Ivezic et al., 2009) is predicted to detect ~ 10 million transients per night (Kantor, 2014).

While continuous improvements are being made in classification using light curves alone (Bloom et al., 2012), the task is much more straightforward with spectroscopic

observations (Blagorodnova et al., 2014). To differential SNe from other objects relatively low resolving power ($R \sim 100 - 500$) is sufficient (Ngeow et al., 2013) although for some other observation such as accurate classifications of star type and AGN higher resolving power is needed (Table 6.2).

1.2.7 The Liverpool Telescope and SPRAT

The SPRAT spectrograph operates on the Liverpool Telescope (LT, Figure 1.7) situated at the Roque de los Muchachos on the Canary island of La Palma (IAU observatory code J13, altitude 2363m, Lat. $28^{\circ}45'44''\text{N}$, Long. $17^{\circ}52'45''\text{W}$). The median monthly seeing at the site typically varies from 1.14 – 0.72 arcsec throughout a year. The LT is a 2.0m Cassegrain of Ritchey-Chrétien design (TTL, 2004) with an effective focal ratio of $f/10$ and plate scale $10.3 \text{ arcsec mm}^{-1}$ at the focal plane. The telescope mount is an alt-azimuth design with altitude range between $25^{\circ} - 87^{\circ}$ and an pointing accuracy ~ 6 arcsec. Instruments can be mounted on one of 8 ports side ports on the acquisition and guidance (A&G) de-rotator box with a 9th instrument located on the straight-through port.

The LT is fully robotic and operates autonomously. It dynamically schedules remotely submitted observations for the different instruments. The unattended operation of the LT requires that instruments are self-configuring and have a higher level of internal diagnostics and monitoring than for operator managed telescopes. The SPRAT spectrograph supplements a suite of existing instruments housed in an A&G box. It is fitted to a side port 8 and is selectable by the rotation of a deployable science-fold mirror within the A&G box which deflects the incoming beam 90° from the primary optical axis.

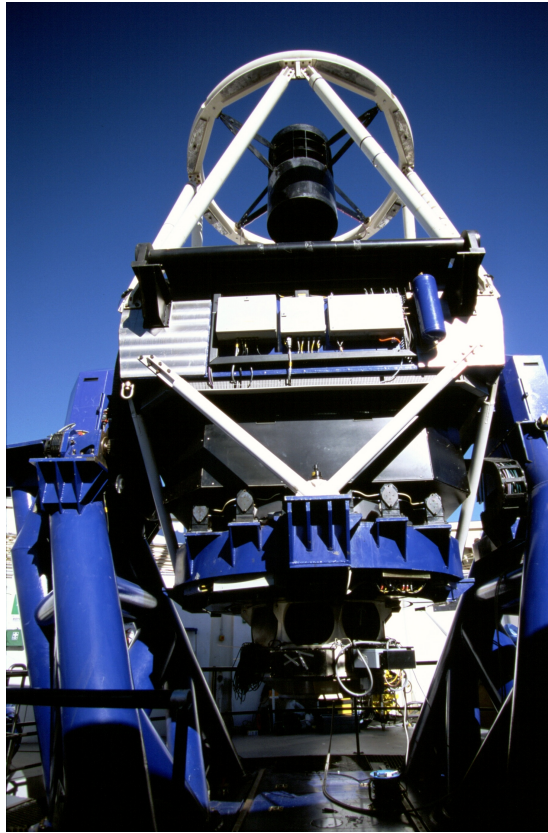


Figure 1.7: The Liverpool Telescope at La Palma. The spectrograph was mounted on an instrument port on the white A&G box situated below the blue primary mirror cell (Image courtesy of R. J. Smith).

1.2.8 Thesis Aims

The development of the optical low resolving power ($R \simeq 350$), high throughput, SPRAT spectrograph which operates in the optical range 4000 – 8000 Å.

The application of SPRAT for classification of SNe and other transients using the supernova identification software utility SNID.

The optimization of SN classifications using SNID via the modification of input parameters.

The creation of a semi-automatic pipeline to aid in SN classification.

The use of an optimised SNID to classify candidates as Gravity Wave (GW) counter-

parts.

Chapter 2

SPRAT Design and Laboratory

Testing

2.1 Optical Design

The basic spectroscope design described in Chapter 1 is generic and needs further adaptation to be used on the LT. We identified the following additional constraints from the measured telescope performance:

- Slit width in the range 1.5 to 2.5 arcsec. The upper limit is set by the known acquisition performance of the telescope (TTL, 2004) and the lower limit by our aspiration for better spectral resolution should it be improved upon.
- The imaging acquisition mode must be integral to the instrument. At ~ 6 arcsec the LT telescope pointing would be insufficiently accurate to reliably position an object on a 2.5 arcsec slit.
- The instrument must fit into the available space envelope when attached to the A&G box and the total length must be short enough to avoid contact with the

base-box and support columns at all altitude and azimuth orientations.

Given the uncertainty in optimal slit width, a variable width, symmetrically opening, knife-edge design made by Speirs-Roberston was chosen. The requirements naturally lead to a transmitting spectrograph design with a straight optical path where the slit and dispersive mechanism can be removed from the beam in acquisition, and then reinserted for spectroscopy. A disadvantage of a straight-through optical design is its length, both in terms of potential for flexure and the physical space envelope at the telescope A&G box which dictate a maximum instrument length of ~ 740 mm including the detector assembly and exit cabling.

2.1.1 Grating

In order to obtain a high efficiency a volume phase holographic (VPH) grating (Hill et al., 2003b) was chosen as the dispersive element. Commercial versions of these gratings are now available at low cost off the shelf with grating densities between 600 and 1800 lines/mm and diameters of 25 and 50 mm. Sandwiching the grating between two small angle prisms provides a straight through optical arrangement (Hill et al., 2003b) which deflects the input beam onto the grating at an optimal angle (i.e. the Littrow condition ‘blaze’ angle in a conventional lined grating) for maximum throughput. A 600 lines/mm dichromated gelatine VPH grating manufactured by Wasatch of diameter 25 mm mounted between B270 substrate glass was chosen. This requires an input angle of 10.2° and the grating equation (1.13) shows that at first order it has a similar output angle of 10.2° at 6000 \AA . To avoid the need to laterally offset the VPH grating the air-gap between it and the prisms is <2 mm.

Gratings require operation in a collimated beam which gives the opportunity to adjust the image scale at the detector as compared to the focal plane by suitable choice of focal length of collimating and camera lenses. There are two basic constraints that

must be satisfied in arriving at the eventual choice of these values; the overall field of view in imaging mode (to ensure sufficient objects are observed so that a World Coordinate System, WCS, fit may be made to allow automated acquisition) and pixel scale (to ensure that the re-imaged slit is optimally sampled on the detector). Considering the field of view requirement for acquisition, the experience with FRODOSpec (Morales-Rueda et al., 2004) and its operation with the previous imaging camera RAT-Cam showed that with a field of view of 21 square arcminutes, successful acquisition is possible in $> 94\%$ of cases.

The instrument uses a combination of prism and grating (grism) to deflect the incoming beam so as it strikes the diffraction grating at the optimal blaze angle. To retain a linear optical path the resulting dispersed beam is then re-directed by a second, exit prism into the camera lens of the detector (Figure 2.2). The variance of refractive index with wavelength is characterised by the Abbe number, V (Equation 1.12). For this instrument the primary purpose of the prisms is to deflect the beam. The BK7 glass selected for the prism has Abbe number $V = 64.2$ which will only produce small dispersion but has a high transmittance over the operating wavelength range.

2.1.2 CCD Selection

The detector chosen was the Andor iDus 420 BV camera which has a 1024×255 pixel CCD, aligned with the wavelength direction running along the long axis. The camera has high quantum efficiency (QE) $> 70\%$ over most of the $4000\text{-}8000 \text{ \AA}$ range (Figure 2.1), peaking to 97% at 5500 \AA . The pixel size is $26 \times 26 \mu\text{m}$ with a low readout noise ($9 e^-$ max.) and a low dark current ($\sim 0.01 e^- \text{ pixel}^{-1} \text{ sec}^{-1}$) at -60°C (Figure 2.12).

For the LT (with final focal length 20m) this detector would give an image size on the sky of $\sim 4.6 \times 1.1$ arcminutes (i.e. ~ 5 square arcmin) with a pixel scale of 0.27 arcsec/pixel in direct imaging. This pixel scale is rather small compared to the median

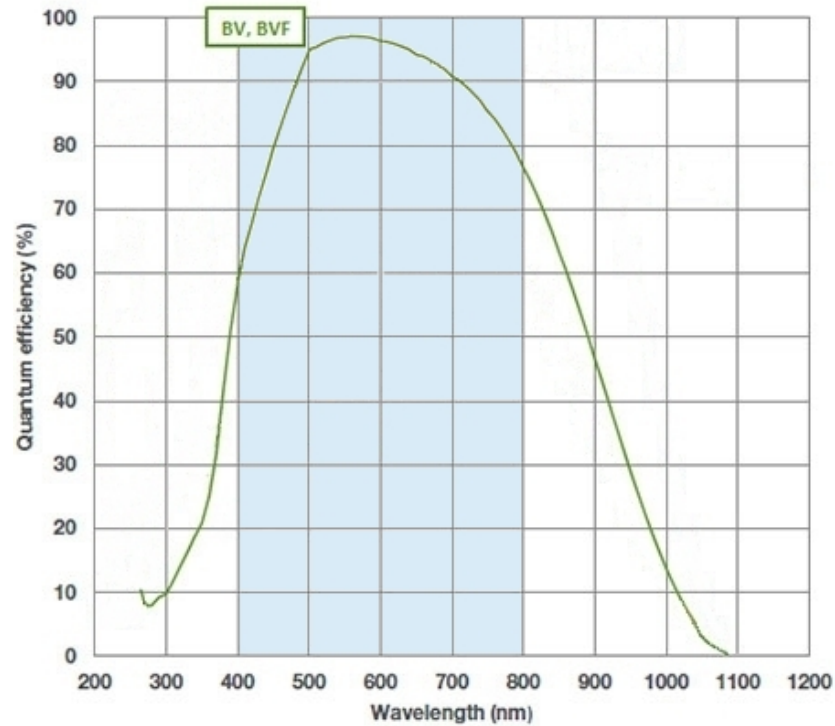


Figure 2.1: Quantum Efficiency for the BV (visible optimised) variant of the iDus CCD. The instrument operating wavelength range is shaded. Graph courtesy of Andor Technology.

telescope image quality of ~ 0.9 arcsec and the area of sky imaged too small for reliable World Coordinate System (WCS) acquisition. A ratio of $\sim 2:1$ for the imaging system is therefore required to increase the pixel scale to the optimal ~ 0.5 arcsec/pixel and ~ 20 square arcmin field of view. After considering a variety of trade offs, an optical system with collimator focal length 150 mm and camera focal length 85 mm was selected. This yields a beam width $W = 15$ mm and hence a resolving power with a 1.5 arcsec slit (Equation 1.16) of $R \sim 350$. The linear dispersion at the detector will be 0.2 Ångstroms per micron, i.e. ~ 5 Ångstroms per pixel. A wavelength range from 4000 to 8000 Å can therefore be accommodated on the detector over ~ 800 pixels and the spectral sampling will be close to optimal with ~ 2.5 pixels per resolution element. The slit height is 27.5 mm stopped down to 9 mm at the exit to produce ~ 200 pixel high aperture image centered on the CCD (~ 1.5 arcmin on the sky). The un-illuminated areas provide a measure of the bias and dark level in the images.

It is important to match the optical design of the instrument to the telescope it will be used with (Harmer, 1974). Ideally the exit pupil of the telescope will be coincident and co-axial with the grating of the spectrograph. In addition, space constraints at the A&G box limited the maximum instrument length to 740 mm and preferably <720 mm to avoid minimum radii on the rear exiting Andor camera cables. To meet these conditions an achromatic doublet field lens, ($D=50$ mm, $f=200$ mm) immediately following the slit was added. The field lens mounting also includes a long-pass $4000 - 10000\text{\AA}$ order blocking filter. With the field lens in place, the exit pupil was moved forwards 48.6 mm after the collimator lens, giving an acceptable final total instrument length excluding cables of 645.0 mm.

For the collimator lens an achromatic doublet, ($D=50$ mm, $f=150$ mm) with a VIS-NIR anti-reflection coating was chosen.

The optical layout was first calculated Gaussian geometric optics and assumed a thin lens approximation. This model was confirmed using LensForge and Zemax software.

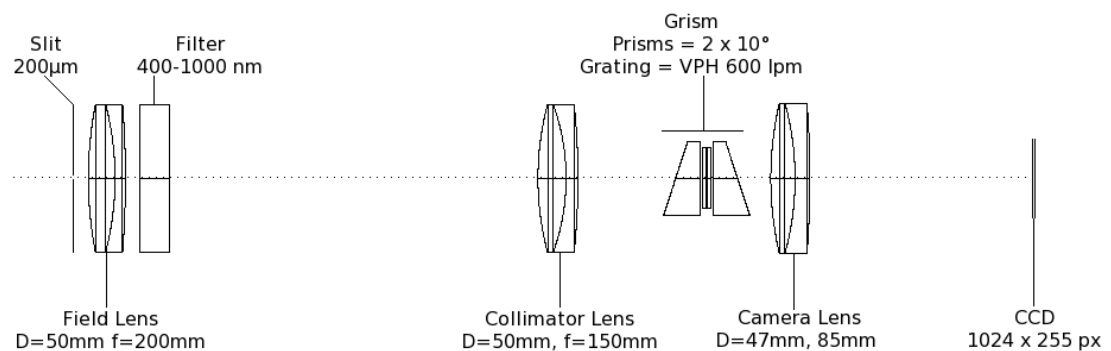


Figure 2.2: The instrument layout showing the position of the optical elements. For clarity the camera lens is shown as a single doublet rather than the actual 6 elements of the AF Nikkor.

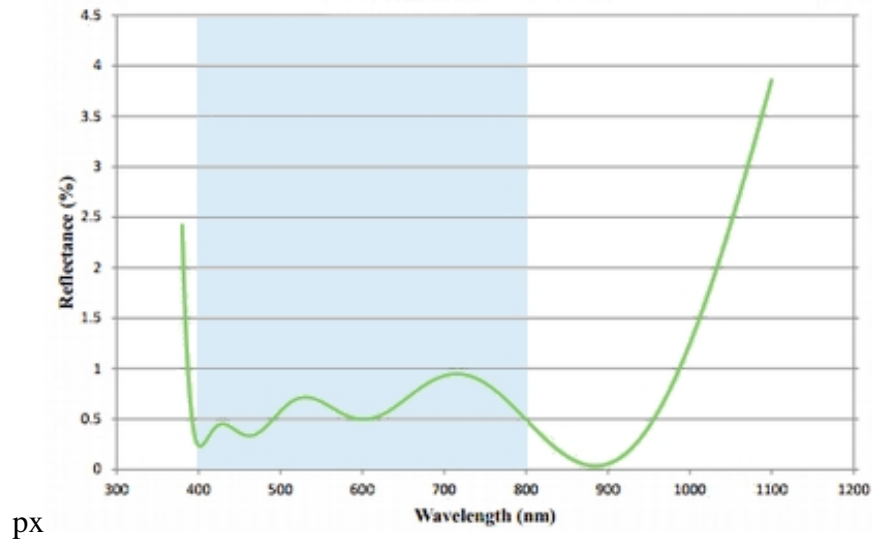


Figure 2.3: VIS-NIR (visible near IR) coating reflectance curve for light normally incident to a surface. Instrument operating range is shown shaded. (Courtesy of Edmund Optics)

2.1.3 Anti-Reflection Coating Selection

Reflection losses can be reduced by the application of appropriate thin-film surface coatings. The three coating options available from optical parts suppliers suitable for use in the visible were,

- $\frac{1}{4}\lambda$ MgF_2 : Single layer. Optimised to 550 nm. Rejected because of higher losses in the range 400 – 800 nm, ranging from 1.25 – 2.50%, when compared with VIS-NIR multi-layer.
- VIS^o Multi layer. Optimised for 425 – 675 nm. Losses <0.25% up to 700 nm but climb rapidly to 2.25% at 800 nm. Rejected because of the poor performance at $\lambda > 700$ nm.
- VIS-NIR Multi-layer. Optimised for 400 – 1000 nm. Losses range from 0.3 - 1.0% over the instrument range of 400 – 800 nm (Figure 2.3). Selected as the preferred coating and used on the field lens, collimator lens, long-pass filter and 10° prisms.

2.1.4 Predicted Throughput

The photon efficiency E_{total} is the proportion of photons arriving at the telescope aperture that can be detected by the camera. It is the product of the camera quantum efficiency (QE), and the throughput of each individual element along the optical path, assuming ideal minimum losses:

$$E_{total} = QE \times E_{pri} \times E_{sec} \times E_{sideport} \times E_{instrumentoptics} \dots \quad (2.1)$$

In addition to losses from the primary E_{pri} and secondary mirror E_{sec} reflection efficiencies, the instrument will be mounted on a side-port and suffers an additional attenuation from the instrument selection mirror $E_{sideport}$. Table 2.1 shows the optical elements and individual throughput at 6000 Å. The predicted throughputs over the full instrument range 4000 – 8000 Å are shown in Figure 2.4.

Element	E per Element	Elements/ Surfaces	Total
Liverpool Telescope ($E_{pri} \times E_{sec} \times E_{sideport}$)	0.810	1	0.810
Slit	0.970	1	0.970
Field lens - VIS AR coating	0.995	2	0.990
Long pass filter - VIS AR coating	0.910	1	0.910
Collimator lens - VIS AR coating	0.995	2	0.990
Prism - VIS AR coating	0.995	4	0.980
Grating substrate - AR coating	0.995	4	0.980
VPH grating	0.850	1	0.850
Camera lens - AF Nikkor 85 mm f/1.8D	0.940	1	0.940
CCD QE - Andor iDus 420-BV	0.850	1	0.850
Total Efficiency (E_{total})			0.457

Table 2.1: Estimated Photon Efficiency at $\lambda = 6000 \text{ \AA}$. Slit losses have been calculated assuming a 2.16 arcsecond slit and modelling the atmospheric seeing as a Gaussian profile with FWHM = 1.0 arcseconds.

Shown in Figure 2.5 are predicted signal-to-noise ratios for a selection of object magnitudes. Objects with magnitude $m_v=20$, will required extended exposures $\sim 500 \text{ s}$.

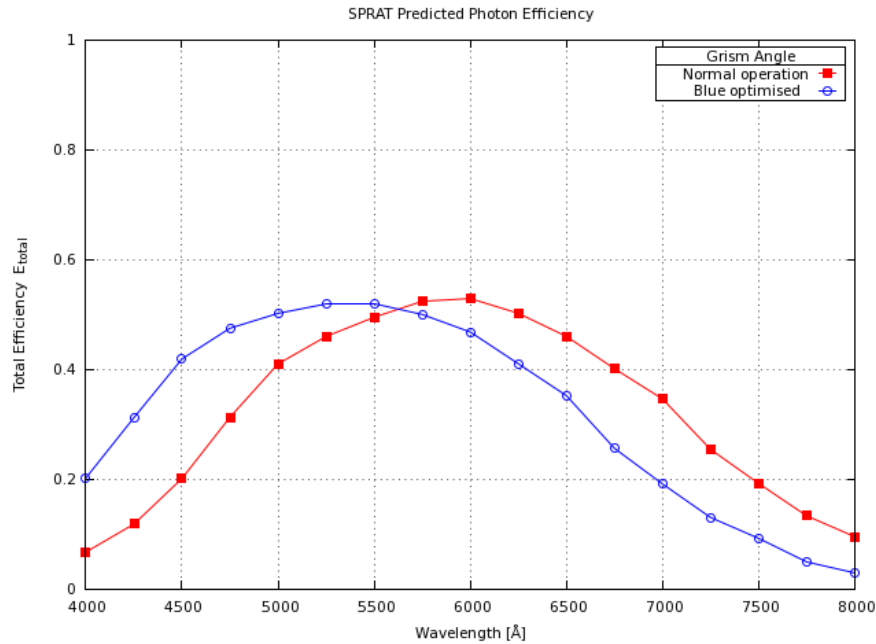


Figure 2.4: The predicted total photon efficiency for normal operation is shown in red and is centered on 6000 Å with the beam normally incident onto the grism assembly. When the grism is rotated, the response becomes centered on ~5500 Å as shown by the blue plot.

2.2 Experimental Layout

2.2.1 Optical Bench

Initial development was begun on a conventional laboratory bench using a small Melles Griot base plate. The laboratory room suffered from light leakage and the optical path of the first prototype required additional baffles and light-proofing when performing optical tests (Figure 2.6). Whilst adequate for characterising throughput against wavelength using a monochromator, the lack of mechanical stability and stray light contamination impaired reproducibility of other measurements.

Stability was improved by moving to an all-metal Edmund Optics bench installed in a dark-room. The CCD sensitivity necessitated additional baffling to eliminate stray light from equipment, particularly around the arc and flat-light sources. Optical elements from Speirs-Roberston and Spindler & Hoyer kits plus additional components

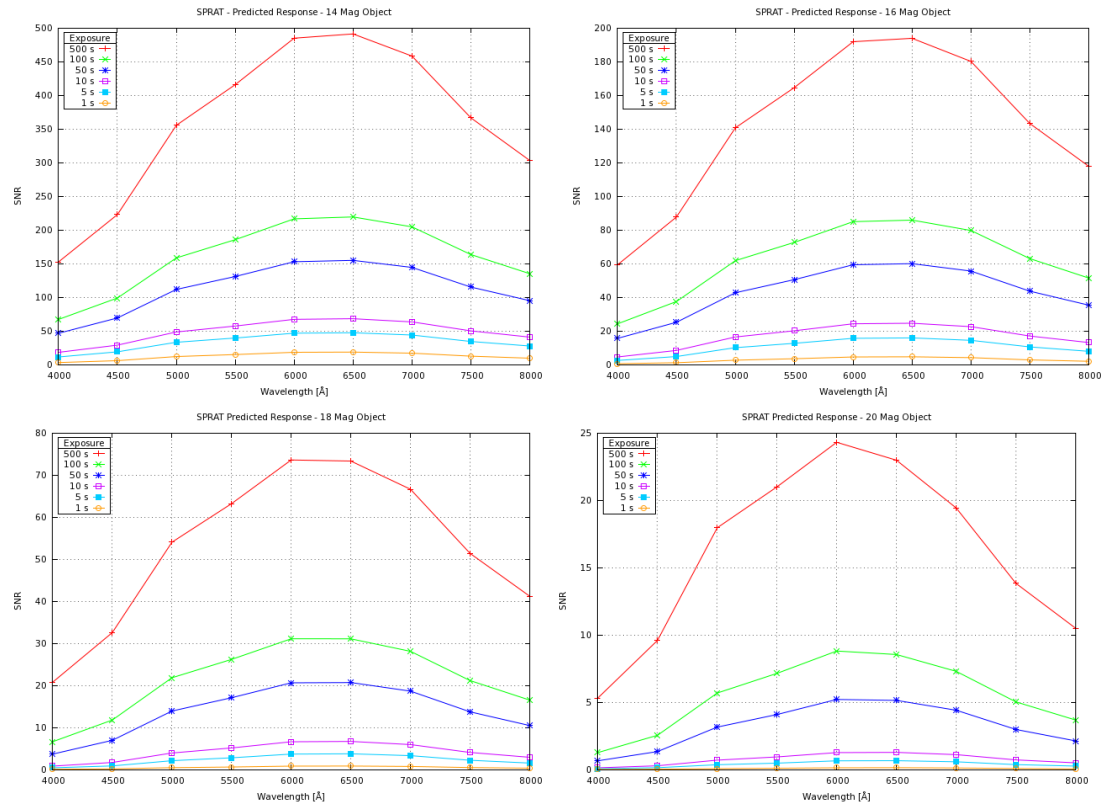


Figure 2.5: Predicted SNRs at selected exposures for object of magnitude $M_v=14,16,18$ & 20 in normal operation.

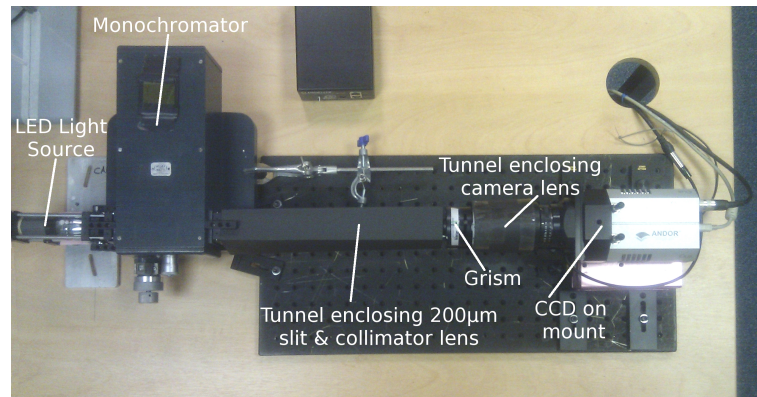


Figure 2.6: Initial Optical Bench Layout. Measurements were taken with lights out and extraneous light from other equipment was excluded by enclosing the optical paths as shown. The CCD mount was an adjustable scissor type but exhibited excessive vertical and lateral play of several millimeters.

from Edmund Optics were used to create the experimental instrument set-up (Figure 2.7). The adjustable scissor mount was replaced with a rigid, fixed-height, frame and a front-face alignment frame was made to ensure the camera lens was orthogonal to the

optical axis of the rest of the instrument. Positioning repeatability of the camera was further improved by using alignment plates affixed to the bench, reducing the lateral displacement error to $< \pm 0.1$ mm.

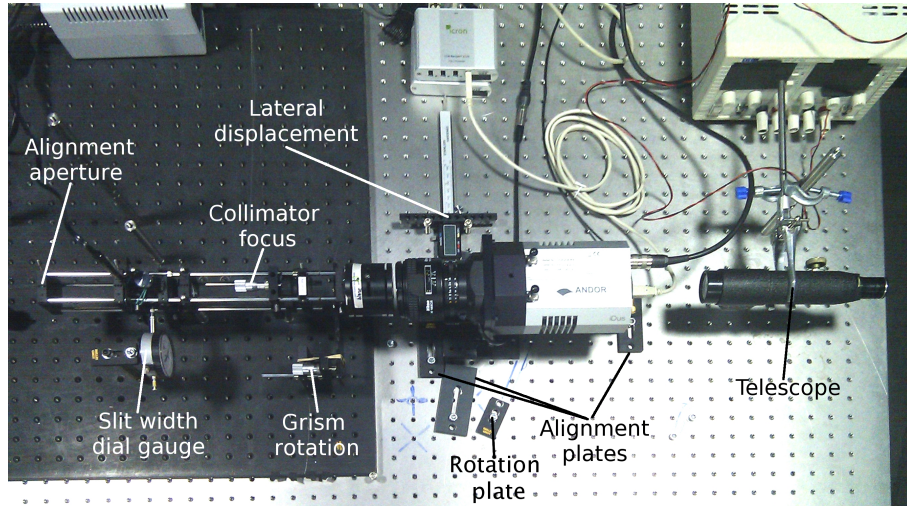


Figure 2.7: Final Optical Bench Layout. To allow instrument focusing and slit calibration by the telescope the Andor camera was removable and placed on top of the main optical bench (silver). Accurate camera re-positioning was achieved by fixed alignment plates and confirmed with a lateral displacement caliper. An additional small rectangular rotation plate and adjacent blue marks positioned the camera with a fixed rotation for viewing the 0th order diffraction minimum. The other optical parts were mounted along a 4-bar optical cage secured to a large Melles Griot plate (black) bolted onto the main bench. The grism assembly was mounted on a front pivoting 4-bar mini-cage that could be rotated through -0.5 to $+6.0$ degrees via a micrometer acting on a sprung lever-arm. The lever geometry gave an angular rotation of 0.64° per mm. The slit opens symmetrically and the width was measured by directly using a dial-gauge.

The prototype test instrument was assembled from following components fitted into a 4-bar optical cage kit:

- A green 532 nm laser pointer and surrounding screen used to define an optical axis for the alignment of the optical components by aligning the beam through two central co-linear apertures. Normal reflection of the beam from optical surfaces back to the source was done to check that they were orthogonal to the primary axis of the prototype instrument. This laser also provided an intense point source for the investigation of ghost reflections.

A red 635 nm laser was also evaluated for use in aligning the optical axis.

- Alignment apertures. A 3.5 mm diameter central circular aperture at the optical cage entrance and a second temporary 1.0 mm aperture placed at the cage exit. Used to define a beam parallel to the longitudinal mounting bars to an accuracy of $\pm 0.05^\circ$. The front of the camera lens was then centered on this beam using a surface mounted target. Further alignment was done by removing the target and auto-collimating a reflection back to the source laser.
- Flat-light source lamps and filters. Several low voltage (6-12V) incandescent bulbs and LED light sources were evaluated for suitability as a flat-field calibration source, particularly in providing sufficient high flux in the blue part of the spectrum. A selection of blue gel filters were evaluated for suitability in increasing the effective colour temperature.
- Noble gas discharge lamps manufactured by LOT-Oriel. Three gas discharge lamps, Ne, Kr and Xe, were available as wavelength calibration sources.
- A variable width, symmetrically opening, knife-edge slit. After calibration, the slit width was set using a $5\mu\text{m}/\text{div}$ dial-gauge. The slit was 27.5 mm in height but stopped down to 9.0 mm at the exit port to provide a blank zone above and below the edges of the spectrum image to detect ghosting. The blanked off zone also served as an overscan region as the Andor CCD chip does not have one.
- Field lens, BK7/SF10 achromatic doublet with VIS-NIR coating, $f=200$ mm. Added to reduce the overall length of instrument to fit within the available space on the A & G box.
- A long pass filter, $>4000 \text{ \AA}$, to prevent 2nd and higher diffraction orders from impinging on the 1st order.
- Iris set to 15 mm to stop the beam width down. This simulated the expected beam diameter at the collimator for the Liverpool Telescope.

- Collimator lens, BK7/SF10 achromatic doublet with VIS-NIR coating, $f=150$ mm, Collimated the beam from the field lens before it entered the grism. Collimation was adjusted using a micrometer and verified using the telescope focused to infinity.
- The grism was mounted in a vertically rotating assembly, deflected via a lever arm using a micrometer. The grism comprised a central grating between two beam deflection prisms. The prisms are 10° deflection wedge BK7 prisms with a VIS-NIR coating. The grating is a 25.0 mm diameter dichromated gelatine VPH made by Wasatch Photonics, 600 lines/mm, mounted on a 1 mm substrate glass with a 1 mm cover glass. The substrate glass is B270 glass with an AR coating. A metal mounting ring reduced the effective grating diameter to 20.4 mm.
- The detector, comprising of a Nikon Nikkor AF 85 mm f/1.8D lens focused to ∞ , an Andor modified Nikon NS25B 5-bladed diaphragm shutter on an F-type mount, and an Andor iDus DU420A-BV 1024×255 pixel back-illuminated CCD with multi-stage Peltier cooler.
- A small telescope focused to ∞ with integral eye-piece graticule used to verify collimation of the beam entering the grism and for calibrating the variable width slit. An Edmund Optic $200 \pm 5 \mu\text{m}$ slit was used as a reference slit for verifying the calibration (Section 2.3.5).

2.2.2 Additional Equipment

The following equipment was temporarily added to the test layout as required for specific tests.

- Hilger & Watts monochromator served as a light source for selectively scanning through the target wavelength range. The wavelength selector suffered from

severe backlash which was avoided by starting scans from below the lowest frequency and always increasing the wavelength throughout a run. It was also discovered that the monochromator was out of calibration. A re-calibration was done using a Kr arc lamp and checked with Ne and Xe arc lamps.

- Red 635 nm, green 532 nm & purple 405 nm laser pointers used in an unsuccessful attempt to directly measure the light loss through the Nikon Nikkor camera lens at 3 wavelength. The red laser was also used for auto-collimation of the optical components and identification of sources of ghosting within the grism and camera lens as it provided a brighter and more clearly focused beam than the other available lasers.
- Fluke model 52 dual sensor thermometer using K-type (Cr/Al) thermocouples used to investigate thermally induced de-focusing and loss of alignment.
- Hoya NDX400 neutral density filter. Fitted to the camera lens prevent saturation when imaging a bright source.
- Mercury lamp vapour lamp. A bright source for testing in the violet using the intense line at 404.7 nm.

2.2.3 Software

The images were read from the CCD using custom software written by the ARI and running under 32-bit Centos 5.1 on the acquisition PC. A preliminary check of images taken was done using DS9 and GAIA FITS file viewers. The raw data was then transferred to the analysis PC running 64-bit Centos 6.5 and analysed using the following software.

- SAOImage DS9 Version 7.2 - An image viewer/analysis tool. Used to produce video sequences for analysis of ghosting and variation in frequency response

with grism angle.

- Starlink GAIA version 4.4.3 - General purpose fits image viewer and analysis tool. Used for the initial inspection of images, grism and slit alignment, photon counting.
- Figaro version 5.6-6 - A suite of data reduction and image manipulation utilities. A rudimentary pipeline using a set of C command shell (csh) scripts was used to call Figaro routines to pre-process the images and extract 1-D spectra and generating data for graphing by GnuPlot.
- NOAO/IRAF PC-IRAF version 2.16 - Another suite of data analysis tools used for calibration.
- GnuPlot version 4.6-4 - A general purpose plotting tool used for curve fitting and creation of final graphs.
- LibreOffice (a variant of OpenOffice) version 4.0.4.2 - The spreadsheet Calc component of this office suite was used to calculate Gaussian optical layouts, signal-to-noise ratios, thermal effects, etc.

2.3 Instrument Testing

2.3.1 Nikon Camera Lens Transmittance

An experimental layout of the spectrograph using the final optical components but temporary mechanical mountings was setup on an optical table as described in Section 2.2. This was used to evaluate the optical design, characterise components and verify the system stability.

The optics were centered on a principal axis defined using a 532 nm green laser. The

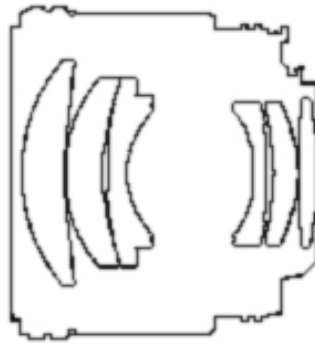


Figure 2.8: The AF Nikkor f/1.8D camera lens internal layout showing the 6 air-gapped elements. The 12 curved surface interfaces present potential sources of light loss and internal reflections.

axis was aligned to $< 0.1^\circ$ using pin-hole templates separated by 280 mm. The lateral alignment of the optical components was checked relative to this axis. Angular alignment was done using a simple auto-collimation method of reflecting the laser light from the centre of an optical component back to the laser source.

The detector camera lens was the 6 element Nikon AF Nikkor 85 mm f/1.8D. Figure 2.8 shows the internal optical arrangement. No published information was available for the lens coatings, glass or light transmission so the transmittance across 400-800 nm was investigated.

The initial method employed low power (3-5 mW) lasers of different wavelengths and attempted to focus and attenuated beam onto the CCD with lens present and absent. However, the narrow beam was found to be highly susceptible to small surface contamination (primarily dust) causing variation in light loss by scattering. Reproducibility was also poor because of mechanical play within the laser and camera mounts causing variation in losses from reflection. Additionally, although the red laser purity was good, it was discovered that the light in the other lasers was contaminated, probably from the lower wavelength light used to pump the laser's frequency doubler so this method was abandoned.

The transmission was then measured using a Hilger & Watts monochromator as the wavelength selectable source. The output was imaged onto the CCD and the incident flux summed using the GAIA statistical functions. The larger beam size onto

the Nikkor lens reduced the variation caused by scattering and a rigid camera mount plus positioning plates improved reproducibility. A lossless pin-hole lens allowed the monochromator output to be imaged onto the CCD even when the Nikon lens was absent and the attenuation was measured by comparing the flux at several wavelengths with and without the lens present (Figure 2.9).

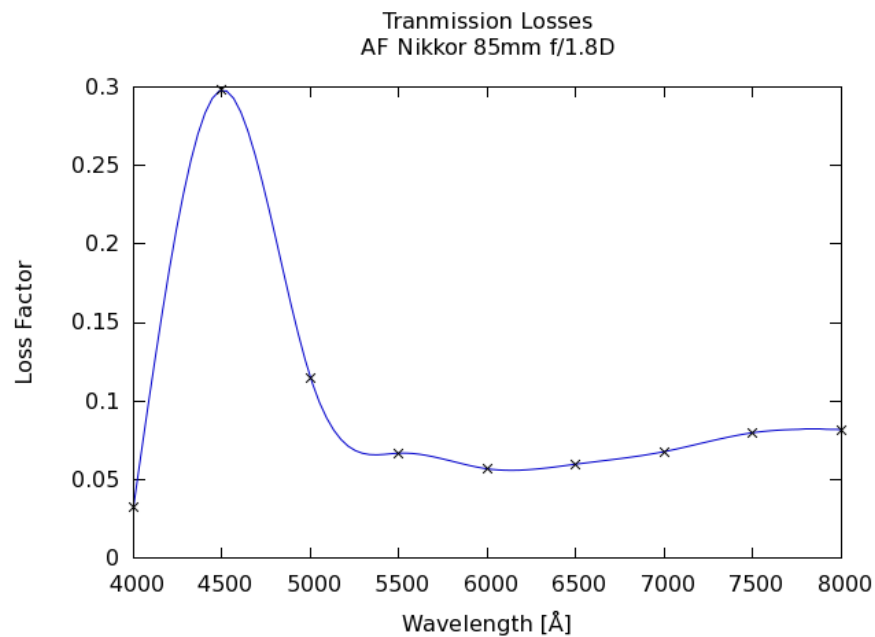


Figure 2.9: The Nikon Nikkor CCD camera lens transmission losses

The flux from the monochromator lamp was low in violet giving a poor SNR. A mercury discharge lamp source providing a strong emission line at $\lambda=404.7$ nm was used to confirm transmittance at this extreme end of the operating wavelength range.

The Nikon camera lens was attached to the CCD via a non-standard shutter. The thickness of the shutter could potentially introduce a focus offset. The camera lens focus was adjustable and the accuracy of its ∞ setting was verified by imaging a distant (>2 km) object and confirmed as correct.

2.3.2 Monochromator Calibration

The monochromator for measuring photon efficiency was a Hilger & Watts model D292 of early 1970's vintage which has a Czerny-Turner optical layout. After the initial tests it became clear that there were problems with the device and tests were done to verify and correct its operation and calibration.

Exit Slit Alignment and Calibration

To correct a misaligned and non-uniform knife-edge on the exit slit it was re-assembled and aligned to be approximately vertical with respect to the main body of the monochromator. The monochromator was then leveled using the adjustment screws to produce vertical image in the CCD camera. The slit was slowly closed to confirm the knife edges were parallel and the width-setting micrometer cylinder was reset to read 0.0. The slit was then opened and closed to verify the zero point.

Reading Reproducibility

Several High→Low and Low→High wavelength sweeps were performed with a white light source. Sweeping Low→High showed the presence of step changes indicating a mechanical problem and on investigation was found to be caused by a sprung slider sticking on a internal guide rail. In the reverse High→Low direction, a smooth frequency variation with no step changes was observed. Bi-directional sweeps indicated the presence of mechanical backlash in the frequency reading introducing an error >10 nm. Subsequently all test were be only done by decrementing wavelength to eliminate backlash and ensure a smooth sweep.

Reading Accuracy

A discrepancy between the value displayed on the dial for known emission lines was noted, e.g. for $\lambda=556.5$ nm the dial reading was 525.0 nm, a significant error. The device was calibration against a Pen-Ray[®] krypton source using the reproducible High→Low sweep method. Krypton was chosen because it produces two bright, easily identifiable, lines in green [556.2 + 557.0 nm pair] and orange [587.0 nm] (Figure 2.10).

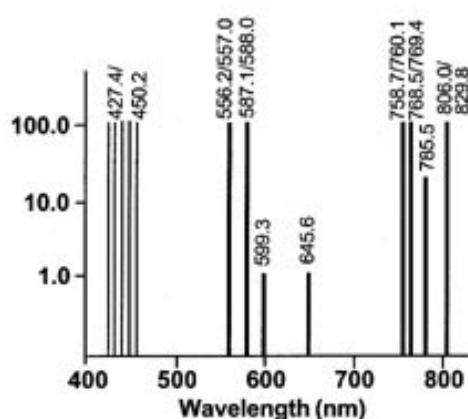


Figure 2.10: Krypton bright emission lines in the visible. Courtesy of LOT-Oriel

The monochromator was unable to resolve the green pair which appeared as single broad line, with median value $\lambda=557$ nm. The dial was set to match the wavelength at the Kr green and orange emission lines and the calibration was re-checked and was confirmed using the 540 nm line in neon.

Monochromator Post-Calibration Readings

Source	λ	Dial Reading [nm]					
Kr	557.0	556.5	557.0	557.0	558.0	557.0	557.5
Kr	587.0	587.0	586.0	587.0	586.0	587.5	587.0
Ne	540.0	540.0	539.0	539.0	539.0		

2.3.3 CCD Operating Temperature

The Andor iDus CCD employs a staged Peltier cooler and was operated in forced air-cooling mode. The minimum CCD temperature achievable is limited by the temperature difference from ambient, ΔT . At a typical dark-room ambient temperature of 25 °C the minimum CCD temperature was around -70 °C giving $\Delta T \approx 95$ °C but took an excessive time to be achieved (Figure 2.11). For all dark-room tests an operating temperature of -60 °C was used.

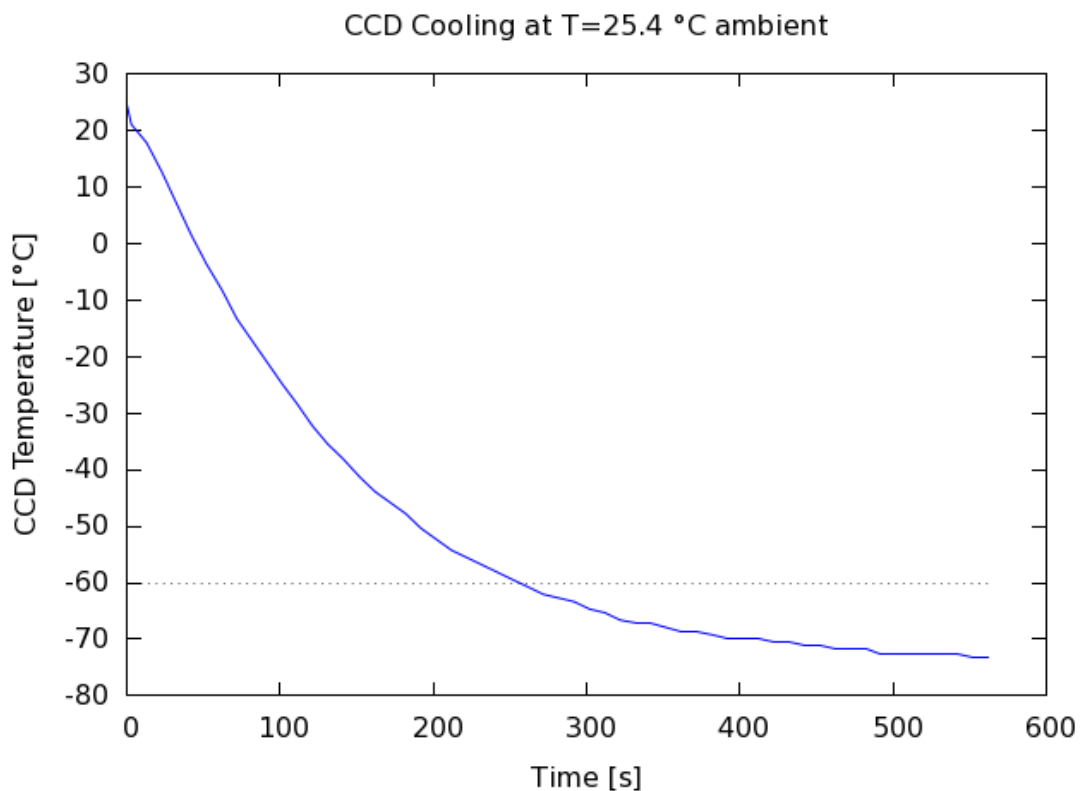


Figure 2.11: The CCD cooling at a typical dark-room ambient temperature showing the cooling rate tail-off as ΔT increases. -60 °C was the target temperature used for dark-room testing.

At -60 °C the dark current is ~ 0.02 e^- pixel $^{-1}$ sec $^{-1}$ (ANDOR, 2012). At the LT site the observing ambient is usually <15 °C allowing a CCD operating temperature of -80 °C with a dark current in the order of ~ 0.002 e^- pixel $^{-1}$ sec $^{-1}$ (Figure 2.12).

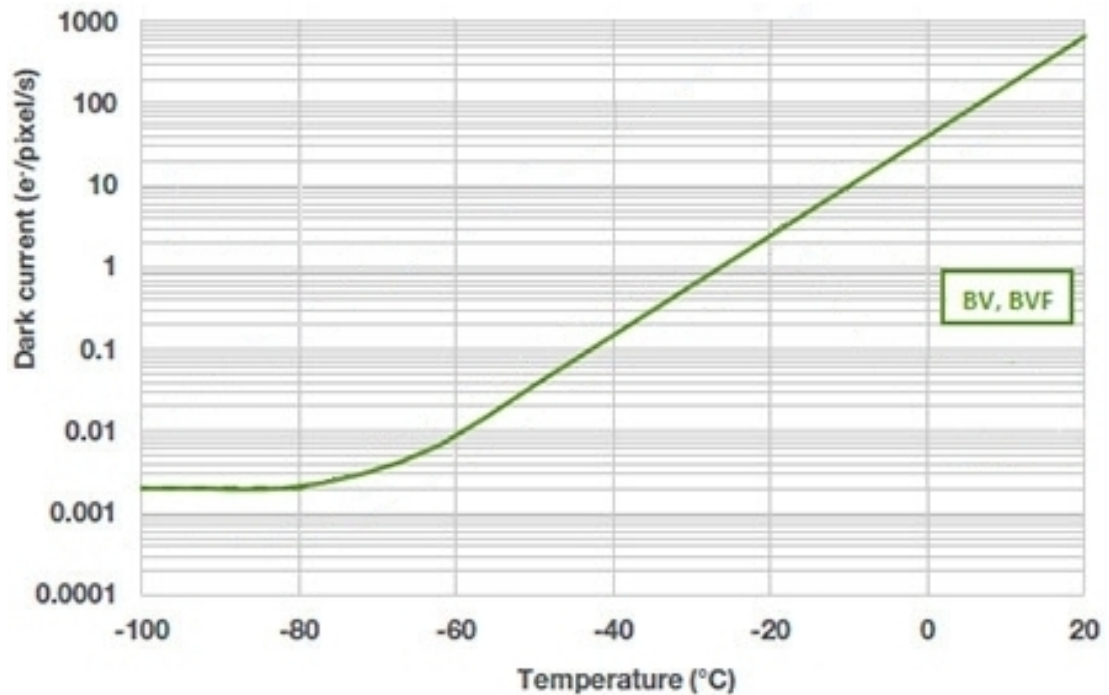


Figure 2.12: The variation of current variation with temperature for the BV variant of the iDus CCD. The tail-off at -80°C indicates that further cooling provides little further benefit in reducing electron noise. Graph courtesy of Andor Technology

2.3.4 Grism Rotation

The diffraction efficiency of VPH gratings is described by Baldry et al. (2004). The effect of varying the angle of incidence on the grating was investigated by rotating the grism assembly away from the beam axis by up to 6° . The axis of rotation was vertical, parallel to the VPH grating lines, and coincident with the centre of the first surface of the leading prism. The optimal throughput for a specific wavelength was set by rotating the grism assembly to achieve minimum intensity of the 0^{th} order diffraction for $\sim 5500\text{\AA}$. Shifting the peak sensitivity 500\AA towards the blue is intended to improve the overall SNR when observing objects which are stronger in the red. The change in emission line intensities from a Kr arc are shown in Figure 2.13.

As a result of this the instrument will operate one of two selectable wavelength optimised modes. A normal mode centered at 6000\AA and a blue optimised mode peaking at 5500\AA . The rotation angle will be set using a simple pneumatically actuated lateral

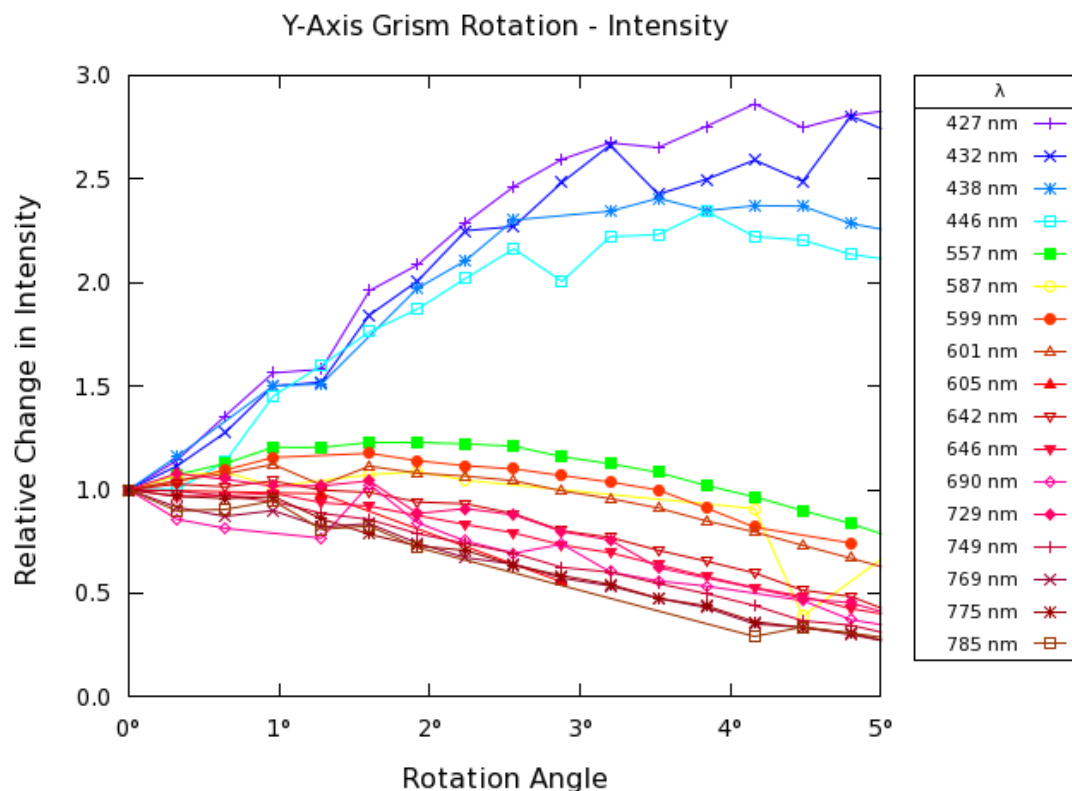


Figure 2.13: The rotation of the grism illustrates the relative change in Kr emission line intensities. During testing, the instrument was optimised for green, 557 nm, which peaks at $\sim 1.75^\circ$. The blue 446 nm line peaks at $\sim 3.5^\circ$, more than double the intensity, suggesting that a selectable grating position would be of advantage.

stop with two selectable docking positions to improve reproducibility.

2.3.5 Wavelength Calibration Lamp

For all spectrographs, calibration is essential to provide a mapping between pixel position along the dispersion axis of a spectrum image and the corresponding wavelength. A noble gas arc lamp spectrum provides a stable source of identifiable emission lines with accurately known wavelengths. Three single noble single gas arc lamps were available for testing (krypton, neon and xenon) made by LOT-Oriel (Figures 2.14 & 2.15). The limited range of Ne lines ($\sim 5800 - 7000 \text{ \AA}$) made it unsuitable as a source.

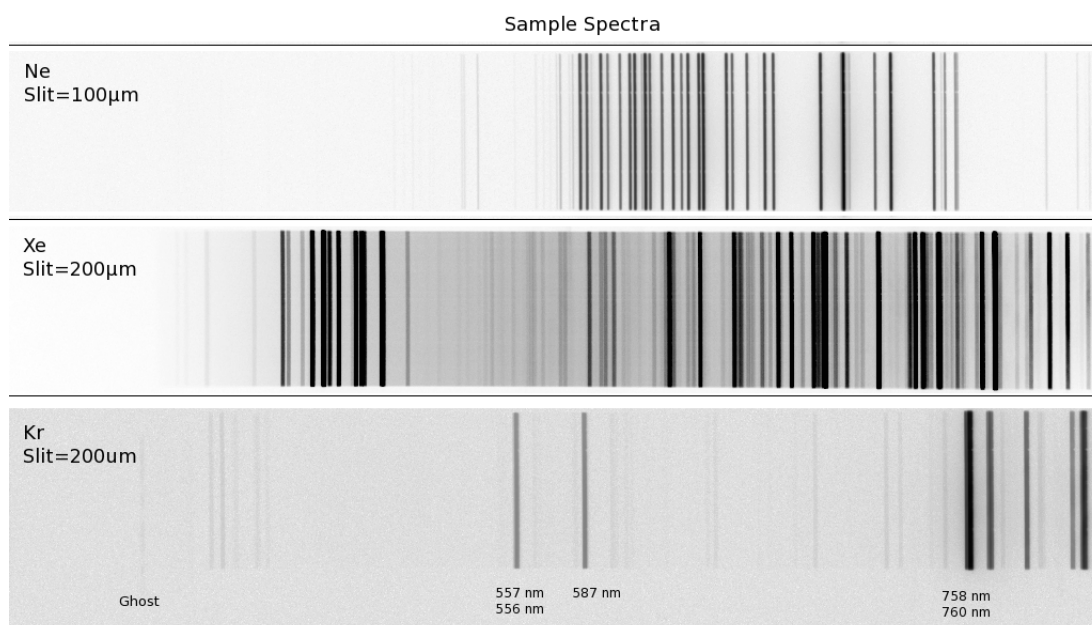


Figure 2.14: Example of spectra taken during evaluation of wavelength calibration sources. Neon had a limited set of lines available for wavelength calibration in the visible. The slit width was reduced to 100 μm to sharpen lines and exposure increased in an attempt to improve detection of fainter lines.

Xenon provided the best set of calibration lines without saturating any prominent lines.

Krypton shows the green, 556/557 nm and orange, 587 nm lines used when calibrating the monochromator. The prominent doublet at 758/760 nm is also evident and produced the ghost image on the left of the spectrum. To eliminate saturation of this line the image was taken with a neutral density filter reducing the intensity of other lines.

Krypton had the widest range but has a bright 7602 Å line which saturated the CCD when longer exposures were taken to detect weak lines. However the relative brightness of this line compared to others was useful in the detection of ghosting. All the arc spectra exhibited a gap around 5300 Å. To reduce the gap and extend the ranges of Kr and Xe, the manufacturer's standard list was augmented with lines from the NIST reference web-site and the arc calibration was repeated. The updated results (Figure 2.16) show xenon's greater range and lacks the bright line feature of krypton. Xenon was therefore selected as the arc calibration source.

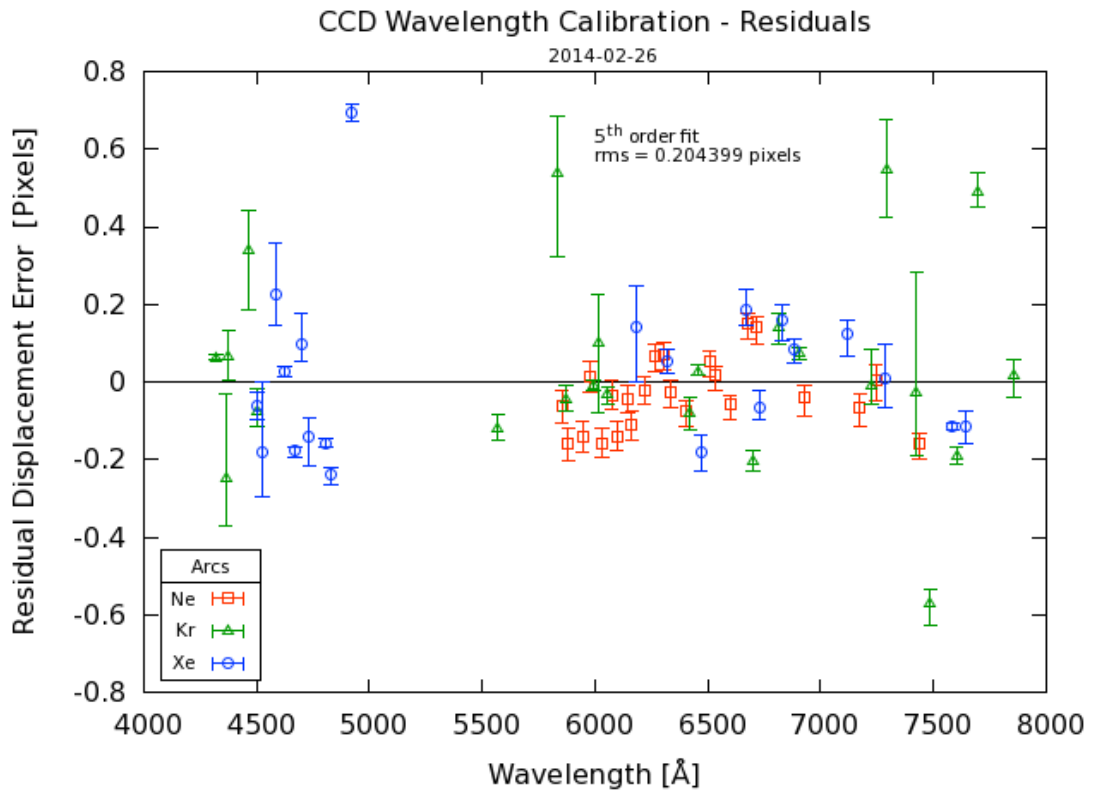


Figure 2.15: Initial calibration arc lamp evaluation showed Ne as unsuitable because of its limited range of lines in the visible. Kr provided the widest range but produces a bright line at 7602 Å. All arcs showed a gap at centered around 5300 Å.

2.3.6 Flat-Field Lamp

The instrument will incorporate an internal flat-light source for characterising the response of the CCD pixels and vignetting (e.g. camera lens will exhibit edge darkening). With the slit and grating removed this will provide data on small (pixel) scale sensitivity variations. In addition with the slit and grating in place it will provide data on the larger scale system spectral response assuming it is a continuum source. Sky flats will be used to provide data on the slit profile. The flat light source is introduced into the beam ahead of the slit via a movable mirror and light pipe. Several white LEDs and low voltage incandescent lamps were evaluated as suitable flat light sources. The LEDs showed a discontinuous spectrum and continue to phosphoresce, emitting light after they were turned off, so were discounted.

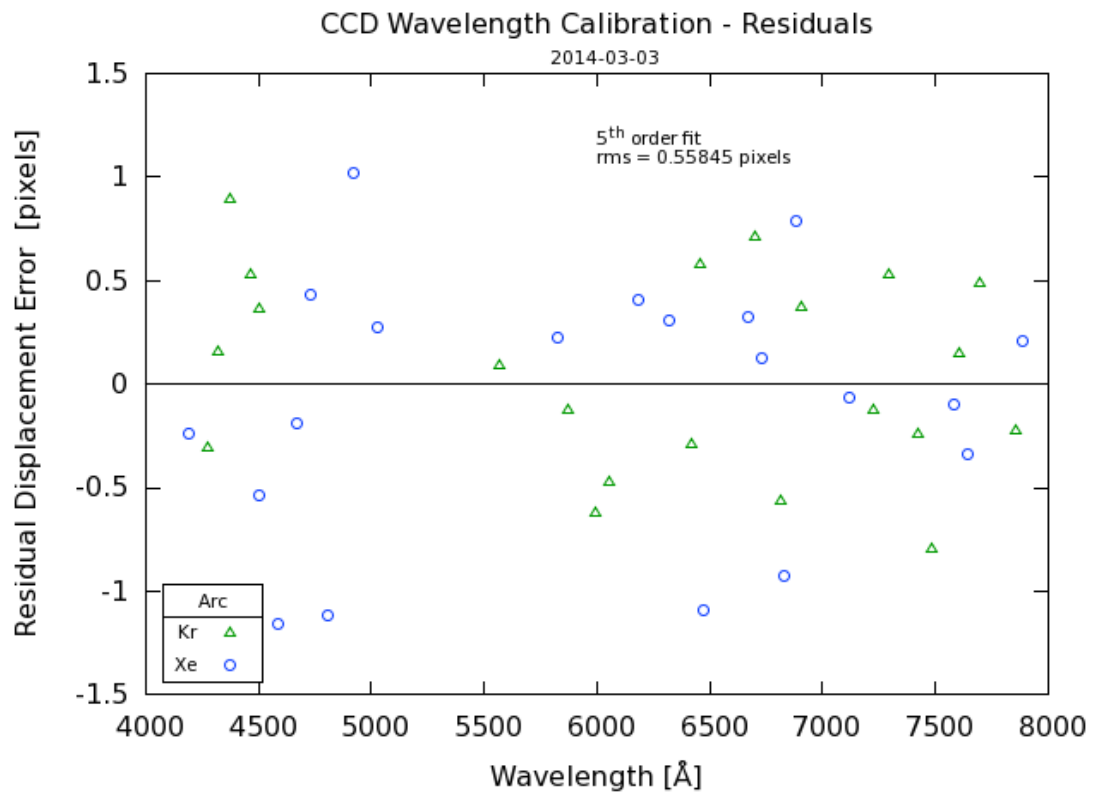


Figure 2.16: Calibration arc evaluation augmented with lines from NIST. Xenon now has the widest overall range and a reduced $\sim 5300\text{\AA}$ gap so was selected as calibration source.

The spectra for a variety of $\sim 12\text{V}$ incandescent lamps were investigated (Figure 2.17). The clear Bosch434 tungsten halide lamp at 13V showed the best blue response. The effective colour temperature of a lamp was increased by suppressing long wavelengths with a blue filter to “flatten” the spectrum. Filters are often manufactured using a combination of dyes and produce a modulated response. Figure 2.18 presents the 4 least modulated spectra from the Roscolux set of blue filter gels. Roscolux 3216 1/8th Blue was chosen as the companion filter to go with the Bosch434 flat lamp.

2.3.7 Reflections and Ghosting

The grism rotation tests using the Kr arc source (which has a very bright 7602 Å line) clearly showed several ghost lines and other reflection artifacts. To identify the origin

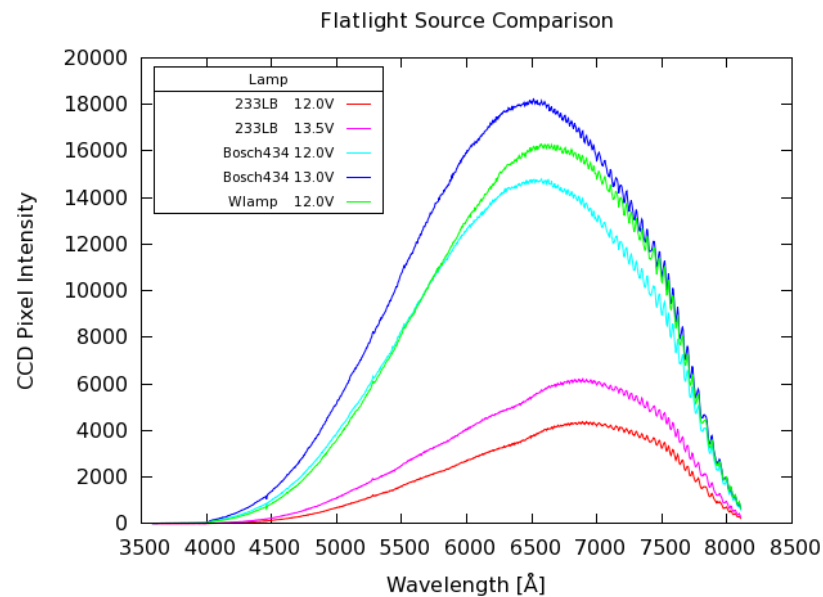


Figure 2.17: Wlamp is a generic 12V tungsten torch bulb. Two automotive lamps were evaluated. 233LB is tungsten with blue filter and Bosch434 a clear tungsten halide. Automotive lamps are designed to operate at 12.6V so were operated at 12.0V and at a small over voltage for comparison.

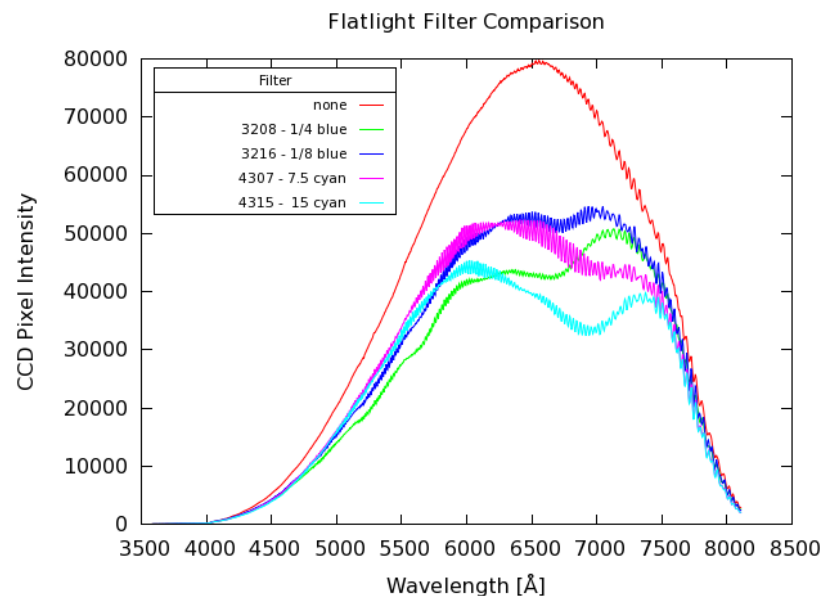


Figure 2.18: The effect of blue gel filters on the spectrum of the Bosch434 tungsten halide bulb was evaluated. Roscolux 3216 showed the least modulation and increased the relative intensity in the blue.

of the ghosting the optical axis alignment laser and Kr lamp were used as bright sources together with a white screen/surface to detect reflections. For these tests the slit width

was often set to between 10-50 μ m to avoid ghost lines being hidden by real ones.

Variation in ghosting in the camera lens caused by lateral and angular mis-alignment were investigated. A red 635 nm laser replaced the normal alignment laser as it produced a less distorted image spot. The camera lens was centered using a target mounted on a lens filter ring and the angular alignment set a test jig and verified by auto-collimation. Figure 2.19 shows the effect of changing the lateral mis-alignment. Several images were combined to form movies showing the relative motion of ghosts. The lateral alignment will need to be <0.2 mm on the final instrument.

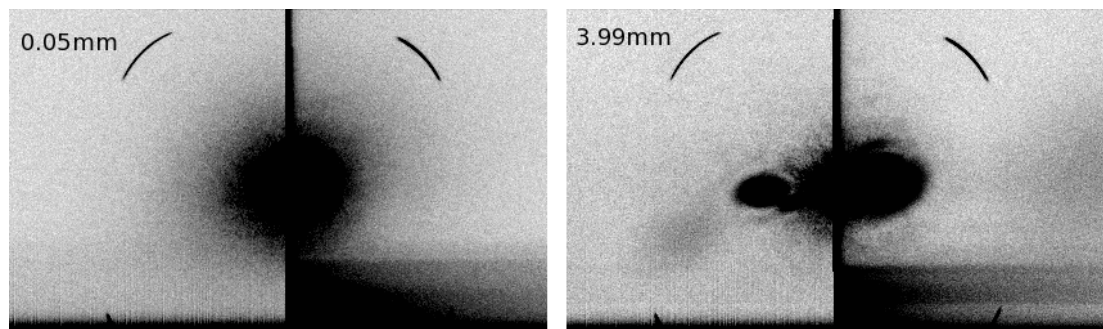


Figure 2.19: The effect of lateral mis-alignment of camera lens at 0.05 mm and 3.99 mm offsets from the optical axis. Not shown here but at a 0.50 mm offset the central reflection began to exhibit the ellipticity that is prominent in the right image. At 3.99 mm the additional ghosting extended beyond the field of view. Angular mis-alignment showed similar effects. The reflection arcs also show the unexpected displacement between the CCD chip center and the lens mount center.

The grism body was machined from acetal polymer giving the entrance and exit ports a smooth reflective surface. Placing a white paper on these surfaces and illuminating with the optical axis alignment laser showed secondary reflection from within the grism impinging on the port sides. In the final instrument the ports were therefore redesigned to reduce the length from 20 mm to 9.2 mm and a bevel added to allow light to escape to the instrument enclosure and be absorbed by baffles. The acetal surface was bead blasted to reduce specular reflection. In the laboratory setup installing non-reflective lining material successfully removed a large diffuse feature at the red end of the spectrum.

Optical elements were sequentially removed or rotated to detect any corresponding change in ghosting. It was identified that the long-pass filter placed immediately ahead the grism was re-reflecting light coming from the front/rear surfaces of the grating. This was eliminated by moving the long pass filter to immediately behind the field lens. Internal baffling was added to absorb the redirected reflections.

To detect ghosting originating from optical elements within the grism, deformable elastic rings were placed between the grating and prisms to mechanically decouple the elements. The screws holding the prism mount were then adjusted to selectively move a single prism. Reflections were observed on screens placed ahead and behind the assembly. The primary ghosting source was established to come from the grating glass and was reduced by tilting it down $\sim 1^\circ$ in the direction of the optical axis.

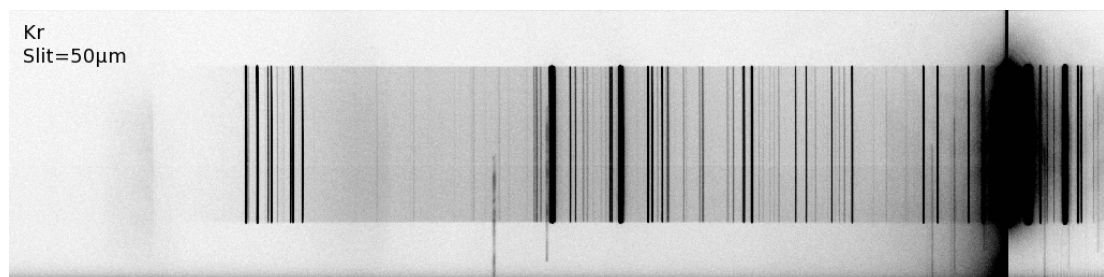


Figure 2.20: This over-exposed Kr spectrum was made during ghost detection with a narrow $50\mu\text{m}$ slit. The bright 7602 \AA line on the right is saturated and ghost lines extend into the lower masked region. Their intensity varies along the y-axis and can exhibit a ribbon like appearance.

For very bright sources causing pixel saturation, 2 residual ghost lines remained but were determined to be >2 orders of magnitude fainter than the saturated line and ignorable. It was noted these ghost lines are displaced vertically from the main spectrum. As an additional ghost line detection method the slit was masked so that the spectrum occupied a central band ~ 200 vertical pixels in height. Ghost lines are easily identified if they extend beyond the upper or lower edges of a spectrum, into this masked-off region (Figure 2.20).

2.3.8 Slit and Grating Alignment

To obtain the highest image quality the slit and grating lines need to be aligned parallel to the CCD pixels columns. Since the camera is fixed, the slit and grating were rotated into alignment.

Slit-to-pixel alignment was done by imaging a narrow slit, $\sim 5\mu\text{m} = \sim 1$ pixel width onto the CCD, and rotating the slit until the maxima was confined to 1 pixel column on the CCD.

For grating-lines-to-pixel alignment grating is rotated until the upper or lower edge of the slit exit mask is parallel with horizontal pixels. Figure 2.21 shows a Kr spectrum prior to alignment.

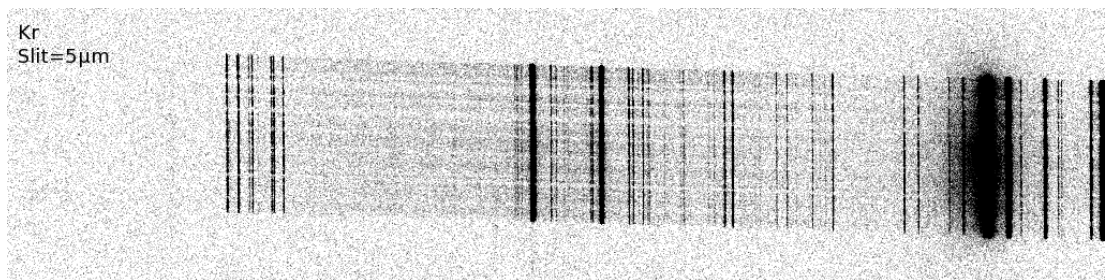


Figure 2.21: A mis-aligned grating is evident in this Kr spectrum where the upper and lower edges are not horizontal and was corrected by rotating the grating within the grism assembly. A very narrow slit width was used, $\sim 5\mu\text{m}$ and dust contamination on the knife-edges produced streaks. The dust was removed using compressed gas optical cleaner.

2.3.9 Slit Width Calibration

The Speirs-Roberston variable width slit was uncalibrated and operates by distorting a circular metal ring to produce a symmetrical separation of two knife edges. Width was measured using the telescope graticule. The graticule was first calibrated by measuring fixed slits of known width to establish a scaling factor. The displacement of one edge of the slit was measured using a dial-gauge and the resulting calibration curve shows a small non-linear response (Figure 2.22) indicating asymmetric or non-uniform move-

ment of the knife edges. Although a variable aperture was used in testing, it will be

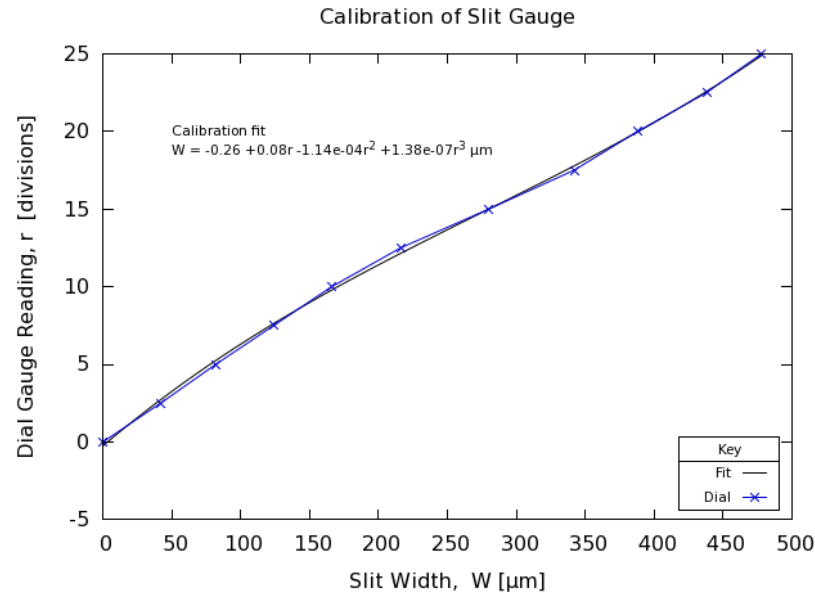


Figure 2.22: Variable width slit calibration curve. The non-linear response is indicative that the knife-edge movement was not symmetric.

set to a fixed width in the final instrument and hence the asymmetric opening was only relevant during the experimental phase. The reproducibility and stability of the zero position was verified to check for backlash and sticking. Tapping the gauge was required to achieve a stable reading with an error of $\sim\pm 0.2$ of a division.

2.3.10 Thermal Stability

Focus tests showed a noticeable slit image defocus for changes of ± 0.028 mm in the slit to collimator distance, ~ 150 mm. The potential for thermal instability was confirmed by thermally cycling the optical cage through 20–30°C.

The operating temperature for the instrument is -5 to 20°C . Over this range only a few conventional steels provide an acceptably low expansion, e.g. austenitic steel produces ± 0.025 mm which is just acceptable. Invar was therefore selected as the baseplate material for mounting the optical mounts between slit and collimator with a predicted

expansion of ± 0.0025 mm. Exiting the collimator lens, the beam is parallel so distance changes will not effect focus.

2.4 Mechanical Design

2.4.1 Materials

The selection of the material for construction of the instrument were done in consultation with ARI engineer Mr. Stuart Bates with responsibility for mechanical design and FE analysis of thermal expansion and flexure.

The structure of the instrument is predominantly aluminium due to its reduced cost, easy machinability and relatively light weight. As accurate distances between the optics must be maintained, the design employs an internal pseudo optical bench made from Invar because of its substantially lower coefficient of thermal expansion. One end of the Invar plate is pinned to the instrument structure at the slit position, (coincident with the telescope focus plane). The other end ‘floats’, allowing the rest of the instrument to expand at a higher rate without deforming the structure. To compensate for changes in the gravity vector, the floating portion of the Invar is constrained using Belleville washers stacked back-to-back to apply a relatively high clamping force (240N) within a small space envelope.

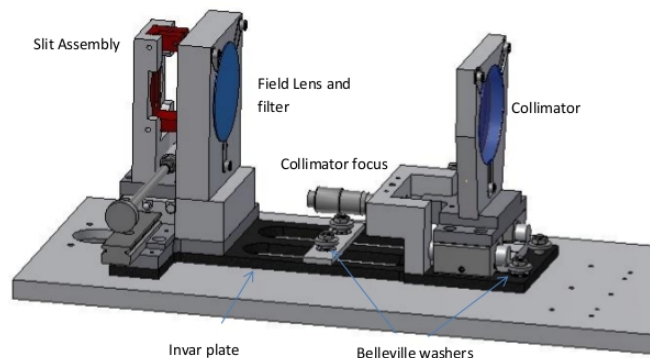


Figure 2.23: Pseudo optical bench sub-assembly.

2.4.2 Movable Components

At commissioning the collimator will require a one-off adjustment of the focus. The numbered components are movable along re-circulating ball linear guides and deployed using SMC compact pneumatic cylinders.

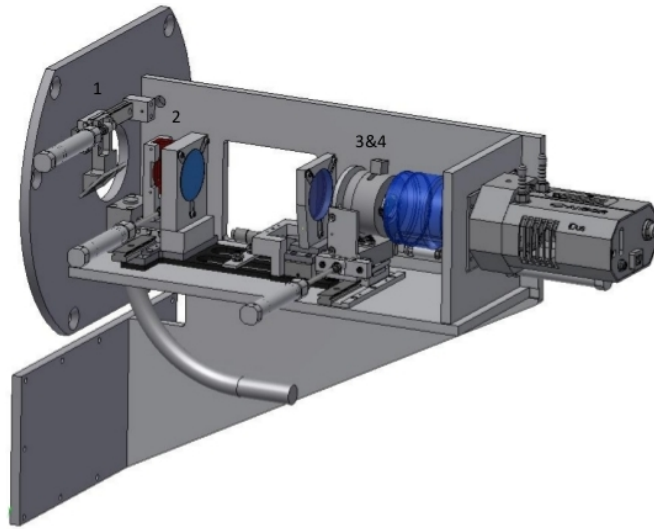


Figure 2.24: 1. Calibration mirror deployment, 2. Slit deployment, 3&4. Grism and rotation angle stop deployment

2.4.3 Flexure

Figure 2.25 (telescope at zenith, instrument upright and horizontal) and Figure 2.26 (telescope at horizon, instrument on its side and horizontal) are derived from finite element analysis (FEA) modeling of the instrument mounting and enclosure showing the expected deflections. The yellow arrow indicates the direction of the gravity vector. The colour regions indicate magnitude of deflection and are drawn with an exaggerated displacement from the un-deflected instrument (outlined in black). The worst case mechanical flexure is an order of magnitude less than 0.023mm needed for a $\frac{1}{2}$ pixel shift. To further minimise the flexure both the upper and lower ports of the LT A&G box are utilised to provide an angled brace.

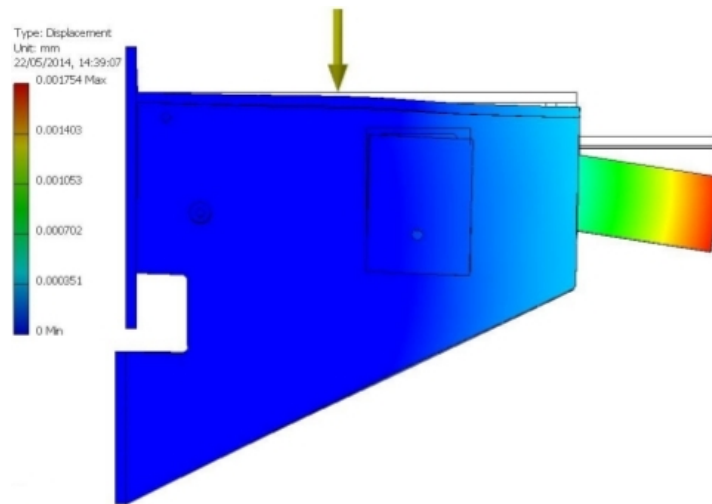


Figure 2.25: Telescope at zenith, A&G box rotated with instrument upright and horizontal, the maximum predicted deflection at the rear of the camera is 0.0017mm.

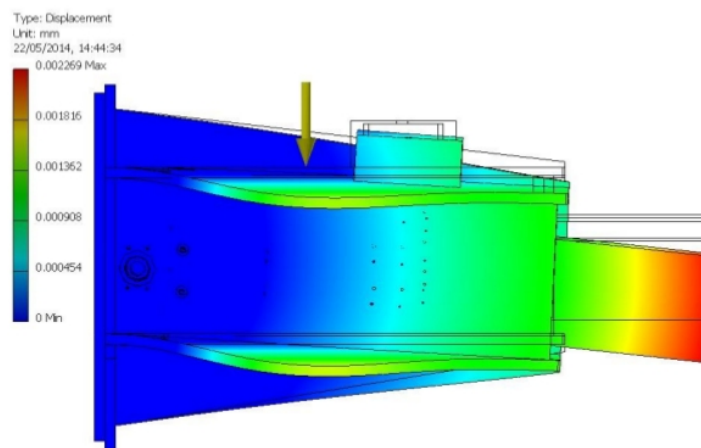


Figure 2.26: Telescope at horizon (worst case and not actually possible as minimum altitude angle is 25°), A&G box rotated with instrument on its side and horizontal, the maximum predicted displacement at the rear of the camera is 0.0022mm.

2.4.4 Plan View of Instrument

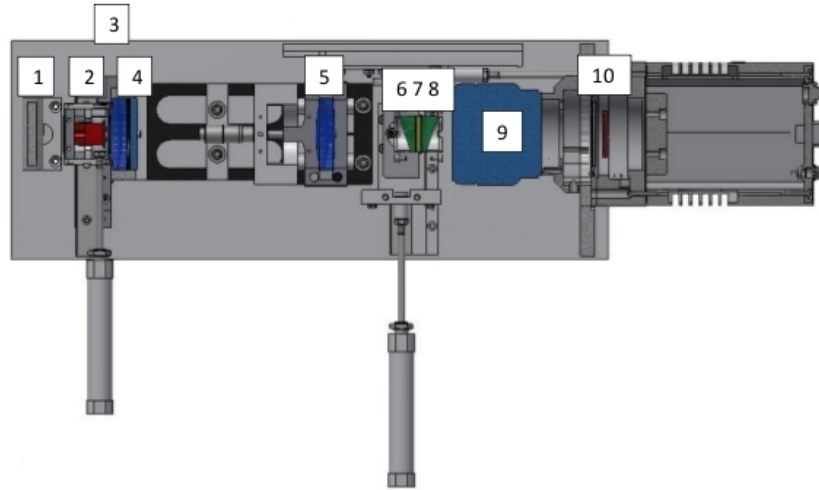


Figure 2.27: A plan view of the instrument identifying the optical elements. 1. Arc/Flat Calibration Angled Mirror (dark grey), 2. Slit (red), 3. Field Lens (blue), 4. Long-pass Filter (cyan), 5. Collimator Lens (blue), 6. 1st Prism (green), 7. VPH Grating (yellow), 8. 2nd Prism (green), 9. Camera Lens (cyan), 10. CCD (dark red)

2.5 Summary

The space envelope and target acquisition constraints led to a compact linear design for the instrument (Figure 2.27). An additional field lens was required to achieve a sufficiently short overall final length of ~ 645 mm, leaving 95 mm leeway for exit cables. To maintain thermal stability of the focus an adjustable internal Invar optical bench was employed for mounting the optics from the field lens to the collimator. The Speirs Robertson slit used in the prototype design was adopted for the final instrument allowing the final resolution to be chosen. The grism mount is pivoted to provide two peak wavelength throughputs, red or blue, to be selected. Of the available calibration arc lamp sources, Xe was selected as the most suitable for the range 4000 – 8000 Å. Evaluation of flat lamp sources led to the selection of automotive tungsten halide Bosch434 filtered through a Roscolux 3216 1/8th blue filter.

Chapter 3

SPRAT Commissioning and On-Sky Characterisation

3.1 Preliminary Set-Up and Calibration

The instrument was assembled, optically aligned and tested at the LT group of the ARI in Liverpool prior to shipping to the Liverpool Telescope located at the Roque de Los Muchachos observatory on the Canary Island of La Palma. Site commissioning took place between 1st– 4th September 2014. Mechanical assembly of the instrument at the ARI and installation on the LT was undertaken with the assistance of engineer Mr. S. Bates. Mr C. Mottram was responsible for the assembly/testing of the control panel electronics and for the host computer software at the ARI and provided remote assistance to site. Dr. R. Smith assisted at site with observations and applied changes to Telescope Control System (TCS) configuration to integrate target acquisition using SPRAT. The LT on-site facilities were managed by Mr Dirk Raback.

The controller and communication hardware is contained in an on-mount control panel separate from the main instrument which is on port 8 of the Acquisition and Guidance

(A&G) box beneath the main mirror. Umbilical cables run from the on-mount control panel, along the outside of A&G box, to the instrument and carry the actuator control and position sensor signals, and communicate with environmental sensors via a 1-wire protocol. The power supplies for the Andor CCD and Xe arc lamp are mounted externally on the top of the instrument together with the Uniblitz shutter controller (Figure 3.1). The Andor CCD communication interface to the host control computer, *iO11*, is via USB 2.0 which has a cable length limited of 5 m. The CCD USB 2.0 range was increased via a USB-to-fibre cable extender. The instrument was set-up with all cables and peripherals to be shipped to site to test components apart from fibre-optic link which was simulated with a short cable section.

Alignment of the optics at the ARI and site verification was achieved with a custom made auto-collimator for the instrument. The auto-collimator was constructed in two sections and fitted to the front entrance port of the instrument. It comprised a 5mW 650nm red laser pointer assembly mounted between two, 2-axis adjustable, ring mounts. The dual ring mounts permitted lateral adjustment of the laser pointer along x- and y-axes and rotation in the x- and y-planes. The laser beam passes through a pinhole aperture in a white circular card mounted ~ 3 cm ahead of the laser exit pinhole aperture. The circular card acts as the screen to detect the reflected beam. Collimation was achieved when the returned beam coincided with the pinhole aperture. The laser assembly was fitted to a pair of demountable optical bench bars bolted to the outside of the front plate. The brightness of the laser was adjustable (0–3V) via a bench power supply. A lower voltage was used to reduce the laser dot size to obtain greater accuracy in positioning. The auto-collimator mounting bars were fitted and the laser assembly attached and aligned with the centre of the instrument entry port (Figure 3.1).

The first step in alignment was to establish a principal optical axis between the laser and the Nikon Nikor camera lens. The other optics were then aligned to this axis. To achieve this all other optical elements were removed from the path. A pre-printed

circular target with a centre circle marker was fitted on a neutral density filter. The filter and target was fitted to the camera lens and the laser adjusted until the beam landed in the centre circle as a first approximation of alignment. The filter and circle target were removed and the laser position and orientation adjusted until auto-collimation with the centre of the camera lens was achieved. The camera lens was masked and the collimator lens was installed and orientated using the adjustable mount screws until auto-collimation was achieved. This process was repeated with the other optics, progressively aligning the order blocking long-pass filter and field lens towards the laser and masking the optical elements behind. A final check was done with all optics un-masked and it was found that the collimator lens required re-alignment. The slit was deployed and the hard stop screw adjusted until the laser beam passed through the centre to align it.

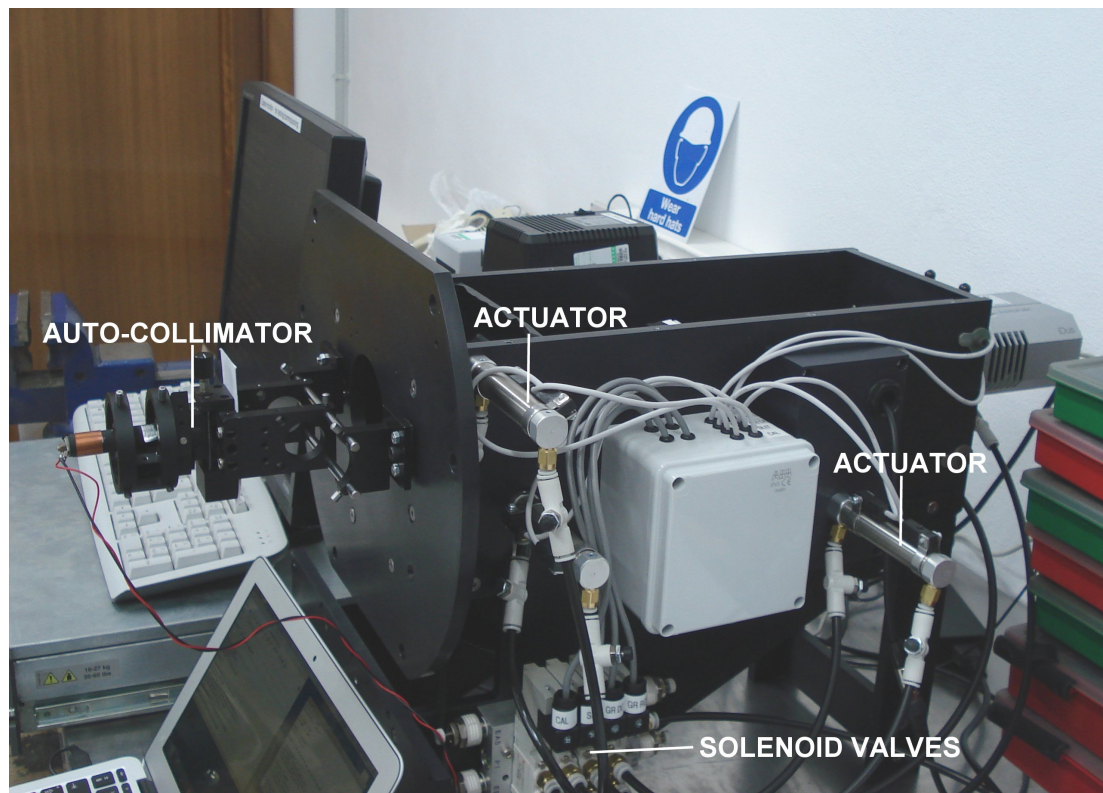


Figure 3.1: View of SPRAT with auto-collimator fitted to entrance port. The auto collimator bolts onto the front plate and is centered on the entrance aperture. The optics were aligned prior to shipping and re-checked at site before the installation on the LT. This view shows the pneumatic valves and silver actuator pistons, and gray electrical junction box.

SPRAT employs an internal Invar optical-bench to minimise the effect of temperature changes on the focus caused by a change in distance between the field lens and collimator. The collimator is located on a movable mount situated on the optical bench and can be positioned with a setting micrometer to focus the instrument. An approximate focus was established by illuminating the slit with a LED torch and adjusting the focus micrometer. The slit aperture was closed and slowly opened until a thin, continuous vertical illumination was visible. This method highlighted that the slit knife edges are not truly parallel as the very thin aperture was not uniformly illuminated along its length. The focus micrometer was adjusted until the CCD image of the slit reached an apparent minimum width, ~ 8.5 pixels, at a micrometer position 6.80mm. A finer setting of focus settings was later achieved after the slit was aligned with the CCD pixels. The focus micrometer was backed off and moved through the initial approximate focus point in 0.25mm increments and a minimum slit width was found graphically to be at position 7.00mm (Figure 3.2).

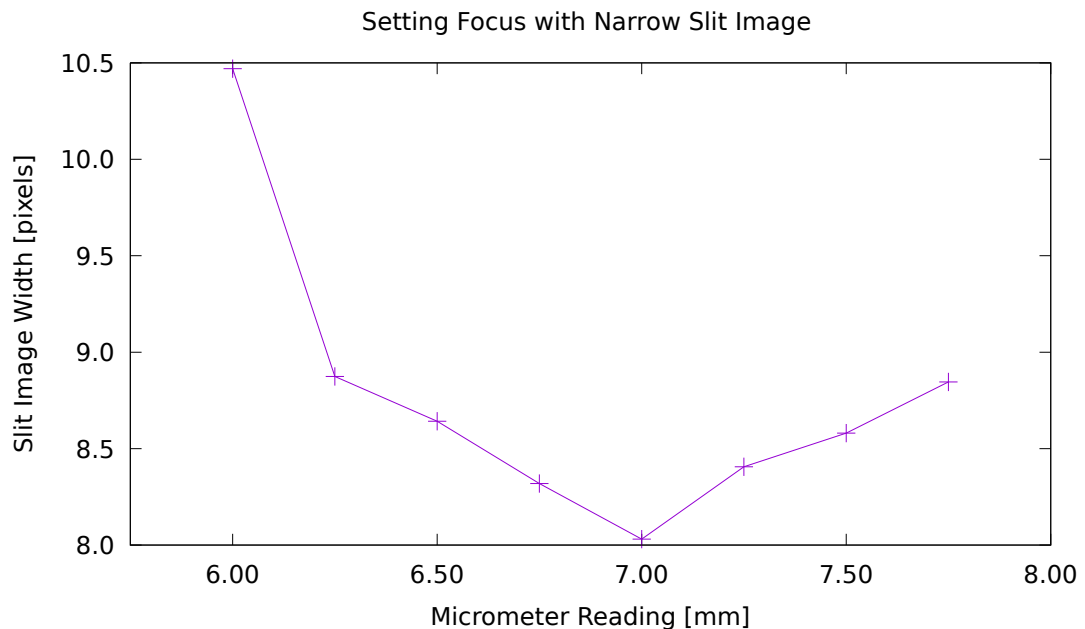


Figure 3.2: Fine focus setting using the slit image. A narrow slit was illuminated with an LED torch. The focus micrometer was moved through the visually estimated focus point at 6.80mm in 0.25mm increments. The minimum width of the slit image, and hence best focus, occurred at 7.00mm.

The grism was deployed and an attempt made to take a Kr spectrum for aligning the slit and grating with the CCD pixels. Kr was selected for testing in preference to the Xe calibration arc as it has bright lines at 5570 Å 5871 Å and doublet at 7602 & 7587 Å. With fewer bright emission lines than Xe and sparser dark spectrum regions, the Kr arc made detection of ghosting and stray light easier. However the resulting first spectrum was heavily contaminated with a central, non-uniform, band of light that had not been seen in the prototype (Figure 3.3 upper).

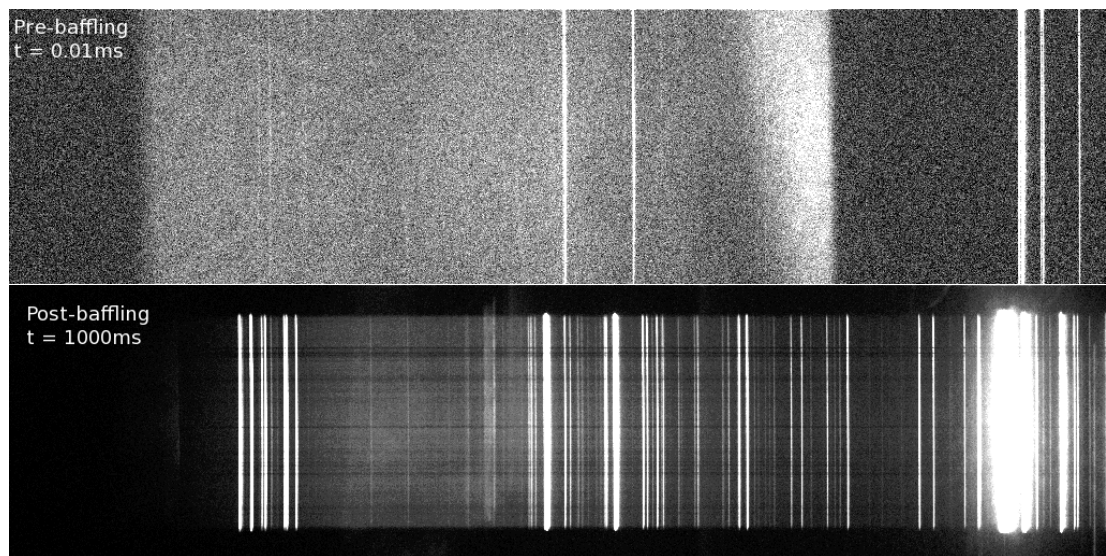


Figure 3.3: Comparison of Kr arcs before and after the addition of baffling to exclude stray light entering from the front of the instrument. A thin slit width was set during alignment and testing. Contamination from stray light is evident in the centre of the spectrum in the upper pre-baffled image. The exposure was $t = 0.01$ ms to avoid saturation and highlights the bright band on the right of the region affected. The lower image was taken with $t = 1000$ ms, the longer exposure showing the improvement after the addition of 3 sets of baffles. Two baffles were across the full internal width, surrounding the order-blocking/field lens mount and around the slit. A third baffle was added to the slit front to block light by-passing the knife-edge support ring. The aperture masking on the slit front was later modified so the top of the spectrum was included.

To identify if the cause was unwanted internal reflection the auto-collimator laser was re-attached and a small white target screen used to trace the routes of any reflections. No significant additional source of ghosting was found by this method. A section of black card was progressively placed around the internal optical path to selectively block potential light contamination arriving from different directions. It was discov-

ered that the direction of stray light was from the entrance port of the instrument. A permanent full-width baffle surrounding the order blocking filter/field lens mount significantly reduced stray light in images.

A further reduction was achieved by placing a temporary full baffle around the slit. However this is not a practical solution as the slit must be movable. A permanent 3/4 baffle surrounding the slit above and to the side away from the actuator piston was installed. For the side towards the moving actuator piston, a collapsible concertina baffle was necessary. It was assembled from sections of 1 cm wide black fibre-glass package tape connected together with flexible black fabric adhesive tape. The concertina baffle was trimmed to the full internal height of the instrument before being attached to the slit mount and side panel. The addition of the concertina baffle produced a further reduction in the stray light seen in images.

Comparison with prototype spectra indicated that some extra stray light was still contaminating the image. The only remaining path by which stray light into the instrument from the entrance port was via the knife-edge mount in the slit. Experimenting with an LED torch shone at different angles into the slit aperture showed that light could indeed leak past the circular spring holding the knife edges. This was minimised by gluing a black card baffle with a $\sim 0.5 \times 2$ cm aperture to the front of the slit assembly. The front slit baffle masked off the lower 34 pixels of the spectrum to provide an unilluminated reference region for identify any future ghosting or stray light. The three additional retro-fitted baffles successfully eliminated the uneven extraneous illumination on images (Figure 3.3 lower)

Ideally the image of a slit should be vertical on the CCD, in alignment with pixels. The slit is held in a movable sub-assembly and was rotated incrementally until the knife edges were vertically aligned with pixels on the CCD. Collapsed cross-sections of the slit image 11 pixels high were sampled, centered at $Y=15$ and $Y=235$. The shift in X-axis position in the slit centre was 0.6 pixel between the two sampled points. The

slit width increased from 6.4 to 8.1 pixels along the sampled range.

Similarly the grating was rotated to be in alignment with the slit. The grating within the grism was incrementally rotated until the upper and lower edges of spectral lines were horizontally aligned with CCD pixels. The Y-axis shift in the position of emission line ends across 740 pixels was ~ 1 pixel.

The peak wavelength sensitivity can be biased towards red or blue by rotating the grism assembly (Figure 3.4). The rotation angles for the two modes are set with an adjustable stop. It was decided to move the red mode peak from the original central $\lambda = 6000 \text{ \AA}$ in the prototype to $\lambda \approx 6500 \text{ \AA}$ so that the two modes peak wavelengths were $\sim \pm 500 \text{ \AA}$ from the central wavelength.

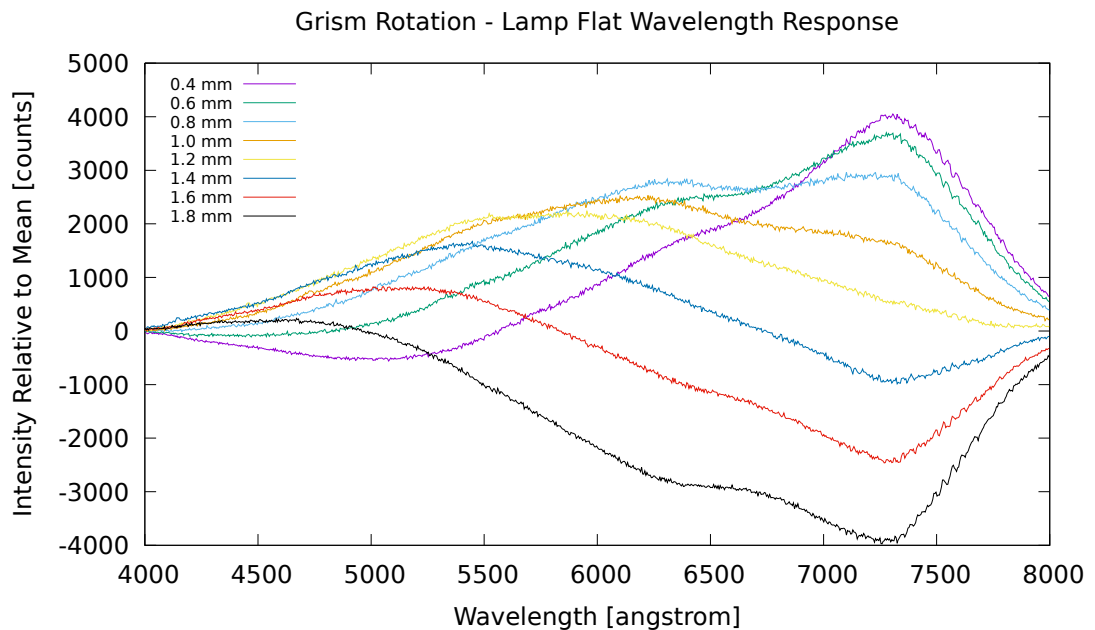


Figure 3.4: The change in spectral response of a flat lamp image with grism rotation. The intensity change is the difference in counts relative to the average value. Grism rotation is expressed in mm displacement of the position stop. The maximum mean value is $\sim 12,000$ counts.

3.2 On-Site Electrical and Software Setup

Prior to installation on the telescope the instrument was first set-up in the LT site workshop to check optical alignment, wiring and valve operation and communications with Arduino and host computer.

The communication and control software for SPRAT was installed on the computer node `ioi1`. The instrument control mechanisms and sensors are accessed via the telescope LAN to the network enabled EtherMega Arduino single-board controller in the on-mount control panel. Commands to control and retrieve status from SPRAT are sent in plain text to Telnet port 23, specified by `-p`, using the `send-command` utility. The SPRAT Arduino controller host has the DNS name `spratmechanism`, specified by `-h` option. For example, to execute a command, specified by `-c`, to deploy the slit,

```
/icc/bin/commandserver/test/i386-linux/send-command -h spratmechanism -p 23 -c "slit in"
```

The list of commands to control lamps and actuators are shown in Table 3.1. If no command parameter is supplied then the current status is returned. Actuator status is determined by reading two magnetic sensors set to detect the limit of travel. A status can also indicate ambiguity in position with neither sensor set, `state = Unknown`, or a contradictory condition where both are set, `state = Error`.

Table 3.1: Commands to control SPRAT using `send-command`. If no parameter is supplied to a command then the state is returned.

<code>wlamp on off</code>	Tungsten flat lamp, On/Off
<code>arclamp on off</code>	Xe calibration arc On/Off
<code>mirror in out</code>	Xe calibration arc mirror position, in=Deployed, out=Stowed
<code>grism in out</code>	Grism position, in=Deployed, out=Stowed
<code>rotation 0 1</code>	Grism rotation, 0=Red mode, 1=Blue mode
<code>slit in out</code>	Slit position, in=Deployed, out=Stowed

The Andor camera driver software was pre-installed on node `ioi1` and communicates to the CCD camera USB port via a fibre extender. Exposures were taken using the same `test_exposure_andor_lowlevel` application used when developing the instrument. Initial attempts to communicate with the Andor CCD camera failed until it was discovered that an essential generic Linux library USB package was missing from `ioi1`. This was resolved by installing the USB development package as the privileged user `root`, `yum install libusb-devel`.

Space envelope constraints around the current installed instrument set made it necessary to mount the SPRAT Arduino control panel vertically on the auto-guider panel adjacent on port 7 of the A&G box. Two larger umbilical cables carry the pneumatic valve control and position sensor signals for the actuators. The three remaining smaller cables return internal/external data from the temperature and humidity sensors, and orientation information from a 6-axis gyroscope in the instrument. The umbilical cables were threaded around the A&G box to the gray electrical distribution panel on the left side of the instrument (Figure 3.5). Mains power to the control panel was taken from an on-mount network addressable power-distribution strip to allow remote power-cycling of the panel.

The first attempt to install the instrument failed as a mis-alignment was found between the front plate mounting holes and those on the A&G port. The holes were re-machined on-site and the instrument was successfully bolted onto port 8 of the A&G box on the second attempt (Figure 3.5).

The actuator pistons contain a magnet and the deployment position is sensed by two reed-relay proximity sensors mounted externally towards each end of the actuator cylinder. Once all hard stop screws had been set to limit actuator travel, the sensor position must be set to correctly detect deployment or stowage. A `send-command` was scripted to run every 2s to monitor the actuator deployment state. The sensor was moved through the piston position and locations where detection ceased were marked.

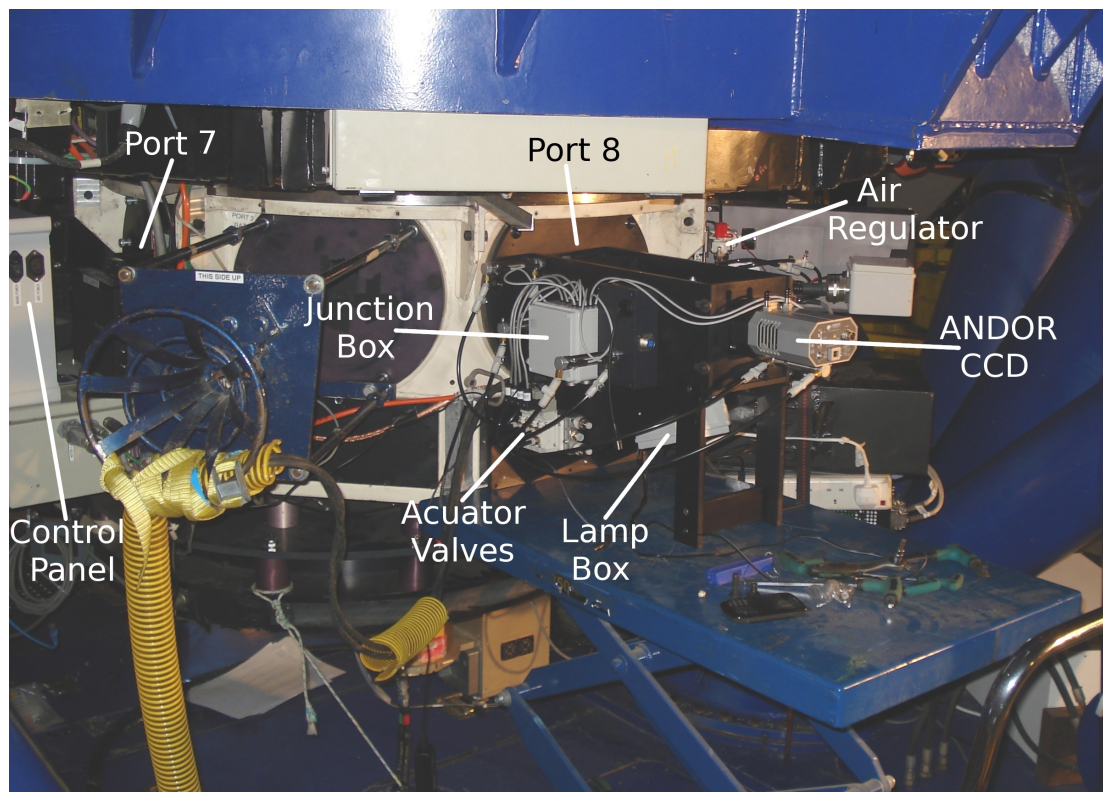


Figure 3.5: The mounting of SPRAT on port 8 of the Liverpool Telescope. A de-mountable rear stand was attached to keep the instrument horizontal on scissor-lift table during installation. Gray cables carry electrical signals to the left side square junction box. Below it is a white block housing the pneumatic valves controlling the actuators. The black feed pipes have in-line regulators to set the maximum applied force and lead to the actuator cylinders. On the extreme left is the vertically mounted control panel containing the Arduino and power supply. The photo was taken mid-installation without the top cover fitted to allow actuator operation to be verified. Still to be fitted are the umbilical cables from the control panel and the Andor PSU, shutter control box and calibration arc power supply. The USB fibre extender (not shown) was installed next to A&G port 1, immediately to the right of the instrument.

The sensor was positioned mid-way between the two marks and screw-locked in place. This process was repeated for each pneumatic actuator in both deployed and stowed state. Correct operation of the actuators and position sensors was first verified on-bench with actuators horizontally. Actuator operation was re-verified during flexure testing with the telescope altitude lowered to 30° and the Cassegrain rotated so the gravity vector acted in the direction of actuator deployment. The Cassegrain rotation was moved through 180° to reverse the gravity vector so it acted against the direction of actuator deployment.

An automated data reduction pipeline from the existing integral field spectrograph Frodospec (Barnsley, Smith, & Steele, 2012) was adapted for use with SPRAT by Dr. Robert Barnsley. This processed the images and spectra to produce different levels of reduced data products, L1 and L2. The L1 pipeline pre-processed images and spectra to correct for low level instrumentation signatures. It removes bias, performs flat-fielding and un-distorts the image. The L2 pipeline extracts the spectrum using 2x binning, performs a sky subtraction and wavelength calibration.

3.3 Measured Instrument Parameters

Wavelength calibration with the Xe arc lamp was done using the FIGARO `arc` utility. A list of usable bright emission lines (Appendix D) was created from the lamp manufacturer data sheet (Oriel-Instruments, 2008) and supplemented with lines from the National Institute of Standards (NIST) website (physics.nist.gov, 2013).

In blue mode, the `arc` utility was used to manually calibrate 3 Xe arc lines. Additional calibration lines were then found using `arc` automatic detection which suggested possible lines by interpolation. Some automatically identified lines were found to be incorrect and manually rejected. To improve the detection of partially blended lines the arc line half width parameter `SIGMA` was reduced from the default of 3 down to 1 pixel. The default 3rd polynomial fit reliably found 19 lines producing a maximum wavelength error 1.10 Å and RMS error 0.60 Å. The fitting polynomial order can be selected and other values were tried. With `ORDER = 4`, the wavelength maximum error was reduced to 0.65 Å and RMS error to 0.30 Å. Polynomial fit with `ORDER < 4` produced larger errors and `ORDER > 4` offered no significant improvement. The arc line identification was repeated with Xe arc in red mode to ensure that the same lines were also detected at modified amplitudes (Figure 3.6). In red mode a 4th order polynomial fit produced a maximum wavelength error = 0.60 Å and RMS error = 0.30 Å (Figure

3.7).

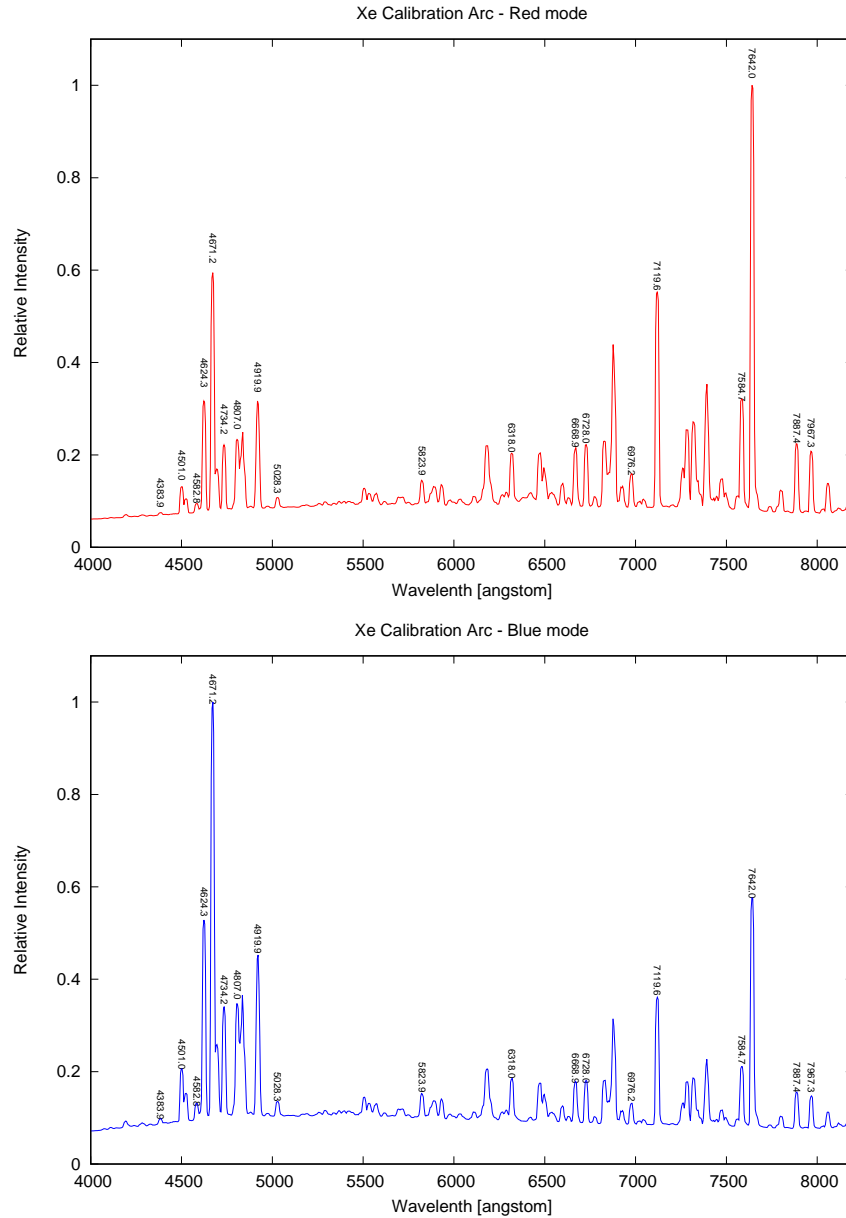


Figure 3.6: Xe emission arc in red (upper) and blue (lower) mode. The arc lamp manufacturer list of identifiable lines (Oriol-Instruments, 2008) was supplemented with bright lines from the NIST online database (physics.nist.gov, 2013). The intensity is derived from count and normalised to the brightest observed line.

The mapping of X-coordinate to wavelength is non-linear (Figure 3.8). Rotation of the grism causes a small shift between calibration and change in overall range between the two modes. Red mode mean wavelength dispersion = $4.55 \text{ \AA pixel}^{-1}$ whereas for blue

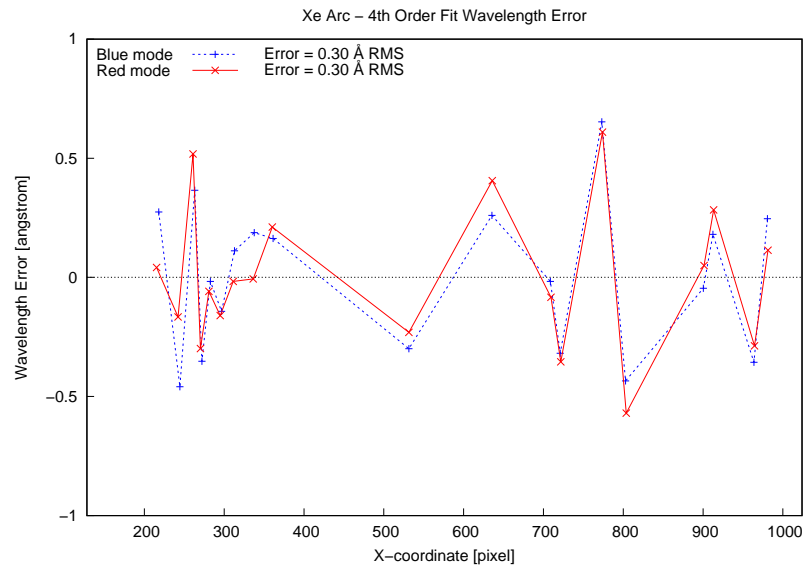


Figure 3.7: The error between individual emission line wavelengths and a 4th order polynomial fit. The overall RMS error is 0.30 Å in both modes.

mean dispersion = $4.58 \text{ \AA pixel}^{-1}$. An on-site estimate of plate scale was determined

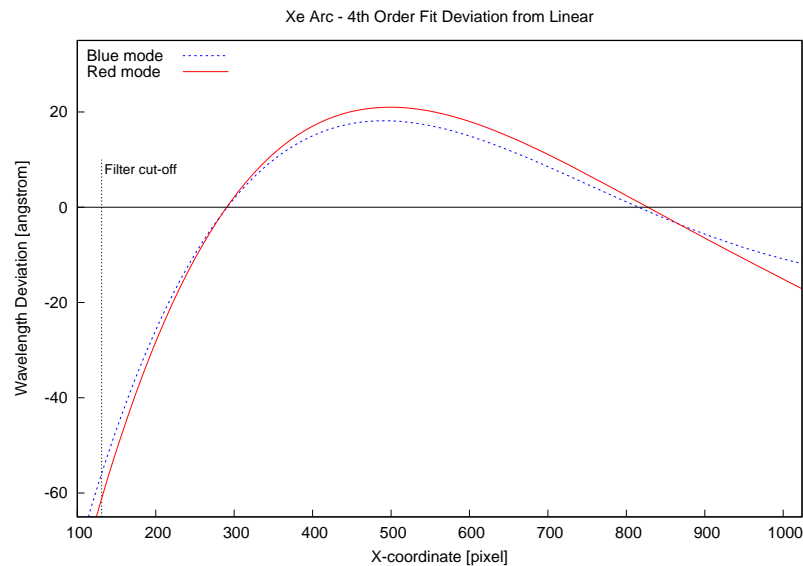


Figure 3.8: The deviation from linear wavelength to pixel mapping of the image of a spectrum image in red and blue modes. A 4th order polynomial fitted to identified Xe emission lines has an RMS error of 0.30 Å in both modes. Rotating the grism produces a horizontal shift of 4 pixels in the spectrum image between red and blue modes. The order blocking filter cut-off clips the spectrum below $\sim 4020 \text{ \AA}$ X=129 in blue and X=133 in red mode.

using the on-line plate-solver service Astrometry.net. Submitting acquisition images

of star BD+40 4032 and Cyg OB2 yielded a mean plate scale of $0.438 \text{ arcsec pixel}^{-1}$.

The lower wavelength range towards blue is limited by the order blocking filter with a nominal cut-off at $\lambda = \sim 4000 \text{ \AA}$. The tungsten lamp flat shows the filter roll-off actually cuts off at a slightly higher minimum wavelength of 4020 \AA . The end of the red spectrum extends beyond the CCD and wavelength value for an edge pixel corresponds to $\lambda = 8045 \text{ \AA}$.

The adjustable slit width was used to set the instrument resolving power during commissioning. The Xe arc spectrum was used to measure the dispersion, $d = 4.55 \text{ \AA pixel}^{-1}$ and the mean FWHM width of the slit, $W = 4.8 \text{ pixels}$. The resolving power, R , is given by

$$R = \frac{\lambda}{\Delta\lambda} = \frac{\lambda}{d \times W} \quad (3.1)$$

The initial mid-range resolving power at 6000 \AA was $R_{6000} = 274$ which was lower than desired. The slit width was reduced to $W = 4.3 \text{ pixels}$ to achieve a resolving power of $R_{6000} = 307$. SPRAT internal temperature was not recorded but the value of the telescope main tube temperature $T = 13.3^\circ$ (286.4 K).

The resolving power R is slit limited and assumes the target completely fills the slit width. The size of a point source is seeing limited so may not fill the slit giving a higher resolving power. This is illustrated by comparing the Xe arc FWHM emission lines widths with 1H0323+342 (Figure 3.9).

The effective focal length (EFL) of the field-lens and collimator combination is 146 mm and the camera EFL is 85 mm . The ratio of these two gives a de-magnification factor 0.58 of the slit image.

Evaluation of the instrument + telescope optical throughput was done post-site visit using spectra of spectrophotometric standard star BD+33 2642 (Oke, 1990). BD+33 2642 is post-AGB star and was selected as it was observable at relatively high altitude

82° to minimise airmass corrections, $AM=1.0093$.(King, 1985).

Blue and red mode spectra under photometric observing conditions were acquired on MJD=57206 with an exposure time $t = 60$ s. The flux at specific wavelengths was extracted from the Starlink data file `bdp332642.tab` (Stone, 1977) and converted from mJy to the expected ADU counts per second for each wavelength bin assuming the manufacturers quoted CCD quantum efficiencies. The expected ADU counts for a pixel with center frequency ν approximates to

$$\text{Expected Counts} = \frac{f_\nu \Delta_\nu A t Q.E.}{E_\nu \text{Gain}} \quad (3.2)$$

where f_ν is the standard star flux [$\text{Wm}^{-2} \text{s}^{-1}$], Δ_ν is the frequency range across pixels [Hz], the effective collecting area of the telescope aperture $A = 2.5 \text{ m}^2$, t is the exposure time [s], E_ν is the photon energy [J], Q.E. is the quantum efficiency, Gain is the CCD gain $2.45\text{e}^- \text{ADU}^{-1}$ from the manufacturer calibration data-sheet (ANDOR, 2012). The L2 pipeline processed spectrum was used which performs $2 \times$ pixel binning, doubling the effective dispersion in the data to $9.1 \text{ \AA pixel}^{-1}$.

The observed wavelengths did not directly map those for the standard star fluxes so interpolated values were calculated. The ratio of the two gives the total throughput of instrument and telescope (Figure 3.10). The blue mode peak is $\sim 5250 \text{ \AA}$ with throughput = 0.29, and red mode peak is $\sim 6450 \text{ \AA}$ with throughput = 0.35. Both throughputs fall below the predicted values (Figure 2.4) of ~ 0.46 for both. The comparison with red mode is not a direct one since the prototype predicted wavelength assumed central wavelength $\lambda = 6000 \text{ \AA}$.

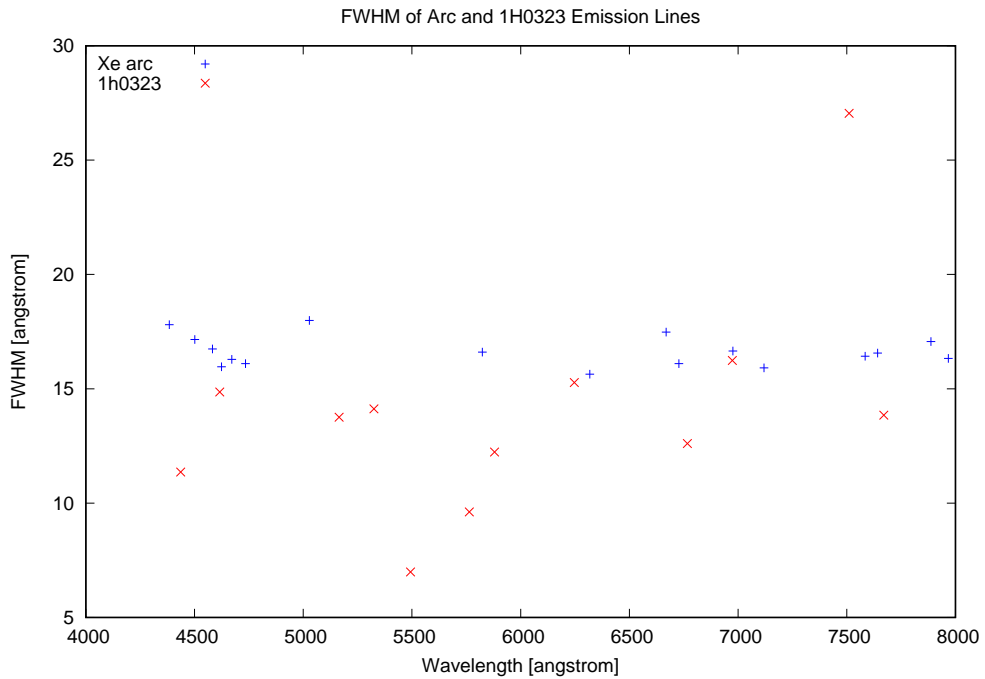


Figure 3.9: Comparison of Xe arc and 1H0323+342 emission lines widths. The width was determined at FWHM (Full Width at Half Maximum). The arc line widths are approximately constant across wavelengths while those of 1H0323+342 are on average narrower. A point source does not fill the slit width resulting in a higher resolving power.

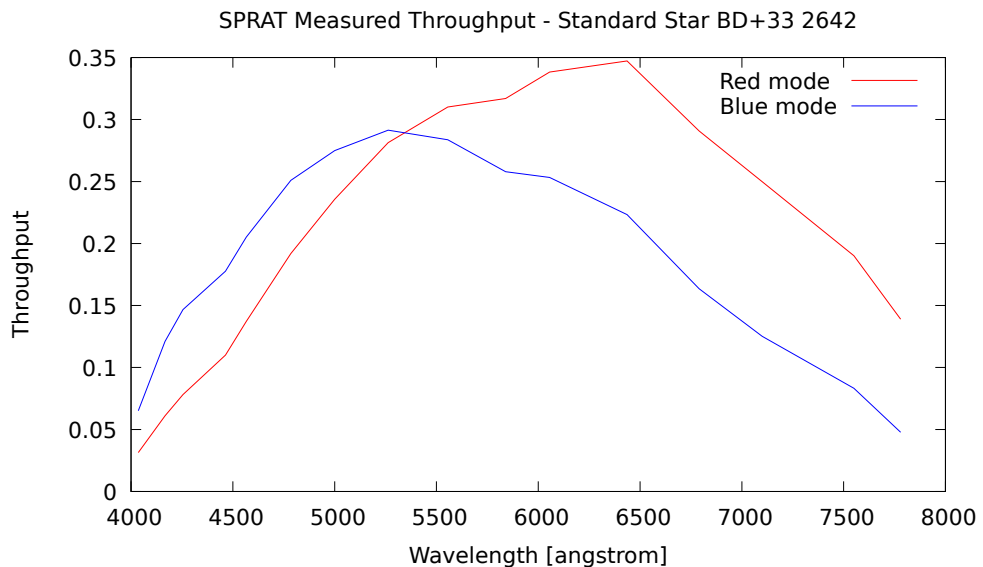


Figure 3.10: Measured optical throughput in red and blue modes.

3.4 Locating the Magic Pixel

Ideally a target object should be centered horizontally within the slit to minimise flux loss at the slit edges. Vertical placement is less critical but ideally should lie in the

middle of the vertical region searched by the L2 pipeline for the spectrum. The pixel location coinciding with these two optimum co-ordinates is referred to as the “magic pixel” and is an instrument specific parameter in the acquisition software. To avoid dust lines the magic pixel is vertically offset from centre to $Y = 179$. In the X-axis the magic pixel is set to $X = 479$ and was set during commissioning from an on-sky image of the slit the vertical centre was determined using `peak`.

The acquisition accuracy by blind pointing is ~ 6 arcsec which is greater than the ~ 2 arcsec slit width hence an alternative method must be used to reliably place a target within the slit. SPRAT can be used in imaging mode to achieve this. The field-of-view (FOV) is imaged and the acquisition software iteratively adjusts the telescope pointing until the target is on the magic pixel. Other LT optical imagers can be used to similarly locate a target onto the “magic pixel” specific to it, which will coincide with the optimum slit co-ordinates when instrument selection is switched to SPRAT.

The different operating configurations are illustrated in the observation sequence of standard star BD+40 4032 (Figure 3.11) during commissioning.

1. Target acquisition is performed in imaging mode with all deployable optics stowed out of the optical axis. The instrument operates as a camera focused onto the image plane with a magnification factor of 0.58 and FOV of 7.5×1.9 arcmin. This is the final image of an acquisition sequence with the target on the magic pixel. A maximum of 10 attempts to position the target on the magic pixel are made before the software declares an error and aborts the observation. Two methods for locating the target object within the FOV are available, plate solving the image to establish WCS coordinates or selection of the brightest target. An alternative imaging instrument can be used to acquire the target on a pseudo magic pixel for that instrument before selecting SPRAT by rotating the A&G pick-off mirror.

2. Imaging mode with grism stowed and slit deployed to image the slit. This is a 10s exposure of photometric standard BD+40 4043 to verify the target object is correctly centered within the slit. This check only introduces a small overhead and is recommended for observations.
3. Slit and grism remain deployed. A long-slit spectrum of BD+40 4043. This is the most common mode for observing.
4. Slit stowed and grism deployed. A slit-less spectrum of BD+40 4043 acquisition field.
5. The Xe calibration arc is normally taken at the end of observation. During commissioning an arc was taken prior to the spectrum but during normal observation the order is reversed. The Xe arc lamp is positioned externally on the underside of the instrument. A fibre-optic bundle light-pipe can direct either the Xe arc or flat lamp light into the instrument. A 45° mirror is deployed at the entrance to reflect the Xe arc from the light-pipe into the instrument optical path towards the slit. The slit and grism are both deployed. The grism rotation actuator would be deployed if blue mode was selected as in this case.

3.5 Effect of Temperature and Orientation

Thermal expansion and mechanical flexure alter the position and alignment of optical components, displacing the image of the slit on the CCD and causing the object to move away from the optimum location centered on the magic pixel. SPRAT is fitted with internal and external temperature sensors and the readings are tagged in FITS files as ENVTEMP0 and ENVTEMP1 respectively. FITS headers also include the telescope altitude, azimuth and Cassegrain de-rotator position, tagged as ALTITUDE, AZIMUTH and ROTANGLE, and are used to derive the instrument angular orienta-

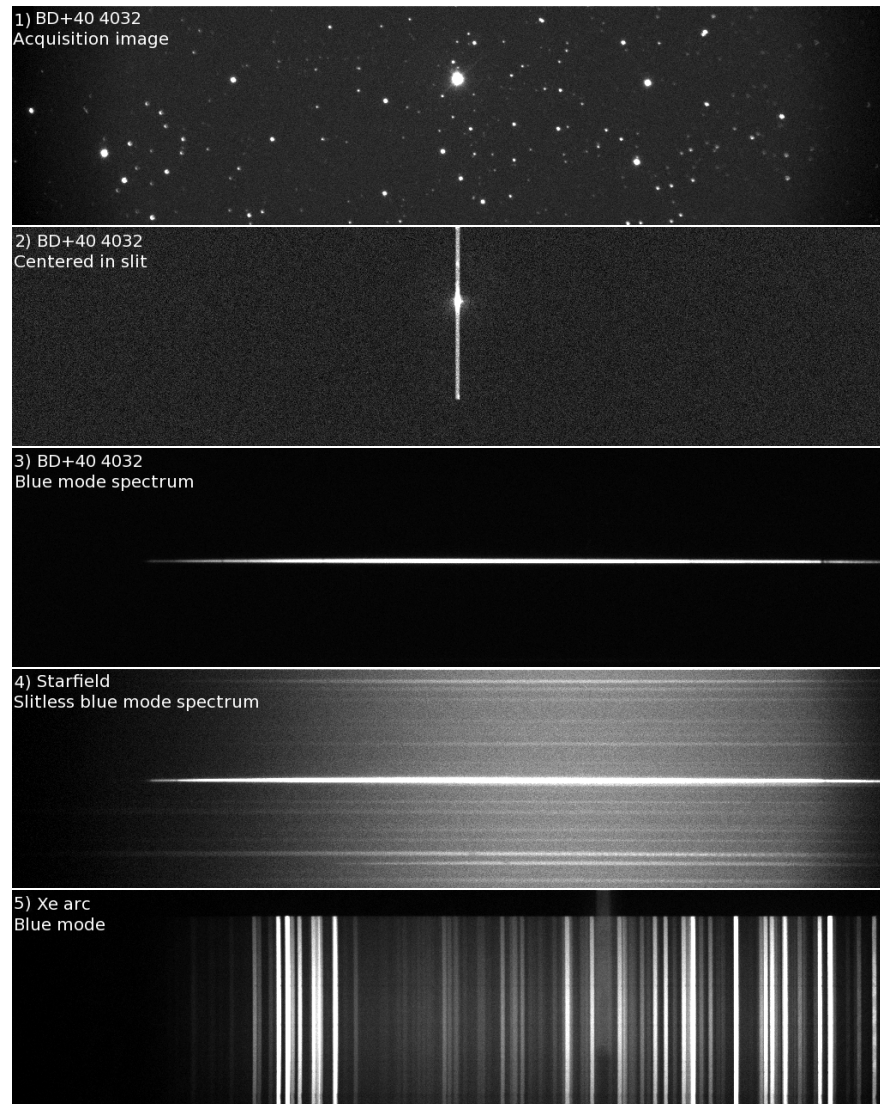


Figure 3.11: Sequence to observe standard star BD+40 4032 in blue mode taken during commissioning. 1) Acquisition mode showing target on magic pixel prior to slit deployment. 2) Slit deployed to confirm target star centered within slit. 3) Normal long-slit spectrum in blue mode. 4) Slit-less spectrum in blue mode. 5) Slit, grism and calibration mirror deployed for wavelength calibration using the built-in Xe arc lamp.

tion. To detect any long term trends it was desirable that the data was from a wide range of observing dates. 2 groups of data were used to analysis stability and are treated separately.

- Calibration arc images of the Xe spectrum with both slit and grism deployed, which provided the most extensive sample set.

- Acquisition images of Seyfert galaxy 1H0323+342 positioned within the slit, taken with the grism stowed.

3.5.1 Calibration Arc

Here we use images of the built-in Xe calibration arc lamp to assess the stability of the optical path with respect to changes in temperature, instrument orientation and time. The arc data set covered an epoch from Jan 2015 (MJD=57028) to Feb 2017 (MJD=57789) but included gaps where no data was available. Calibration arc images were routinely taken during observations with SPRAT and set of 831 arcs were extracted the LT data archive. The data set included faulty arc images taken during a period of Xe arc power supply outage plus several failed observations resulting from slit deployment failures. Removing faulty images yielded 500 red-mode and 256 blue-mode calibration arcs.

The arcs were raw images with no L1 pipeline corrections applied and suffer from pin-cushion distortion. To improve the shift detection the distortion was corrected to straighten arc and dust lines using the FIGARO `cdist` utility to apply an undistortion in the X- and Y-axes. The shift was measured using the FIGARO `scross` utility which performs a cross-correlation between two spectra and returns the relative X-axis pixel displacement. The Y-axis shift the image was rotated 90 degrees and process repeated with the dark lines created by dust on the slit serving as pseudo-absorption lines. The shifts were first measured relative to a datum red and blue standard star calibrations arcs taken on MJD=57474, `v_a_20160326_66_1_0_0.fits` and `v_a_20160326_66_1_0_0.fits`, approximately mid-way through the sample period.

The X-axis shifts relative to the datum observations for all the good red and blue mode calibration arcs are shown in Figure 3.12. The blue and red data were analysed separately as switching modes involves a rotation of the grism assembly thus altering the

path of light from the exit prism. Grism rotation was expected to introduce a displacement and is evident in the ~ 0.1 pixel offset between red and blue modes. Additionally there is a bimodal distribution with a separation of ~ 0.4 pixels. There is a periodic seasonal variation in X-shift amplitude with a peak-to-peak period of 1 year. The initial peak at MJD=57100 is offset by ~ 0.6 pixel with respect to later peaks. Engineering work undertaken before MJD=57200 involved evaluating a replacement camera lens to reduce vignetting. The reduction in the subsequent peaks was attributed to an offset introduced when re-fitting the camera and original lens. Data prior to MJD=57200 were excluded in subsequent analysis to eliminate any effects introduced by disturbing the optics. This reduced the data sample to 418 red-mode and 244 blue-mode arcs.

The metric selected to establish a dependence between a measured physical parameter and pixel shift was the Spearman's rank correlation coefficient, ρ , and probability, P , of the correlation being random. Spearman's rank correlation does not assume a linear relationship and is tolerant of outliers in the input data. Although Xe spectrum emission lines are reproducible, the dust lines used to measure a Y-axis shift could change over time. A blink comparison of the first and last Xe arc in the data set was performed and showed no change in position or number of the 5 prominent dust lines.

The shifts were calculated relative to the mean of all shifts for a particular colour mode. Given the apparent annual variation in shift we first investigated the temperature dependence of the slit position. The X-axis pixel shift with instrument internal temperature is shown in Figure 3.13. The plots show significant correlation, $\rho_{\text{red}} = -0.55$ and $\rho_{\text{blue}} = -0.44$, and both have $P = 0.000$. The combined data gives a mean thermal coefficient of X-axis shift -0.023 pixels K^{-1} . Correcting for the thermal effects more clearly shows an unexpected bimodal distribution and a ~ 0.4 pixel separation between the two populations. Since the instrument contains deployable optics a possible cause is a mechanical component adopting one of two stable positions.

The Y-axis pixel shift of the dust lines (Figure 3.14) also shows a strong correlation

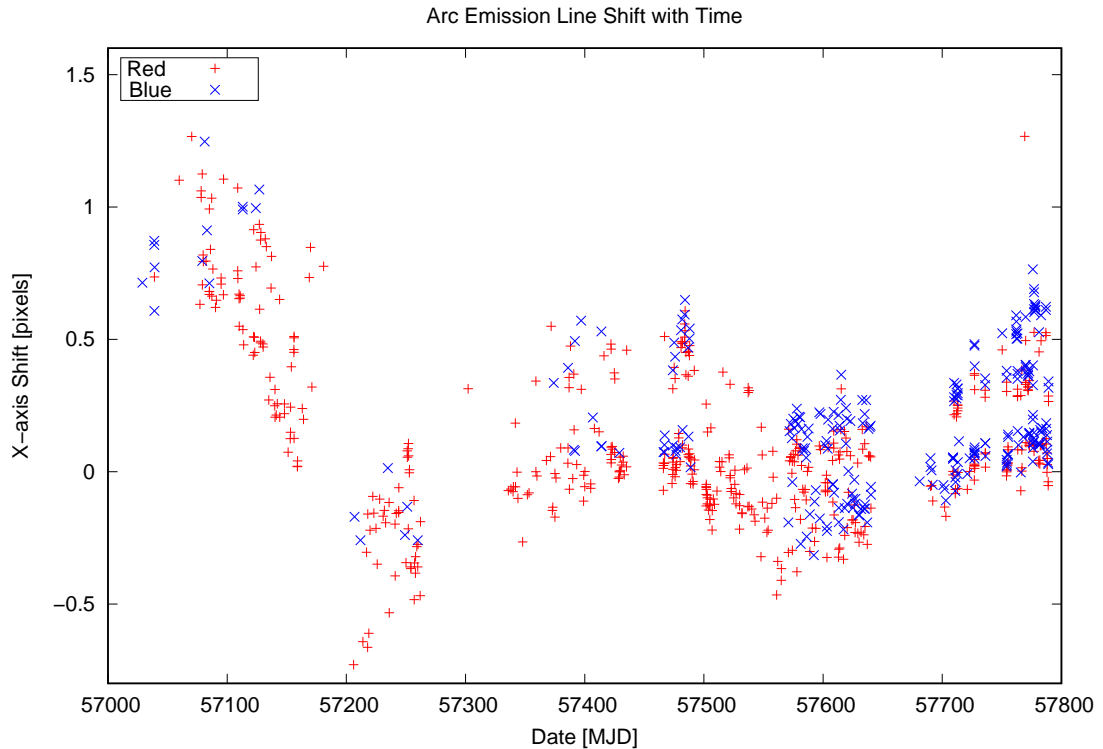


Figure 3.12: The emission line X-axis shift relative to datum spectra taken on MJD=57474 of a standard star BD+33 2642. The displacement between red and blue is a result of grism rotation shifting the optical beam when switching modes. The initial peak at MJD=57100 is prior to testing an alternative camera lens which disturbed the optical alignment. Post MJD=57200 the SPRAT optical system remained unmodified. A seasonal variation is evident in the 1 year interval between maxima. Gaps in the data are associated with engineering work and hardware outages.

with temperature $\rho_{\text{red}} = -0.70$ and $\rho_{\text{blue}} = -0.78$, and both have $P = 0.000$. The combined average Y-axis thermal shift coefficient = -0.067 pixels K^{-1} , three times greater than for the X-axis. For a purely thermal effect it would be expected for the Y-shift at a particular temperature to remain constant over time. However isotherms taken from the more populated temperatures (Figure 3.15) show it does change over time, $\rho_{\text{red}} = -0.67$, $P = 0.000$. The long term drift in Y-shift is ~ 0.5 pixel year^{-1} .

The instrument is attached at slit end to side port of the Cassegrain de-rotator but is not supported at the camera end. The turning moment acting on the instrument will vary with the orientation, possibly altering the optical alignment. The Cassegrain de-rotator angle is normally set close to 11 degrees to align the slit vertically, in line with the

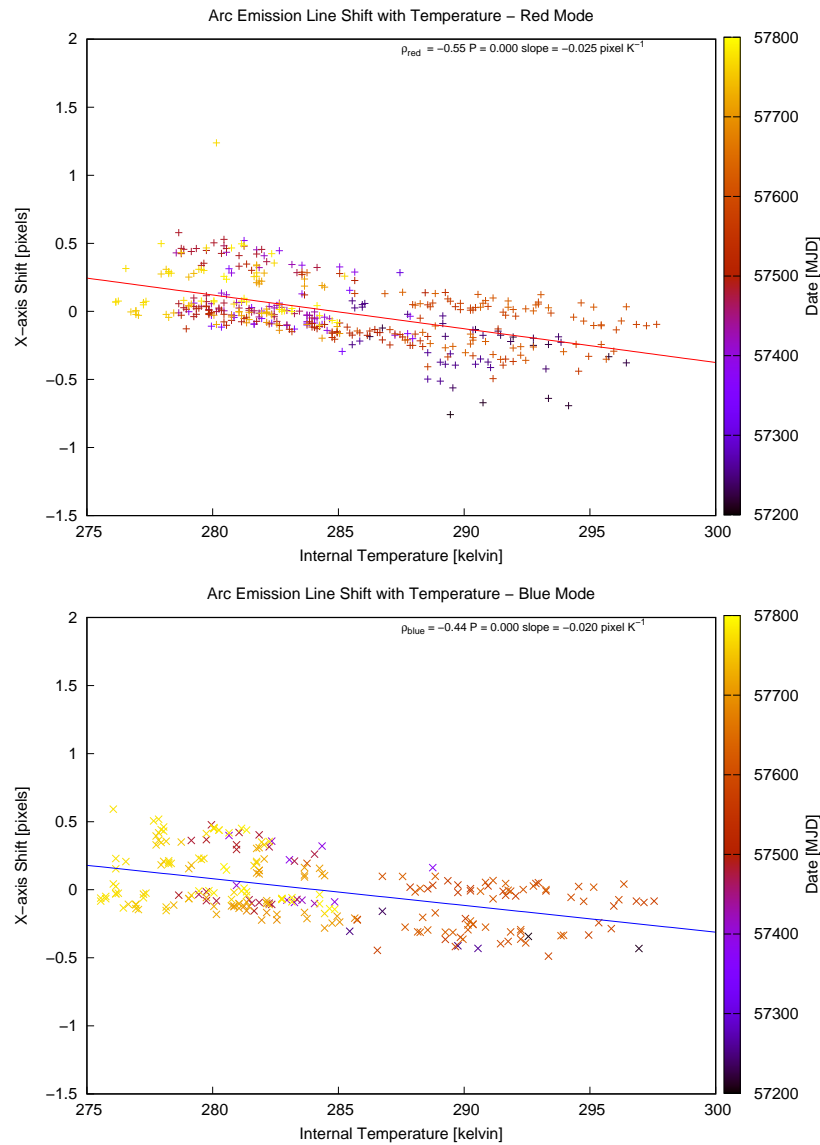


Figure 3.13: The variation in the X-axis position of the Xe calibration emission lines. There is a correlation between X-axis shift and instrument internal temperature in both red and blue modes. Red and blue were analysed separately to remove any shifts caused by grism rotation when changing peak colour sensitivity modes. The bimodal distribution of data into two groups with a separation of ~ 0.4 pixel was unexpected. The points are colour coded by MJD date to show seasonal change which is evident in the grouping of yellow and blue points.

atmospheric dispersion to avoid a loss of flux. This resulted in a data sample heavily biased around the 11 degree rotation angle (Figure 3.16) although the blue-mode angle is more widely sampled than the red. There is little correlation in X-axis shift with both ρ_{red} and $\rho_{blue} \sim 0.000$. The Y-axis blue data shows an apparent correlation, ρ_{blue} ,

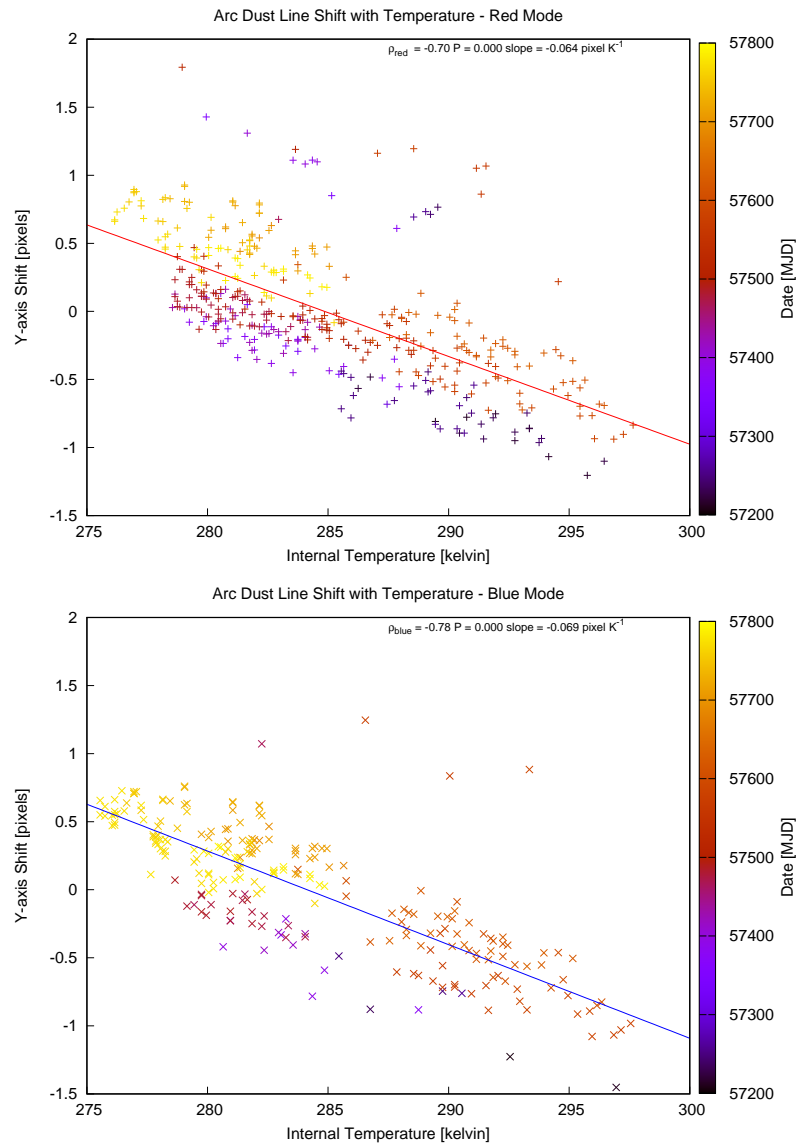


Figure 3.14: The variation in Y-axis shift with temperature was measured using dust lines as pseudo-absorption lines. The Y-axis shift shows a significant temperature correlation. The bimodal distribution that was shown in the X-axis data is much weaker and is largely absent from the blue mode data. The data points are colour coded by MJD date to highlight seasonal changes. The spread of coloured date coded points is evidence of a long term change, $\sim 0.5 \text{ pixel year}^{-1}$.

$= -0.22$ and $P = 0.001$. This is not reflected in the red, $\rho_{\text{red}} = -0.09$, possibly because of fewer samples below an declination of -20 degrees.

The altitude angle also changes the orientation of the instrument and provides a more even spread of angles than Cassegrain rotation. To de-couple temperature effects from

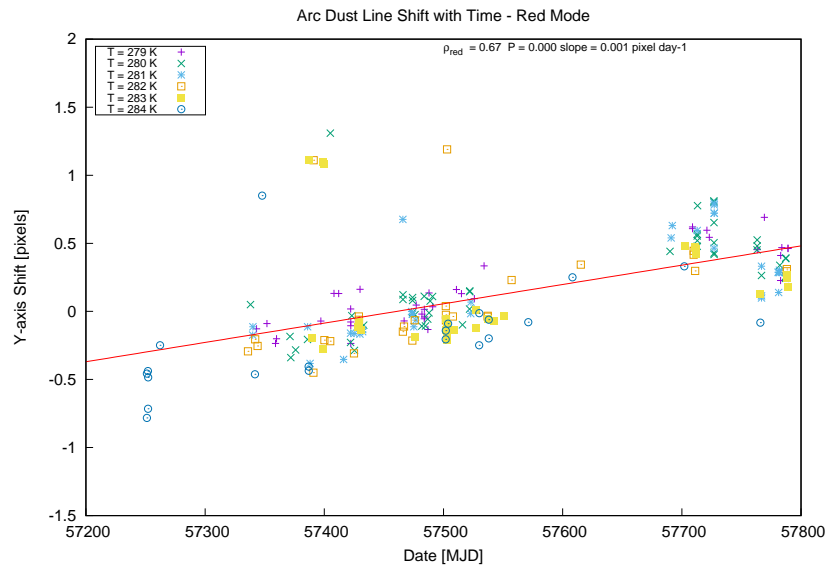


Figure 3.15: The variation in Y-axis shift over time of 5 isotherms in the range $T = 279 - 284$ K. The most populated temperature intervals in red mode were selected resulting in a preferential clustering of dates centered around Spring 2015 and Spring 2016. The drift is 0.0014 pixel day⁻¹ which equates to an annual rate of ~ 0.5 pixel year⁻¹.

mechanically produced shifts resulting from altitude angle, data was selected for an isotherm at $T = 281$ K (Figure 3.17). The temperature $T = 281$ K was chosen as it had the largest number of readings within a 1 K interval, 48 red and 30 blue points. The correlation from this smaller sample was inconclusive with $P > 0.150$ for both red and blue. To increase the sample size the mean thermal coefficient derived from Figure 3.13 was applied to correct data at other temperatures. The variation of X-shift with altitude (Figure 3.18) shows a good correlation, $\rho_{red} = 0.18$ and $\rho_{blue} = 0.29$, with $P \sim 0.000$ for both. The mean gradient for the two modes is 0.003 pixels degree⁻¹.

Telescope azimuth angle does not change the instrument orientation so was not expected to correlate with a shift in X- or Y-axes and is included for completeness (Figure 3.19). This is confirmed by almost flat linear fit gradients, $< \pm 0.0001$, and low Spearman's rank coefficient for both X-axis $\rho_{red} = -0.07$ and $\rho_{blue} = -0.23$, and Y-axis, $\rho_{red} = 0.01$ and $\rho_{blue} = 0.13$. The clustering at some azimuth angles was caused by frequent arcs taken for observations of standard stars and long term monitoring of Seyfert

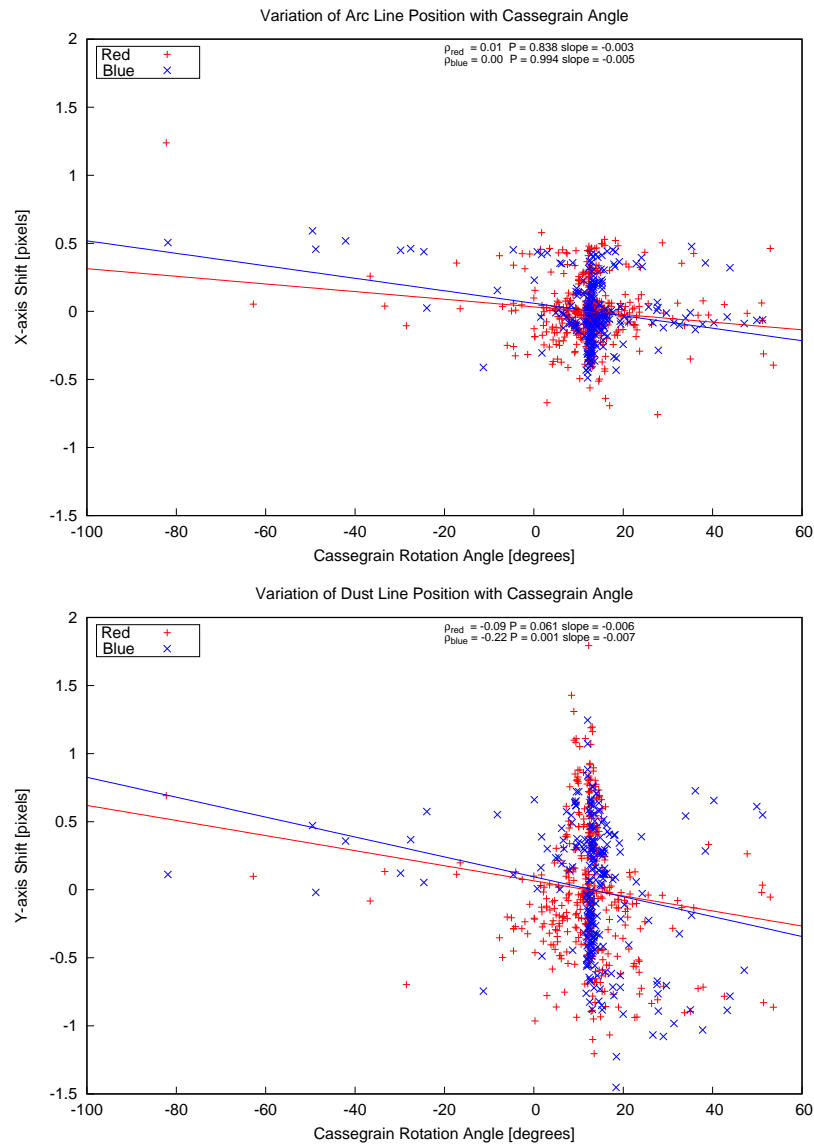


Figure 3.16: X- and Y-axis shifts with change in Cassegrain rotator angle. The sample is heavily biased to 11 degrees as this aligns the slit with the parallactic angle. The X-axis shift shows no correlation with Cassegrain angle with high values of $P > 0.8$. For Y-axis shift Spearman's rank correlation is ambiguous, $P_{\text{red}} = 0.061$, too low a confidence yet $P_{\text{blue}} = 0.001$. A change in gravity vector would be expected to have a common effect on both modes. Around the 11 degree point the data has a large scatter with mean red/blue s.d. = 0.47 pixels. Together with the large sampling bias means that the correlation is inconclusive.

galaxy 1H0323+342. Again we find a distinct bimodal distribution in the X-axis shift with a separation of ~ 0.4 pixels.

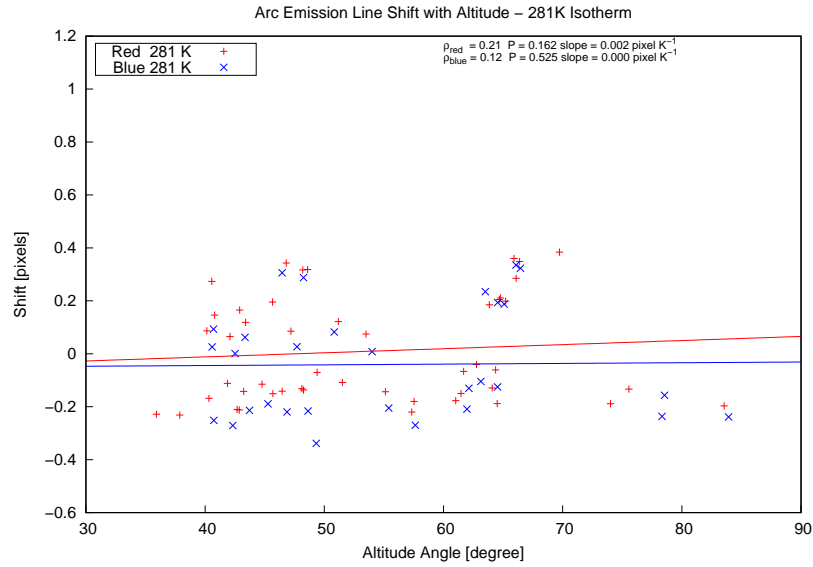


Figure 3.17: Variation of X-axis shift with altitude angle at temperature $T = 281$ K. Temperature effects were minimised by selecting a reduced data set with $\Delta T = 1$ K. There is no indication of a correlation with temperature. Both blue and red data is poorly sampled above altitude angle 70 degrees with only data 3 points.

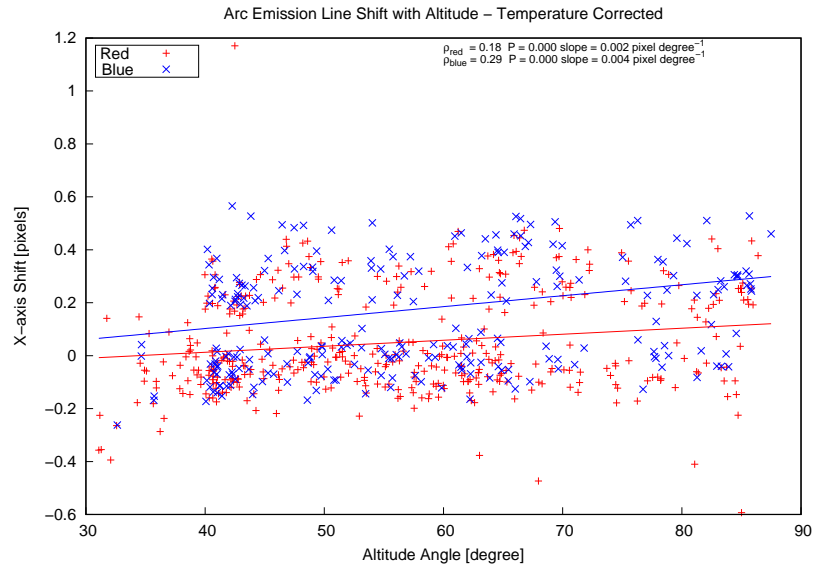


Figure 3.18: Variation in X-axis shift with altitude angle corrected for temperature. Compensating for thermal effects and the larger data sample shows a correlation between instrument orientation and X-axis shift.

3.6 Stability of Slit Position

In addition to the calibration arcs SPRAT observations of a narrow-line type 1 Seyfert galaxy 1H0323+342 were available from MJD 56998 to MJD 57714 providing a total

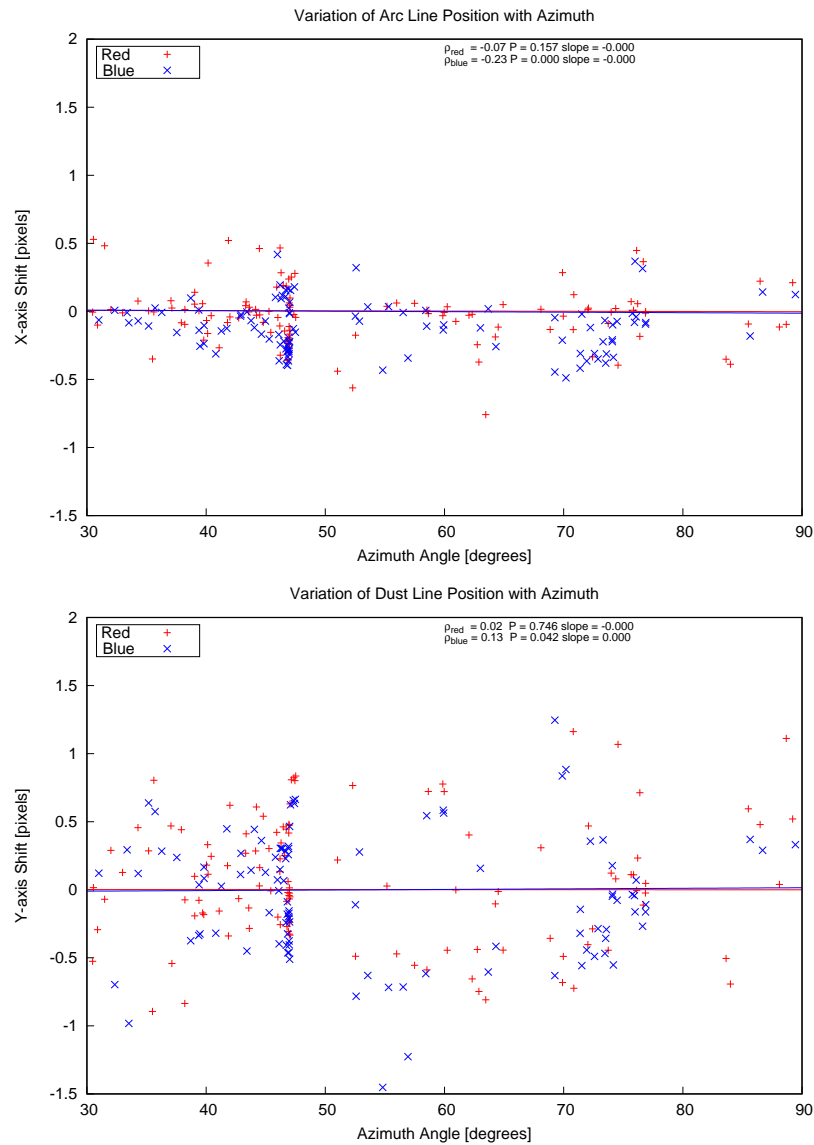


Figure 3.19: Xe calibration arc X- and Y-axis shifts were not expected to correlate to azimuth position. The clustering of observation points is from arcs taken for standard stars and long term monitoring of 1H0323+342. Both X- and Y-axis shifts show no correlation with telescope azimuth angle.

of 111 usable blue-mode spectra (Figure 3.20).

Each observation included two acquisition images of the object in the slit, one immediately prior to a blue mode spectrum and one post observation. Eliminating failed acquisitions gave a total of 228 usable images (114 pre- and post-observation pairs) of the target within the slit. The stability of the slit width and accuracy in positioning the

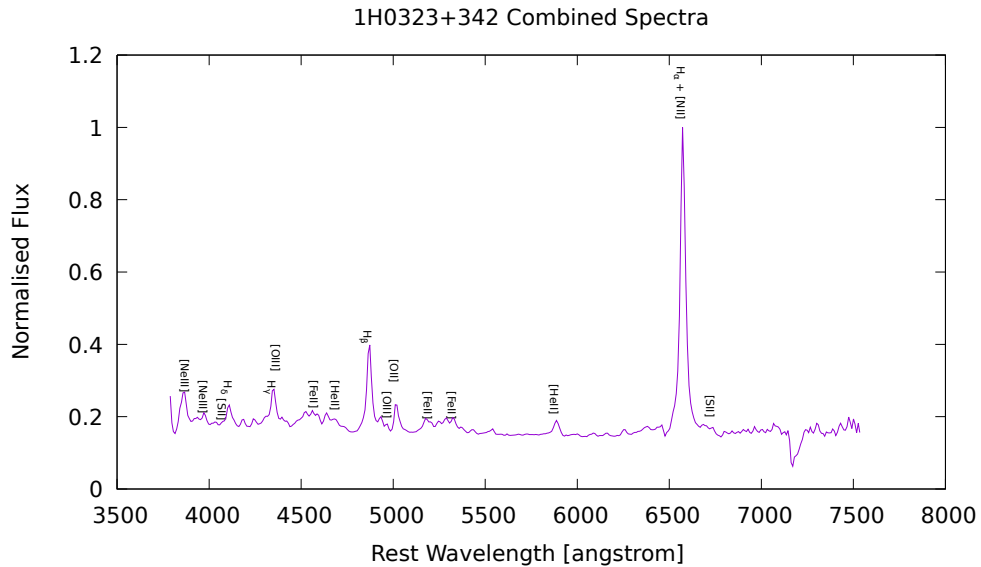


Figure 3.20: A stacked spectrum of Seyfert galaxy 1H0323+342. This is the combined spectrum from 111 observations taken between MJD 56998 and 57714.

target was assessed using the acquisition images. Images prior to 57200 MJD were excluded to eliminate the optical path change introduced by the camera lens evaluation. This left a total of 160 slit images covering 505 days from 57210 to 57714 MJD. The slit image was treated as a pseudo-spectrum with a single bright emission line. Skyglow was assumed to be uniform along the 170 pixel (~ 1.4 arcmin) length of the slit image. The slit was sampled over shorter ranges, an upper $Y = 100\text{--}120$ and lower $Y = 200\text{--}220$ region, to avoid features from the target object near the magic pixel at $Y = 179$. The repeatability of the X-axis positioning of the slit image was measured using FIGARO `scross`, a cross-correlation utility which returns the X-axis displacement between two spectra. A datum slit image, `v_e.20160213_4_1_0_1.fit`, was selected as approximately mid-way through the sampled period and at a temperature within 1K of the data set mean value of 286.5K. The sample region was collapsed with FIGARO `extract` before cross-correlating with `scross`. `scross` is designed for use with spectra and to verify the validity of applying it to a slit image an alternative method was tried for comparison. The position of the collapsed slit image was measured with

FIGARO `peak` which returns the X-axis position and FWHM width of the highest peak in a data array. The same sample ranges were used and variation with instrument internal temperature producing similar results for the two methods and ranges (Figure 3.21). There is a clear correlation with temperature, typically $\rho = 0.59$ and $P = 0.000$, and the mean X-shift temperature coefficient = -0.039 pixels K^{-1} . There was little difference between the two measurement method results and `peak` was adopted for analysing the slit images as it also returns a FWHM width.

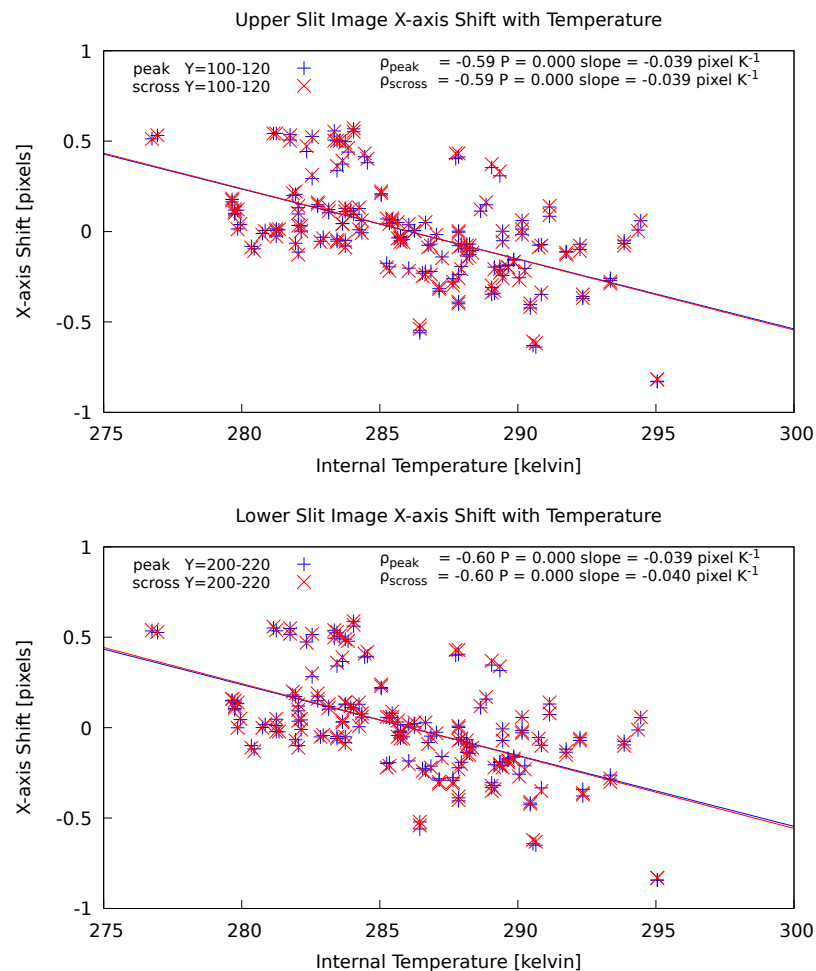


Figure 3.21: The relative X-axis displacement of the slit image relative to a datum image taken a temperature $T = 286$ K. The shift was determined with FIGARO `scross` and `peak` utilities sampling 21 pixel long sections of the slit above and below the target over the two Y co-ordinate ranges shown. The different sampling methods and regions produce consistent results. There is a clear correlation with temperature with the mean X-shift coefficient value -0.039 pixels K^{-1} .

The slit employed in the instrument is a symmetrically adjustable knife-edge made by Speirs-Roberston. The knife edges are mounted on a circular spring with no mechanical temperature compensation. During laboratory development of the instrument prototype it was noted that the apparent slit width varied with temperature. The slit images were sampled over 21 pixel high regions at co-ordinates $Y = 100\text{--}120$ and $Y = 200\text{--}220$ with width measured using `peak`. A thermal dependence was expected and is evident (Figure 3.22) with correlation values $\rho > -0.75$ and $P = 0.000$. The mean thermal coefficient in slit width change is $-0.016 \text{ pixel K}^{-1}$. There is offset between the two sample points showing the slit width is not uniform along the Y-axis, widening by $0.0016 \text{ X-pixel per Y-pixel}$.

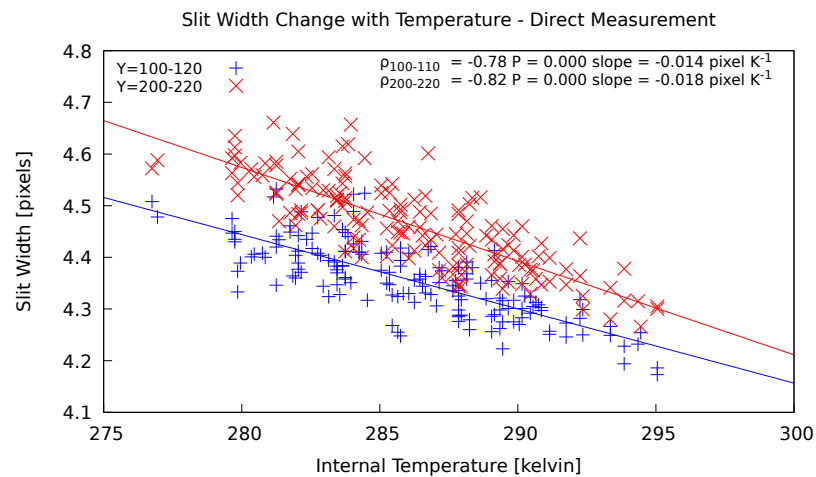


Figure 3.22: The X-axis thermal stability of the slit obtained by measuring the apparent width using `peak`, which returns the FWHM width. A temperature dependence of the slit width was expected and the mean X-axis coefficient was $-0.018 \text{ pixel K}^{-1}$. The difference between the upper and lower width measurement indicates the slit width is not uniform and narrows by $0.0016 \text{ X-pixel per Y-pixel}$. Shortcomings of this method are that it measures the apparent FWHM width and includes any widening caused by a focus change.

A shortcoming with direct measurement of slit width obtained using `peak` is that the apparent slit width also changes with focus. `peak` also assumes the input profile is Gaussian and returns a FWHM width. It was desirable to find a method of de-coupling any changes in focus from the measurement. De-focusing a sharp discontinuity such as the edge of the slit produces a flux re-distribution which is approximately Gaussian.

The point of maximum gradient of the de-focused discontinuity remains coincident with the original sharp edge. Taking the differential of a de-focused slit edge allows the position of the original ideal edge to be determined (Figure 3.23) as the distance between the maxima in both ideal and de-focused derivatives remains constant. A derivative of the slit image was taken with the FIGARO `idiff` utility, which performs a numerical differentiation by evaluating the absolute difference between a pixel and its immediate neighbours. The `idiff` utility does not preserve the sign of a detected edge and instead returns the positive absolute value of the gradient. The centers of the peaks were measured with `peak` to produce a revised width measurement which excluded focus effects (Figure 3.24).

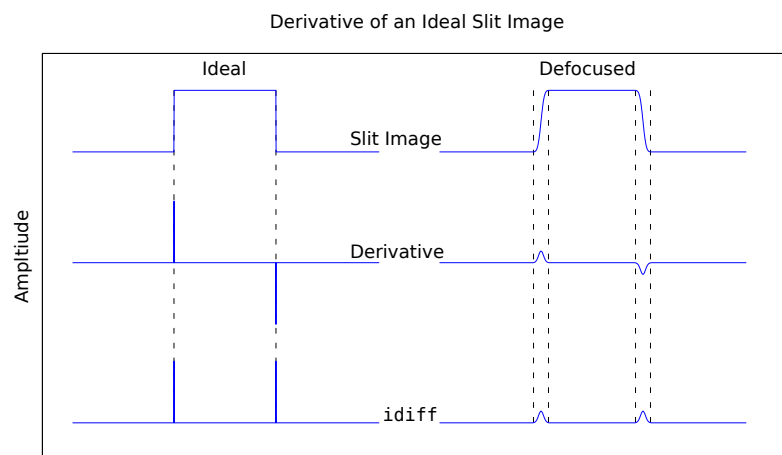


Figure 3.23: A method to decouple the effect of defocus when measuring the slit width. Upper plot is the X-axis cross-section of an ideal slit image (left) and the effect of defocussing (right). The profile of a de-focused edge approximates to a Gaussian curve with the gradient maximum at the mid-point of the curve. The middle plot is the derivatives of the corresponding upper cross-sections. The distance between maxima of the peaks in the derivative remains constant for both an ideal and de-focused image. The FIGARO `idiff` utility does not preserve the sign of a detected edge and returns the positive absolute value of the gradient (lower plot). A change in the width of an edge peak indicates the focus has altered.

The 1H0323+342 observation sequence takes an image of the target in the slit both before and after the spectrum. The slit is deployed by a pneumatic piston and rests against a hard stop while the slit acquisition and target observation images are taken. Comparison of the X-axis positions of the slit edge in pre- and post-observation images

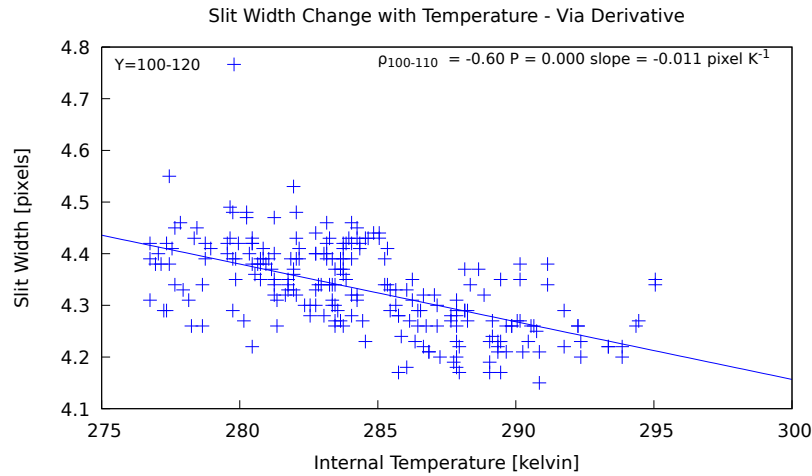


Figure 3.24: The stability of X-axis width with change in temperature obtained using the derivative of the image to detect edges. This method eliminates defocussing effects when measuring the apparent slit width on a raw image and shows a thermal coefficient $-0.011 \text{ pixel K}^{-1}$.

allows the stability deployment during an observation to be assessed (Figure 3.25). To reduce the effect of other thermal changes during an observation data with $\Delta T > 1 \text{ K}$ were excluded, leaving 75 images for analysis. The numerical derivative of the slit image was evaluated `idiff` to locate edges. The left and right slit edges were sampled at $Y=100-120$ and the centres of the edges determined using `peak`. The X-shift of the slit edge was plotted relative to the datum image taken at temperature $T = 285 \text{ K}$. There is no correlation in stability with temperature, $\rho < -0.06$ and $P > 0.6$ for both edges. Combining left and right edge X-shifts gives a mean s.d. = 0.07 pixels. However there are 3 instances of the slit shifting by ~ 0.3 pixel during an observation.

The difference in thermal coefficient between the two methods in measuring slit width is $-0.005 \text{ pixel K}^{-1}$, a possible cause being change in focus. Target acquisition uses the object size to estimated seeing and is included in the FITS header as the `ESTSEE` parameter. An alteration in focus would produce a change in object size and hence the reported estimated seeing. The `ESTSEE` seeing of SPRAT does show a correlation with instrument internal temperature (Figure 3.26 upper) with $\rho=-0.32$, $P=0.000$ and coefficient $k = -0.021 \text{ K}^{-1}$. Data with poor seeing $> 2.50 \text{ arcsec}$ was excluded.

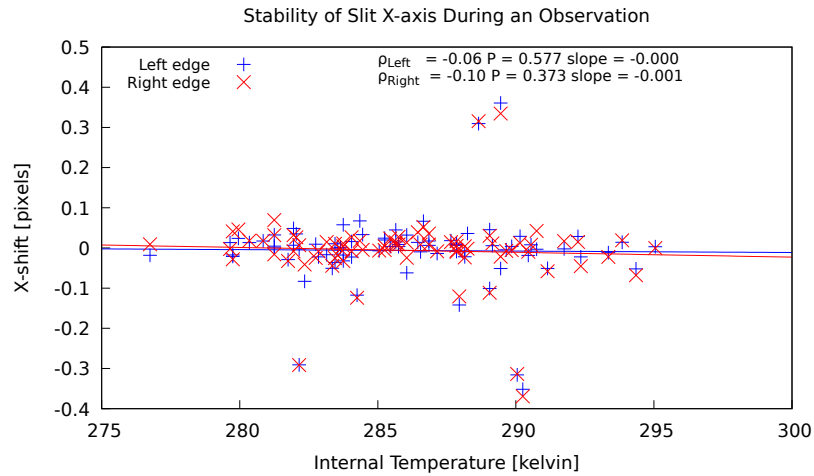


Figure 3.25: The stability of the slit X-axis position during an observation. The position of the slit edges was taken pre- and post-observation and compared to a datum observation taken at temperature, $T = 285$ K. The mean of the standard deviation for left and right edge X-axis shift is s.d. 0.07 pixels, showing that generally there is little movement during an observation. However there are 3 observation with a large shift of ~ 0.3 pixel occurred.

This may be thermal induced defocus within the instrument or may result from an external temperature dependent turbulence within the telescope or local atmosphere. An independent measurement of seeing was available from the RCS (Robotic Control Software) database. The RCS data includes the seeing of a standard star taken at the mid-point of an observing night using the IO:O optical imager mounted on the LT. The RCS seeing also shows a temperature dependence (Figure 3.26 upper) with $\rho = -0.20$, $P = 0.000$ and coefficient $k = -0.010 \text{ K}^{-1}$, approximately half that of the seeing at the instrument slit.

To separate the common mode temperature dependence in slit and RCS seeing the difference between the two was plotted (Figure 3.27) and shows no correlation, $\rho = -0.12$ and $P = 0.460$. Seeing approximates to Gaussian and the difference was calculated in quadrature.

The RCS seeing data is not comprehensive and was searched for dates matching 1H0323+342 observations. Large values of seeing > 2.5 arcsec were excluded from both slit and RCS data reducing the sample to 39 points. The time difference between observations

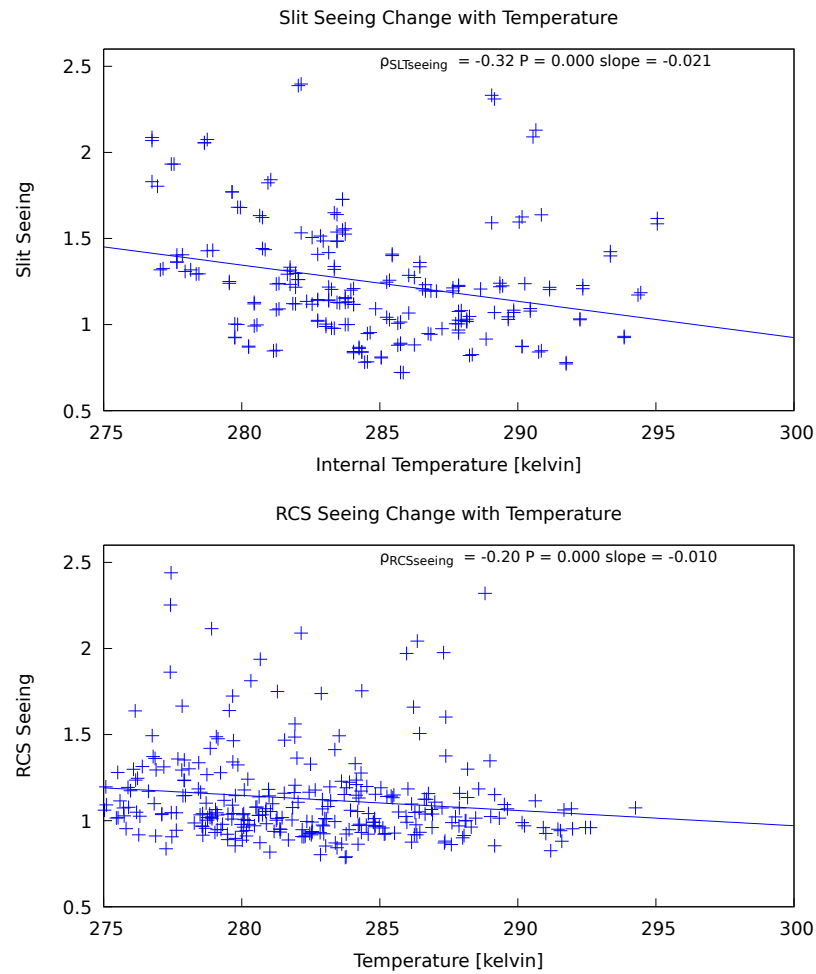


Figure 3.26: Change in the estimated seeing, ESTSEE, viewed at the slit (upper plot) and RCS seeing from the IO:O imager (lower plot) with temperature.

of the seeing in the two data sets and taken on the same night was up to 4.5 hours. The small number of points and potential for the seeing to change between the two observations is not ideal.

An alternative method to measure the focus using the sharpness of the slit edges was attempted. The `idiff` derivative of the slit image was taken and the width of the left and right detected slit-edges was measured with `peak` over the sample range $Y = 100\text{--}120$ pixels. This data set contained the larger sample of 228 slit images. The focus does not correlate with temperature with $\rho < -0.12$ and $P < 0.070$ for both edges sampled (Figure 3.28).

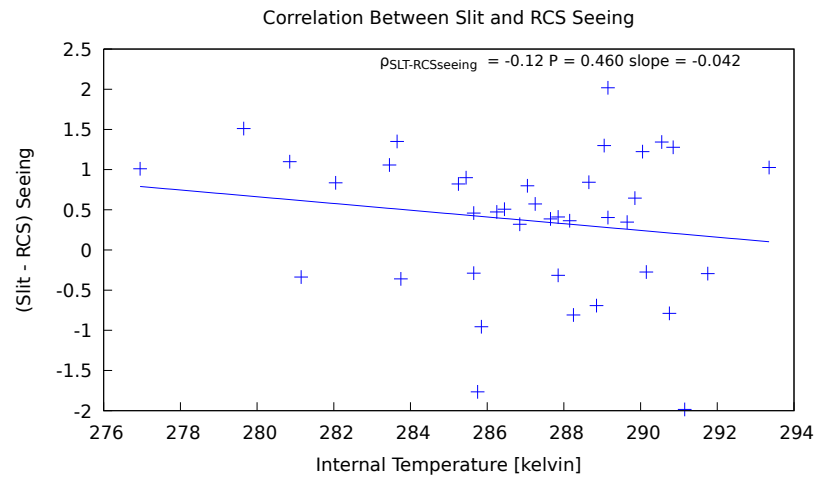


Figure 3.27: The difference between SPRAT slit and RCS reported seeing measured by optical imager IO:O. The atmospheric seeing was derived from the target object size. Both SPRAT and IO:O estimation of seeing show a temperature dependence. To de-couple common-mode thermal effects the RCS reported seeing was subtracted from the SPRAT seeing taken on the same observing night. The resulting plot shows no correlation with the instrument internal temperature and hence no detectable change in image size caused by a thermally induced defocus.

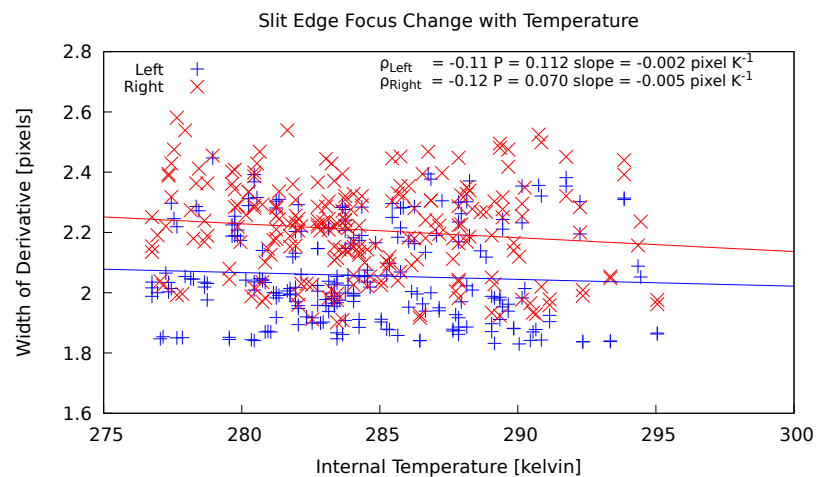


Figure 3.28: Variation in focus with temperature using slit-edge image sharpness. The `idiff` derivative of the slit image was first taken to detect slit edges. The offset between the left and right edges was attributed to differences in their edge sharpness and surface reflectivity. The width of the detected edges was measured with `peak` over the sample range $Y=100-120$. The lack of correlation shows that focus remains stable over the an internal temperature range of 25K.

Variation in focus with altitude using the same edge-detection method is evident (Figure 3.29) with $\rho > 0.33$ and $P = 0.000$. The mean coefficient for the detected edge

width is $0.003 \text{ pixel degree}^{-1}$.

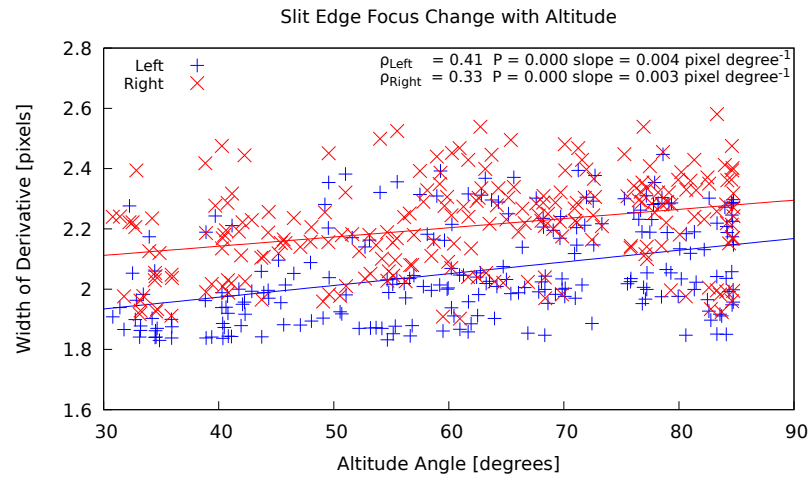


Figure 3.29: Variation in focus with altitude angle using slit-edge image sharpness. The focus does small correlation with telescope altitude angle with a mean coefficient of $0.0035 \text{ pixel degree}^{-1}$.

The offset between the left and right edges was attributed to differences in the slit knife-edge sharpness and surface reflectivity.

Location of the target object within the slit is achieved by telescope acquisition software. The 1H0323+342 data provided an opportunity to analyze the reliability of the software to locate a target onto the magic pixel. The variation in X- and Y-axis offsets with respect to the magic pixel is shown in Figure 3.30. The target offset is centered on the magic pixel $Y=179$ and shows a normal distribution with the displaced object up to ± 6 pixels. The X-axis offset shows a two peaked distribution with the central trough at the magic pixel.

3.7 Instrumental Zero Point

When calculating the instrument throughput using a photometric standard a zero point Z is needed to compensate for atmospheric extinction. The photometric zero point at

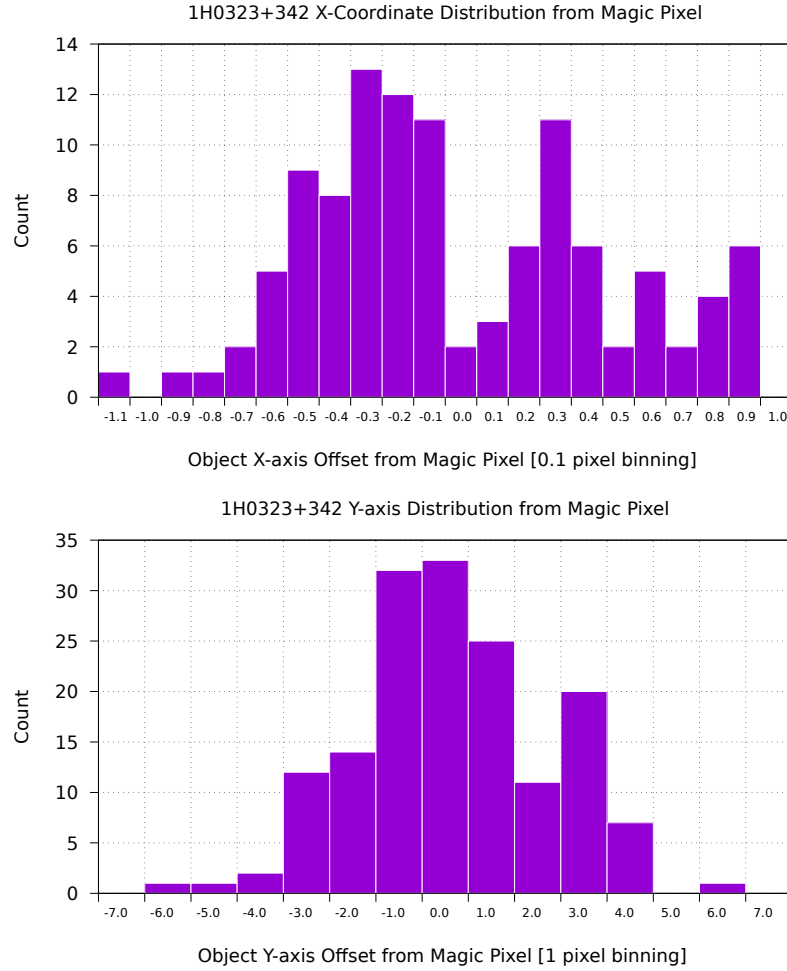


Figure 3.30: The distribution in the X- and Y-axis acquisition position of object 1H0323+342. The offsets are with respect to the magic pixel co-ordinate at X = 479, Y = 179.

a specific wavelength Z_λ is evaluated thus

$$Z_\lambda = m_\lambda + 2.5 \log (N_\lambda) + (A_\lambda \times AirMass - 1) \quad (3.3)$$

where m_λ is the magnitude of the observed photometric standard, N_λ is the photon count per second, A_λ is a site specific coefficient of extinction per unit air mass obtained from King (1985), $AirMass$ is the air mass for the observation. A red and blue mode observations of photometric standard BD+33 2642 taken on 9th April 2016 was used to evaluate Z at $2 \times$ binning (Figure 3.31). As Z_λ is an atmospheric correction it does not remain constant and changes over short term meteorological and longer term

seasonal timescales.

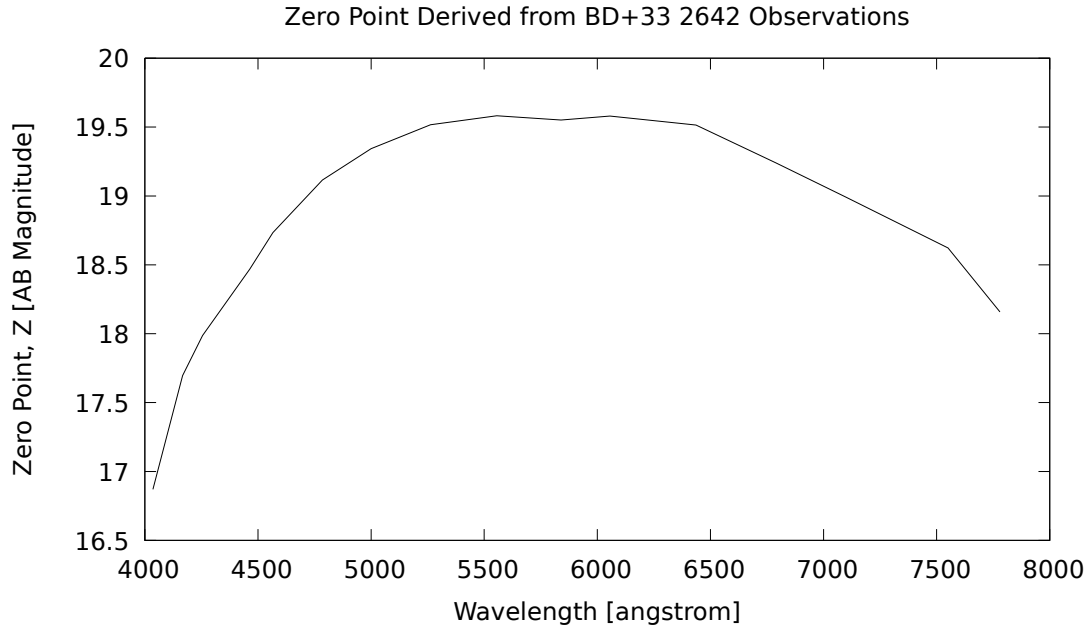


Figure 3.31: The instrumental zero-point Z derived from the observation of photometric standard BD+33 2642. Z was derived from L2 pipeline spectrum which performs 2x pixel binning and should be proportionally scaled for photometry at different levels of binning.

3.8 Measuring Bias that Varies Frame-to-Frame Without an Overscan

Post commissioning characterisation of the instrument revealed an unexpected variation in bias frames taken consecutively and a possible longer term trend in the order of hours/days. Further analysis of this bias instability was conducted by Dr. Robert Smith (Smith et al., 2016) and is presented here.

Repeated, short exposures taken over a timescales of minutes to hours (Figure 3.32) demonstrate the bias level varies sufficiently to require correction on a frame-by-frame basis. It is not sufficient to collect a bias exposure once per night or even immediately before the science observation. Consecutive frames have bias levels that differ by up

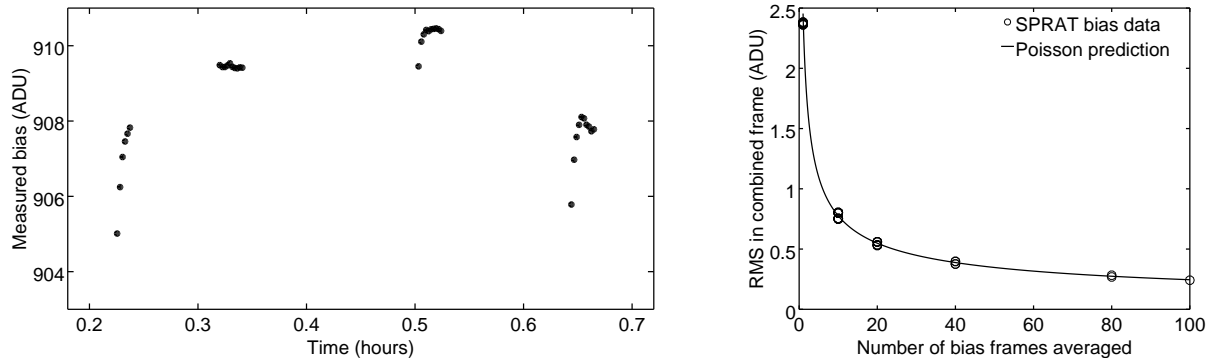


Figure 3.32: Left panel: Example data showing the bias does vary on short time scales. The behaviour exhibited here of the bias changing rapidly at the start of a consecutive sequence of exposures is typical of the camera and means that simply taking a bias frame immediately before the science frame does not work. Right panel: Combining multiple bias frames reduces the pixel value RMS in excellent agreement with Poisson prediction assuming all structure in the bias image is amplifier read noise.

to 1 ADU and the level can vary by up to 50 ADU from night to night. These data also show that the bias is extremely clean in terms of having no photometrically significant 2D structure across the detector. This is demonstrated in Fig. 3.32 where we plot the standard deviation of pixel values in averaged stacks consisting of different numbers of bias frames. The actual observed standard deviation closely matches the prediction of Poisson statistics that when N frames are averaged, the standard deviation falls by a factor of \sqrt{N} . If the bias frame contained structure that was appearing consistently in multiple frames, the measured noise would fall more slowly than this prediction. We therefore do not need a 2D bias image and are able to use a single constant bias value for every pixel in the frame. Our task is to determine that value individually for each science frame taken.

With slit and grating deployed, there are regions of the detector that are completely unilluminated thanks to the slit geometry and 4000 Å long-pass, order-blocking filter. This dark region of the detector provides a direct measurement of the bias+dark signal in every observation and effectively provides the same functionality as would an overscan strip. However, with the slit and grating stowed, the entire detector area is used in

imaging mode and the lack of overscan region becomes a problem.

It should be noted that in the absence of strong vignetting and with a “perfect” detector that shows little pixel-to-pixel quantum efficiency fluctuation then not knowing the bias voltage has little real impact on photometric accuracy. The bias in that case simply looks like extra background flux and is perfectly corrected during sky subtraction. Where the dynamic range of the flat-field is small, precision determination of the bias level is less important. In the case of SPRAT however the imaging mode is strongly vignetted with the throughput at the image edges being less than 25% of the frame centre. This vignetting does not affect the spectral mode because the slit is on axis, out of the vignetted region, but has a major impact on observational efficiency since our ability to use the imaging mode for target acquisition is constrained by field of view. The more field of view that can be accurately corrected for cross referencing to reference star catalogues, the better the effectiveness of the automated acquisition.

The strong vignetting in this case makes determination of the bias level possible. We know the geometric form the field vignetting from the twilight flat-field and we can measure its form in the image frame. The amplitude of the vignetting function in the observation frame is diluted by the addition of uncorrected bias signal. The correct bias level may be algebraically and uniquely determined simply as the constant signal that must be subtracted off to make the vignetting match between the data frame and the flat. In other words, it is simply the bias level that once it is subtracted off allows the flat-field to most effectively create a featureless sky background.

Besides the raw data to be processed, the required inputs are a previously obtained dark frame and a flat-field. We store the dark frame on disk with the bias already subtracted. The flat field is stored on disk bias- and dark-subtracted and normalized to have mean counts of unity in the unvignetted field centre.

Given these inputs, the algorithm runs as follows.

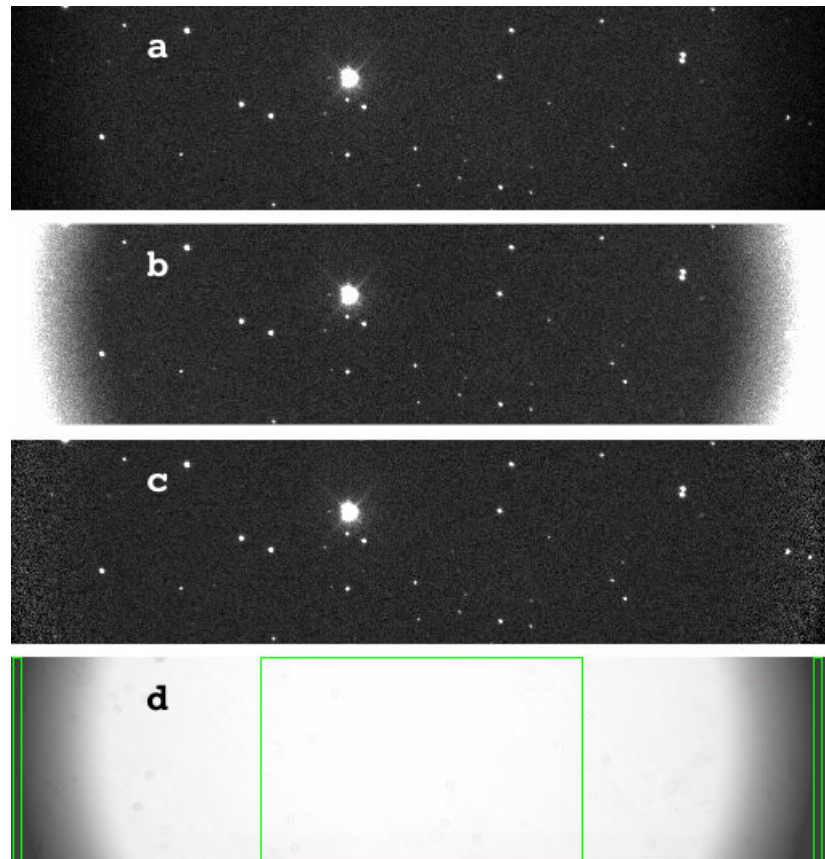


Figure 3.33: Example raw and reduced data from SPRAT in its imaging mode (grating and slit stowed). Raw data direct from the instrument are shown in the top panel (a). Panel (b) shows the gross over-correction of the flat-field when relying on a traditional bias frame and the bias level has drifted between exposures. Panel (c) is our final reduction, using a bias level inferred from the shape of the vignetting. The lower signal means the Poisson noise is exaggerated, but the mean sky level remains constant across the image. The bottom panel (d) is the flat-field used, to clearly illustrate the vignetting present in the raw data. The overlaid boxes are regions from which vignetting statistics are drawn as described in the text.

1. A dark frame is selected from the library, choosing the available frame obtained closest in time to the image being processed.
2. Determine the mean dark current per pixel D as the average pixel value of the whole frame.
3. A twilight flat-field is selected from the library, choosing the available frame obtained closest in time to the image being processed.
4. Pixel value statistics are then taken from two regions within the same image

frame. The mean pixel value in the unvignetted image centre and in a region near the image edge where vignetting is greatest are denoted F_0 and F_i respectively. The precise regions selected are not critical. They should simply be large enough to provide a statistically fair sample of the throughput in that region and not so large that it varies greatly across the selected region. These values are used in the formula given below to represent the relative throughput of the field centre as compared to the vignetted region, F_0/F_i .

5. Repeating the same operation for the data being processed, the unvignetted sky brightness is S_0 and the sky brightness measured at the frame edge is S_i . In order to fairly determine the sky background level, an iterative sigma-clipping algorithm is used to reject flux from stars in contrast to the simple mean used for the flat field frame.
6. The inferred bias value B_i is then given by

$$B_i = \frac{S_0 - S_i(F_0/F_i)}{1 - (F_0/F_i)} - \frac{T_{\text{data}}}{T_{\text{dark}}}D,$$

where T_{data} and T_{dark} are the integration times of the science exposure and the dark frame respectively.

7. Generate a dark frame that contains only the pixel-to-pixel dark current variations. I.e., constant bias and mean dark current levels have both been subtracted off.
8. Subtract this dark frame from the image to remove excess signal from warm pixels.

This algorithm is a very simple implementation of the concept. It may be extended to use multiple sample regions at different places in the vignette pattern or even full 2-dimensional surface fits to the counts in the flat and the image data. For the specific

case of SPRAT, a two region implementation was found to be computationally very fast and operationally robust. We use two vignetted regions, one on each edge of the frame and the bias level applied by the pipeline is the average of the two, $B = (B_1 + B_2)/2$. The image sections selected do not run quite to the very edge of the image, but are in the region where throughput is approximately in the range 25–30% of the field centre. The pixel regions used are shown in Figure 3.33, panel d. They are ten pixel columns wide and extend to the full height of the detector array.

3.9 Data Pipeline

The raw exposures spectra observations produced by SPRAT undergo initial processing by a level 1 (L1) pipeline. The pipeline was originally developed for the FRODOSpec integral field spectrograph (Morales-Rueda et al., 2004) by Dr. Robert Barnsley and modified by him for use with SPRAT. The L1 pipeline performs a bias subtraction and CCD flat fielding of the raw exposures.

The L1 processed data is subsequently fed into a level 2 (L2) pipeline to produce a wavelength calibrated spectrum. The L2 pipeline performs an un-distortion of the L1 image frame to vertically straighten spectral lines. An arc lamp spectrum is used to linearize and wavelength calibrate the image frame. A sky-subtraction is performed using vertically adjacent pixels either side of the object spectrum. The resulting spectrum is collapsed and $2\times$ binned to improve SNR halving the final effective resolving power to $R \approx 150$.

3.10 Conclusions

The 1H0323+342 sample covered an extended time, >700 days, allowing data covering a range of operating conditions to be obtained. The range of internal temperatures

during observation varied from 276 – 296 K with a average value of $T_{286} = \text{K}$ (13° C). From laboratory testing of the prototype it was expected that thermal effects would be observed and indeed produced the largest effects.

The slit width at T_{286} is 4.3 pixels (4.4 arcsec) and varies with temperature coefficient $-0.014 \text{ pixel K}^{-1}$.

At the central wavelength and operating temperature T_{286} , the range resolving power at $R_{6000} = 307$. The thermal variation in the slit width can alter the resolving power by $\Delta R_{6000} \approx \pm 10$ over the sampled temperature range of $T = 276 - 296 \text{ K}$. The value of R is lower the original design goal $R_{6000} = 350$ but acceptable for the classification of SNe. The partially reduced L1 pipeline data product is at this resolving power. The $2 \times$ binning of the L2 data-product halves the resolving power of the finally fully reduced spectrum to $R_{6000} \approx 150$.

The measured peak optical throughputs are red = 0.35, and blue = 0.29. These significantly lower than the theoretical predictions of ~ 0.46 for both modes (Section 2.1.4). The reason for the discrepancy is unclear but may be the result of applying component manufacturers representative values to the theoretical estimate. A more accurate estimate could be attained by measuring the actual performance of all optical elements prior to assembly. It is worth noting that another ARI spectrograph, LOTUS (Steele et al., 2016), also reports a lower than expected peak throughput.

The internal Invar optical bench provides thermal stability with no temperature related defocus over the 276 – 296 K operating range sampled. There is a small dependence on altitude with mean value $0.0035 \text{ pixel degree}^{-1}$ producing a negligible slit defocus of ± 0.075 pixels over the altitude range 30 – 80 degrees.

The mean thermal Y-axis coefficient is $-0.067 \text{ pixel K}^{-1}$ which can produce up to ± 0.7 pixel displacement over the typical operating temperature range. For placement on the magic pixel this is insignificant compared to the ± 6.0 pixel variation introduced

during acquisition. However this displacement will be detrimental to the effectiveness of flat-fielding correction of any imaged pixel scale features. Dust lines have scales of 1-4 pixels although the selection of the magic pixel Y co-ordinate allows them to be avoided. Non-imaged features associated with the CCD such as bad pixels and scaling of pixel response are unaffected. Ideally flat-fielding frames should be taken near the average temperature T_{286} or be shifted prior being applied.

There is a long term drift in the Y-axis of ~ 0.5 pixel year⁻¹. The cause is unknown although since the slit is a moving component it may be a result of bearing wear or movement of the slit in its mount. Any detrimental effect can be mitigate by updating the flat-field images.

The thermal X-axis shift derived from the Xe arc has a mean coefficient is -0.023 pixel K⁻¹. Superimposed on the thermal X-shift is a bimodal error of ~ 0.4 pixels which is not temperature related and appears random. The cause is unknown but may be an optical component adopting one of two stable orientations and may relate to the unusual two peak distribution of the target from the magic pixel (Figure 3.30). Although not being serious enough to warrant immediate investigation with SPRAT, it would be wise to explore the cause in any instrument derived from its design. A thermal X-axis shift was also found from the slit images with mean coefficient of -0.039 pixel K⁻¹, higher than derived the Xe arc. This showed scatter but has no bimodal distribution as with the Xe arc.

Searching the mean position of the slit centre taken from the 1H0323+342 data produced a mean X-co-ordinate = 178. The original magic pixel co-ordinates were established during commissioning and the value has drifted by ~ 1 pixel since then.

As expected, no correlation with image axis shifts were found with azimuth and Cassegrain rotation.

During an observation the slit X-axis image position is stable with negligible shift, σ

= 0.07 pixels.

During commissioning these design and engineering issues arose which should be addressed in future SPRAT-like designs. The contamination by stray light entering via the front of the instrument was unexpected and without the last minute additional baffling would have severely impaired the quality of sky images and spectra. Any future implementation must include a full baffle at the order blocking filter/field lens position and at the slit. Enclosing the optical path in an internal tunnel should also be considered.

Aligning the grating rotation was often inaccurate and hence time consuming because of the coarseness of the adjustment mechanism. Any future implementation of the SPRAT design should consider using a finer setting mechanism

Despite the used of locking connectors on the umbilical cables the instrument suffered post-installation outages attributed to loose connection and failures in these cables/connectors. In any future implementation this designed should attempt to locating the Arduino controller board onto the instrument to eliminate cabling and connectors.

Chapter 4

Classification of Supernovae with SPRAT

Presented here are the results of an observing programme to classify supernovae using SPRAT. Observations of SNe with well determined types are used to optimise the application of the SNID classification tool, which is then applied to the whole sample of observations. A comparison of Gaia and ASAS-SN SNe properties is then presented.

4.1 Supernovae

Supernovae are amongst the most energetic and luminous events in the Universe and can reach an absolute magnitude > -23.5 and total energy $\simeq 1.1 \times 10^{52}$ erg for super-luminous supernovae such as SN2015L (Dong et al., 2016). They mark the end of stellar evolution and the resulting remnant of the explosion depends on the mass and composition of the progenitor. The remnant may be a neutron star, black-hole or the star may be totally disrupted with all the material dispersed into space.

Type Ia SNe and Ia-like subclasses are believed to be the thermonuclear detonation or

deflagration of carbon in a degenerate C+O white dwarf (WD) that has reached the Chandrasekhar mass (M_C) limit of $\sim 1.4 M_\odot$, (Chandrasekhar (1935), Arnett (1969)). The two proposed processes by which the mass limit M_C is reached are by the accretion of material onto a white dwarf from a close companion star (single degenerate) or the merger by collision of two white dwarfs (double degenerate).

All other SN types, Ib/c, II and their sub-variants are assumed to be the result of catastrophic core collapse of stars with masses $M > 8 M_\odot$.

The process by which core collapse is initiated and progresses depends on the progenitor mass, mass loss history and metallicity. An electron capture SN (ECSN) (Miyaji et al., 1980) collapse can be initiated in the degenerate O+Ne+Mg core of stars with masses $M \simeq 8\text{--}10 M_\odot$. If the mass of the degenerate core approaches $M \simeq M_C$ the central density exceeds a critical value, $\sim 4 \times 10^{12} \text{ kg m}^{-3}$. Above this density electrons undergo inverse β decay capture by ^{24}Mg and ^{20}Ne nuclei reducing the degeneracy pressure and causing the core material to contract. The increase in density further enhances the electron capture resulting in a run-away core collapse. With the removal of support by the core's hydrostatic pressure the outer material accelerates inwards under gravity forming a shock front. This rebounds from the newly created neutron core, ejecting the envelope and some of the outer core material (Kitaura et al., 2006).

Stars with mass $M \geq 10\text{--}100 M_\odot$ attain a sufficiently high central temperature, $2.7\text{--}3.5 \times 10^9 \text{ K}$, to burn progressively heavier elements to form a degenerate core of inert ^{56}Fe . As with an ECSN, once the Fe core mass approaches $M \simeq M_C$ electron capture initiates a run-away core collapse to form a neutron core and an inward shock-wave from the now unsupported outer layer of the star. The inbound shock-wave rebounds from neutron core and producing a stagnated shock-front attempting to travel out through inward moving outer material. Depending on progenitor mass and metallicity the neutrino flux from the collapsing core may impart sufficient energy to re-energise the stalled shock-front and produce an explosive SN outburst. Otherwise the

stalled shock-front fails to reach the surface and the star undergoes a gravitationally driven implosion with no optical SN (collapsar) but possibly an observable gamma-ray burst (GRB) (Heger et al., 2003).

Above $>100 M_{\odot}$ the high core temperatures produce photons sufficiently energetic for spontaneous electron-positron pair production to become significant. The loss of high energy photons reduces supporting pressure, initiating a contraction of material in the O and Si cores. For masses $<\sim 140 M_{\odot}$ the contraction rapidly increases photon production by the thermonuclear burning of O and Si. This explosive energy release produces a violent mass ejection event producing a pulsation pair-instability SN (PPISN) with typical mass loss of $\sim 0.1 M_{\odot}$. The star periodically sheds mass by this pulsation process until the $\sim 100 M_{\odot}$ limit is reached and a Fe core collapse ensues as with lower mass stars. (Woosley, 2017)

Super-massive stars, $>140 M_{\odot}$ form massive lower density oxygen cores, $\sim 50 M_{\odot}$ allowing the pair production instability to initiate a collapse prior to oxygen ignition. Once initiated, the collapsing oxygen core undergoes rapidly thermonuclear burning with a release of energy $>10^{52}$ erg, sufficient to totally unbind the star leaving no remnant. (Ober et al. (1983) and Heger et al. (2003))

4.2 Other Transients

Supernova surveys will also detect other transients. For example, cataclysmic Variables (CVs) are close binary systems where mass transfer is accreting material onto the surface of a compact companion such as a white dwarf. The accreted material heats up and eventually undergoes a rapid fusion producing a outburst causing a sudden brightening of the star. Unlike a SNe the disruption is a surface effect with a much lower mass loss and energy production leaving the erupting star intact. The spectra is dominated by hydrogen with helium and iron features although in rare cases the hydro-

gen can be absent producing a helium nova. The classification of CV's include several sub-types, classical novae, recurring novae, dwarf novae and helium novae (Knigge, 2011).

Active galactic nuclei (AGN) are compact central regions of galaxies that exhibit high luminosity. This class of object includes quasars, Seyfert galaxies, blazars (BL Lac and optical violently variable quasars) and some active radio galaxies which otherwise have typical optical luminosities. The energy production mechanism common to all AGN is thought to result from accretion disc material falling into a central super-massive 10^6 – $10^{10} M_{\odot}$ black hole. The accelerated inflow is turbulent and frictional heating raises the material temperature with black body radiation peaking in the ultraviolet. Twin opposing outward flowing relativistic jets can form near the central region of the disk. The interaction of the radiation and jets with interstellar gas and dust produces a variety of secondary emission phenomena. This can result in spectra with strong hydrogen and helium lines which can be confused with early stage normal type II (Rees, 1984).

Gamma ray burst (GRB) are assumed to be the result of highly energetic events. The interaction of any associated shock-wave with surrounding interstellar medium can produce later, progressively less energetic, emissions in the X-ray, optical and radio. Approximately 50% of GRBs produce an associated observed optical or radio afterglow. The persistence of afterglows varies from minutes to several days.

4.3 Supernovae Classification

The basis of the current system of observational classification of SNe was originated by Minkowski (1941). It used an initial sample set of 14 SN spectra which were characterised by either an absence (type I) or presence (type II) of hydrogen. Subsequent observation of SNe identified heterogeneity in the spectral features and light curves of type II SNe (Zwicky, 1965) highlighting a need for sub-classification. The classifica-

tion scheme has since been further expanded with sub-types based on the evolution of the light curve, absolute peak luminosity, and relative strengths or line widths of spectroscopic features. Although spectroscopy is sufficient for basic classification, accurate sub-classification often requires photometric data (Figures 4.1 and 4.3). The spectroscopic features defining the principal class of SN as type I or II are almost always present from explosion to several weeks past the optical peak. However instances of core-collapse SN spectra changing sufficiently to alter the initial classification do exist, for example SN1987K was re-classified from II to Ib (Filippenko, 1988).

4.3.1 Identifying Type I SNe

The principal characteristic identifying type Ia SN is the absence of hydrogen emission lines from the spectrum as opposed to type II SN which show distinct Balmer lines.

The type I classification is further sub-divided into type Ia, Ib and Ic by the presence/absence of silicon or helium spectral lines. Type Ia SNe have a strong absorption feature at $\sim 6355 \text{ \AA}$ formed from a blend of the Si II 6347 \AA and 6371 \AA lines. Silicon lines are weak or absent from Ib and Ic sub-types. Type Ib instead show moderate He I emission lines, especially the 5876 \AA line. In type Ic SNe the He emission is absent (Wheeler & Harkness, 1986). Early phase spectroscopic classification of type Ic based on He emission is not always reliable and He lines have been observed to develop in late Ic SNe requiring re-classification to Ib.

Type Ia SNe form a largely homogeneous group with comparable spectral evolution, light curves and peak absolute magnitude, e.g. blue magnitude, $M_B \sim -19.3$. The peak luminosities exhibit a variation with broad peaked (slowly changing) light curves being ~ 0.3 magnitude brighter than the narrow peaked (fast changing) which limits their direct use as standardisable candles (Figure 4.2)

Fortunately a correlation between the peak luminosity and light curve decay was es-

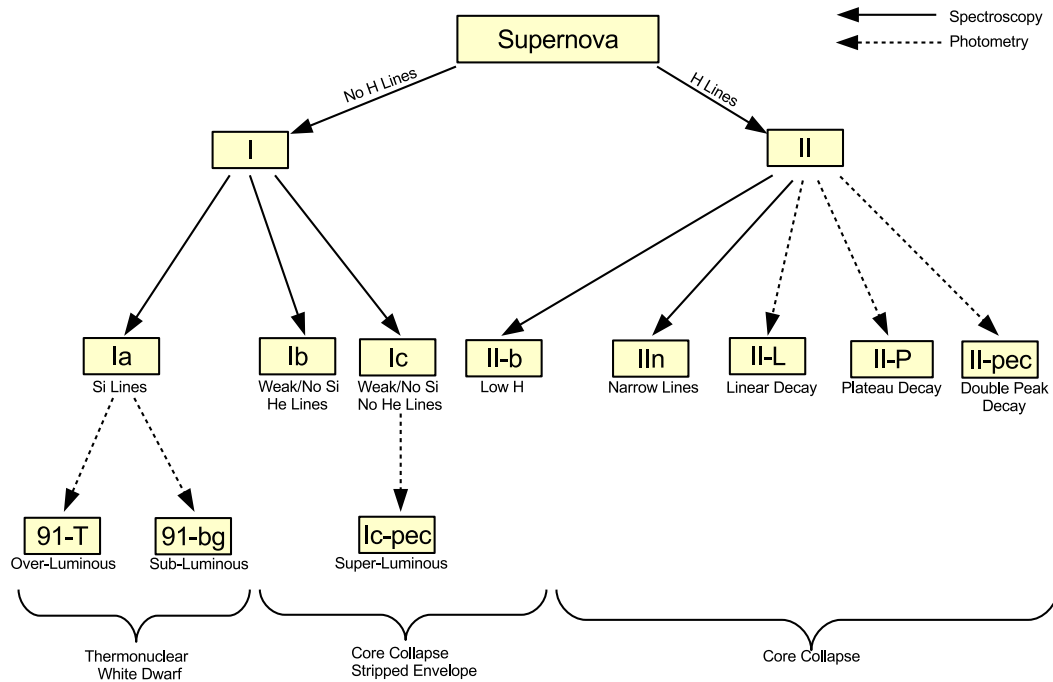


Figure 4.1: Supernova classification uses spectroscopic and photometric features to differentiate the object classes. Progenitors are thought to arise from two population, either Chandrasekhar limit white dwarf stars or late stage massive stars undergoing core collapse. The lack of H and He features in core collapse SNe is thought to be the result of loss of outer layers stripped by a close binary companion or by stellar wind loss in a Wolf-Rayet progenitor. (Image adapted from the original by Stephane Blondin)

established (Pskovskii, 1977) and further refined into the Phillips relationship (Phillips, 1993). This relates the intrinsic peak B-band magnitude, $M_{\max}(B)$, to the decrease in the B-band magnitude at a fixed time (15 days) later, $m_{15}(B)$, (Eqn. 4.1)

$$M_{\max}(B) = -21.73 + 2.70\Delta m_{15}(B) \quad (4.1)$$

Instances of SNe with type Ia spectra have been observed to be significantly over- or under-luminous compared with normal type Ia SNe. Referred to as peculiar (-pec) variants to distinguish them from normal Ia types, these Ia variants are named after the first identification of the type. Identification of peculiar Ia SNe is important so as to excluded their use as standardisable Ia candles.

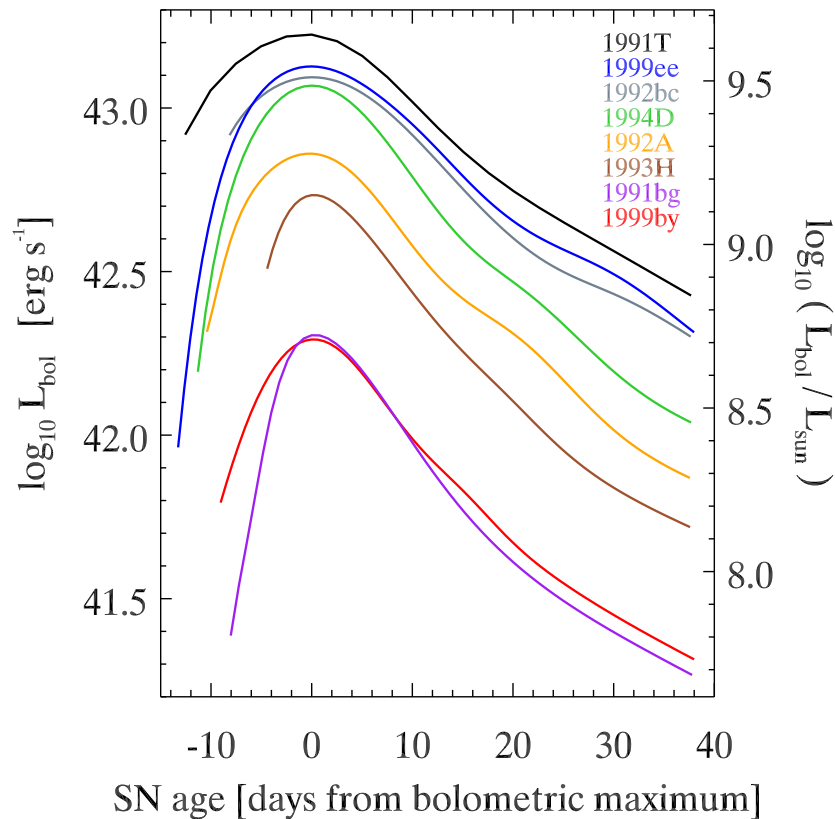


Figure 4.2: Bolometric light curves for type Ia SNe illustrating the correlation between sharpness of the peak and luminosity. 1991bg and 1999by exhibit normal light curves but are under-luminous and 1991T is over-luminous. The remaining SNe are normal type Ia.

91T-like SNe are over-luminous compared to normal Ia, (Phillips et al., 1992). During the early phase the SiII feature is weak or missing but the spectra evolve to look like conventional Ia ~ 8 weeks post maximum. 91bg-like SNe are under-luminous with a typical maximum absolute magnitude ~ 1.5 lower than the normal type Ia SNe, (Filippenko et al., 1992). Spectroscopically they exhibit a broad TiII absorption feature centered around 4200 \AA (Filippenko et al., 1992).

Some rare Ia-like SNe exhibit luminosity and spectral peculiarities greater than shown by the 91T and 91bg variants. 02cx-like SNe are under-luminous, comparable to 91bg-like, but with low expansion velocities $6000 - 6500 \text{ km s}^{-1}$, approximately half those of normal Ia (Li et al. (2003) and Stanishev et al. (2007)). 03fg-like SNe are anomalously over-luminous compared to any other type of Ia. The energy output is nearly twice what should be possible from the ^{56}Ni decay of a standard mass Chandrasekhar

white dwarf (Howell et al., 2006). Super-luminous peculiar Ic variants have also been observed. These have extremely high luminosities, >3 magnitudes brighter than a typical Ic and represent the most energetic SNe observed to date, for example SN2015L (Dong et al., 2016).

4.3.2 Identifying Type II SNe

Normal Type II SNe are dominated by strong hydrogen emission lines. Type IIn are a sub-class differentiated from normal type II SNe by narrowness of the emission hydrogen peaks, typically $\text{FWHM} \approx 100 - 200 \text{ km s}^{-1}$ (Schlegel, 1990), superimposed onto a low amplitude broad emission base. The early-phase continuum is often bluer than normal type II SNe. The sharpness of the hydrogen emission lines make this class more difficult to spectroscopically differentiate from an AGN.

Types II-L and II-P are spectroscopically similar to type II and initially show the same light curve profile. At $>\sim 2$ weeks the decay in magnitude becomes linear for II-L, slower than the exponential decay of normal type II. In type II-p SNe the normal post-peak decay flattens to a plateau, which remains constant for several weeks before resuming the normal exponential type II-like decay. Type IIb have weaker hydrogen but their primary distinguishing feature is they exhibit a second maximum peak.

Super-luminous supernovae have core-collapse like spectra but are 1 – 2 magnitudes brighter .

4.4 Observing Programmes

A series of 3 successful ARI internal proposals for observing time on the LT for the classification of transients allowed a continuous observing run from 2015-01-01 until 2016-08-31 giving a total of 87.0 hours. The proposals had two aims, the general

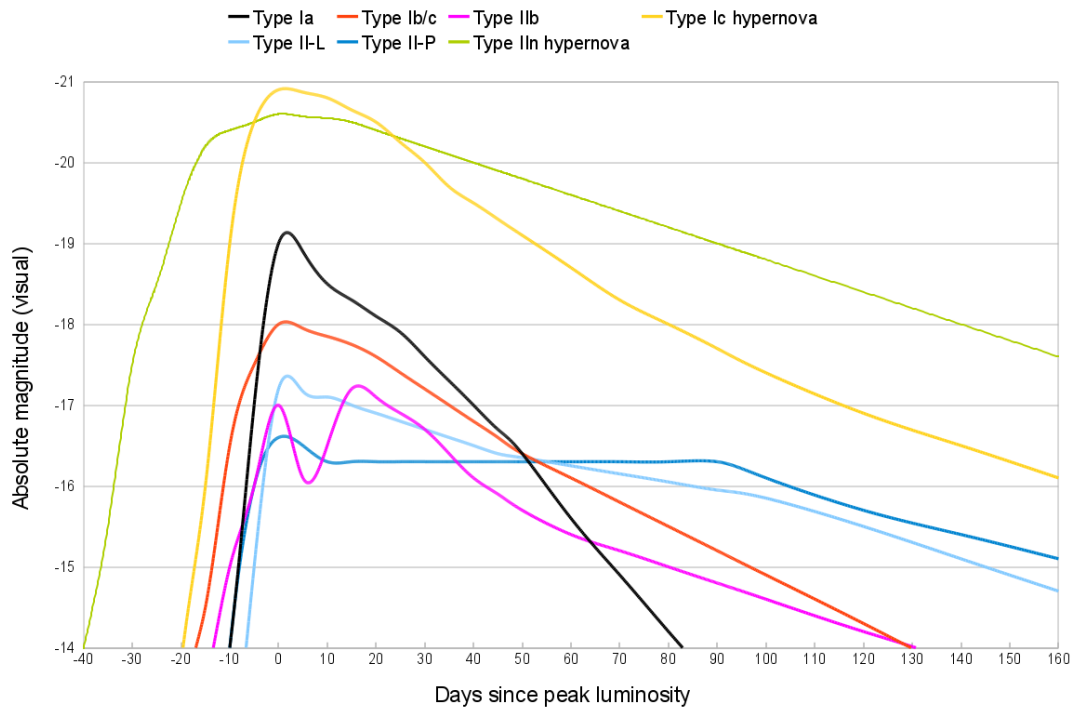


Figure 4.3: Accurate sub-type classification requires photometric data to complement initial spectroscopic observation. (Image from Wiki-commons)

classification of transients detected by the Gaia Photometric Science Alerts and the early stage classification of potential SN using alerts from other sources.

Not all alerts from the sources could be observed because of constraints by the observatory location and operational limits of the telescope. The LT is located at Roque de los Muchachos observatory on La Palma at latitude $+29.76^\circ$. Objects with declination $< -60^\circ$ never rise above the horizon. The limiting altitude of the telescope is $+25^\circ$ above the horizon giving a lowest physically observable declination limit of $\sim -35^\circ$. An airmass limit 2.0 for observation was chosen which for the site further limited the minimum declination to -30° .

4.5 Surveys and Alert Sources

The number of optical sky surveys detecting transients, and hence objects requiring classification continues to increase. Table 4.1 lists a selection of ongoing surveys which have commenced or been upgraded in the last 10 years.

Many of these surveys make alerts available via public services such as Astronomer Telegrams (ATel), Central Bureau for Astronomical Telegrams (CBAT) and the Transient Name Server (TNS). The current surveys typically detected to magnitude ~ 18.0 (V-band) with some such as the space-based Gaia satellite going to magnitude 20.0 (G-band) and Pan-STARRS to magnitude 21.5 (PS1.w filter, 4000–8200 Å). The iPTF survey is enlarging the existing CCD array producing a FOV of 47 deg² to create the Zwicky Transient Factory (ZTF) by 2017.

The Large Synoptic Survey Telescope (LSST), (Ivezic et al., 2009), is a 8.4m f/1.23 telescope to be located at Cerro Tololo. It is planned to start regular operations by 2022 and estimated to detect transients down to magnitude 24.0 for single exposures and produce $>10^5$ events night⁻¹. By comparison the TNS generated an event rate of ~ 4 night⁻¹ for objects down to magnitude 21.5 (V-band) in the first 6 months of operation in 2016.

For the data described here the potential targets for classification were selected from a variety of alert sources. An observing collaboration was formed with the Gaia Photometric Science group and alerts generated via the web-site and Gaia marshall were used in preference when available. As the alert source was still under development and prone to outage other sources such as ATels, TNS and CBAT were accessed. Supplementary follow-up observation and classification request were received directly from non-public surveys such as KISS, iPTF and Crni Vrn observatory.

The Gaia survey is illustrative of the potential increase in rates. During the pre-hiatus period from 2014-07-27 to 2015-05-31, Gaia generated 269 alerts at a rate of 0.87

day⁻¹. During the post-hiatus period from 2016-01-16 to 2016-08-20 the rate increased to 1.67 day⁻¹ and total of 737 alerts for objects down to G-band magnitude 20.0. For G-band objects brighter than 18.5 the daily rate increase was 0.35 day⁻¹ to 1.40 day⁻¹. The mean alert magnitude remained unchanged at ~ 18.1 . Of all Gaia object alerts up to the end of the sample period in 2016-08-20 only 26% were given a classification. Post-hiatus of mid-2015 Gaia survey alerts are still at an intermediate development stage shown by the episodic data releases and further increase in alert rates and reduction in publish delays may be expected.

4.5.1 Gaia Alerts

The Gaia satellite (Prusti, 2012) is an ESA project to perform an astrometric survey of the stars in our Galaxy. It periodically re-images areas of sky at a cadence of ~ 40 – 80 days so can also detect transient phenomena. These transients are filtered and notifications of objects for follow up are made public via the Gaia Photometric Science Alerts programme.

The first public alert marking the start of the validation phase was object Gaia14aab, issued on 2014-07-27 UT, datum day 0 for the sample used here. The validation phase was suspended from 2015-06-02 until 2016-01-16 UT to perform upgrades to the alert filter pipeline by the Gaia Cambridge software team. Alternative object sources were used during this hiatus or when no Gaia alerts were available (Section 4.5.2).

The alerting magnitude (Figure 4.4) shows the change in alert rate, increasing from 0.87 day⁻¹ in the validation phase up to 2.90 day⁻¹ in the post-hiatus phase. The mean G-band alerting magnitude remained ~ 18.1 for both phases. There were few alerts > 19.0 magnitude in both phases and are totally missing after day 74 in the validation phase as is illustrated in the magnitude population (Figure 4.5).

Since the red-shift of observed objects is low, $z < 0.5$, the distribution of sources in

Table 4.1: Transient Surveys - Overview

Survey Name	Identifier	Began	Location	Reference
All-Sky Automated Survey for Supernovae	ASAS-SN	2013	Haleakala USA Cerro Tololo Chile	Shappee et al. (2014)
Catalina Real-Time Transient Survey	CRTS	2004	Tucson USA	
	CRTS-II	2009	Tucson USA	Drake et al. (2009)
CHilean Automatic Supernova sEarch	CHASE	2007	Cerro Tololo Chile	Pignata et al. (2009)
Gaia Photometric Science Alerts	GAIA	2014	L2 Lagrange Point	Prusti (2012)
La Silla-QUEST	LSQ	2009	La Silla Chile	Walker et al. (2015)
intermediate Palomar Transient Factory	iPTF	2013	Mt. Palomar USA	Law et al. (2009a)
Kiso Supernova Survey	KISS		Kiso Japan	Morokuma et al. (2014)
Mobile Astronomical System of Telescope Robots	MASTER	2006	5 x Russia Argentina Sutherland SA Canaries Spain	Lipunov et al. (2004)
Optical Gravitational Lensing Experiment	OGLE-IV	2010	Las Campanas Chile	Udalski et al. (2015)
Panoramic Survey & Rapid Response System	Pan-STARRS1	2010	Haleakala USA	Hodapp et al. (2004)
Sky Mapper Transient search	SMT	2015	Siding Spring Aus.	Keller et al. (2007)

Table 4.2: Transient Surveys - Optical Details

Ident.	Mag.	Aperture	f	FOV	Bands	Cadence	Optics Description
ASAS-SN	17.5	0.14m	f/2.8	4.47 deg ² × 2	V	1d	NIKOR 400mm F2.8G ED VR
CRTS-II	21.5	1.50m	f/2.0	1.2 deg ²	V	14d	Cassegrain
	19.5	0.68m	f/1.7	8.1 deg ²	V		Schmidt
CHASE	18.0	0.41m	f/12	10 arcmin ² × 4		3-4d	Ritchey-Chrétien
GAIA	20.0	1.45 × 0.50m		0.75 deg ²	G	~30d	3-mirror anastigmat
LSQ	20.5	1.00m		8.7 deg ²	Q(r+g)	2-4d	Schmidt
iPTF	20.4	1.22m	f/2.5	7.25 deg ²	g R	5d	
KISS	20.5	1.05m	f/3.1	2.2 deg ²	g	1h	Schmidt
MASTER	20.0	0.4m	f/2.5	4.6 deg ² × 8	V		Catadioptric
OGLE-IV	22.0	1.3m	f/9.2	1.4 deg ²		5d	Ritchey-Chrétien
Pan-STARRS1	21.5	1.8m	f/4.4	3.0 deg ² × 2		4-7d	Ritchey-Chrétien
SMT	20.0	1.35m	f/4.8	5.6 deg ²	g r i z u v	3-4d	Cassegrain

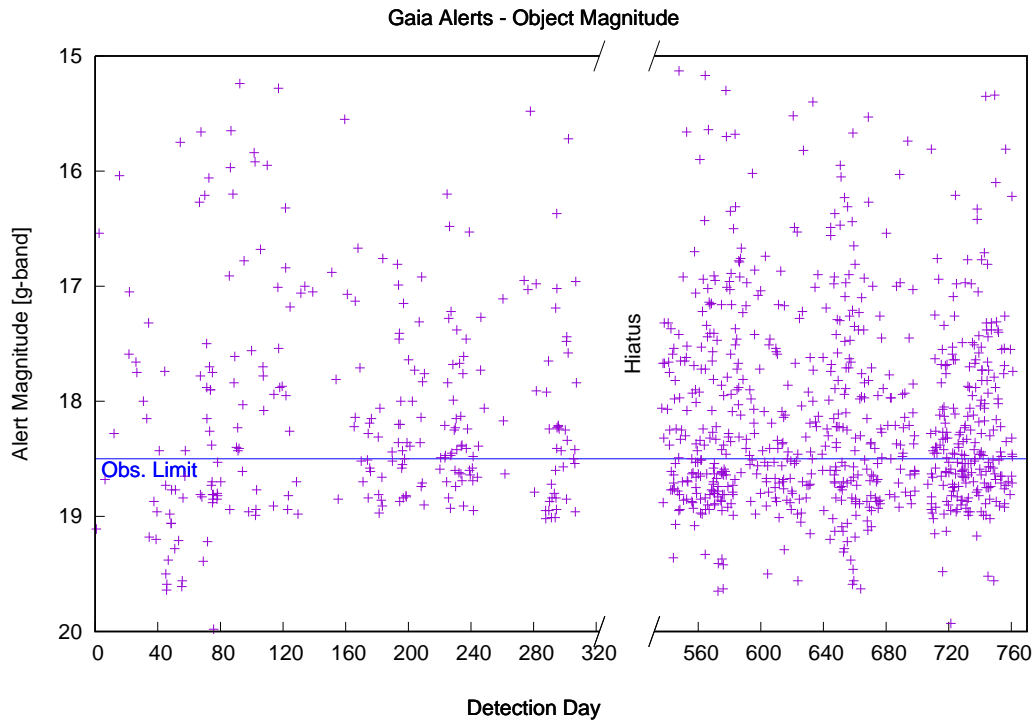


Figure 4.4: Gaia Photometric Survey alerting magnitudes. Spectroscopic observations were scheduled for alert objects brighter than 18.5 magnitude. It was noted that at day 74 of the validation phase alerts were limited < 19.0 although this selection was removed post-hiatus.

Euclidean space should follow a power law, $N \propto S^{-2/3}$, where N is the number of sources with flux $> S$ assuming all sources are detected (the $\log(N)/\log(S)$ completeness test). This implies $\log(N) = -3/2\log(S) + k$, equivalent in magnitude as $\log(N) = 0.6Mag. + k$. The actual magnitude population (Figure 4.5) shows a linear relationship with the expected gradient of 0.5 but begins to tail off at mag. 18.5 – 19.0 indicating incompleteness if the Gaia survey is failing to detect transients below this magnitude.

The alert object declination (Figure 4.6) initially showed a bias towards the northern hemisphere with few alert objects with declination $> -30^\circ$.

Initially the Gaia alerts only reported the detection date and time. After day 103 the publication date was also given allowing the delay to be calculated (Figure 4.7). This shows the evolution of the selection pipeline, up to day 190. The mean delay was ~ 25

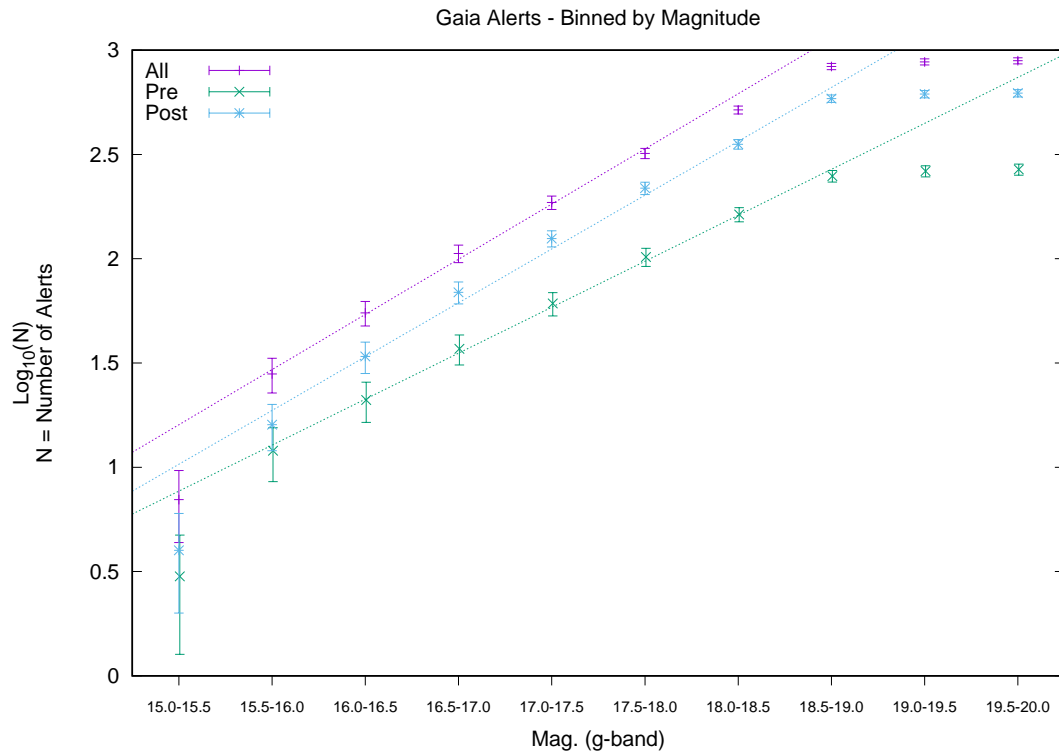


Figure 4.5: The number of alerts generated per 0.5 magnitude interval. The first 8 points show a linear relationship for all 3 sample sets and the dotted lines are fitted to these points. Fainter than magnitude 19.0 and the LogN/LogS relationship breaks down indicating the data is incomplete.

days post detection with a worst case delay of 130 days. The mean delay then dropped to ~ 7 days up to the hiatus. The pattern of data release indicated batch processing was used with detections accumulating and then being published together, this is most clearly shown in the early post-hiatus delays between days 540-565. Post-hiatus the mean delay dropped to 3.8 days although there remains significant variation with a lowest average delay of 1.8 days occurring around day 588 (Figure 4.8).

The minimum threshold magnitude for scheduling an observation from a Gaia alert was set to be 18.5 to ensure sample completeness (Figure 4.4). For objects of this magnitude the pre-hiatus rate was 0.35 per day increasing to 1.27 per-day post-hiatus. A maximum acceptable airmass was 2.0 selected which also corresponded to an azimuth altitude of $\sim +30^\circ$.

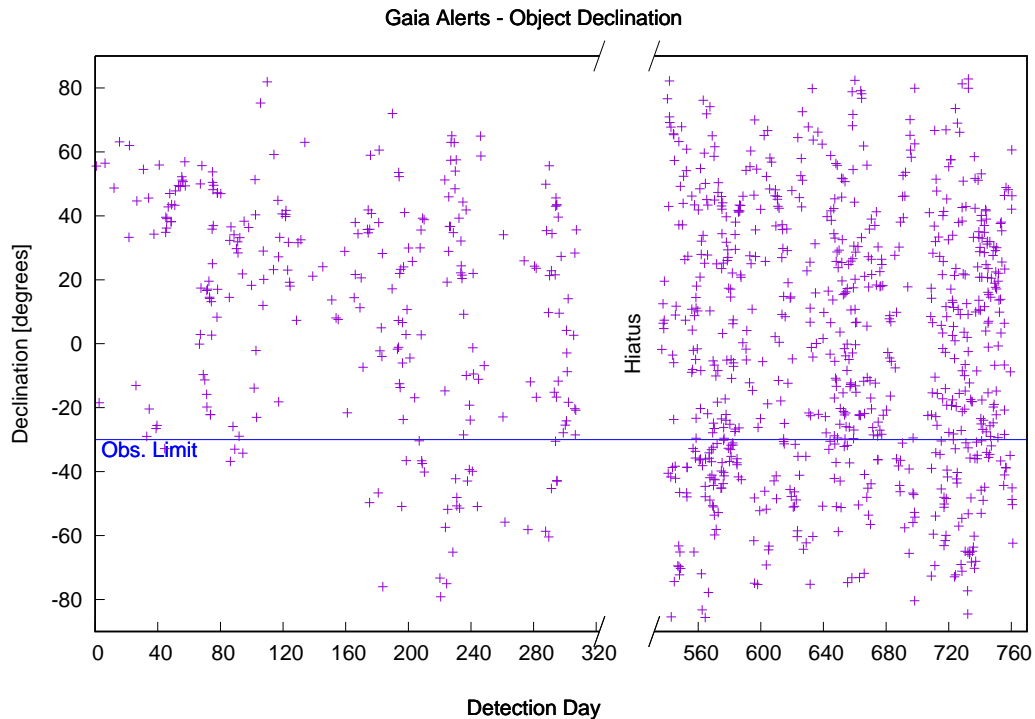


Figure 4.6: Gaia Photometric Survey object declination. The declination observing limit was set to -30° . Some objects above the limit were not observable because of RA. The initial validation phase exhibited a northern hemisphere bias with few objects below -30° .

A SNR of >10 is preferred for reliable classification. The observation of a single object is limited to a total time of <30 minutes, normally implemented as a 3×600 s exposure. Sky brightness limit set to Darkness + 4 to eliminate objects close to the Moon. The observation is scheduled to be active for +7 days from publish date on the Gaia alerts page.

4.5.2 Other Alert Sources

When no Gaia alerts are available for scheduling bright sources, $V < 17.5$, were selected from alternative surveys. The primary alternatives are Astronomer Telegram (ATel) and Transient Name Server (TNS) alerts. Observing was scheduled to be active for +5 days from the published date. The observation was cancelled if the an external classification was published.

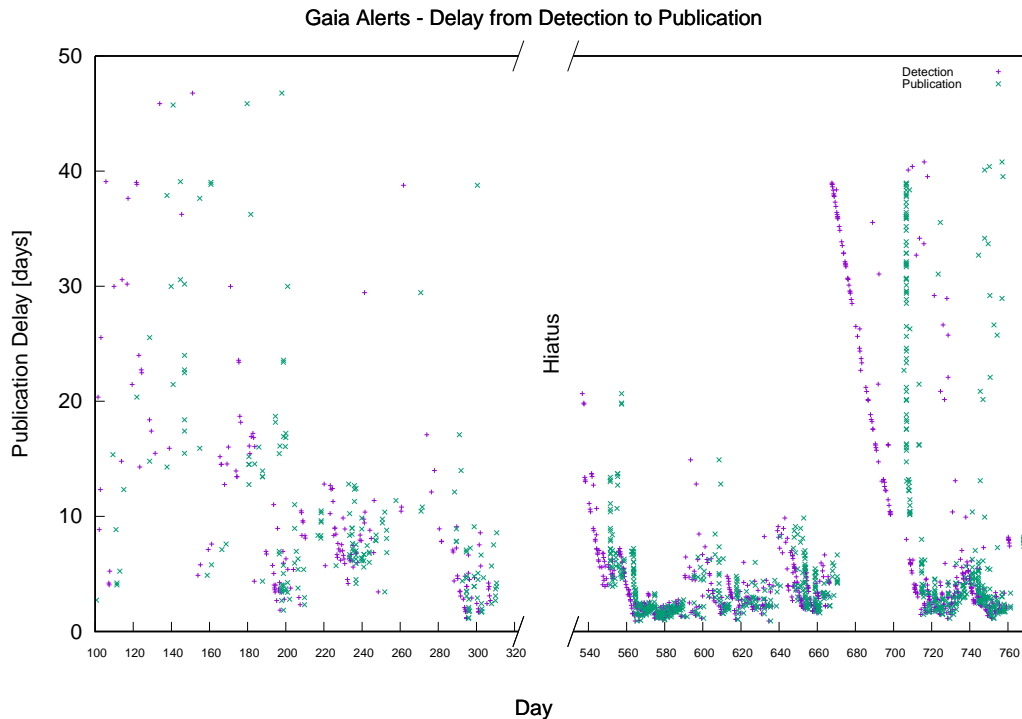


Figure 4.7: The delay between detection and publication of Gaia alerts often exhibited an episodic pattern even post hiatus. The accumulation of detections is shown by a linear decrease in delay (purple) preceding a vertical set of published alerts points (green). The alert list only began providing both the detection and publish dates after 2014-11-07 (day 104). Delays >50 days are not shown.

4.6 Classification Tools

Currently available template matching classification tools include Supernova IDentification Tool, (SNID) (Blondin & Tonry, 2007), GEneric cLassification TOol (Gelato), (Harutyunyan et al., 2008) and Superfit, (Howell et al., 2005).

Gelato uses a set of 2926 template spectra from 127 SNe with no other object types. Templates are periodically added by the maintainers. Although it is possible to select from the provided templates it has no facility for a user to specify templates. It is web based and so not well suited to automated submission of spectra. An estimated redshift must be provided for classification. As redshifts are only available for 66 of the 107 spectra taken it was decided not to use Gelato.

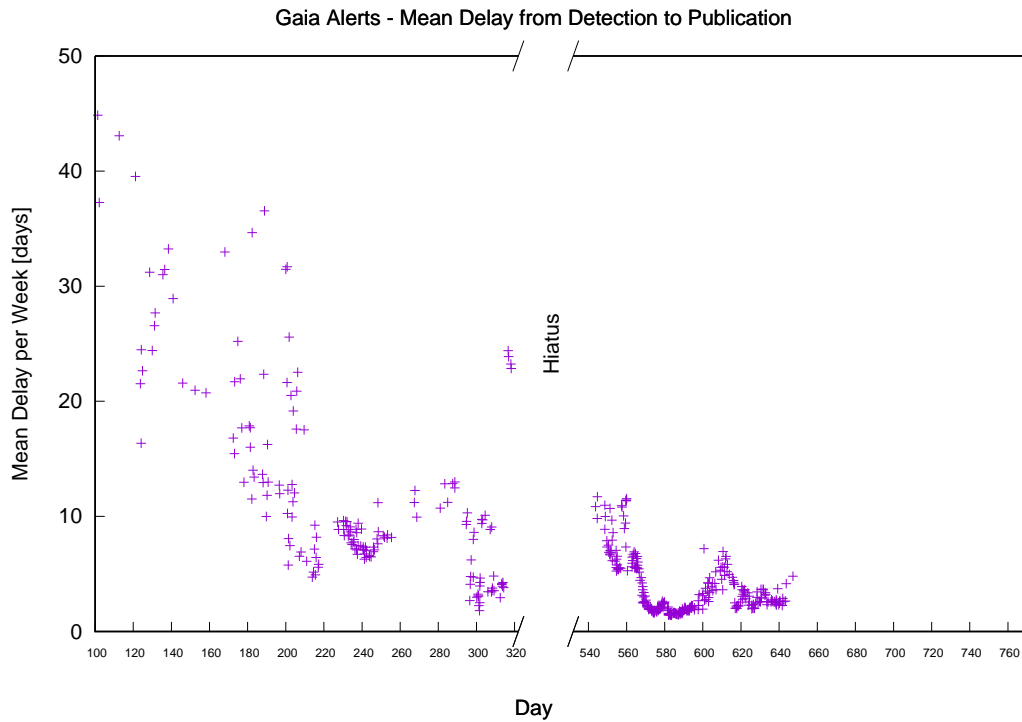


Figure 4.8: The mean publishing delay over a 7 day interval shows a significant decreased with time. The shortest delays, with a mean value of 1.8 days, occurring in the interval between day 570 – 595

SNID performs a pattern match against a set of object templates which primarily containing supernovae spectra but also include other object types. Template set 0, supplied with the initial released of SNID, is comprised of 1515 spectra of 111 objects at different evolutionary phases. The later 2.0 template set extended this to 3754 spectra of 349 objects. Additional templates have been released by Modjaz et al. (2014) to extend the set of core-collapse SNe spectra. This set provided 73 type IIb, Ib, Ic-BL (broad-line) SNe comprising a total of 645 individual spectra. If no redshift is supplied SNID attempts to estimate a value.

4.7 Science Case

The growth in the number and efficiency of surveys will increase the rate of transient detection and the faintness of objects needing classification. The effect of changing default parameters to improve classification reliability was performed for different classes of SNe. Prompt spectroscopic classification of newly detected transients is particularly important for SNe so that any follow up photometry can include the peak of the light curve. This is especially true for type Ia SNe when used as standardisable candles. The aim is to create a semi-automated classification pipe-line tuned to maximise correct identification whilst minimising mis-identification. However classification criteria can differ, the guaranteed identification of only one particular object type may be desirable, e.g. cosmology surveys seeking to select only Ia type as standardisable candles for photometric follow-up may wish to tolerate rejection of a proportion of true type Ia SNe in exchange for a more reliable classification.

4.8 Receiver Operating Characteristic (ROC) Metric for Tuning an Automated System

The spectra used for evaluating the accuracy of classification are of known types and the result from SNID is binary, either a correct identification or a mis-identification. The method chosen to assess the effect of changing SNID parameters was the Receiver Operating Characteristic (ROC), (Fawcett, 2006). With ROC the result of a test is assigned 1 of 4 possible outcomes when attempting to filter an object of a particular type.

- True Positives (TP) - Correct identification. The number correctly assigned as of a type.

- True Negatives (TN) - Correct rejection. The number correctly rejected as not of a type.
- False Positives (FP) - Incorrect identification. The number wrongly assigned as correct type.
- False Negatives (FN) - Incorrect rejection. The number wrongly rejected as incorrect type.

These sum of these outcomes are combined to produce several evaluation metrics. Sensitivity or True Positive Rate (TPR) is used to assess correct identification efficiency. It is the ratio of objects correctly identified, TP, against all those apparently identified as of a particular type, (TP + FN), and varies from +1 (all sought after types correctly detected) to 0.

$$\text{TPR} = \frac{\text{TP}}{(\text{TP} + \text{FN})} = \text{Sensitivity} \quad (4.2)$$

Specificity or True Negative Rate (TNR) is used to assess the rejection efficiency. It is the ratio of objects correctly rejected, TN, against the total that should have been rejected (FP + TN) and varies from +1 (perfect rejection) to 0.

$$\text{TNR} = \frac{\text{TN}}{(\text{FP} + \text{TN})} = \text{Specificity} \quad (4.3)$$

A rejection efficiency related to TNR is the fall-out or False Positive Rate where $\text{FPR} = 1 - \text{TNR}$. It is the ratio of objects incorrectly identified, (FP), against the total that should have been rejected (FP + TN).

$$\text{FPR} = \frac{\text{FP}}{(\text{FP} + \text{TN})} = (1 - \text{TNR}) = \text{Fallout} \quad (4.4)$$

The trade off between correct identification and rejection is represented by plotting the FPR against TPR on an ROC graph (Figure 4.9). It is desirable for test results to

occupy the region on the upper left of the graph with point *A* corresponding to perfect identification and rejection. Points along the central line $TPR = FPR$ line are equivalent of a random choice and indicate a test is useless. Points below the line indicate a test performs worse than random choice and the test result should be inverted.

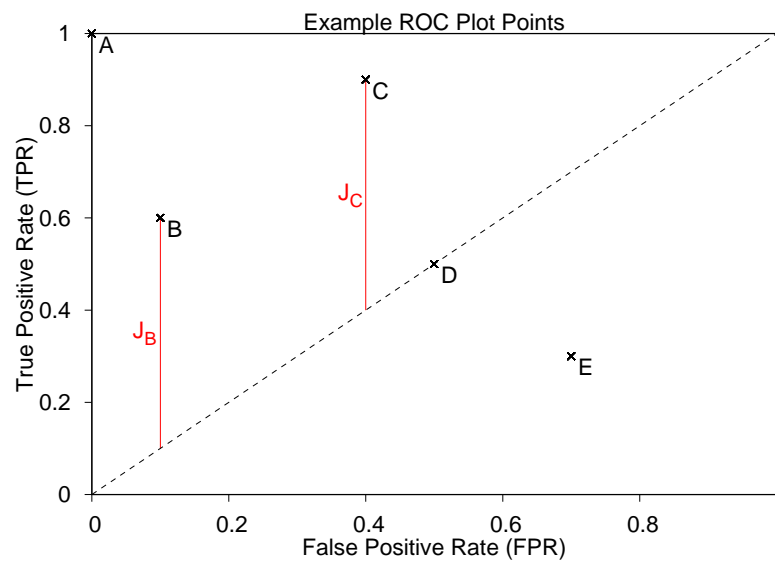


Figure 4.9: An ROC graph plots TPR against FPR for different version of a test. It is desirable for points to occupy the upper left sector. Point *A* is the perfect test result with all classifications correct and no mis-identifications. Points *B* and *C* are more typical, point *B* having a lower proportion of false identifications at the cost of fewer sought after types identified than point *C*. For points on the line $TPR = FPR$ such as *D*, the result is no better than random choice. For points below the line, *E*, the test is worse than random and the test result should be inverted to move the point above the line. Youden’s *J* statistic is the distance of a point above random choice and provides a single evaluation metric, However *J* can have more than one maximum, e.g. both J_B and $J_C = 0.5$ for two different versions of a test.

A single comparison metric, Youden’s *J* statistic, (Youden, 1950), can be obtained using an equally weighted combination of the TPR and TNR. *J* varies from +1 to –1 to indicate how much better a test result performs compared to random choice where $J = 0$ (Figure 4.9). The plot illustrates how *J* can have more than one maximum, e.g. $J_B = J_C = 0.5$, in which case test parameters can be chosen to optimise either high acceptance or rejection of the desired object type.

$$J = (TPR + TNR - 1) = (\text{Sensitivity} + \text{Specificity} - 1) \quad (4.5)$$

4.9 SNID Parameters

When running SNID various parameters can be specified to override the default values. The effect in modifying the following parameters on the resulting classifications was explored.

Window Width: The wavelength range of the observed spectrum was symmetrically reduced by specifying the maximum and minimum wavelengths parameters, `wmax` and `wmin`.

Template Set: The default location of comparison templates used for cross-correlation can be overridden by the `tempdir` parameter. 4 separate directories were created to hold a combination of template spectra sets from the original release 0, release 2 and the Ib/c additional templates.

Redshift: The object redshift was forced using `forcez` to override the value of z estimated by SNID.

Cross-correlation: SNID uses two parameter to evaluate the cross-correlation between the input spectrum and template. The `r1ap` parameter determines the minimum quality of fit when correlating a spectrum with a template. The `lap` parameter is the minimum acceptable overlap between a spectrum and template at the correlated redshift.

4.10 Methodology

An input sample set of 106 spectra with well determined classification was selected from the observing programmes (Appendix A) and supplemented observations taken by Dr David Bersier (Appendix B). Classifications were established by using SNID, manual inspection of the spectra and correlation with external classification reports such as ATels and TNS (see Appendix F). The sample was divided into 4 classifica-

tion group, three groups of SNe types plus a fourth group of non-SN objects to test successful rejection.

Group Ia was made up of all Ia-like with Si II lines and included -pec, Ia-91T and Ia-91bg. Type Ib and Ic either lack or have weak Si II lines that characterise type Ia, constituted a combined input set Ibc. Type II SN, showing both normal and broad-line hydrogen emission features, formed the third set. The remaining objects were not SNe and included AGN, CVs and galaxies. A red-shift derived from the nearest host galaxy was known for 66 of the sampled spectra.

The variation in ROC classification was done for the 4 possible template sets, 0 (Initial release), 0bc (Initial + Liu & Modaz Ib/c), 2 (Second release), 2bc (Second release + Liu & Modaz Ib/c).

4.11 Window Width

The instrument operates with a wavelength window of 4045 – 7970 Å with the SNR being lowest at the extremes of this range. By default SNID does not explicitly limit the input spectrum wavelength range although the range is limited by each individual comparison template. The effect of progressively decrementing the width of the wavelength window centered at 6000 Å in steps of 100 Å was explored. The classification efficiency for combinations of each template set and bandwidth were evaluated for the different SN types (Figures 4.11, 4.12 and 4.13).

The SNR was calculated by taking the mean of the difference between a spectrum and the 3σ smoothed version of itself. The left column plots show the result using SNID's estimation of redshift and the right column when the red-shift is forced using *forcez*, if redshift z is known from the host galaxy. Going from left to right for a specific window width plot the input sample set was reduce to progressively exclude

spectra with low SNR in increments of 5. The left-most points on each line have a SNR > 0 and the right-most SNR > 15. The number of sampled spectra decreases as the SNR threshold is increased from 106 (SNR > 0) spectra to 82 (SNR > 5), 64 (SNR > 10) and 50 (SNR > 15).

4.12 Classification of type Ia SNe

The change in classification for type Ia SN is shown in Fig. 4.11 with the top plot showing the ROC using the initial template set 0. Supplementing Set 0 with type Ib/c templates degraded both the TPR and FPR for Ia spectra with low SNR. Comparison with the equivalent set for Ib/c (Figure 4.12) shows a corresponding increase in the FPR indicating that type Ia SN are mis-identified as type Ib/c, the increased proportion of Ib/c templates produces a classification bias. The effect of this bias is reduced when the extended set 2 and Liu & Modaz Ib/c set were combined (Figure 4.11 lower left).

Using the initial template set 0 and reducing the wavelength window has no improvement effect and the full bandwidth provides the best ROC (Figure. 4.11 upper left) For the combined template set 2bc reducing the window to 3500 Å produced the best ROC at each SNR and with SNR > 10 all type Ia SNe were correctly identified with < 4% mis-identification. This was an unexpected result as truncating the spectrum loses information which is used by SNID to determine the best cross-correlation. It may be explained by several distinct spectral features of a Ia such as the SiII 6355 Å and SiII "W" 5640 Å lying within the window. Noisy data at the extremes of a Ia spectrum would increase the possibility of a false match.

Additionally the result of forcing the value of redshift rather than allowing SNID to estimate z is shown in the right column of Figure 4.11. This reduces the FPR for type Ia SNe at all window width but had little effect on improving the TPR.

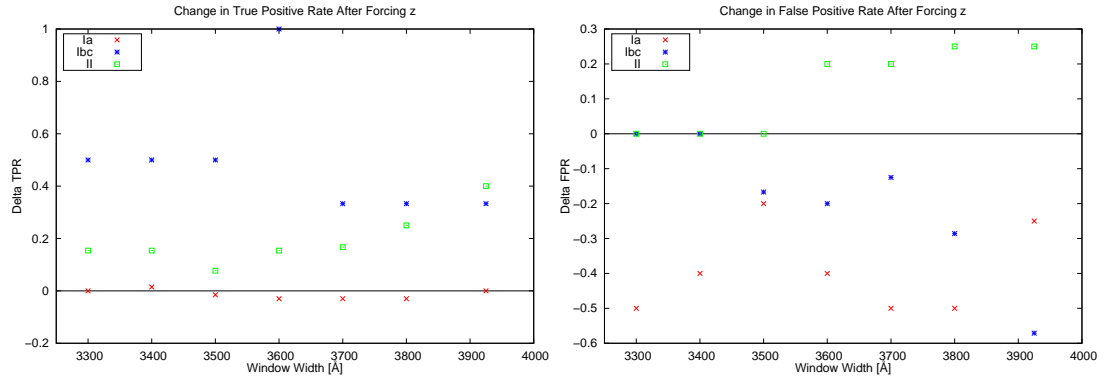


Figure 4.10: The change in TPR (left) and FPR (right) after forcing the redshift z , where known, for all spectra with $\text{SNR} > 0$. Applying a known z was expected to improve both TPR and FPR in all cases but the FPR increased for type II SNe for window size $> 3500 \text{ \AA}$.

4.13 Classification of type Ibc SNe

The change in classification for type Ib SN is shown in Figure 4.12. The trends in the unforced redshift templates (Figure 4.12 left column) show some peculiarities. Supplementing Set 0 with type Ib/c templates unexpectedly degraded both the TPR and FPR Ibc spectra with low SNR but also at high SNR.

Template Set 2 does produce a significant improvement in FPR to 0.4 but at the cost of a lower $\text{TPR} = 0.25$. The truncated spectra $\leq 3600 \text{ \AA}$ have $\text{TPR} = 0.0$. The larger number of templates in Set 2 compared to Set 0 increases the chance of mis-classifying a Ibc. When the Ibc are re-added in Set 2bc (Figure 4.12 lower left) the ROC improves but is not much better than with Set 0 (Figure 4.12 top left), the maximum TPR is 0.5 in both Set 0 and Set 2bc although the FPR is improved at the full windows width of 3935 \AA .

Comparing the spectra with more heavily truncated spectra (window size $\leq 3500 \text{ \AA}$) without forcing z , the FPR decreases as the SNR rises, which is expected, but the TPR degrades or is 0. For window sizes $\geq 3600 \text{ \AA}$ the TPR only shows a small improvement with template Set 2 as the SNR rises. The least truncated spectrum performs the best, which also is true if z is forced (Figure 4.12 right column). For type Ibc classification

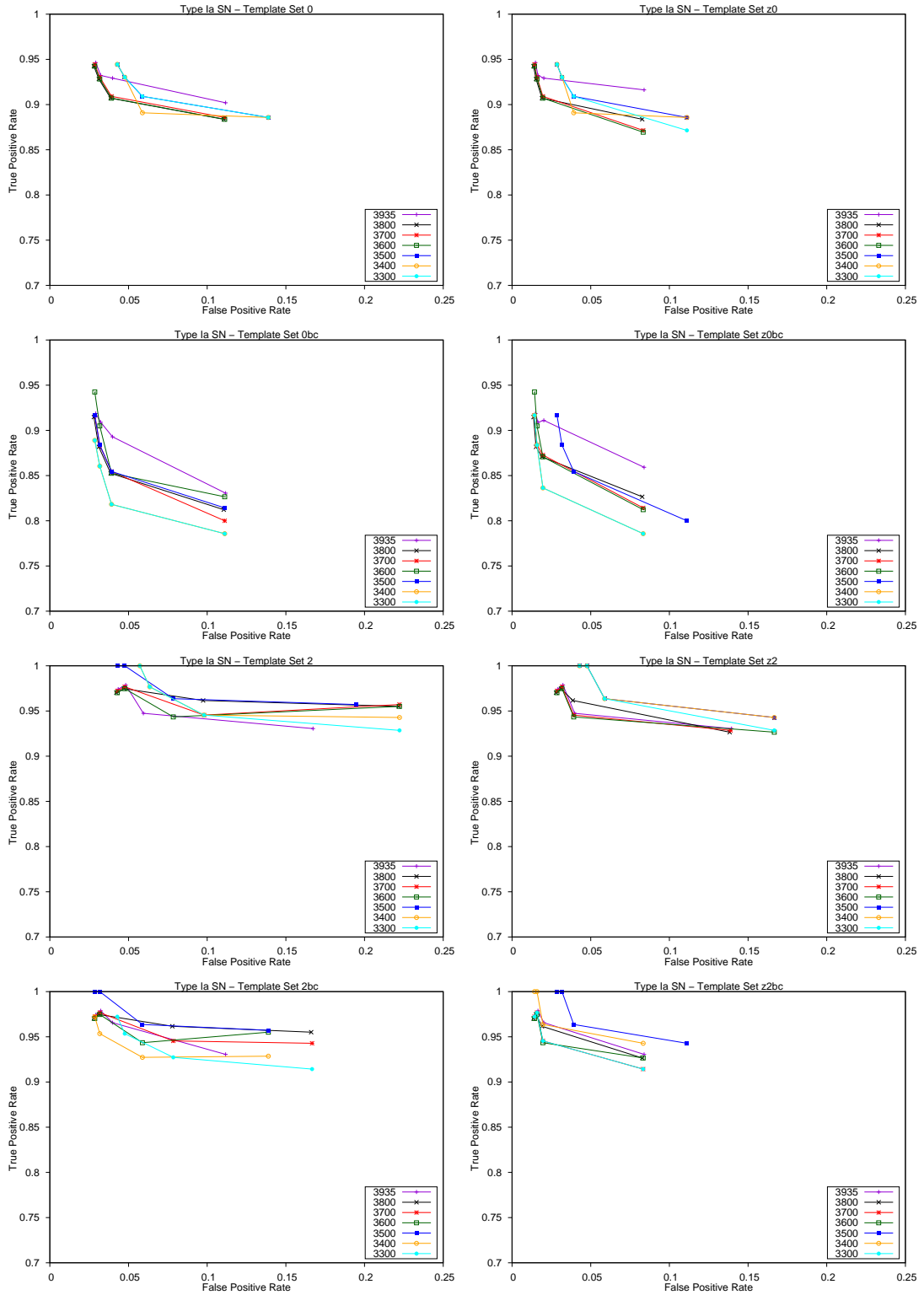


Figure 4.11: Type Ia SN ROC for classification using different SNID template sets. The left column are without z the right column shows the improvement in classification when z is known. For a particular window size the SNR limit of the sampled set is progressively increased from >0 to >15 in increments of 5. SNR increases right to left along each line.

truncating a spectrum degrades the ROC.

Comparing the Set 0 with Set z0 (Figure 4.12 top row) the ROC is identical. Forcing z does not appear to improve the ROC for the base template Set 0.

Comparing Set 0bc with Set z0bc (Figure 4.12 2nd row from top) forcing z improves TPR from 0.5 to 0.75 but not the maximum FPR which remains at 0.2 for the untruncated 3935 Å window.

Comparing Set 2 with Set z2 against the others illustrates the importance of including the Liu & Modaz Ibc templates as the maximum TPR is only 0.25.

Template Set z2bc (Figure 4.12 lower right) provides the best ROC with the untruncated 3935 Å window. At low SNR the FPR = 0.25 and the TPR = 0.7, However even at high SNR >15 the TPR remains below 1.0 at 0.75.

The conclusion is that for most reliable detection of type Ibc a spectrum should not be truncated and preferably the redshift z should be known. As type Ibc evolve intermediate metals (Mg and Ca) become more prominent and truncating the spectrum may eliminate these spectra features.

4.14 Classification of type II SNe

The trends are less clear for type II classification and only observations are made.

The ROC type II plots (Figure 4.13) the plots as a whole exhibit a distinct "L" profile as the SNR increases. Eliminating data with SNR > 5.0 results in a more linear relation between FPR and TPR.

When the Liu & Modaz Ibc templates are added to Set 2bc (Figure 4.13 lower left) the TPR degrades to a maximum of 0.9.

The FPR never goes below 0.02 implying there a some non-type II that are always

identified as type II.

The only conclusion reached are that type II requires a high SNR >10 to reduce FPR to its 0.02 limit. However this is stating that a high SNR makes classification better which is already known. And if Set 2bc template set is used then knowing the redshift significantly improves classification.

Increasing the `rlap` value to 6.0 (Figure 4.14) does introduce a ~ 0.06 increase in TPR.

4.15 Automated Classification Programme

Having determined the optimal SNID parameter it was decided to apply a fully automated classification with no human intervention to all of the spectra in the sample.

The number of exposures taken per observation varied from 1 to 6 with a maximum single exposure time of 800s to reduce the number of cosmic rays in each raw spectrum image. Cosmic rays were primarily detected by visual inspection of the raw spectrum images. Where two or more exposures were taken, cosmic rays were also detected by taking the absolute difference of two raw spectra and looking for sharp 1-2 pixel wide peaks. Correction was done using a linear interpolation using data points either side of the location of the cosmic ray. With 3 or more exposures it is possible to remove cosmic rays by taking the median at each wavelength. This method was tried with noisy exposures but produced resultant spectra with lower SNR than visual removal. As a typical example, cosmic ray removal using the median method for transient Gaia16apd resulted in spectrum SNR = 6.7 whereas for visual removal the SNR=8.7.

The final spectra were submitted for automatic classification using SNID. Where the host galaxy redshift was known the initial estimate was forced using the `forcez` parameter.

During the observing programme a total of 155 transient alerts were followed and re-

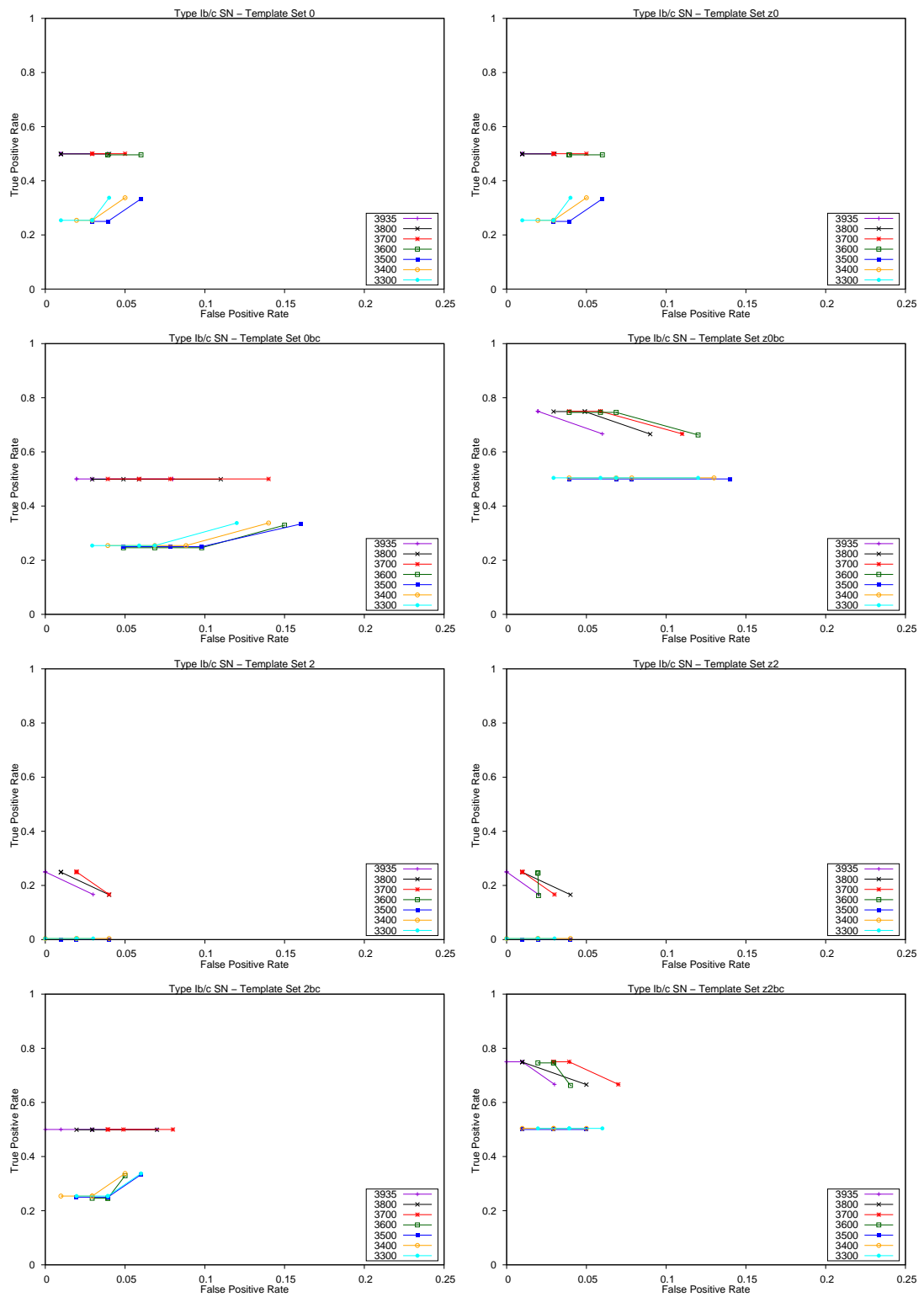


Figure 4.12: Type Ibc SN ROC for classification using different SNID template sets. For a particular window size the SNR limit of the sampled set is progressively increased from >0 to >15 in increments of 5. SNR increases right to left along each line.

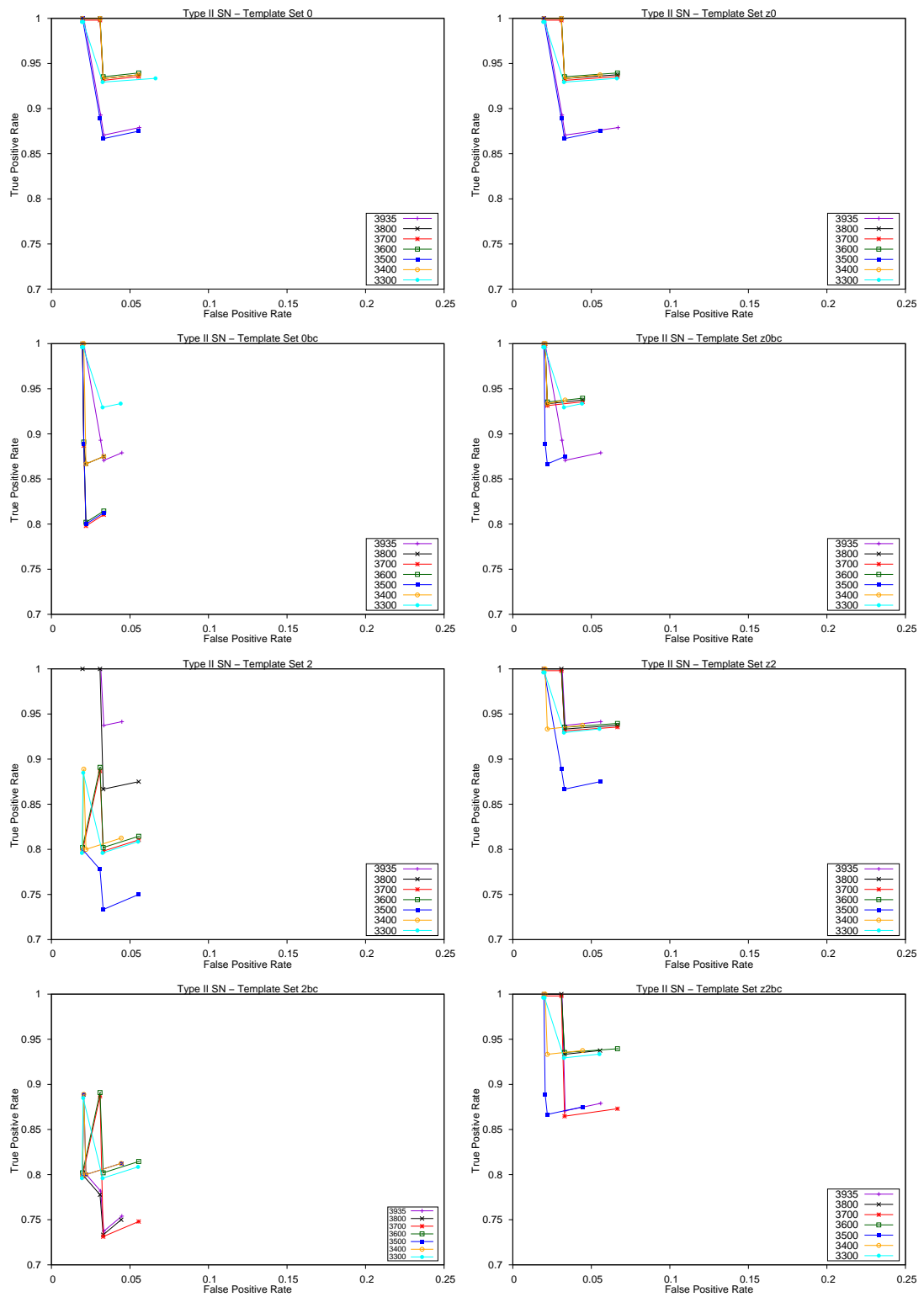


Figure 4.13: Type II SN ROC for classification using different SNID template sets. For a particular window size the SNR limit of the sampled set is progressively increased from >0 to >15 in increments of 5. SNR increases right to left along each line.

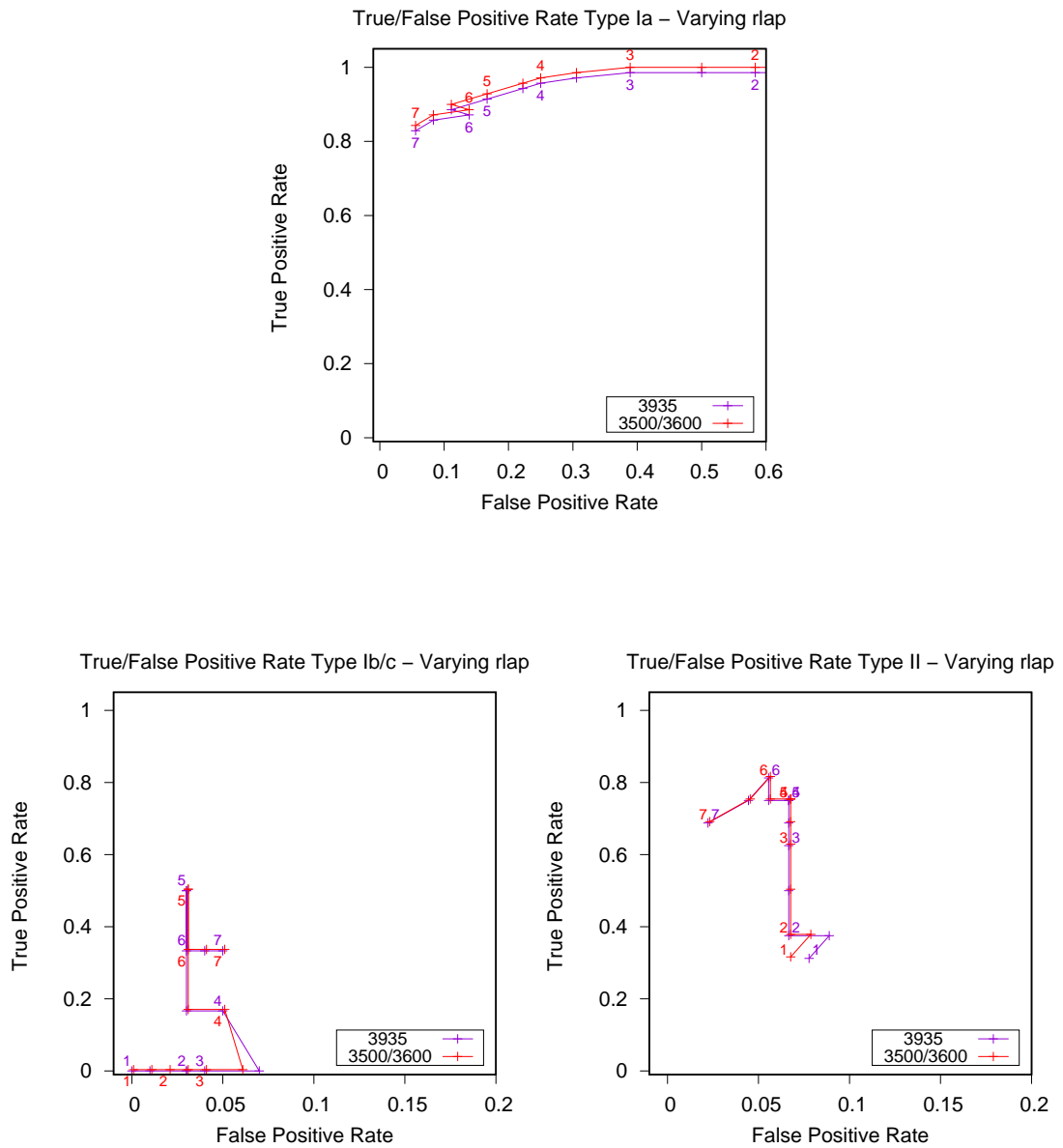


Figure 4.14: All SN ROC for classification using different SNID template sets. For a particular window size the SNR of the sampled set is progressively changed from >0 to >15 in increments of 5.

sulted in 180 observations (Appendix F). The classification of transients from produced a successful SNID template match are shown in Appendix A, although some of them are mis-matches and were manually re-classified or rejected as a failed observation, for example AT2016coi (Figure 4.15). Additional data was obtained from the observing

programme of Dr. David Bersier (LJMU) taken over the same period and include some duplicated observation, shown in Appendix B.

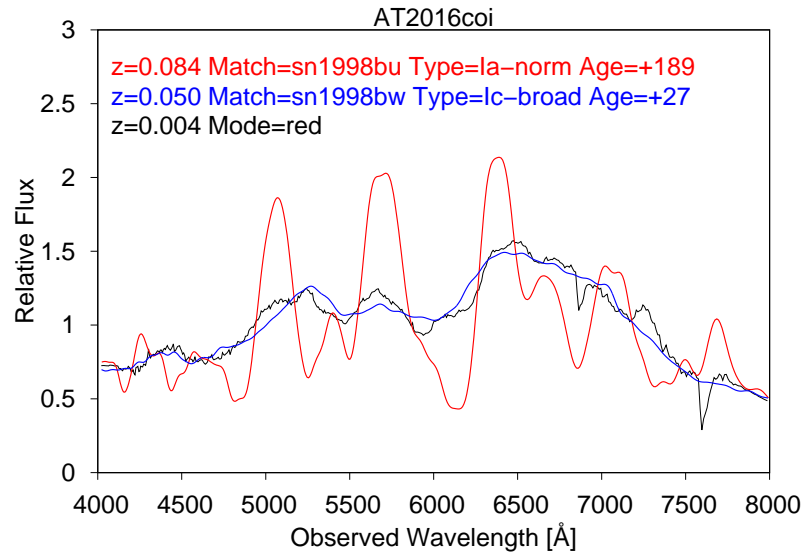


Figure 4.15: AT2016coi is example of a SNID template mis-match. In red is best type match as suggested by SNID ($r_{lap}=0.625$, $r_{lap}=5.7$), blue shows the closest match ($r_{lap}=0.685$, $r_{lap}=5.7$) obtained by visual selection from other suggested templates.

An aim of the observing programme was to produce early classification of transients published by several public surveys and sources. Initially the principal survey sources used were Gaia, ASAS-SN and Pan-STARRS, TNS was used as a source when it became available in January 2016. TNS aggregates alerts from many survey sources and including ASAS-SN and Pan-STARRS which were previously obtained via an ATel.

ASAS-SN and Pan-STARRS notifications were obtained from the ATel web-site and E-mail, Gaia from the public web-site and later using the Gaia marshall and TNS via E-mail alerts. An aim of the observation survey was rapid publishing of classifications. The delay between the initial detection of transient objects by surveys and classification by the programme is shown in Figure 4.15. TNS achieved the lowest overall delay with a mean/median of 3.6/2.1 days and two observations <1 day. The mean/median delay for ASAS-SN are 4.9/3.2 days with 4 <1 day delays including the lowest classification

delay of 0.5 day. Both these surveys have a single long delay outlier, when excluded mean is reduced to 2.8 days for TNS and 3.6 days for ASAS-SN. The mean/median delays for Pan-STARRS are 5.0/4.5 days. Gaia show a reduction in mean/median delay from 13.1/13.2 days down to 6.4/6.4 post-hiatus attributed to the improved Gaia pipeline.

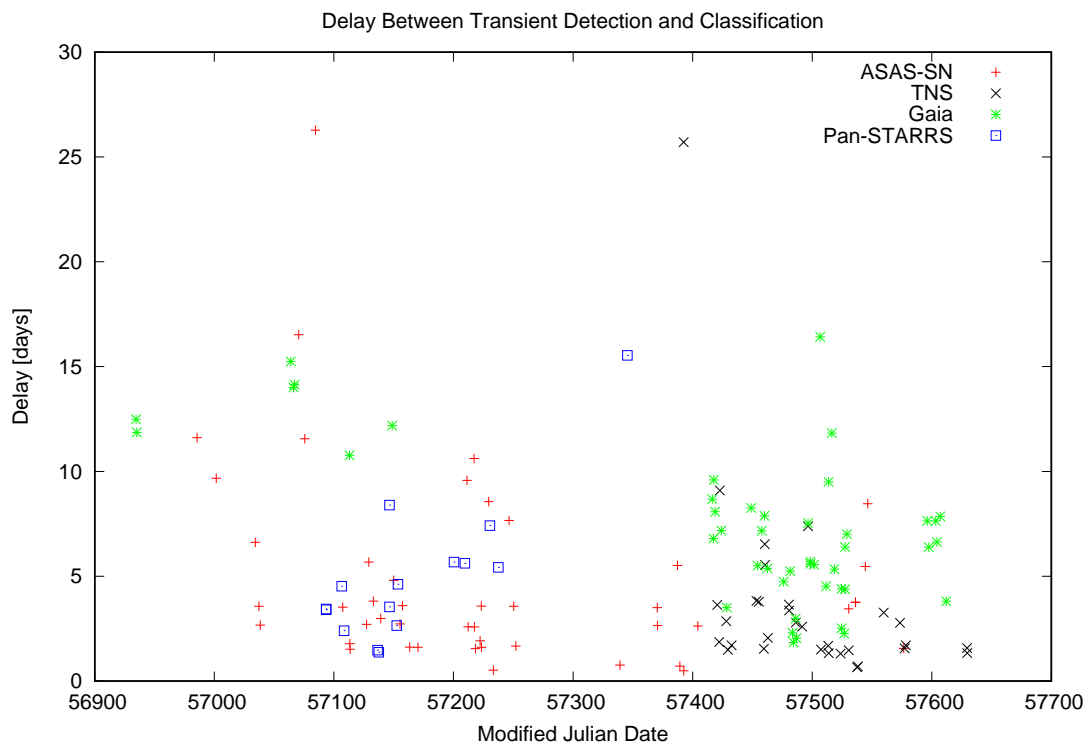


Figure 4.16: To capture the earliest phase in the evolution of a transient, the delay between the initial detection and the classification should be a minimum. The delays for the 4 principal sources of transient surveys used in the observing programme are shown here. The lack of data points centered around 57300 MJD were a result of engineering work on the telescope.

The relation between SNID estimation redshift of objects identified as SNe and expected redshifts is shown in Figure 4.17. A total of 72 redshifts were obtained from the value quoted in alerts and confirmed against the nearest host galaxy redshift from NED and SIMBAD online databases where possible. This sample set was comprised of 56 type Ia, 10 type II and 6 type Ib/c of which SN2016coi was the only type Ic. The SNID estimated redshift for the single type Ic was $z = 0.2400$ which differs significantly from the value from NED reported value $z = 0.0035$ for the host galaxy UGC

11868. This point was excluded from the analysis to avoid skewing the Ib/c redshifts to yield a total of 71 SNID redshift estimations for comparison. A linear fit for all SN types is shown in solid black, gradient $m = 0.96$, and the ideal fit, $m = 1.00$, indicated with a dashed black line.

In estimating a Si ejecta velocity for type Ia the host a galaxy red-shift is needed to correct for radial motion. The host velocity is not always available from a catalogue and the SNID estimate of redshift, z_{snid} could be used instead. In this sample the mean catalogue redshift of Ia SNe was 0.034 and the s.d. in SNID estimated redshift was $\sigma_{Ia} = 0.007$ giving an average error of 21%. For type Ibc $\sigma_{Ibc} = 0.003$ and for type II $\sigma_{II} = 0.001$.

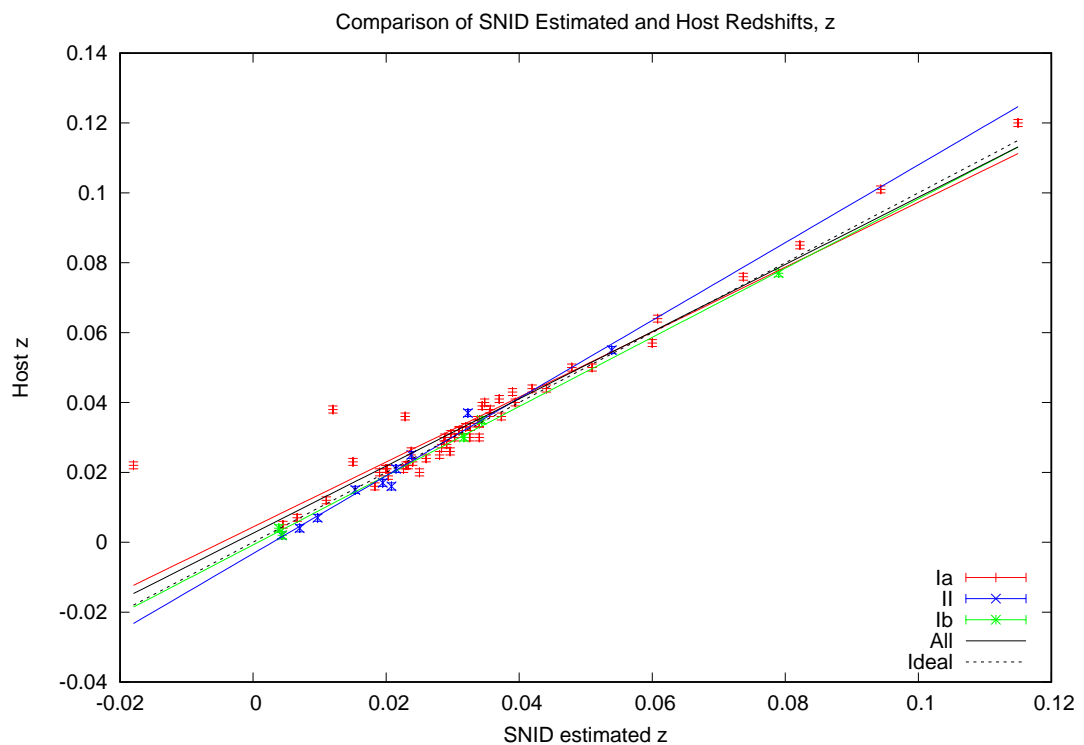


Figure 4.17: This shows the correlation between SNID estimated redshifts and those derived from host galaxies for particular SN types. The solid black line is the linear fit for all SN types and the dashed black the ideal fit. The correlation including all types except Ic is shown in black and has gradient 1.11

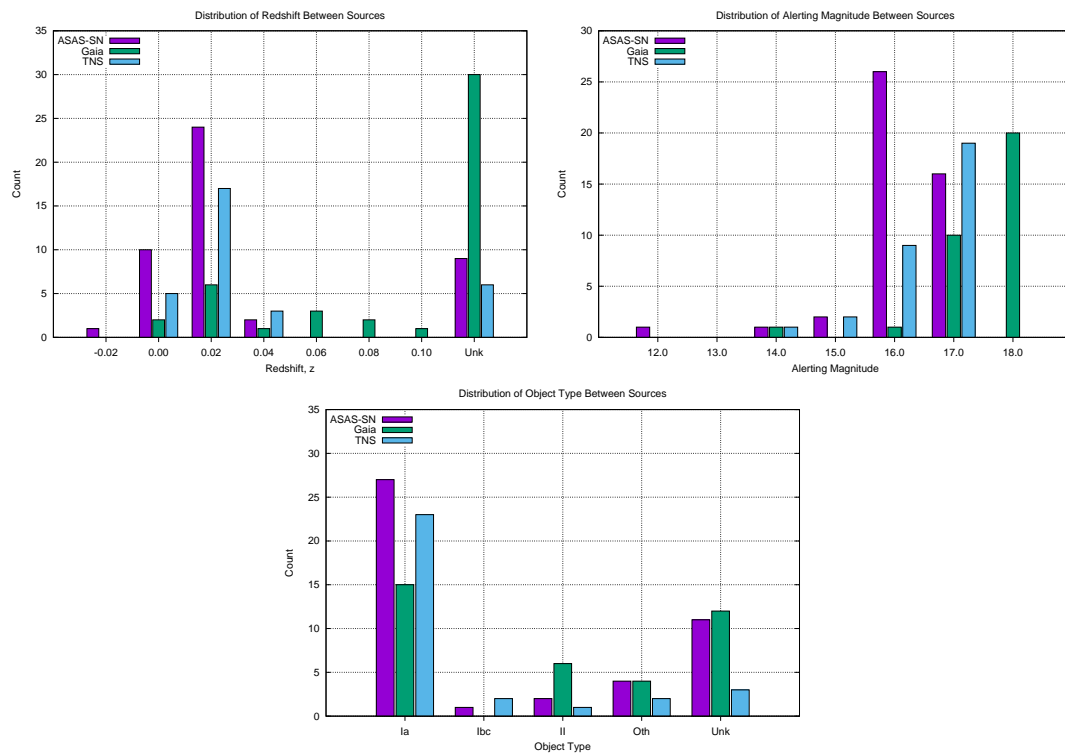


Figure 4.18: The distribution of redshift, magnitude and classification from the 3 main alert sources used. Gaia and ASAS-SN are surveys whereas TNS aggregates alerts from many sources. Oth denotes other non-SN objects. Unk indicates an unknown classification indicating an ambiguous or failed observation.

4.16 Summary and Conclusions

An overview of SN classification and other types of transients was presented followed by a review of active transients surveys.

Gaia survey alerts were to be the primary source of transients for classification and the alert reporting rates and trends were analysed. The episodic nature of Gaia alerts prompted a broadening of alert sources used with ASAS-SN becoming significant source.

In surveys yielding the largest source of suitable targets were ASAS-SN 46 objects, and Gaia 45 objects. The distribution of magnitude, redshift and type is shown (Figure 4.18). TNS yielded 31 objects and is included for comparison although it is not a survey and aggregates alerts from many surveys. The ratios are in some ways reflective

Table 4.3: Comparison of redshift and alerting magnitudes

Redshift				Alert Mag.			
	ASAS-SN	Gaia	TNS		ASAS-SN	Gaia	TNS
Min	-0.0180	0.0044	0.0036	Min	12.90	14.27	14.80
Max	0.0454	0.1150	0.0510	Max	17.50	18.87	17.95
Avg	0.0245	0.0508	0.0277	Avg	16.66	18.08	17.01

of the survey limiting magnitude (Table 4.1). Gaia is the only survey yielding object with known high $z > 0.05$ redshift transients and faint $m > 17.5$ magnitude objects but with few brighter objects. ASAS-SN is productive in bright $m < 16.5$ SNe, which formed 65% of the alerts.

Gaia produces a high proportion of alerts with unknown redshift which will degrade classification accuracy with low SNR sources.

The effect of changing SNID templates set, `rlap` parameter, truncated spectrum and having a known redshift spectrum was explored. For type Ia the optimum classifications were achieved with template set 2bc with known z and symmetrically truncating the spectrum width to 3400 Å. Having a known redshift was significant in reducing the false identification at low SNR. The value of the `rlap` parameter represents a trade off with higher values reducing False Positives at the expense of True Positives. `rlap < 3` provides no gain in rejecting False Positive rejection.

For type Ibc template set 2bc is similarly optimal but the best ROC results are obtained with the full wavelength range. A known z improves correct identification at low SNR. The SNID default `rlap = 5.0` produces the best ROC.

For type II if z is known template sets 2 and 2bc with symmetrically truncating the spectrum width to 3400 Å produced the best ROC. If z is not known the template set 0 with symmetrical truncating spectrum width to 3300 Å produces the best ROC. Setting `rlap = 6.0` produces a slight improvement over the default value.

For all SN types template set 2bc and full spectrum width produced the best ROC both

if z is known or unknown.

Chapter 5

Classification of Optical Counterparts for Gravitational Waves

The search for optical counter parts to Gravitational Wave (GW) events is an example of the utility of combining a rapid response robotic telescope and high sensitivity spectrograph. An object identification programme was conducted using the LT and SPRAT by C.M. Copperwheat as PI, together with COIs I.A.Steele conducting the observations and myself performing classification of the spectra obtained. Some of the material presented in this chapter was published in Steele, Copperwheat, & Piascik (2017) and Copperwheat et al. (2016).

5.1 Follow-up of aLIGO Alerts by the LT with SPRAT

The Advanced Laser Interferometer Gravitational-wave Observatory (aLIGO: Aasi et al. 2015) made the first direct detection of a gravitational wave (GW) signal on 2015 September 14 (Abbott et al., 2016c). The event's waveform was shown to be characteristic of the compact binary coalescence (CBC) of two stellar-mass black holes. This event, since named GW150914, was detected just prior to the beginning of the first

official science run (O1), which lasted until January 2016. In Abbott et al. (2016a) it was announced that a second black hole CBC was detected during O1.

Prior to the beginning of this advanced detector era, a worldwide collaboration of astronomers was established with the aim of detecting electromagnetic (EM) counterparts to a GW event. It is expected that binary mergers involving one or more neutron stars (NS–NS or NS–BH) would show a transient EM signature due to energetic outflows from the merger event (Abbott et al., 2016b). The signature might be the short gamma-ray burst ‘prompt’ emission if the observer is within the opening angle of the jet from the merger event (see, e.g. Berger 2014), or more likely the kilonova emission powered by the radioactive decay of heavy nuclei synthesized in the merger ejecta (Li & Paczyński, 1998; Metzger & Berger, 2012; Barnes & Kasen, 2013; Kisaka et al., 2015). This kilonova is more isotropic than the prompt emission, although it may contain a somewhat collimated optical/blue component (Metzger et al., 2015; Martin et al., 2015; Kasen et al., 2015; Radice et al., 2016). Supernovae may also produce GW signatures, whose waveforms depend on whether a transitional massive neutron star is formed, or whether a black hole and accretion disc is the primary source of GW emission.

The aLIGO and Advanced Virgo (AdV) team can identify a GW candidate within their data stream and propagate this event and its inferred sky location to the EM collaboration as quickly as 30 minutes after detection of the event, although the latency was much higher in the first science run. The main challenge for EM follow-up is the poor localisation of any event. Currently, with only two GW detectors in the network operational, the median uncertainty in the sky position of any detection is of the order of hundreds of square degrees (e.g. Singer et al. 2014; Kasliwal & Nissanke 2014; Berry et al. 2015; Abbott et al. 2016d). This presents two individual problems: the difficulty of searching such a large area for transient sources in a timely fashion, and secondly the difficulty in distinguishing the true counterpart from the long list of possible candidates

which will exist in a sky area of this size.

The LT is one of the telescopes which participated in the O1 campaign. The field-of-view of the LT ($\sim 10' \times 10'$) makes it poorly suited to the search for candidate counterparts, however its diverse instrument suite makes it the ideal tool for the classification of candidates reported to the collaboration by other facilities. Over the course of the campaign, three triggers were issued to the collaboration. Two of these were for the published events GW150914 and GW151226. The third trigger was for a target with the internal designation G194575 (LIGO Scientific Collaboration and Virgo, 2015a). A more detailed analysis of G194575 yielded a much reduced significance and it was later retracted after 29 days of follow-up by the EM collaboration (LIGO Scientific Collaboration and Virgo, 2015b).

The EM collaboration was unsuccessful in identifying a counterpart to either of the GW events in O1. Connaughton et al. (2016) did report a weak and short-lived transient detected by Fermi ~ 0.4 s after the detection GW150914, but this was not detected by any other instrument (Savchenko et al., 2016). A non-detection of either event is not surprising given that they were both classified as binary black hole (BH-BH) mergers from the GW analyses. Without an interaction with matter a BH-BH merger involves the coalescence of the black hole event horizons without the possibility of jet formation. The sensitivity of the aLIGO detectors in this run were such that the discovery threshold for a binary neutron star merger event extended to 75 Mpc. The increased sensitivity in future runs will mean a much larger volume of space is probed and the discovery of merger events with EM counterparts is significantly more likely.

A complete log of LT observations taken over the course of O1 is given in Table 5.1. The reduced spectroscopic data were analysed using the Supernova Identification tool (SNID: Blondin & Tonry 2007) to determine the quantitative classifications presented here. For spectra where SNID classification was ambiguous we attempted further clarification using Gelato (Harutyunyan et al., 2008). Where host galaxy redshift was not

available we used the SNID estimated redshift.

5.2 Gravitational Wave Events

5.2.1 Follow-up of GW150914

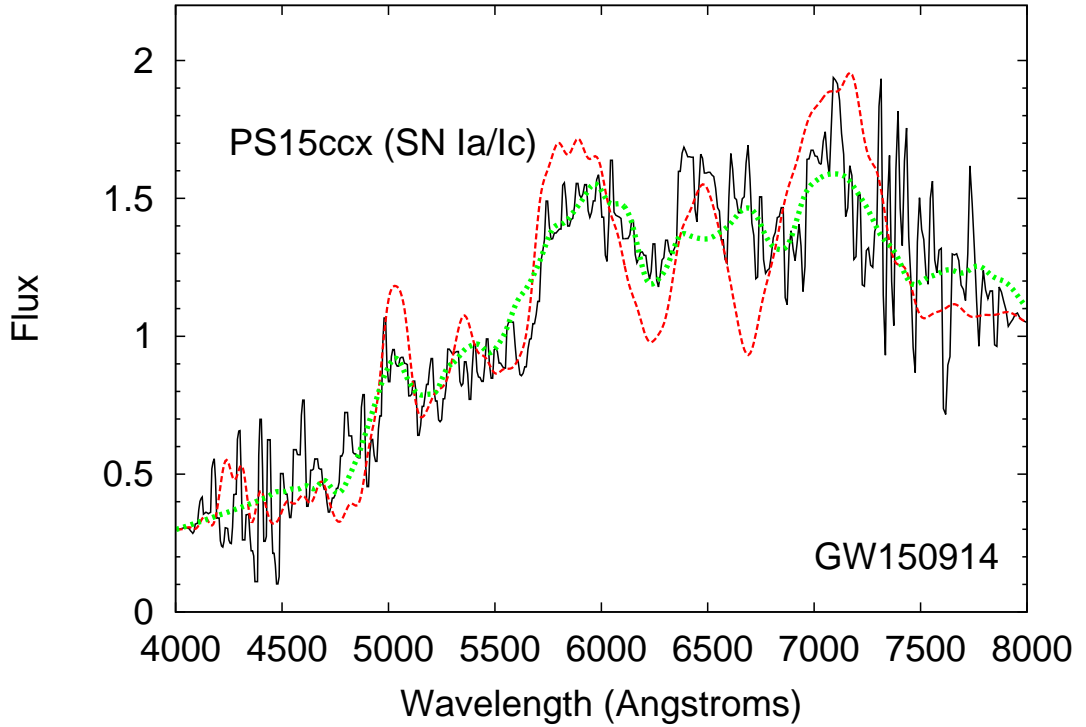


Figure 5.1: Spectrum of PS15ccx obtained during the follow-up campaign of event GW150914. We also plot the best supernova Type Ia (red, dashed) and supernova Type Ic (green, dotted) template fits.

GW150914 was reported in Abbott et al. (2016c) as the signature of the merger of two black holes with masses 36_{-4}^{+5} and $29_{-4}^{+4}M_{\odot}$ at a luminosity distance of 410_{-180}^{+160} Mpc corresponding to a redshift $z \sim 0.09$. The detection was made at 2015 September 14 09:53UT.

An alert was issued to the EM follow-up collaboration on 2015 September 16 (Singer, 2015). The alert was not sent in real-time because the detection was made before

Table 5.1: Log of LT observations taken over the first aLIGO science run. For each object we provide the candidate ID and detection date, time and magnitude, as reported to the EM follow-up collaboration via the GRB Coordinates Network. The remaining columns give the date, time, instrument and exposure times of the LT classification observations. We provide references to the GRB Coordinates Network (GCN) circulars for both the transient discovery and the LT follow-up, and other relevant discovery papers, as follows: ¹Smartt et al. (2015), ²Steele et al. (2015a), ³Steele et al. (2015b), ⁴ Smartt et al. (2016), ⁵Singer et al. (2015a), ⁶Steele et al. (2015c), ⁷Steele et al. (2015d), ⁸Steele et al. (2015e), ⁹Cenko et al. (2015), ¹⁰Copperwheat & Steele (2015b), ¹¹Steele & Copperwheat (2015), ¹²Copperwheat & Steele (2015a), ¹³Palliyaguru & Corsi (2015), ¹⁴Copperwheat & Steele (2015c), ¹⁵Copperwheat et al. (2015a), ¹⁶Rabinowitz et al. (2015), ¹⁷Lipunov et al. (2015), ¹⁸Itoh et al. (2015), ¹⁹Palliyaguri et al. (2016, in prep.)

Candidate ID	Detection date/time	Detection magnitude	LT follow-up date/time	Instrument	Exposure time (s)	References
<i>GW150914</i>						
<i>Event detected 2015-09-14 09:53:51. Alert sent 2015-09-16 05:39</i>						
PS15ccx	2015-09-17 13:42	19.42 (<i>z</i>)	2015-09-27 05:31 2016-04-29 20:50	SPRAT IO:O	1800 150 (<i>r</i>)	1, 2, 3, 4
<i>G194575</i>						
<i>Event detected 2015-10-22 13:35:44. Alert sent 2015-10-22 20:03:45</i>						
iPTF-15dkk	2015-10-23 05:38	19.43	2015-10-28 20:34	SPRAT	1500	5, 6
iPTF-15dkm	2015-10-23 03:39	18.66	2015-10-28 21:41	SPRAT	1500	5, 6
iPTF-15dkn	2015-10-23 05:34	19.17	2015-10-28 21:09	SPRAT	1500	5, 6, 19
iPTF-15dld	2015-10-23 08:15	18.50	2015-10-27 23:48 2015-11-06 20:54 2015-11-06 21:30	SPRAT SPRAT IO:O	1500 2100 200 (<i>u</i>) 200 (<i>g</i>) 600 (<i>r</i>) 600 (<i>z</i>)	5, 19 8 8 8 8
iPTF-15dln	2015-10-23 09:15	18.81	2015-10-28 00:24	SPRAT	1500	5, 6, 19
iPTF-15dmk	2015-10-23 10:58	19.60	2015-11-02 23:37	SPRAT	1500	5, 7, 19
iPTF-15dmn	2015-10-23 09:07	18.37	2015-10-28 22:15	SPRAT	1500	5, 6, 19
iPTF-15dnh	2015-10-23 10:01	19.45	2015-10-29 01:16	SPRAT	1500	5, 6, 19
iPTF-15dni	2015-10-23 10:23	17.72	2015-10-28 23:08 2015-11-04 20:56 2015-11-08 01:25	SPRAT SPRAT IO:O	1500 1500 300 (<i>r</i>) 900 (H_{α})	5, 6, 19 8 8 8
<i>GW151226</i>						
<i>Event detected 2015-12-26 09:44:37. Alert sent 2015-12-27 17:39:45</i>						
iPTF-15fed	2015-12-28 02:00	19.93	2016-01-01 20:03	SPRAT	1800	9, 10
iPTF-15fel	2015-12-28 02:27	18.96	2015-12-30 20:20	SPRAT	1500	9, 11, 12
iPTF-15fev	2015-12-28 02:42	17.64	2015-12-30 21:55	SPRAT	1500	9, 11, 12
iPTF-15ffh	2015-12-28 03:46	18.93	2015-12-30 19:04 2016-01-02 19:29	SPRAT SPRAT	1500 1800	9, 11, 12 13
iPTF-15ffi	2015-12-28 04:06	18.71	2015-12-30 19:43	SPRAT	1500	9, 11, 12
iPTF-15ffk	2015-12-28 04:06	19.19	2016-01-01 21:16	SPRAT	1800	9, 10
iPTF-15ffm	2015-12-28 03:47	19.81	2016-01-03 19:49	SPRAT	1800	9, 15
iPTF-15ffz	2015-12-28 03:44	19.65	2016-01-01 19:26	SPRAT	1800	9, 10
iPTF-15fgy	2015-12-28 05:47	19.52	2016-01-01 21:55	SPRAT	1800	9, 10
iPTF-15fhd	2015-12-28 09:42	19.70	2016-01-03 21:02	SPRAT	1800	9, 15
iPTF-15fhl	2015-12-28 12:42	19.09	2015-12-31 02:48 2016-04-22 22:31 2016-04-23 00:49	SPRAT IO:O SPRAT	1800 150 (<i>r</i>) 1800	9, 11, 12, 13, 19
iPTF-15fhp	2015-12-28 04:06	19.43	2016-01-01 00:58 2016-01-02 23:31 2016-04-22 21:34	SPRAT SPRAT IO:O	1800 1800 150 (<i>r</i>)	9, 10 14
iPTF-15fhq	2015-12-28 09:47	18.92	2015-12-30 21:22 2016-04-25 20:50 2016-05-04 21:27	SPRAT SPRAT IO:O	1500 1500 150 (<i>r</i>)	9, 11, 12
iPTF-15fib	2015-12-28 05:33	19.54	2016-01-01 20:39	SPRAT	1800	9, 10
LSQ15bvw	2015-12-29 02:25	18.8 (<i>V</i>)	2015-12-29 23:20	SPRAT	1500	11, 16
MASTER OTJ020906	2015-12-27 20:30	18.3 (unfiltered)	2015-12-28 20:59	IO:O	300 (<i>r</i>) 900 (H_{α})	11, 17
UGC 1410 transient	2015-12-28 13:42	17.3 (<i>I</i>)	2015-12-29 19:48	SPRAT	1500	11, 18

the formal beginning of O1. A complete overview of the resultant electromagnetic follow-up campaign is given in Abbott et al. (2016b) and Abbott et al. (2016e). The sky localisation uncertainty region was large, with the northern part close to the Sun at the time of the event making follow-up challenging. However, Smartt et al. (2015) reported a number of candidates detected by Pan-STARRS (Kaiser et al., 2010). A complete account of the Pan-STARRS follow-up of GW150914 is provided in Smartt et al. (2016). One of these candidates, PS15ccx, with z-band alerting magnitude of 19.4 was observed by the LT in evening twilight at 2015 September 17 13:42UT (Steele et al., 2015a,b). A 1800 second SPRAT spectrum was obtained, and in Steele et al. (2015b) we reported a SNID best-match classification of a supernova Type Ia at age 15–23 days post maximum with $z \sim 0.097$. However, there is a lack of strong Fe lines in the spectrum and so a possible alternative classification is a supernova Type Ic with $z = 0.089$. In Figure 5.1 we plot the spectrum with both of these template fits but find an inconclusive match.

We observed this target again in April 2016, seven months after our initial classification, obtaining a deep r -band IO:O image. We find no evidence of the transient, suggesting it has faded below the background level of the host galaxy, which we estimate as $r \sim 20.5$ at the object coordinates.

5.2.2 Follow-up of G194575

An alert was issued on 2015 October 22 to the EM follow-up collaboration regarding event G194575 (LIGO Scientific Collaboration and Virgo, 2015a). The false alarm rate (FAR) of this event was given as 9.65×10^{-8} Hz, which was above the alert threshold. However, a subsequent offline analysis was reported by the LIGO Scientific Collaboration and Virgo (2015b) on 2015 November 11 as giving a significantly reduced FAR of 8.19×10^{-6} Hz, or one in every 1.41 days, meaning G194575 was determined not likely to be a real event and therefore no longer of interest. However, in the ~ 30 days

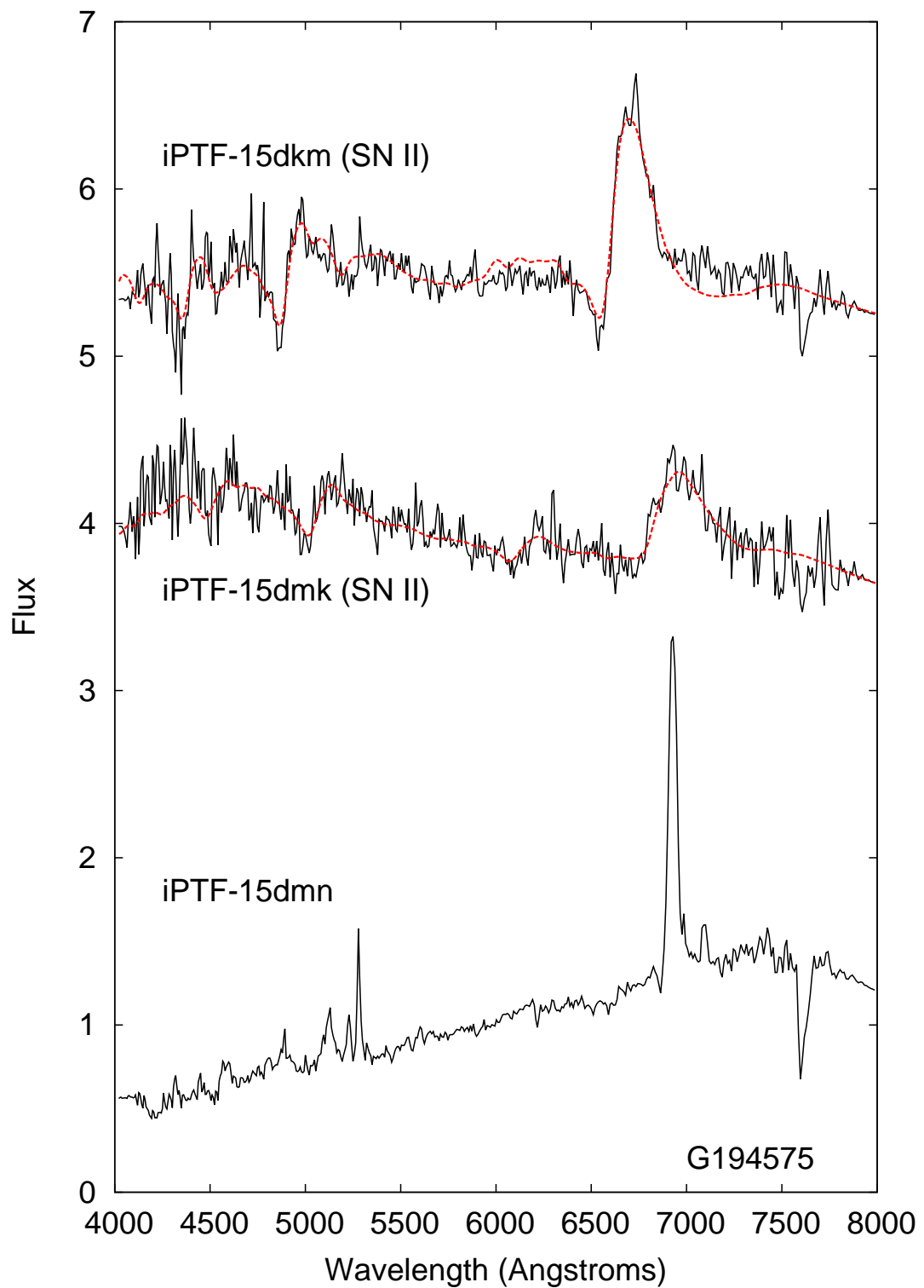


Figure 5.2: Spectra obtained during the follow-up campaign of event G194575. We omit candidates for which our observations showed no evidence of a transient. For objects where a supernova identification is obtained via SNID, we overplot the best template fit (red line, dashed).

Table 5.2: Classifications of transients candidates followed by the LT in response to event G194575. Where we obtain a secure supernova classification we provide a redshift, the time t since peak, and the percentage of matching templates in the SNID database which are consistent with the spectrum.

Candidate ID	Comments
iPTF-15dkk	No obvious transient detected. Emission from host galaxy with $z = 0.061$
iPTF-15dkm	Supernova Type II, $z = 0.03$, $t = +4$ d, 96.5 per cent template fit
iPTF-15dkn	No obvious transient detected. Emission from host galaxy with $z = 0.074$
iPTF-15dld	Some broad emission features, with evidence of contamination by the host galaxy (Consistent with Type Ic supernova.)
iPTF-15dln	No obvious transient detected. Spectrum shows host galaxy with $z = 0.051$
iPTF-15dmk	Supernova Type II, $z = 0.069$, $t = +2$ d, 98.1 per cent template fit
iPTF-15dmn	Consistent with host Seyfert galaxy with $z = 0.056$. Distinct OIII emission line at 5007 Å
iPTF-15dnh	No obvious transient detected. Emission from host galaxy with $z = 0.056$
iPTF-15dni	Weak H-alpha emission with host galaxy absorption at $z = 0.020$

between these two notifications, a sizeable number of follow-up observations were reported by the collaboration. In this section we detail the LT contribution to this search.

The LT observations are listed in the second section of Table 5.1. Follow-up data was obtained for nine transients which were reported to the collaboration by Singer et al. (2015a). All of these transients were detected by the intermediate Palomar Transient Factory (iPTF: Law et al. 2009b). The iPTF methodology for selecting candidates during the EM follow-up campaign is described in Kasliwal et al. (2016). A summary of our classifications is provided in Table 5.2, and the spectra obtained are shown in Figure 5.2. We comment on individual targets below.

iPTF-15dkk, iPTF-15dkn, iPTF-15dln, iPTF-15dmn, iPTF-15dni, iPTF-15dnh

We obtained SPRAT spectra centred on the reported positions of these six targets, and in each case found no evidence of a transient source. The acquisition images indeed show no obvious point source distinct from the host galaxy emission, and the spectra also are apparently dominated by the host galaxy. We estimate the redshifts of the host galaxies from absorption lines in the spectra, and list them in Table 5.2. The spectrum of iPTF-15dmn shows narrow H_α line and a distinct OIII emission line at 5007 Å with velocity width $\sim 1000 \text{ km s}^{-1}$ (*c.f.* instrument velocity resolution of 550 km s^{-1}). We

classify this host as probable Seyfert galaxy with $z = 0.056$.

We should emphasise that our non-detections here is not a criticism of the iPTF image subtraction techniques. Typically our non-detection is due to the transient being sufficiently close to its host galaxy nucleus that it cannot be distinguished above the bright galaxy core emission. In other cases the transient may have faded between detection and our follow-up, or our observations might have been taken in poorer conditions.

iPTF-15dkm, iPTF-15dmk

We classify iPTF-15dkm as a Type II supernova at approximately 4 days after explosion at $z \sim 0.03$. A supporting determination was obtained by D’Avanzo, et al. (2015), who reported a spectrum obtained 6 days after ours which they used to classify this object as a Type II supernova at approximately 10 days after explosion at $z \sim 0.026$.

We classify iPTF-15dmk to also be a Type II supernova, at approximately 2 days after explosion at $z = 0.065$.

iPTF-15dld

The first follow-up of this transient was reported by Tomasella et al. (2015). A re-analysis of these data was then discussed by Benetti, et al. (2015), in which the spectrum was found to be consistent with that of a broad line Type Ic supernova, close to maximum light, at a redshift of $z = 0.046$. The authors identified this as a source of particular interest, albeit one unrelated to any GW event, since the spectrum resembles that of SN 2006aj (Campana et al., 2006; Pian et al., 2006; Mazzali et al., 2006), a rare event likely associated with jet-like core collapse. Further optical observations were reported in Tomasella, et al. (2015), and this object was also observed with Swift, which did not detect an X-ray counterpart (Evans et al., 2015, 2016).

The unusual nature of this event prompted us to obtain multiple epochs of spectroscopy supplemented by multi-wavelength photometry. These data are published in a detailed study of this object Pian et al. (2017).

5.2.3 Follow-up of GW151226

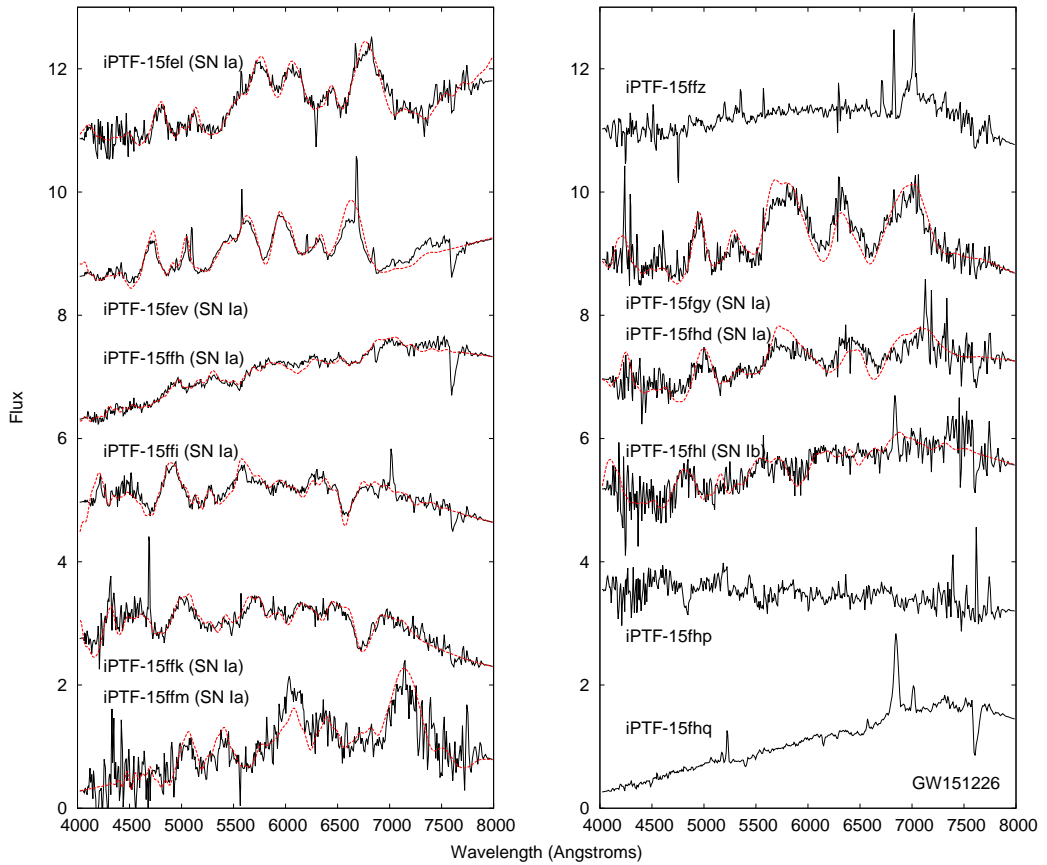


Figure 5.3: Spectra obtained during the follow-up campaign of event GW151226. We omit candidates for which our observations showed no evidence of a transient. For objects where a supernova identification is obtained via SNID, we overplot the best template fit (red line, dashed).

GW151226 was reported in Abbott et al. (2016a) as a CBC of two black holes with masses $14.2^{+8.3}_{-3.7}$ and $7.5^{+2.3}_{-2.3}M_{\odot}$, at a distance of 440^{+180}_{-190} Mpc ($z \sim 0.09$). The gravitational wave signal was detected at 2015 December 26 03:39UT, and an alert was issued to the EM follow-up collaboration at 2015 December 27 17:40UT, identifying

Table 5.3: Classifications of transients candidates followed by the LT in response to event GW151226. Where we obtain a secure supernova classification we provide a redshift, the time t since peak, and the percentage of matching templates in the SNID database which are consistent with the spectrum.

Candidate ID	Comments
iPTF-15fed	No transient detected to limiting magnitude of $R \sim 19.1$
iPTF-15fel	Supernova Type Ia, $z = 0.038$, $t = +40$ d, 97.7 per cent template fit
iPTF-15fev	Supernova Type Ia, $z = 0.023$, $t = +50$ d, 94.7 per cent template fit
iPTF-15ffh	Possible supernova Type Ia, $z = 0.061$, $t = +15$ d
iPTF-15ffi	Supernova Type Ia, $z = 0.085$, $t = +3$ d, 89.1 per cent template fit
iPTF-15ffk	Supernova Type Ia, $z = 0.102$, $t = +5$ d
iPTF-15ffm	Supernova Type Ia, $z = 0.094$, $t = +36$ d
iPTF-15ffz	Emission lines consistent with AGN at $z \sim 0.07$
iPTF-15fgy	Supernova Type Ia, $z = 0.076$, $t = +20$ d, 84.7 per cent template fit
iPTF-15fhd	Possible supernova Type Ia, $z = 0.091$, $t = +11$ d
iPTF-15fhl	Possible supernova Type Ib, $z = 0.043$, $t = +18$ d
iPTF-15fhq	Possible supernova Type Ic, $z = 0.129$, $t = +1$ d
iPTF-15fhq	Consistent with AGN at $z = 0.043$. Distinct OIII emission line at 5007 \AA
iPTF-15fib	Slow moving asteroid
LSQ15bvw	No transient detected to limiting magnitude $R \sim 19.5$
MASTER OTJ020906	No transient detected to limiting magnitude $R \sim 20$
UGC 1410 transient	No transient detected. ID'd as minor planet 2 606 Odessa (Cenko et al., 2015; D'Avanzo, et al., 2015)

the event as a CBC containing at least one black hole (LIGO Scientific Collaboration and Virgo, 2015c). The localisation region for this source was well placed for follow-up from La Palma, and we took classification data for 17 candidates over the course of the week following the alert. The majority of the sources we followed were originally detected by iPTF and reported to us by the collaboration Cenko et al. (2015) in batches. We were not able to observe every transient in this report and selected targets without existing spectroscopic classifications and with a discovery magnitude less than 20.

A complete account of the iPTF follow-up of GW151226 will be presented in Kasliwal et al. (2017, in prep). A summary of all of the classifications we made is provided in Table 5.3, and the spectra obtained are shown in Figure 5.3. We comment on individual targets below.

iPTF-15fed, iPTF-15fib, LSQ15bvw, MASTER OTJ020906, UGC 1410 transient

For these five sources we found no evidence of a transient source in either our SPRAT acquisition image or spectrum. As noted in Section 5.2.2, this could be for a num-

ber of reasons: contamination from the host galaxy, a fast fading transient, or poor weather conditions at the time of our follow-up observations. iPTF-15fed in particular was originally reported (Cenko et al., 2015) with a magnitude that was fainter than the estimated limiting magnitude of our acquisition frames. We obtained r -band and H_α photometry of MASTER OTJ020906 (Lipunov et al., 2015), using an H_α filter redshifted to a central wavelength of 675.5nm to match the host galaxy. We did not detect a transient, and observations by D’Avanzo et al. (2015) on the subsequent night confirmed this source had already faded below its host galaxy level.

Two of these non-detections were due to the source being a solar system object. iPTF-15fib was identified by iPTF as a slow moving asteroid, and was erroneously included in Cenko et al. (2015) as a candidate. Itoh et al. (2015) reported a transient in the galaxy UGC 1410. We did not detect a transient in our follow-up data, and this object was subsequently identified as the minor planet 2606 Odessa (Cenko et al., 2015; D’Avanzo, et al., 2015).

iPTF-15fel, iPTF-15fev, iPTF-15ffi, iPTF-15ffk, iPTF-15ffm, iPTF-15fgy

These targets were all classified by SNID as Type Ia supernovae. In Table 5.3 we list redshifts and the times in days relative to the time of maximum light.

iPTF-15ffh, iPTF-15fhd

We obtained two epochs of observation for iPTF-15ffh. In the first epoch the data were of poor quality and we could not discern any emission from a transient source over that of the host galaxy. In the second visit we obtained a very red spectrum from which we tentatively classify it as a Type Ia supernova using SNID. We also classify iPTF-15fhd as a Type Ia, although again the quality of the data is such that we consider this less secure than some of our other classifications.

iPTF-15ffz, iPTF-15fhq

These sources show distinct OIII emission lines and we classified them as AGN. We observed iPTF-15fhq again in April/May 2016, four months after our initial observation, and obtained a SPRAT spectrum and a deep r -band IO:O image. We find no significant differences in the spectrum or target brightness compared to our first visit, which supports this identification.

iPTF-15fhl

In Copperwheat & Steele (2015a) we reported that the spectrum of this source shows an emission line on top of the host galaxy spectrum. This is at a wavelength consistent with H_α at a redshift of $z = 0.044$, which is consistent with the redshift provided by Cenko et al. (2015). A further analysis with SNID identified the transient as a possible supernova Type Ib with $z = 0.043$ at 18 days after peak, although the spectrum suffers from significant contamination from the host galaxy. We observed this target again in April 2016, nearly four months after our initial classification, obtaining a deep r -band IO:O image and a SPRAT spectrum. The image shows no evidence of the transient, suggesting it has faded below the background level of the host galaxy, which we estimate as $r \sim 20.7$ at the object coordinates. The spectrum shows no emission other than that of the host galaxy, with the H_α emission line still present.

iPTF-15fhp

We obtained two epochs of observation for this target. The first epoch of data were of poor quality and the best classification was a Type Ia supernova at 7 days before peak. A second epoch was obtained two nights later and the acquisition image showed that the transient had not brightened, confirming this initial classification to be erroneous. The data obtained for this second epoch were still too noisy for reliable classification,

but is consistent with a Type Ic supernova at one day past peak. We observed this target again in April 2016, nearly four months after our initial classification, obtaining a deep r -band IO:O image. We find no evidence of the transient, suggesting it has faded below the background level of the host galaxy, which we estimate as $r \sim 21.5$ at the object coordinates.

5.3 Automated Classification

GW detection is another example of a multi-collaborative observing programme that will potentially require the classification of a large number of transient objects. The suitability of using SNID as part of an automated classification pipeline was therefore examined. A Unix csh script was written to perform the following

1. Automatically extract L1 pipeline processed spectra as they became available
2. Remove cosmic rays if possible
3. Stack the resulting spectra
4. Perform a flux calibration
5. Submit the spectrum to SNID for classification
6. Parse the results for success or failure in classification and populate a destination directory

These could then be compared with the manual classifications presented in section 5.2

The SN classification programme (Section 4.4) selected targets down to a maximum magnitude $m = 18.5$ and set an exposure time to achieve a $\text{SNR} > 5.0$. For the GW programme the criterion was changed to maximum magnitude $m = 20.0$ using standard exposure times of either 1500 or 1800 seconds (Table 5.1).

Several GW transients initial spectra were too noisy for a successful classification and required additional observation epochs with a longer exposure time to improve the SNR. Despite this limitation, 5 manual classifications were obtained from the 9 spectra with $\text{SNR} < 5.0$. The SNRs of the final epoch observations are shown in Figure 5.4 together with effect of symmetrically reducing the wavelength range to 3500 \AA in an attempt to improve the SNR in the central region of the spectra. Spectra with $\text{SNR} < 5.0$ show a mean improvement in SNR of $+0.59$ whereas those with $\text{SNR} > 5.0$ the mean increase in SNR was $+4.44$.

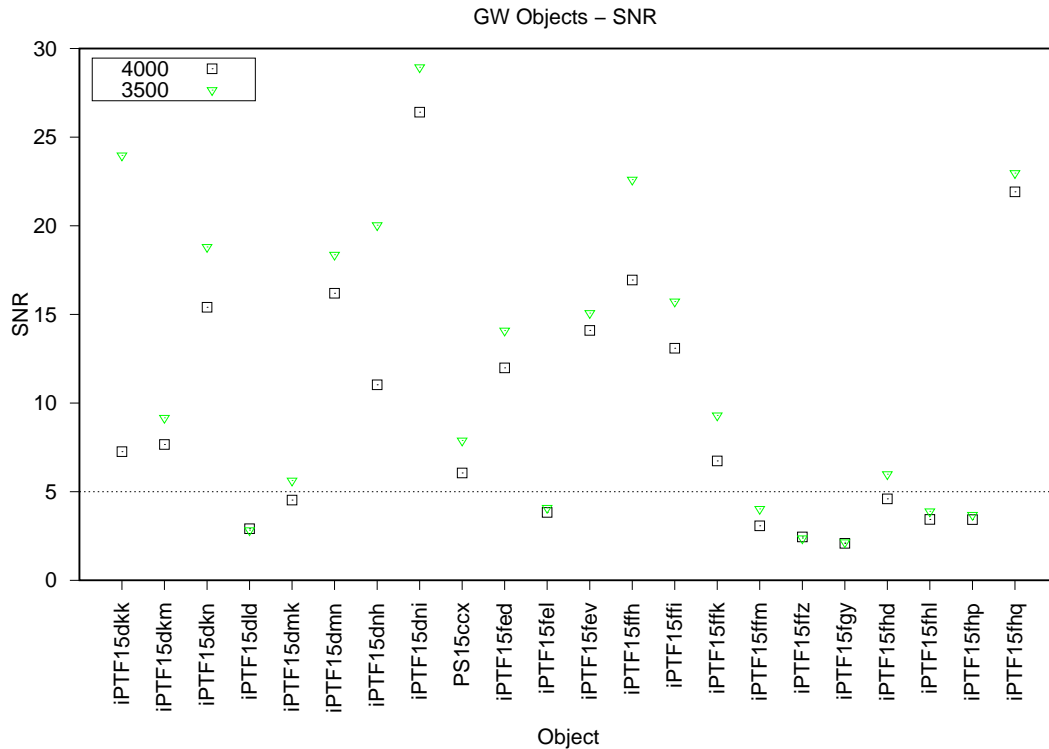


Figure 5.4: The SNR for GW targets for which a classification was obtained. For spectra with $\text{SNR} < 5$, reducing the wavelength range to 3500 \AA the mean improvement was $+0.59$. For spectra with $\text{SNR} > 5$ the mean increase was $+4.44$. Despite a low SNR, 5 of 9 noisy spectra with $\text{SNR} < 5$, produced automatic classification which matched manual identification. The large improvement in the SNR of iPTF15dkk was due to the removal of single broad cosmic ray signal at $\sim 7800 \text{ \AA}$.

The manual classification in section 5.2 was done by selecting the closest matching spectrum from the SNID suggested template spectra using the full 4000 \AA wavelength range. When classifying automatically the template spectrum producing the highest

SNID `rlap` was selected as the best match. A comparison of manual and automatic classification for the full 4000 Å and a reduced 3500 Å wavelength range is shown in Figure 5.5. To test rejection of failed observations the input included LSQ15bvw, MASTERJ020906 and UGC1410. These objects were either missing spectra or had $\text{SNR} < 1.0$ and were not expected to produce a match with any SNID templates. All 3 failed observations were successfully rejected by automated classification.

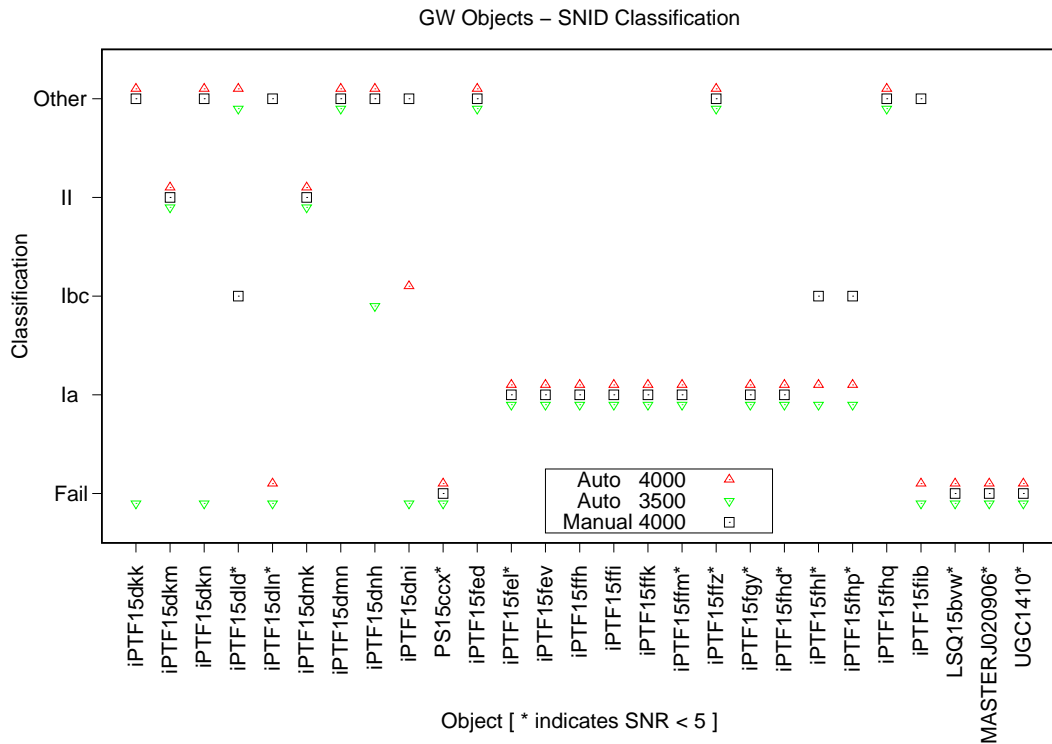


Figure 5.5: Initial classification was done using SNID and selecting the closest matching full 4000 Å width spectrum by manual comparison. This is compared with automated classification which used the closest match as determined by the SNID `rlap` parameter. Automated classification was performed with both the full 4000 Å and a symmetrically reduced 3500 Å wavelength range. The spectrum of PS15ccx could match either Ia or Ic so the classification is shown as Fail.

Although SNID is primarily a SN identification utility it can also identify and estimate the redshift for an AGN/galaxy and identify an M or LBV star. A comparison in the estimated value of z for GW targets is shown in Figure 5.6. Of the 27 GW targets observed only 8 had independently known z , marked with blue circles. 7 of reference values for z were of the nearest host galaxy redshifts obtained from NED and SIM-

BAD online databases with quoted accuracies < 0.0002 . For iPTF15fel (=PS15dpq) the value for z was obtained from ATel # 8498 although this source did not quote an error. The difference, δ_z , between the reference z and the SNID estimated z for matching template with highest `r1ap` value was calculated. The s.d. σ_z of the δ_z values was evaluated for each estimation method. For the full manual range 4000 Å method $\sigma_z=0.0020$ and for the automatic 4000 Å $\sigma_z=0.0019$. The maximum error for both of these methods was $\delta_{zmax}=0.004$. The automatic 3500 Å range failed to classify 3 of the spectra with reference redshifts and over-estimated iPTF15dnh at $z=0.181$, an error of $\delta_{zmax}=0.125$, resulting in a $\sigma_z=0.0557$. Eliminating this high z estimate from the sample reduced $\sigma_z=0.0018$, comparable with the other classification methods. Both automated 4000 Å & 3500 Å ranges failed to classify iPTF15dln, which was manually identified as a galaxy.

The SNID estimates of z from all successful manual 4000 Å classifications were compared with the automatic methods. Both automatic classification methods showed a large $\delta_z > 0.120$ for 3 sources, iPTF15ffz, iPTF15fhl & iPTF15fhp, when compared to manual 4000 Å classification. These 3 sources are part of the group with low SNR < 5.0 spectra. Including these 3 spectra with low SNR the automated 4000 Å z resulted in $\sigma_z=0.0535$ and for the 3500 Å range a $\sigma_z=0.0606$. Excluding the 3 low SNR spectra from the automated 4000 Å sample reduced $\sigma_z=0.0020$. For the automated 3500 Å range it remains high, $\sigma_z=0.0332$, because of a remaining over-estimation of iPTF15dnh. The accuracy in estimating z and age is summarised in Table 5.4.

The 3500 Å range failed to classify high SNR > 5.0 objects iPTF15dkk, iPTF15dkn & iPTF15dni that were successfully identified by the automatic 4000 Å ranges.

SNID estimates the age in days of a SNe relative to the maximum peak optical luminosity with a typical accuracy $\sigma_t < 3$ days (Blondin & Tonry, 2007). Figure 5.7 compares the estimated ages for GW objects. The variation in age of the manual method was compared with the 2 automatic methods in a similar manner to redshifts.

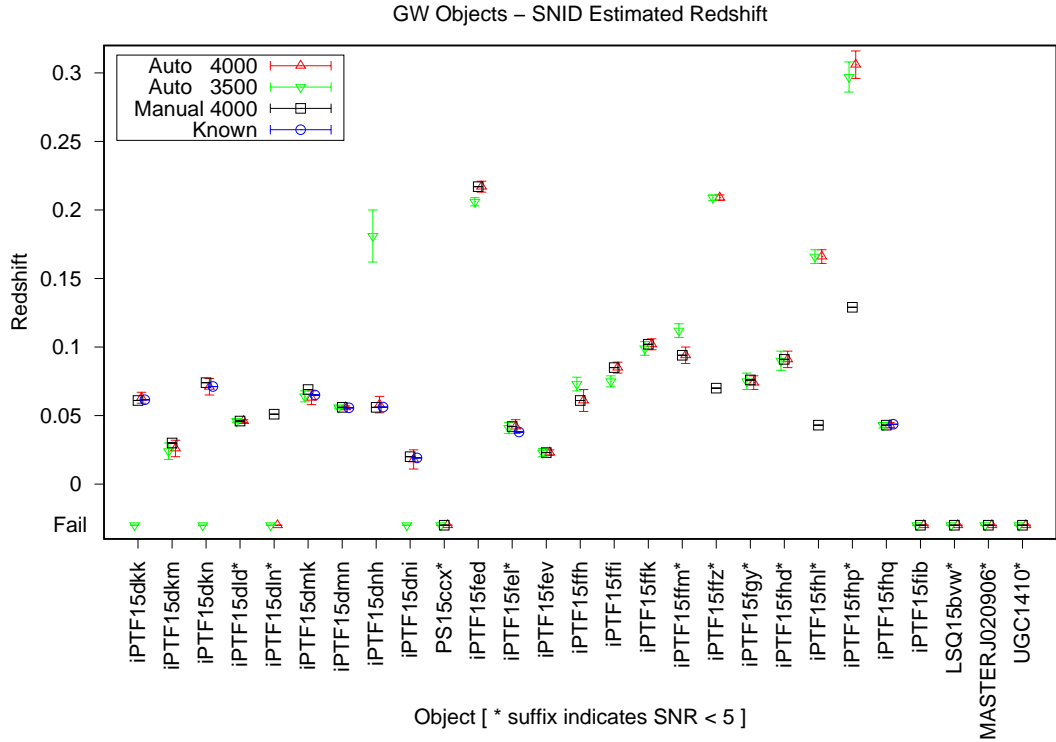


Figure 5.6: The SNID estimated redshift for manually classified objects compared with automated classification at full 4000 Å and reduced 3500 Å wavelength range. All reference redshifts, blue circles, were derived either from nearest host galaxy z , or NED and SIMBAD databases with the exception of IPTF15fel which as obtained from ATel # 8498.

The s.d. of the difference between reference manual and automatic derived ages, σ_t , was calculated, Figure 5.7.

The automatic 4000 Å method has $\sigma_t=2.9$ days, maximum difference, $\delta_{tmax}=8$ days and included 7 ages which match manual classification. This method selected 4 template spectra which match manual classification method. For the automatic 3500 Å $\sigma_t=7.5$ days and a $\delta_{tmax}=17$ days and with only 2 matching the age of manually selected spectra.

There is a general trend in overestimating age by a mean of 4.7 days.

There was no commonality in the type the 4 objects with over-estimated z , which comprised two galaxies, one Ia SN and a possible Ib/c.

Method	Reference	All Spectra		SNR > 5.0
	σ_{zref}	σ_z	σ_t [days]	σ_t [days]
Manual 4000	0.0020			
Auto 4000	0.0019	0.0535	2.9	0.0020
Auto 3500	0.0018	0.0606	17.5	0.0332

Table 5.4: Comparison of SNID redshift and SN age estimation. σ_{zref} is the s.d. when compared against redshifts from 8 external reference sources. All Spectra columns, σ_z and σ_t , are the s.d. of the automated estimates of z and object age against those derived via manual classification. The final columns shows the improvement in age estimation when by eliminating spectra with SNR < 5.0.

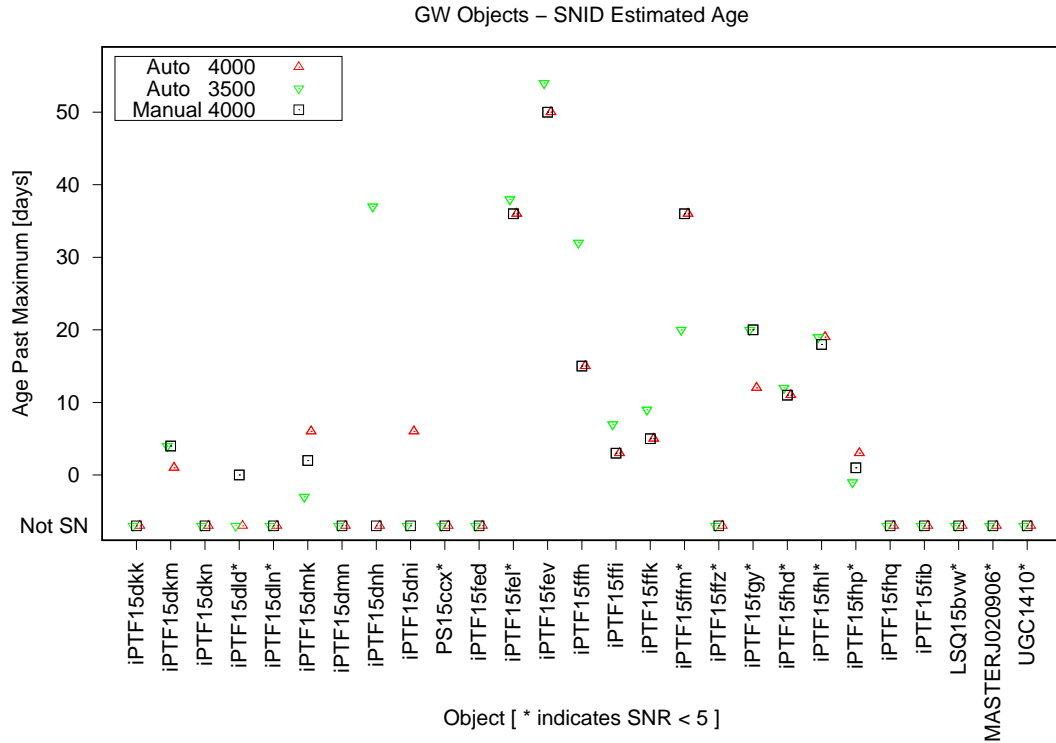


Figure 5.7: The SNID estimated ages relative to day of maximum luminosity are compared between manual and automated classification. Compared with the automated 4000 Å the 3500 Å range over-estimates age by an average of 4.7 days.

5.4 Conclusions

Although the GW sample set is smaller than that used for the classification programme (Section 4.4) it is more representative of random transient. The classification programme preferentially selected objects flagged as possible SNe in alerting sources.

Both automated methods rejected the 4 failed samples correctly.

Limiting wavelength range to 3500 Å reduced noise for spectra with $\text{SNR} < 5.0$ resulted in a only a small, 0.59, improvement in SNR. It produced 5 additional classification failures compared to the manual method and introduced a mean bias of +4.7 days in the estimation of an object age. The mean error in estimating redshift z remained the highest, $\delta_z=0.004$, after removing all z over-estimates. There was no advantage in using this restricted 3500 Å wavelength range for automated classification.

The automated 4000 Å range produced 2 additional classification failures compared to the manual method. For spectra with $\text{SNR} > 5.0$ redshift estimation matched manual classification to ~ 0.0020 even for when the object type differ. However the maximum error was, $\delta_{zmax}=0.180$, when all low SNR spectra were included. For reliability in automatic classification input spectra should be selected to eliminate those with $\text{SNR} < 5.0$.

Of the total 27 objects, 13 were manually classified as some type of SN. Both automated wavelength ranges only generated 1 false positive and 1 false negative SNe classification. This represent a suitable method to filter SN observations irrespective of SNR and thus exclude them as potential EM counterparts to GW events.

Chapter 6

Conclusions

6.1 Summary of SPRAT performance

The instrument has been in use since it formally became available for observation on the LT in January 2015. We described the commissioning and characterisation in Chapter 3 and present here a summary of SPRAT performance characteristics.

The plate scale is $0.438 \text{ arcsec pixel}^{-1}$ giving a field of view in imaging mode of $1.85 \times 7.5 \text{ arcmin}$.

Mean dispersions in red mode is $4.55 \text{ \AA pixel}^{-1}$, and in the blue mode is $4.58 \text{ \AA pixel}^{-1}$. The resolving power at the central wavelength $R_{6000} = 307$ at the average operating temperature $T_{286} = 286 \text{ K}$. This is lower than the original design goal of $R=350$ but has been sufficient for transient classification programmes. The adjustable slit would allow the resolving power to be increased in the future if necessary. The slit width at T_{286} is 4.3 pixels (1.9 arcsec) and varies with temperature at rate $-0.014 \text{ pixel K}^{-1}$. This produced a change in $\Delta R = 10$ over the sampled temperature range 276 – 296 K.

The full wavelength range $\lambda = 4020 - 8170 \text{ \AA}$ meets the design requirement. Note that L2 pipeline truncates the range to 4020 – 8004 Å and performs a $2 \times$ binning reducing

the resolving power to $R_{6000} \approx 150$.

Peak red mode throughput is 0.35 at $\lambda = 6450 \text{ \AA}$, 27% lower than predicted. Peak blue mode throughput is 0.29 at $\lambda = 5250 \text{ \AA}$, 45% again lower than predicted. The throughputs are below those predicted as described in Chapter 2. Although lower than expected the sensitivity was sufficient for classification of SNe down to transients with alerting magnitude $m = 19.9$, achieved with an exposure time of 1800s.

The focus has proven thermally stable with negligible gravity vector induced defocus. The slit image remains stable during an observation with a typical shift of 0.07 pixels ($= 0.3 \text{ \AA}$).

The thermal stability of the Y axis is $-0.067 \text{ pixel K}^{-1}$ ($0.030 \text{ arcsec}^{-1}$). The thermal stability of the X axis is lower at $-0.039 \text{ pixel K}^{-1}$ ($0.017 \text{ arcsec}^{-1}$). The X-axis stability is additionally affected by a bimodal “flip”, assumed to be mechanical, of ~ 0.4 pixels (0.18 arcsec).

Since commissioning the optimal magic pixel X-coordinate appears to have drifted by 1 pixel to X=178. As accurate placement of the target in the slit centre is important to avoid obscuration, further investigation is warranted.

6.2 Summary of Supernova Characterisation Results

A transient classification programme ran from January 2015 to August 2016 in collaboration with Gaia Photometric Science Alerts (Prusti, 2012) with the aim of classifying Gaia alert objects. The pattern of Gaia alert publishing was episodic (Figure 4.7) and so ASAS-SN and Pan-STARRS were used when no Gaia alerts were available. A total of 180 individual observations of 155 transient alert objects were made, 43 of which we identified and published via a classification ATel. Table 6.1 summarises the classifications with detailed information available in Appendix F.

Table 6.1: Summary of Transient Classification Programme

Source	Ia	Ib/c	II	Other	Unknown
Gaia	16	2	6	6	15
ASAS-SN	28	1	2	4	11
TNS	23	1	1	2	3
Pan-STARRS	4	0	5	2	4
KISS	3	1	2	0	0
Other	6	2	2	0	3

The spectra acquired were used in optimising SNID parameters for classifying SNe in the same groups as in Table 6.1. SNID template releases 0 & 2 and supplementary Ib/c templates (Modjaz et al., 2014) were evaluated singly and combined in sets 0, 2, 0+bc and 2+bc. The criteria adopted for optimal identification of a SN was a maximum number of true positive matches should be found with a minimum number of false positives. To explore the effect of modifying SNID default parameters, a semi-automated pipeline was constructed.

The default SNID parameters are well configured as it was found that for general classification of any SN the defaults using templates 2+bc with the full spectrum performed best. This also applies if Ib/c are the desired type.

If attempting to reliably classify only type Ia, symmetrically truncating the spectrum to 3400 Å wide is optimal.

In the case where the redshift z is known and only type II SNe are to be identified then using template 2 and symmetrically truncating spectrum to 3400 Å is optimal. If z is not known and only type II SNe are to be identified then using template set 0 and symmetrically truncating spectrum to 3400 Å is optimal. Setting `rlap = 6.0` produced a small improvement in the correct identification of type II SNe.

6.3 Summary of GW results

The LT with SPRAT followed up on 3 aLIGO gravity wave alerts GW150914, G194575 and GW151266 in a search for optical counterparts and several SNe. Of particular interest was the unusual iPTF-15ddd, a low luminosity broad-line Ic SN (Pian et al., 2017).

GW events provided an opportunity to evaluate the reliability of automated classification using SNID. The 27 GW transients candidates represented a typical selection of faint transient types with magnitudes to $m_z=20$ and low SNR <5 . Automated classification with restricted wavelength to reduce noise produced an excess of 5 failures over the manual classification. Re-running with the full 4000 Å range was more successful with only 2 excess failures but still worse than manual. Automated classification does not appear to offer greater reliability for faint, low SNR samples. However it only generated 1 false positive and 1 false negative so may be useful in pre-filtering spectra to exclude SNe.

6.4 Future Work

The SPRAT spectrograph was followed by a second low-resolution ($R \sim 330$) spectrograph, LOTUS (Steele et al., 2016), employing a similar design philosophy and which operates in the UV-optical, 3200-6300 Å. Originally intended specifically to monitor the post perihelion behaviour of 67P/Churyumov-Gerasimenko, LOTUS is used to provide UV spectra for other objects. Presented here are the criteria for combining and extending the spectrograph designs to produce a generic core instrument that can be tailored to a particular science use on telescopes with primary apertures of 1.5m – 3.0m. This work was published in Piascik & Steele (2016).

Since the principal criterion for any instrument design should be science led we use

the examples of SPRAT and LOTUS (which arose to meet two different observational needs) to define a common core for modular design that must at least be able to satisfy those. We also discuss possible extensions based on other science use cases.

6.4.1 Observational Criteria

The following three principal criteria are identified in the specification of an optical long-slit spectrograph:

1. **Wavelength Range.** This can be defined as the start and end wavelength obtainable in a single exposure. However we note that spectrograph designs with control over the grating angle and/or grating pitch can often access a wider range than they can obtain in a single exposure.
2. **Resolving Power.** This is usually defined in terms of $R = \lambda/\Delta\lambda$ where λ is the centre of the observed wavelength range and $\Delta\lambda$ the minimum resolvable separation between two spectral lines.
3. **Slit Length.** This is usually defined in arcseconds projected on the sky.

We shall consider each of these in turn.

Wavelength Range

The selection of the appropriate wavelength range is governed by the object to be observed. For ground based optical astronomy observation the lowest wavelength is limited by the atmospheric cut-off in the UV to $\sim 3200 \text{ \AA}$ and beyond 9000 \AA absorption by water vapour bands becomes significant. In general only a subset of the lines shown can be observed and must be selected as appropriate for the target type. For a non-cross dispersed single beam spectrograph order overlap will limit the wavelength

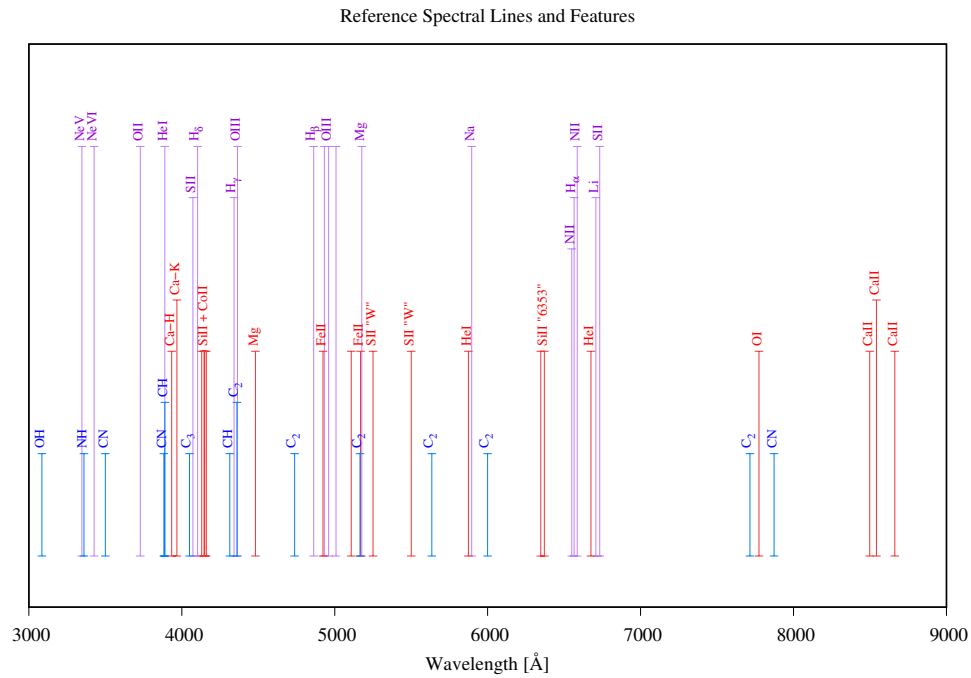


Figure 6.1: The possible spectral range in the optical from which a sub-range can be selected for a final instrument. The upper (violet) lines are from the SDSS reference list which includes H, He and metals. The center (red) are lines and features significant for differentiating supernovae types. The lower (blue) lines show cometary molecular species which predominate towards the blue/UV.

range to one octave. For example, if we wish to observe down to the UV cutoff at 3200 Å our maximum wavelength will be 6400 Å. Figure 6.1 shows the reference lines from the Sloan Deep Sky Survey (SDSS) together with additional lines for SN identification and classification and a set related to cometary molecular emission lines.

Taking first the example of transient classification, our experience with SPRAT is useful here. A prime use of the SPRAT spectrograph is for the classification of transient objects such as AGN, novae and supernovae (SNe) and cataclysmic variables (CV). The universal prevalence of hydrogen means that for all of these objects a classification instrument must include the principal Balmer H_α , H_β , H_γ lines (6563Å, 4861Å, 4341Å) down to H_γ (4102Å) in the blue. Various metallic lines are also of value. In novae Fe II and O II lines are frequently observed and can further help define the useful wavelength range. The spectral classification of SNe is based on the presence or

absence of H, He or Si lines (Figure 4.1). This defines a minimum wavelength range for differentiating SN type.

In particular we investigated the effect of progressively reducing the spectral width symmetrically about the central wavelength 6000 Å for objects of different SNR.

Turning to the case of observations of comets, they are composed primarily of water-ice together with dust and simple low molecular weight compounds such methane, ammonia and carbon dioxide. As it approaches the Sun these volatiles undergo sublimation taking dust with them to form the characteristic coma. At UV-optical wavelengths, cometary spectra are characterised by emission from the dissociated molecular species formed by the photo-dissociation and photo-ionisation of volatiles e.g. OH, NH, CH, CH and carbon C₂, C₃. The emission lines are observable from the UV limit to mid-optical, 3200-6000 Å with weaker lines C₂ and CN lines in the IR, (Figure 6.1).

Two other examples of optical spectroscopy that we might consider are associated with classical stellar classification on the Morgan & Keenan system (Morgan et al., 1943) where a wavelength range stretching from Ca II K to H_β ($\sim 3800 - 4600$ Å) is usually employed. For extension to cooler objects, where, for example molecular band species in the near-infrared dominate (Kirkpatrick et al., 1999), a range from 6000-9000 Å is generally used.

Wavelength Resolution

We now consider the wavelength resolution needed for various science cases. For supernovae, the high velocities mean that all features are heavily broadened, with typical expansion velocities in the range $\sim 5000 - 15,000$ km/s. Spectral resolving power of as little as $R \sim 100$ have therefore been used to efficiently classify these objects (Ben-Ami et al., 2012). For novae typical velocities are in the range 1,500 - 4,000 km/s, implying $R \sim 200$ is the absolute minimum required to begin to resolve line

widths. For AGN line widths (Peterson, 2006) are typically ~ 350 km/s in the narrow line region. In the broad line region they can vary between ~ 500 to $\sim 30,000$ km/s with a typical velocity of ~ 5000 km/s. This implies that for AGN (Seyfert 1 vs 2) typing a resolving power of $R \sim 850$ is required.

For comets, since the principal features are molecular bands, low resolving power is appropriate. For LOTUS, the science team determined that a resolving power $R \sim 300$ was appropriate, corresponding to a velocity resolution of ~ 1000 km/s.

Classical spectral typing of early type objects is typically carried out with spectra of resolving power $R \sim 2000$ (Gray et al., 2001). For later objects, where molecular bands dominate, a resolving power of $R \sim 500 - 1000$ is often used (Kirkpatrick et al., 1999). For observations of Doppler effects in close binary stars, similar resolving powers of around $R \sim 2500$ are often employed.

Slit Length

For many sources slit length is not an issue, as we are merely interested in obtaining a spectrum of a point source. However there are occasions either when the source itself is extended (e.g a comet or galaxy) or we wish to observe two objects simultaneously when slit length is critical.

As an example in taking the spectrum of a SN associated with a galaxy without a known red-shift, z , we have shown in Chapter 4 that the classification accuracy can be improved if we simultaneously acquire a spectrum of the host to obtain even an approximate value for z . From the sample of 112 supernovae with identifiable host galaxies observed by SPRAT, we therefore obtained the angular distance to the centre of the host using the NASA Extragalactic Database (NED) (Figure 6.2). The largest observed separation was 44 arcsec which suggests a minimum slit length of ~ 50 arcsec is needed for simultaneous observations of supernovae with the core of their

host galaxies.

Although comets can present a large apparent size, up to several arcminutes, a slit length of 90 arcsec is sufficient to sample the coma for the majority of comets (Steele et al., 2016).

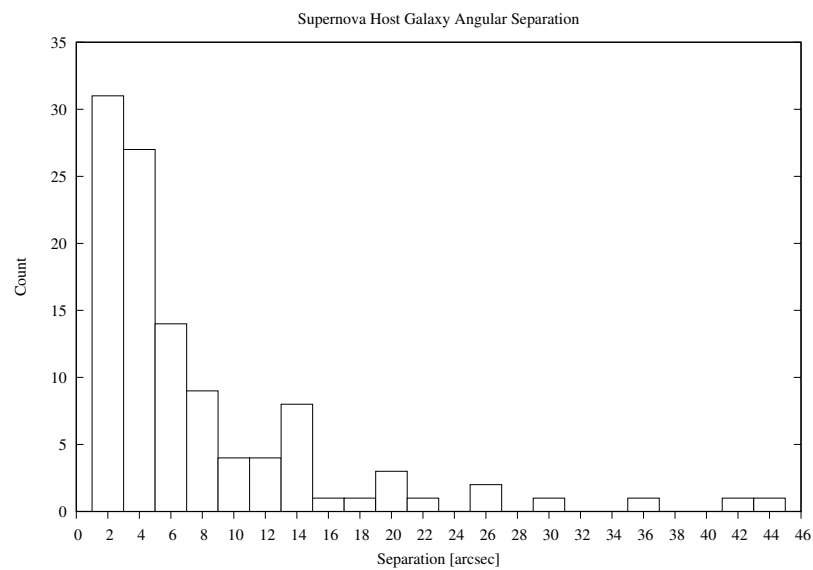


Figure 6.2: Angular separation between for 112 SN observed using SPRAT showing that >50% of SN were within 4 arcsec of the host galaxy. The largest observed separation being 44 arcsec, less than half the slit length limit set by the requirements for observation of comet coma.

In observing rapidly variable sources (such as binary and exoplanet systems) it is often advantageous to place a comparison star in the slit along with the science target to provide a comparison spectrum that can correct for slit losses under the same atmospheric conditions. Figure 6.3 shows the average number of stars above a certain magnitude at 4 different radii around a central star (Allen, 1973). For objects with $V \sim 15$ a slit length of at least 2.5 arcmin is required to have reasonable confidence that a comparison star will be available.

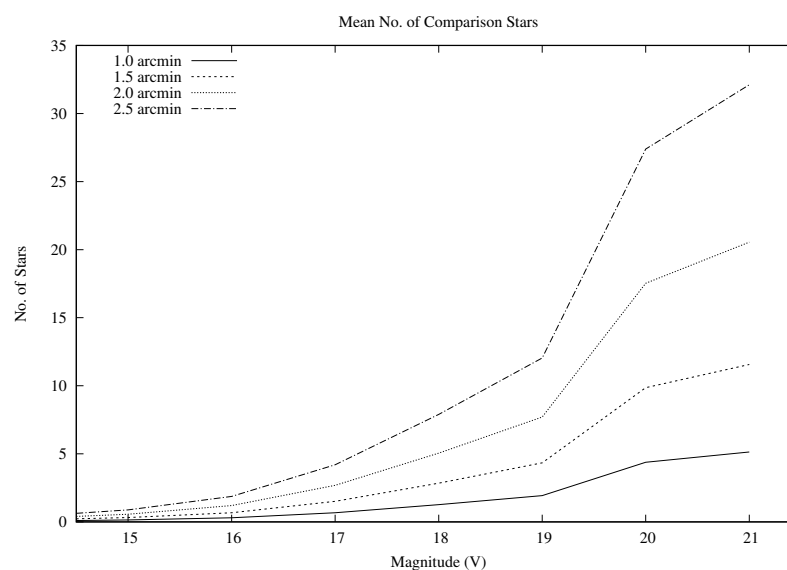


Figure 6.3: The average number of stars above a visible magnitude within a fixed radius of a central star. This is an all sky mean and does not take account of the higher density of stars in the galactic plane.

6.4.2 Design Implications

Slit Width

The key decision in the design of a long slit spectrograph is the width of the slit to be employed. For example this simple parameter affects ease of acquisition, spectral resolving power, wavelength accuracy, sensitivity and spectrophotometric calibration. We shall briefly consider each of these in turn.

As a general rule, acquisition of the target star into the spectrograph slit will always be easier with a wider slit. For robotic telescopes, or for instruments where a simplified non-expert mode of operation is required a wider slit may be needed than a conventionally telescope under manual control where the pointing can be iteratively “tweaked” into position by the operator. For SPRAT on the robotic Liverpool Telescope we found that using a “self-acquisition” mode where the spectrographs own detector can also be used as the imaging camera, a slit width of 1.8-arcsec was needed. For LOTUS, where we have to use the main telescope imager for acquisition, this value increased to

2.5 arcsec. These are much wider values than those associated with a conventionally operated telescope which tend to be in the range 0.7 – 1.5 arcsec.

Slit width (or the size of the stellar seeing disk in the case of a wide slit) has a direct effect on the achieved spectral resolving power (Equation 1.16).

As well as affecting resolving power, slit width has an important influence on the attained wavelength accuracy. A wide slit will mean that the centroid of the seeing disk is poorly defined as the image could lie at a range of positions within the slit and still have the majority of its flux accepted.

The effect of slit width on sensitivity (i.e. signal-to-noise ratio) is complex. A wide slit will obviously ensure the full point spread function of the target source is recorded. However it will also increase the sky background proportional to the width. The optimal slit width is therefore of order the full width half maximum of the seeing disk.

Spectrophotometric accuracy is affected by the slit width in two ways. Firstly, a slit sufficiently wide enough to encompass the full point spread function is needed. However other than for objects located at zenith, the atmosphere has a prismatic effect on light from extraterrestrial sources. The degree of refraction at a particular wavelength is dependent on the altitude angle (Figure 6.4) and results in an wavelength dispersed, elongated image of the object within the slit (Filippenko, 1982). At low altitude angles the dispersed image can exceed the slit width leading to loss of flux at the extremes of the image. To eliminate this the slit is normally oriented so that atmospheric dispersion is along the slit (i.e. at the “parallactic angle”). However, if we wish to observe a pair of objects in the slit (as per Section 6.4.1) we can not use this approach. This implies that an even wider slit than first thought of may be needed. For targets at altitudes $>70^\circ$ the dispersion between 3200 and 9000 Å is <1 arcsec so with well centred targets two objects can be simultaneous observed. However at altitude 30° the spread over the range 4000-8000 Å (for example) is > 2 arcsec, adding a further requirement on slit

width.

In summary, there are many different possible trade offs to be considered in the selection of the optimal slit width. It is therefore clear that our generic design should have the capability to support many different widths. We also note a potential (partial) solution used in the LOTUS spectrograph where a stepped width slit (with sections of 2.5 and 5.0 arcsec width) was provided giving different options in operation.

Implications for Other Components

In designing a generic instrument we would ideally require the collimated beam width to be a fixed value as this defines the size of the dispersing element. This implies a collimator lens that has a focal length that scales in proportion to the telescope focal ratio. Similarly the physical slit size to obtain the same slit width on the sky will scale with telescope focal length. We would also prefer to use a standardized detector with a fixed size and pixel scale. This implies a camera lens focal length that also must change with the telescope and collimator focal length in order to achieve the desired linear dispersion on the detector.

From Equation (1) above we can see that the product of the projected slit width on the sky and the telescope ($\chi \times D$) is a constant for a given beam width and grating resolution. This implies a trade off between the two quantities, with a larger diameter telescope able to sustain a higher resolving power with a narrower slit. This is useful, as larger telescopes will often (but not exclusively) be on sites with better atmospheric seeing than smaller telescopes.

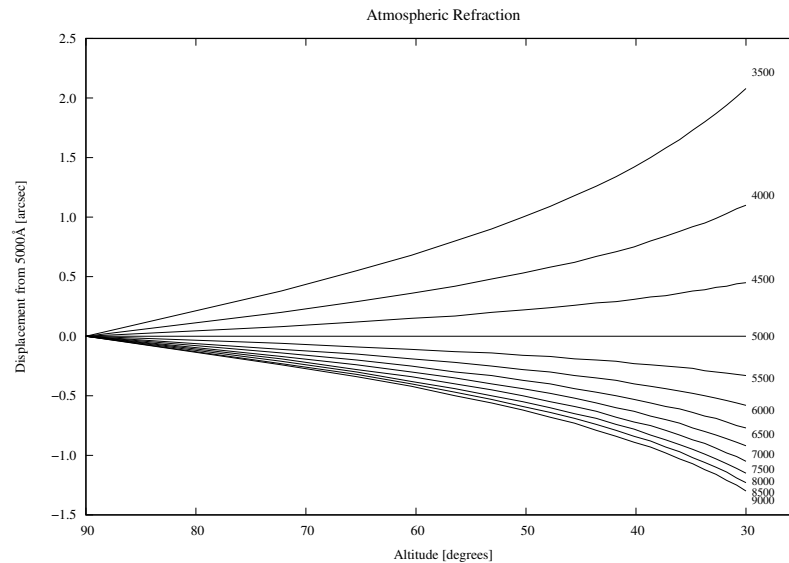


Figure 6.4: Angular displacement from a central wavelength of 5000 Å caused by atmospheric refraction.

6.4.3 Summary and Conclusions

We have carried out a basic exploration of the requirements for a simple, long slit spectrograph. We have considered the use cases of transient classification (supernovae, novae and AGN), spectral classification and observations of comets. A summary of the requirements is presented in Table 6.2. Taking this table at face value, the resolving power requirements identified range between $R \sim 100$ and $R \sim 2500$, the wavelength range is between 3200 and 9000 Å and the slit length between a few and 150 arcsec. Designing a single spectrograph that covers such a wide range of parameters would be very difficult. However it may be that the requirements can be grouped into relatively few groups (for example into “low” and “medium” resolution) and “long” and “short” slits) that may make the possibility of a modular generic design with a common optical core covering multiple science cases possible.

We have also briefly discussed the various trade offs that are necessary when designing such a spectrograph, particularly in the area of projected and physical slit width. Different science cases again will have very different requirements here. In particular

Table 6.2: Summary of spectrograph requirements for the different science use cases considered. Note that for supernovae and AGN we assume we are observing sources with redshift $z < 0.1$. This is a reasonable reflection of the redshift distribution of supernovae observed to date with SPRAT.

Use Case	Resolving Power R	Wavelength (\AA)	Slit Length (arcsec)
Supernova Classification	100–300	4250–7750	50
Supernova Physics	300+	3800–9700	any
Novae	200+	3800–6800	any
AGN Classification	850	3600–7700	any
Early Type Stellar Classification	2000	3800–4600	any
Late Type Stellar Classification	500–1000	6000–9000	any
Binaries	2500	3800–6800	150 arcsec
Comets	350	3200–6000	90 arcsec

requirements of sensitivity/resolving power and wavelength accuracy will have to be traded off with requirements for ease of acquisition and spectrophotometric calibration, especially in the case where we wish to use a long slit at non-parallactic angles.

6.5 Final Conclusion

In this thesis I have described the successful construction of SPRAT, a SPectrograph for the Rapid Analysis of Transients. By exploiting the availability of high-throughput volume phase holographic gratings SPRAT has been used to classify SNe down to $m_v \sim 19.5$ and potential EM counterparts to gravity waves down to $m_v \sim 20$ with exposures times < 30 minutes on a 2.0m telescope.

The instrument was both space and cost constrained and there are improvements that could be made with looser design restrictions which should be considered in any future implementation.

- Replacement the detector with the later version Andor iDUS 420 BVF deep-depletion CCD to reduce fringing in the red.

- Longer instrument envelope, $\sim 1\text{m}$, to eliminated the need for a field lens.
- Redesign of the grism exit and a larger camera lens to reduce vignetting.
- The addition of a filter into the optical path during imaging mode to obtain basic photometric observations during acquisition.
- Mounting the Arduino controlling the actuators on the instrument to improve operational reliability by eliminating connectors.
- More than one slit width. Either using a fixed notched slit or a motor driven adjustable slit.
- Elimination of the red/blue grism rotation mode as it was rarely used.

The linear optical path in SPRAT in either imaging or spectroscopic mode means that robotic acquisition onto a narrow 1.8 arcsec slit is possible without human intervention. In combination with the automated pipelining of spectroscopic data and optimisation in the use of the SNID classification tool.

I have shown the feasibility of construct a completely autonomous observation and classification system. Such a system will be crucial in the forthcoming transient deluge anticipated in the era of LSST, SKA and the full sensitivity aLIGO/Virgo expected to begin at the start of the next decade.

Appendices

Appendix A

Observing Programme Spectra

These SNID classification are of transients observed using the SPRAT spectrograph on LT taken during observing programmes from January 2015 to August 2016.

Prior to classification using SNID, cosmic rays were identified by visual inspection of the raw pre-pipelined spectrum and replaced in post-pipeline data by an approximate linear interpolation using adjacent data points.

The plots in black show the SNID flux corrected spectra with the closest automatic template match shown in red. Where a closer match was found by visual comparison of other SNID templates a blue plot is also shown. Where manual classification differs from all SNID suggested template matches, the type is marked as `Match=type` in blue. If a host galaxy redshift is known it is shown in black and used to override SNID estimated value using the `forcez` parameter.

Since the classification in red show the automated SNID best match it does not always correlated with externally determined classifications such as ATel. For example, `asassn-015-ua` was externally classified as `IIn` (ATel #8408, Masi et al), `asassn-15uu` as `Ia` (ATel #8480, Masi et al) and `ASASSN-16gf` as type `Ia` (ATel #9146, Fausnaugh et al).

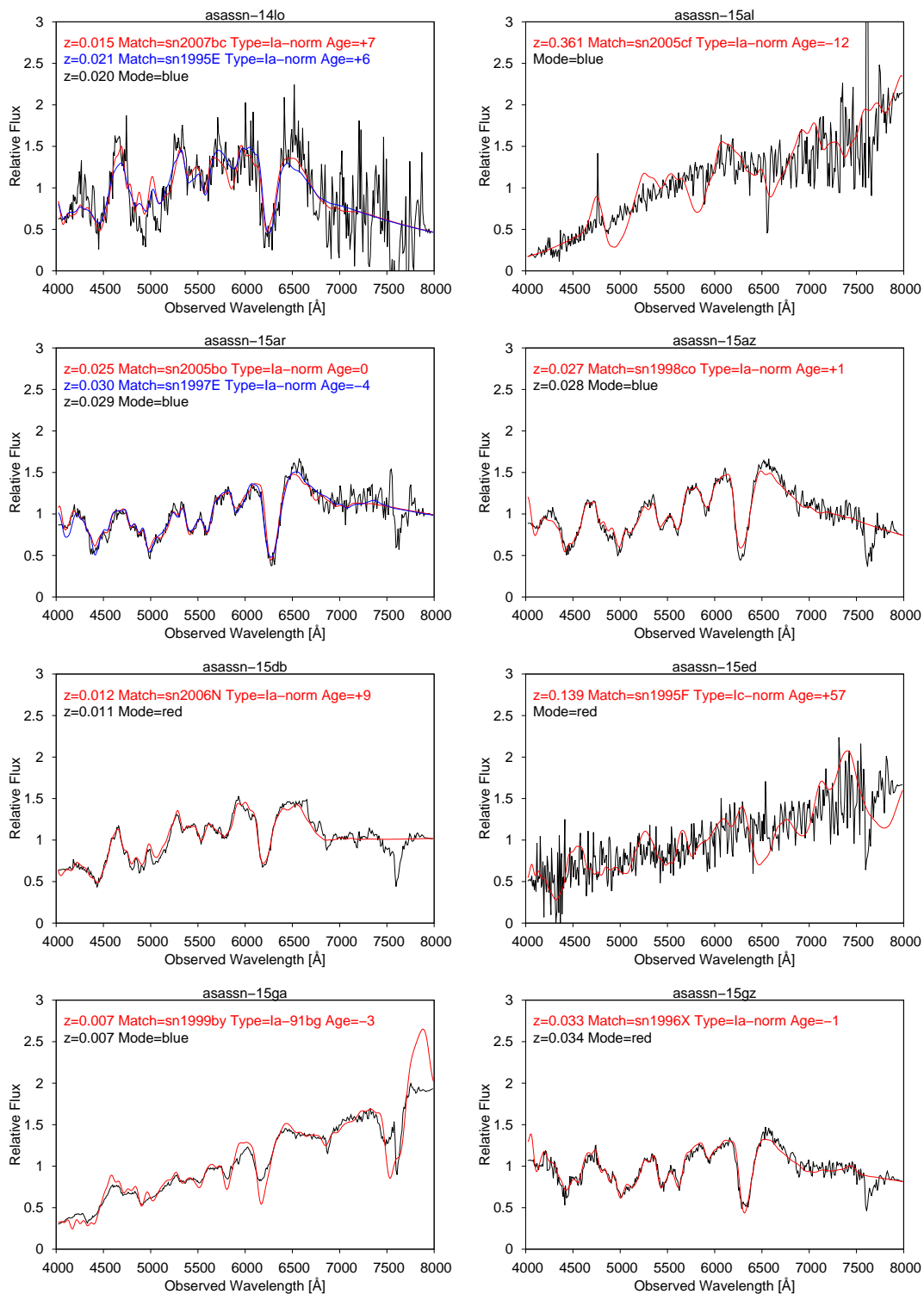


Figure A.1: ASAS-SN - 1

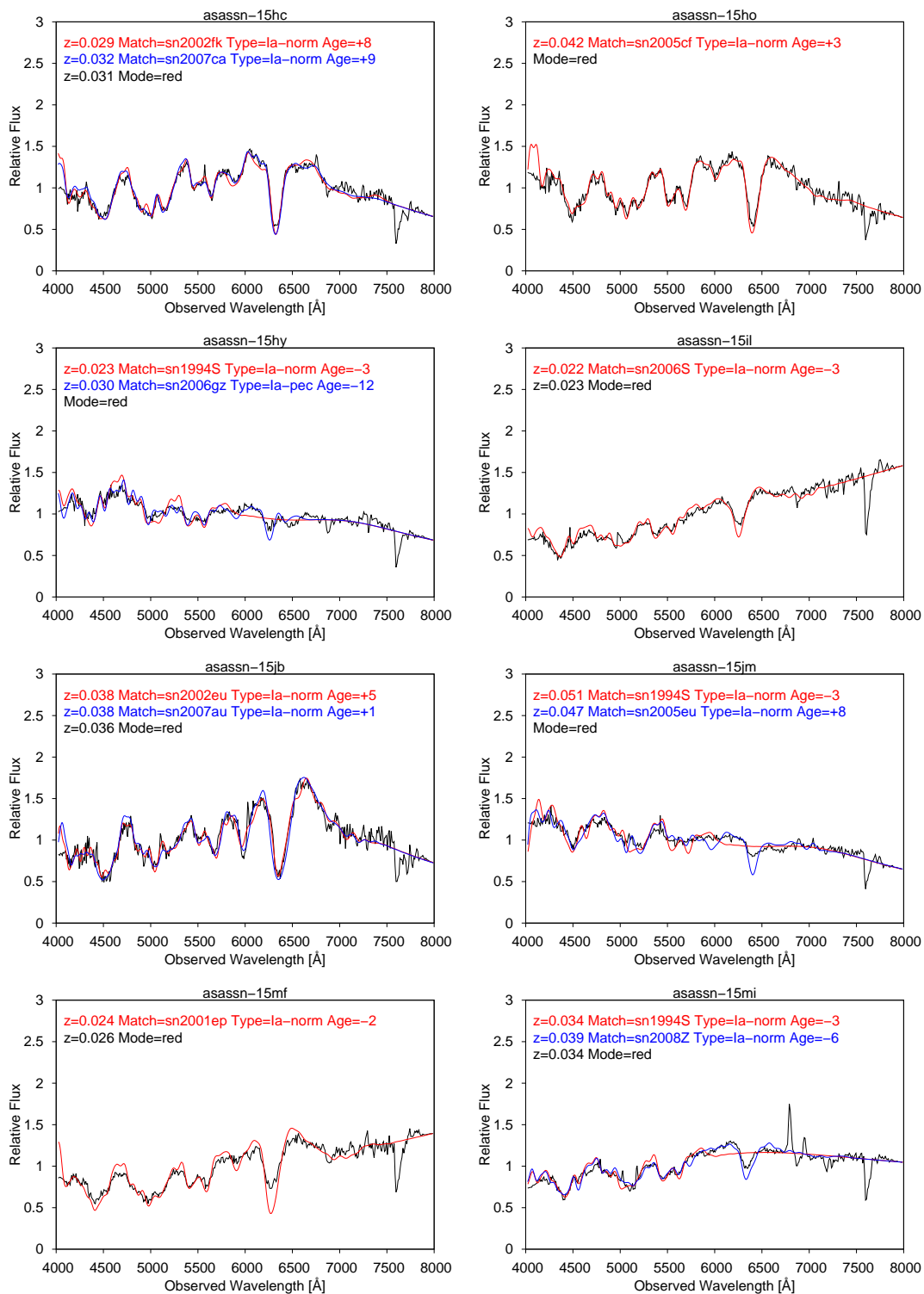


Figure A.2: ASAS-SN - 2

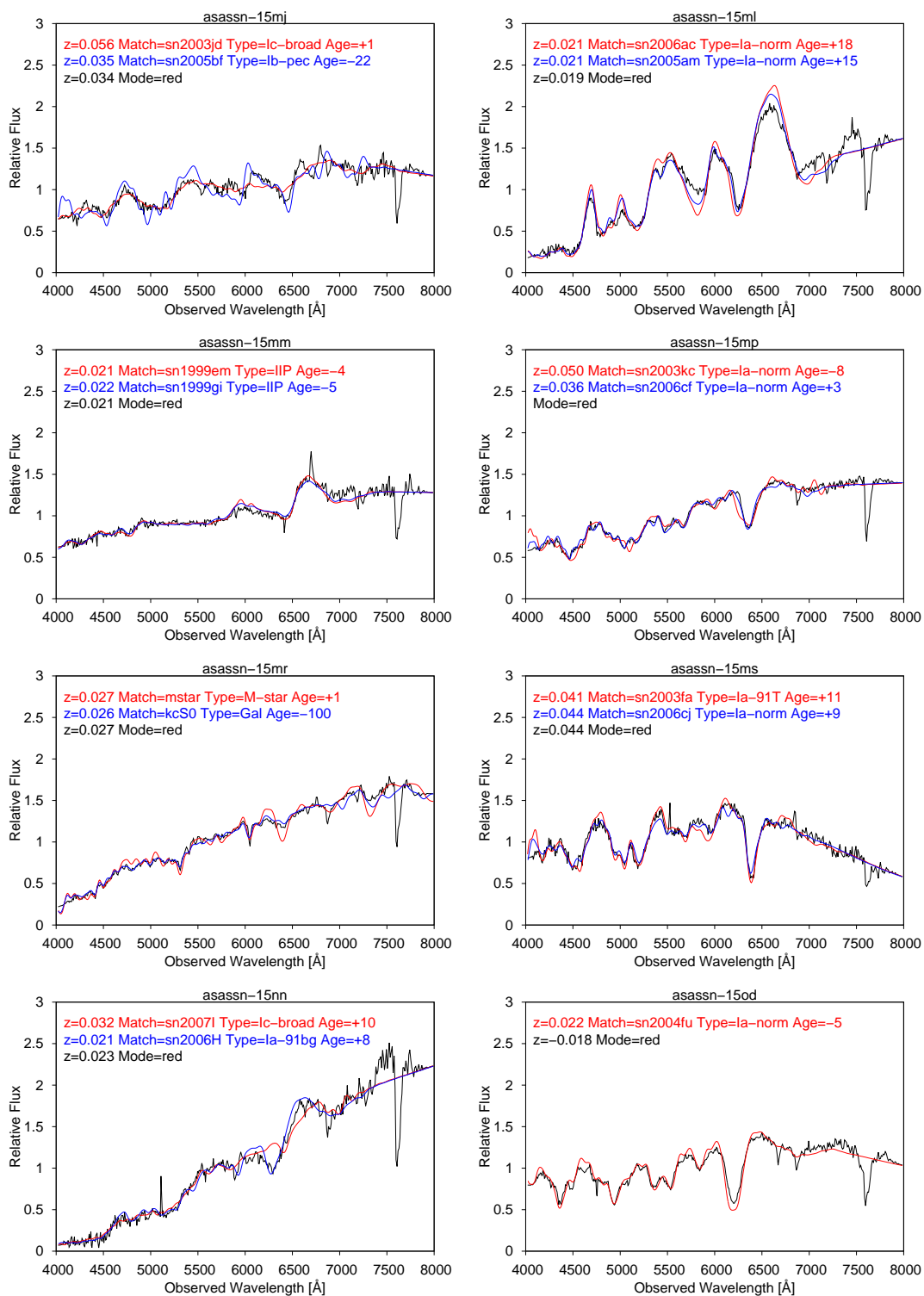


Figure A.3: ASAS-SN - 3

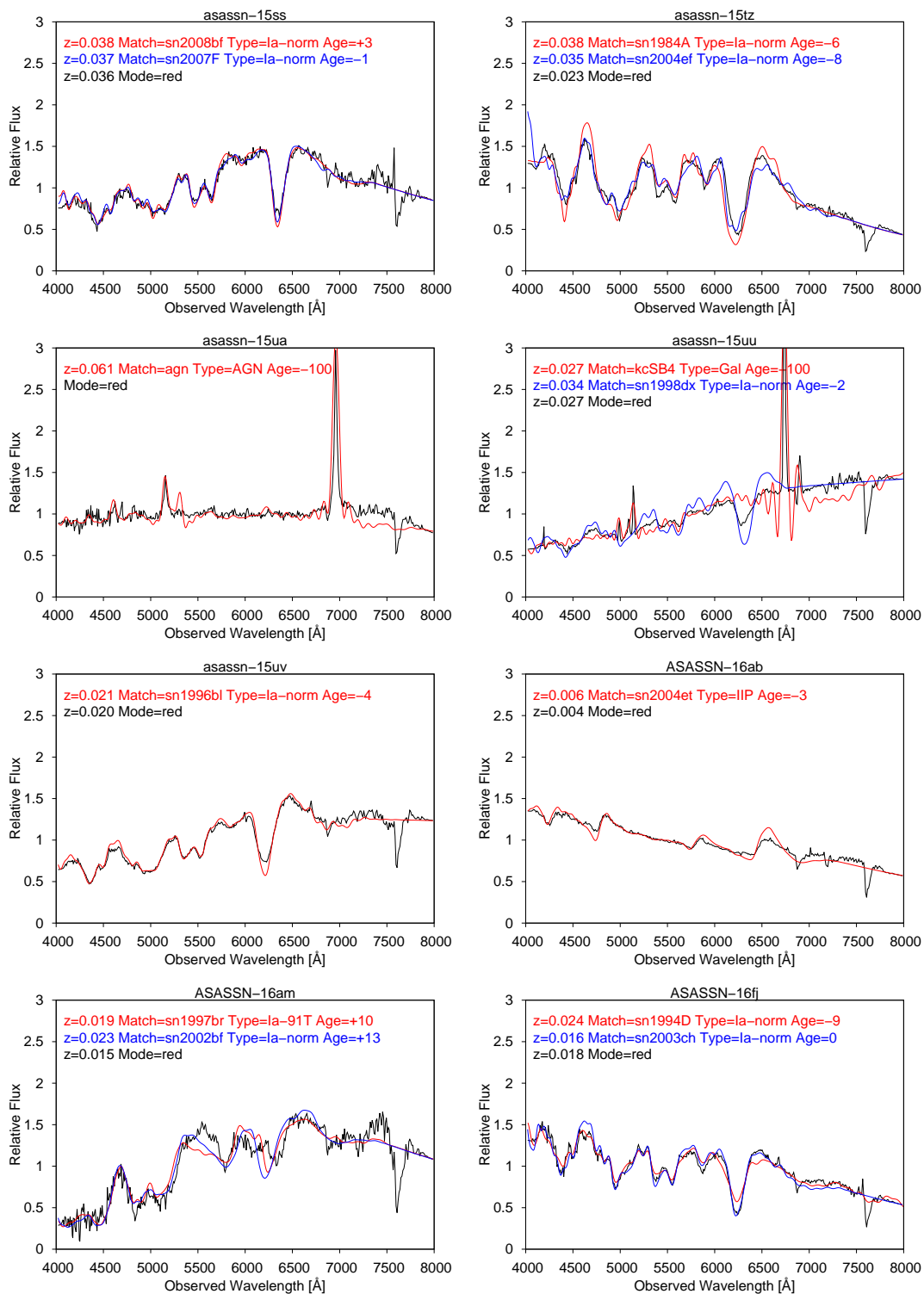


Figure A.4: ASAS-SN - 4

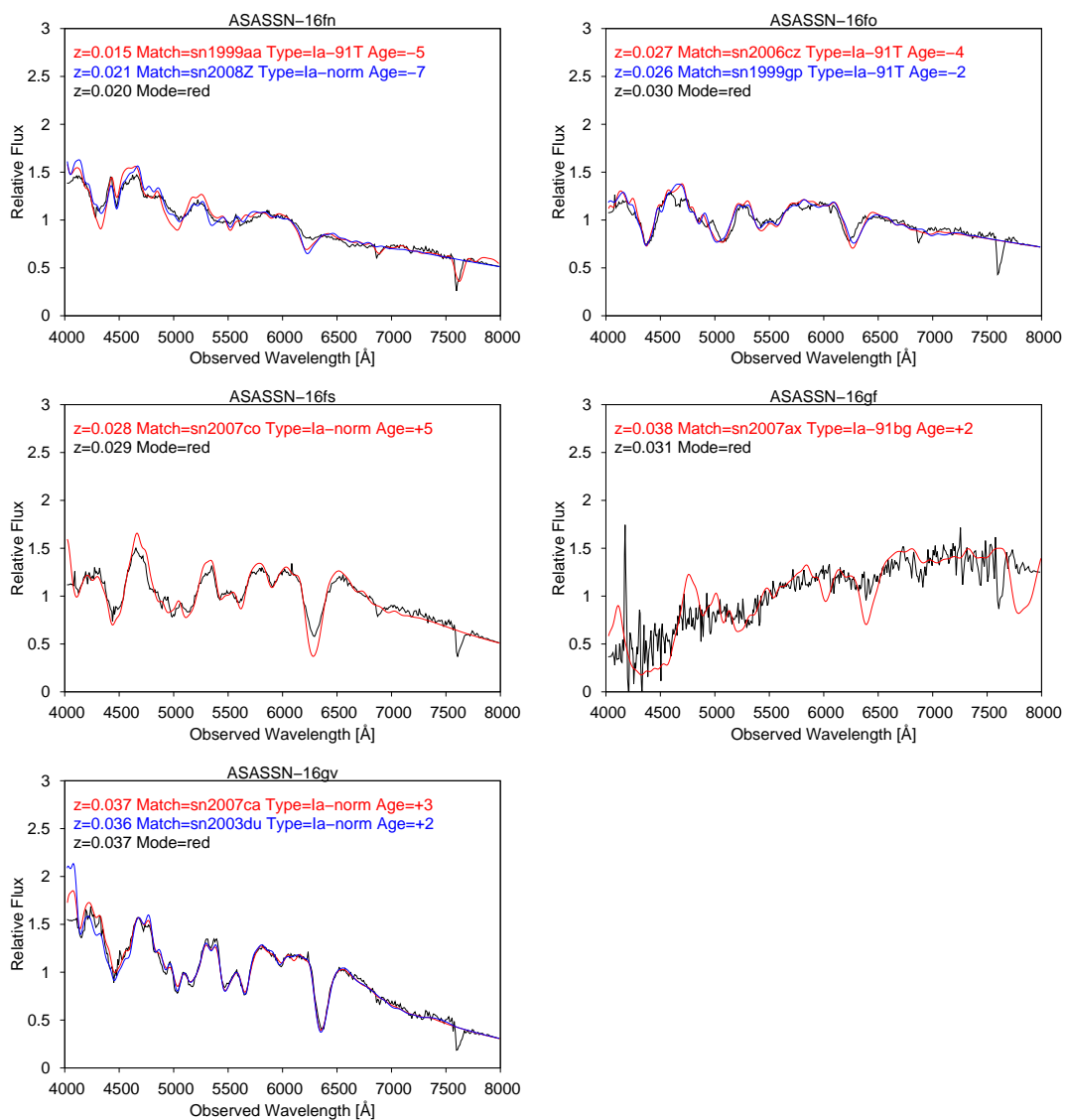


Figure A.5: ASAS-SN - 5

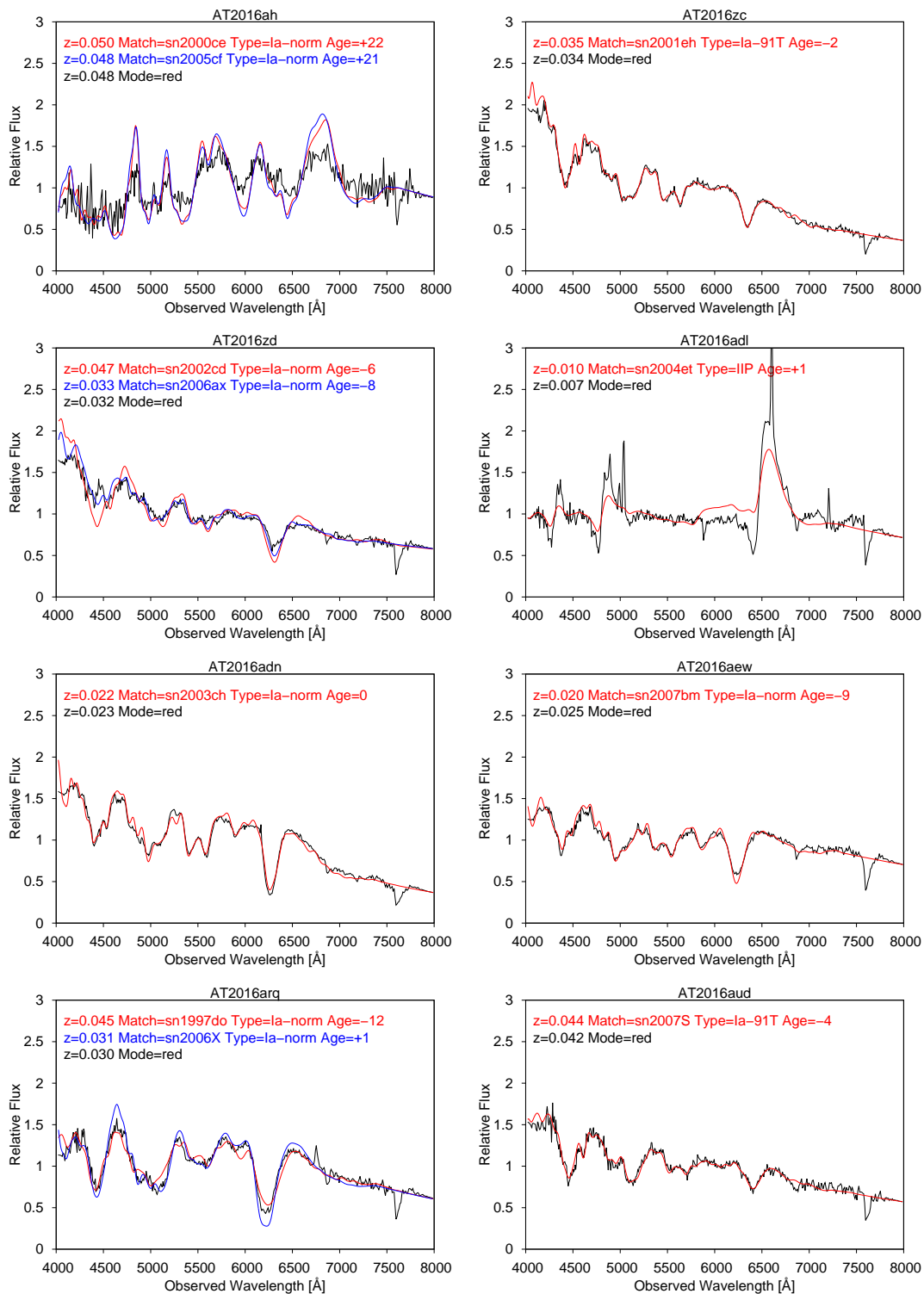


Figure A.6: TNS - 1

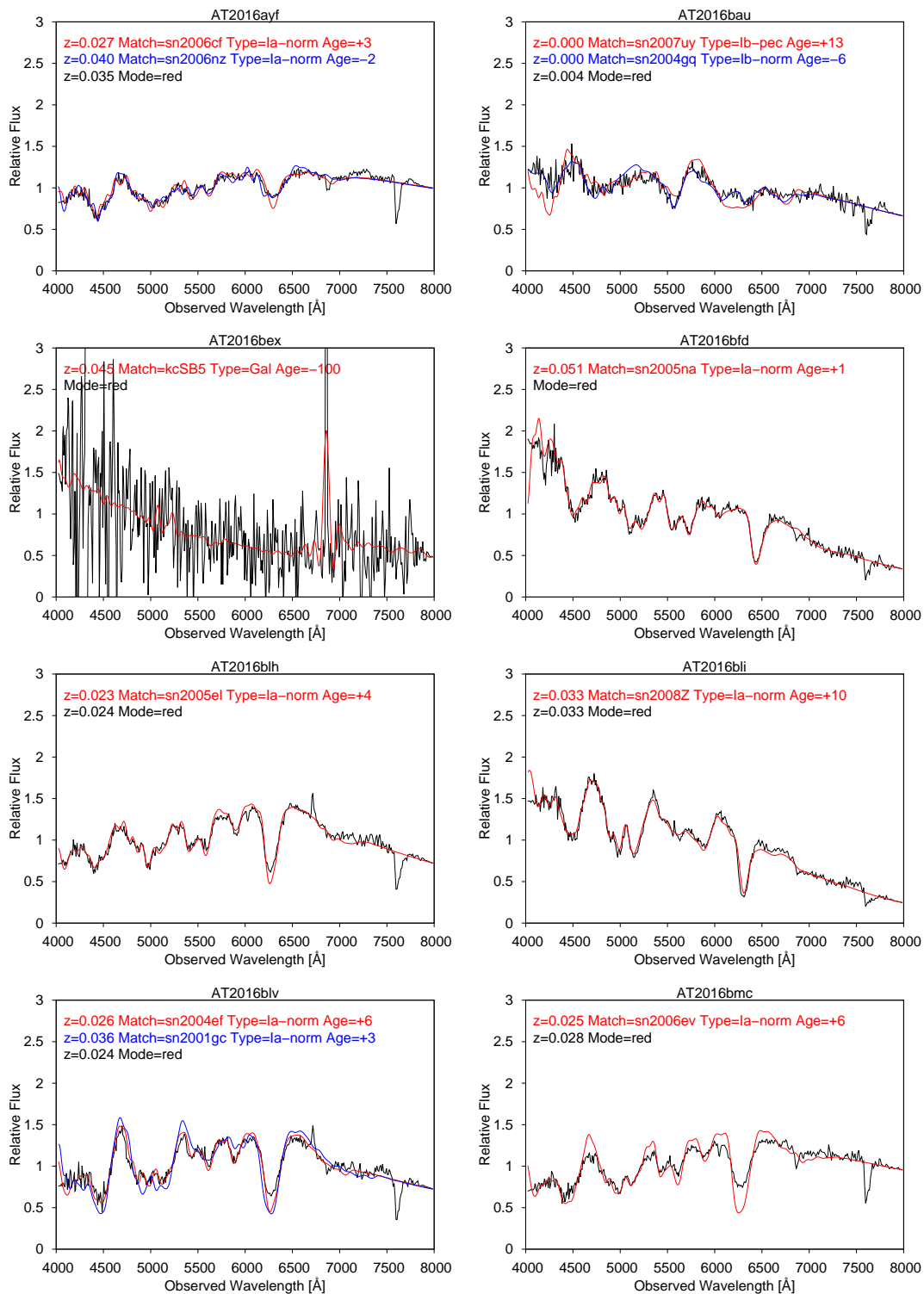


Figure A.7: TNS - 2

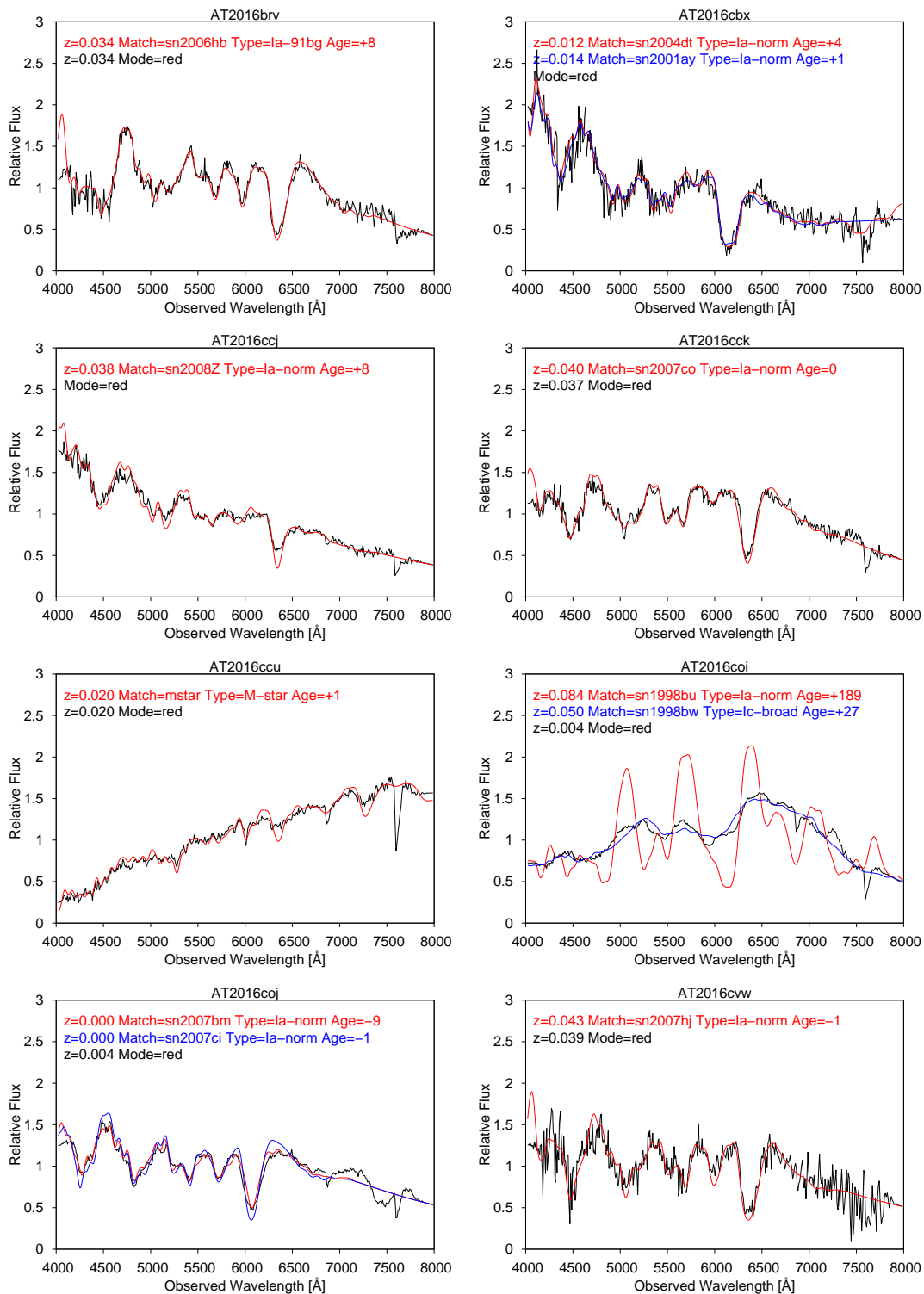


Figure A.8: TNS - 3

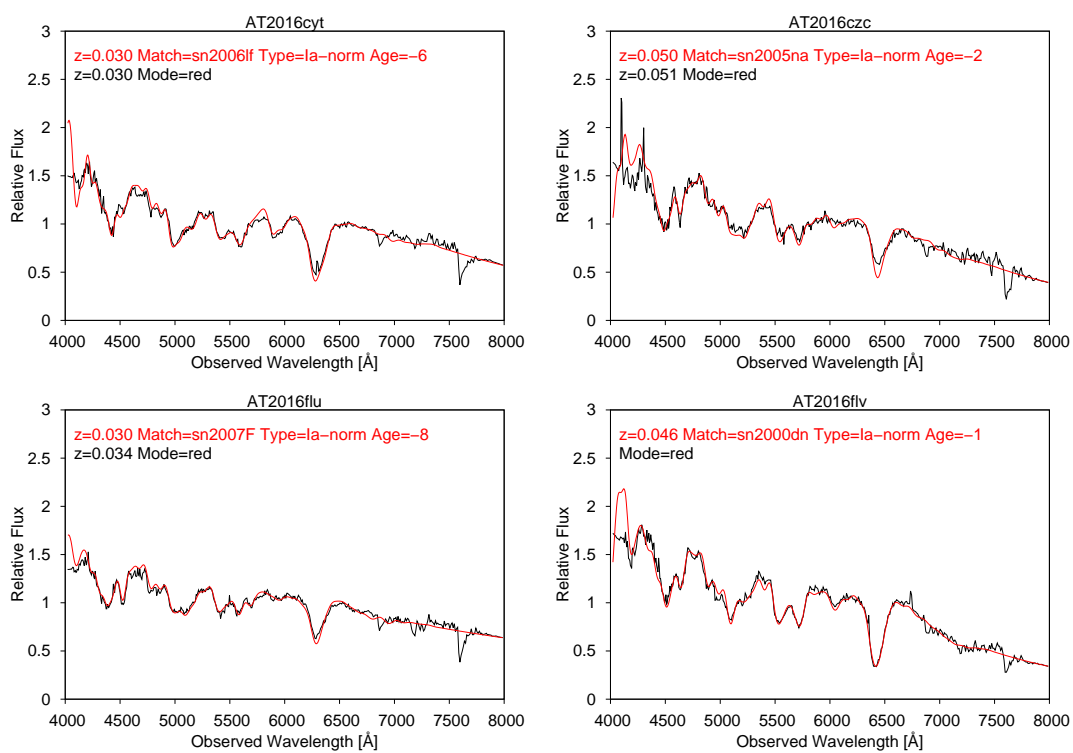


Figure A.9: TNS - 4

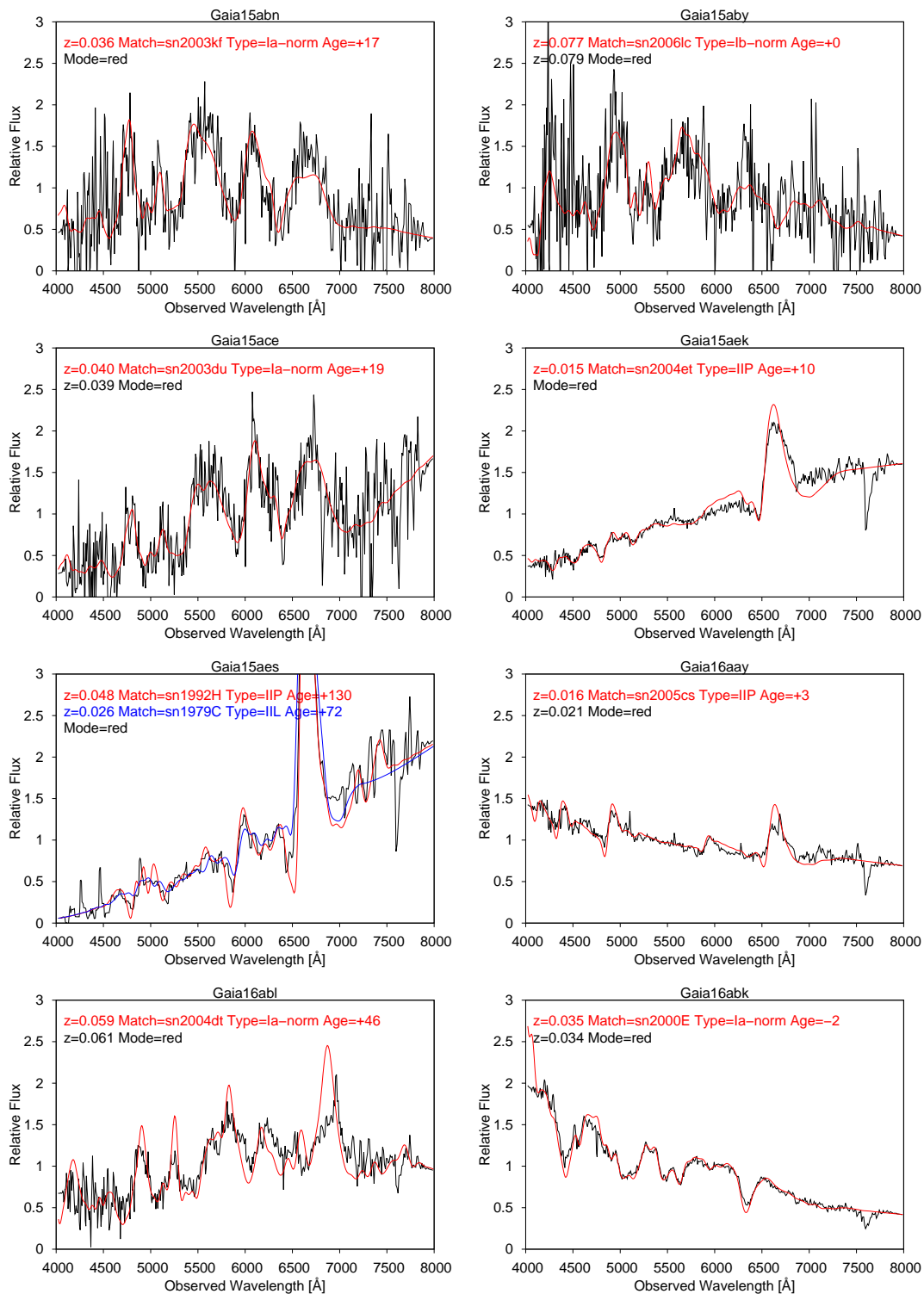


Figure A.10: Gaia - 1

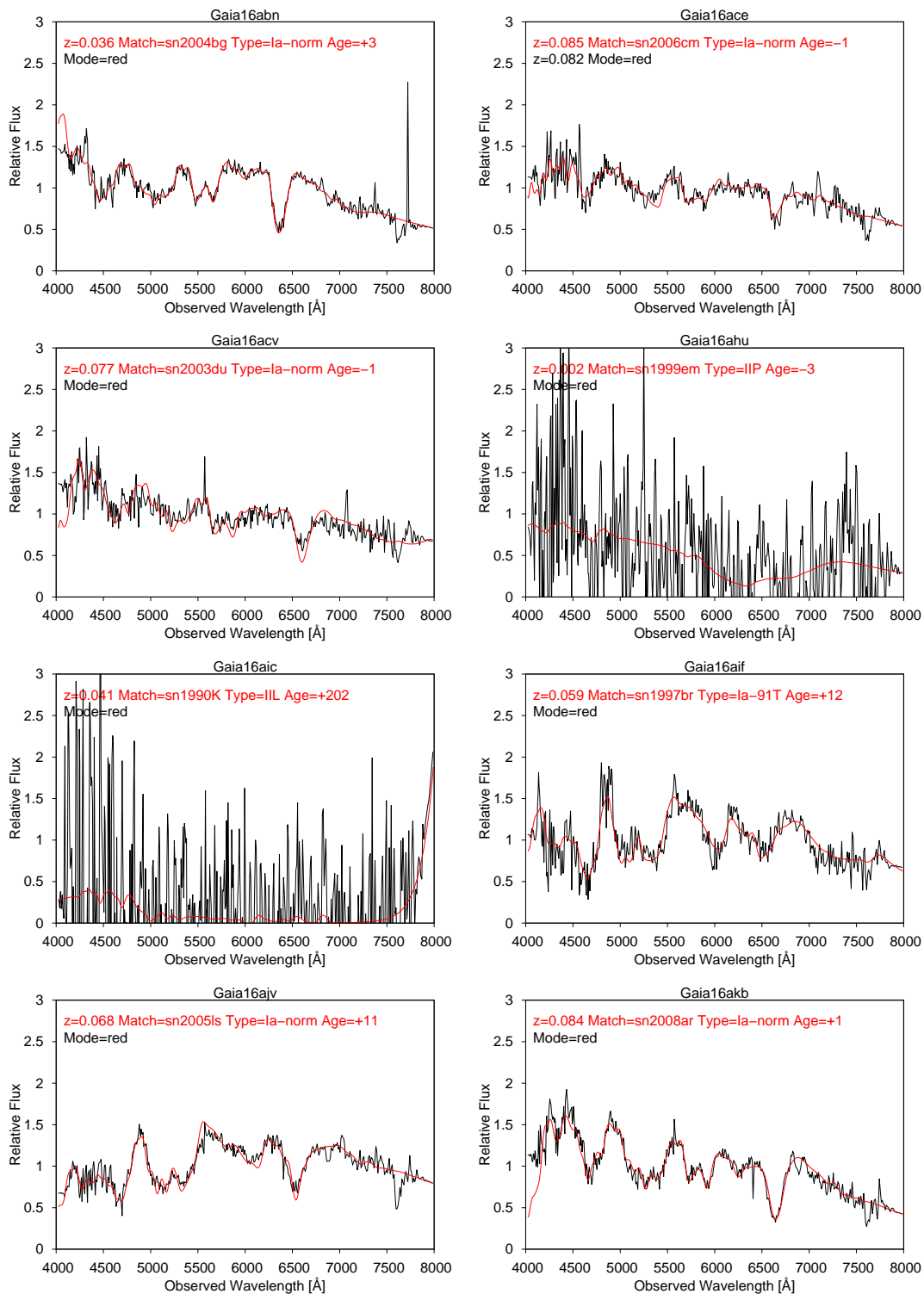


Figure A.11: Gaia - 2

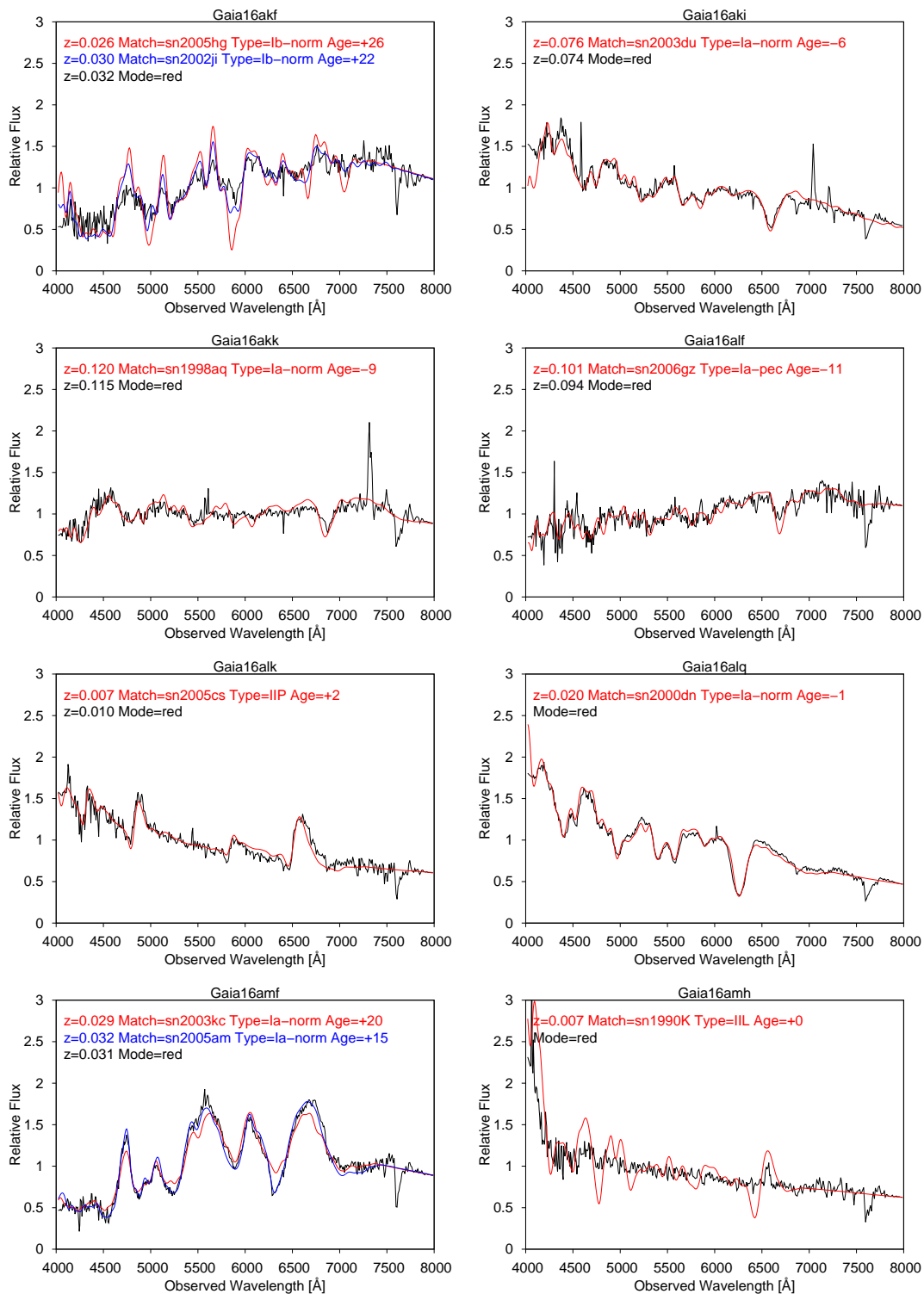


Figure A.12: Gaia - 3

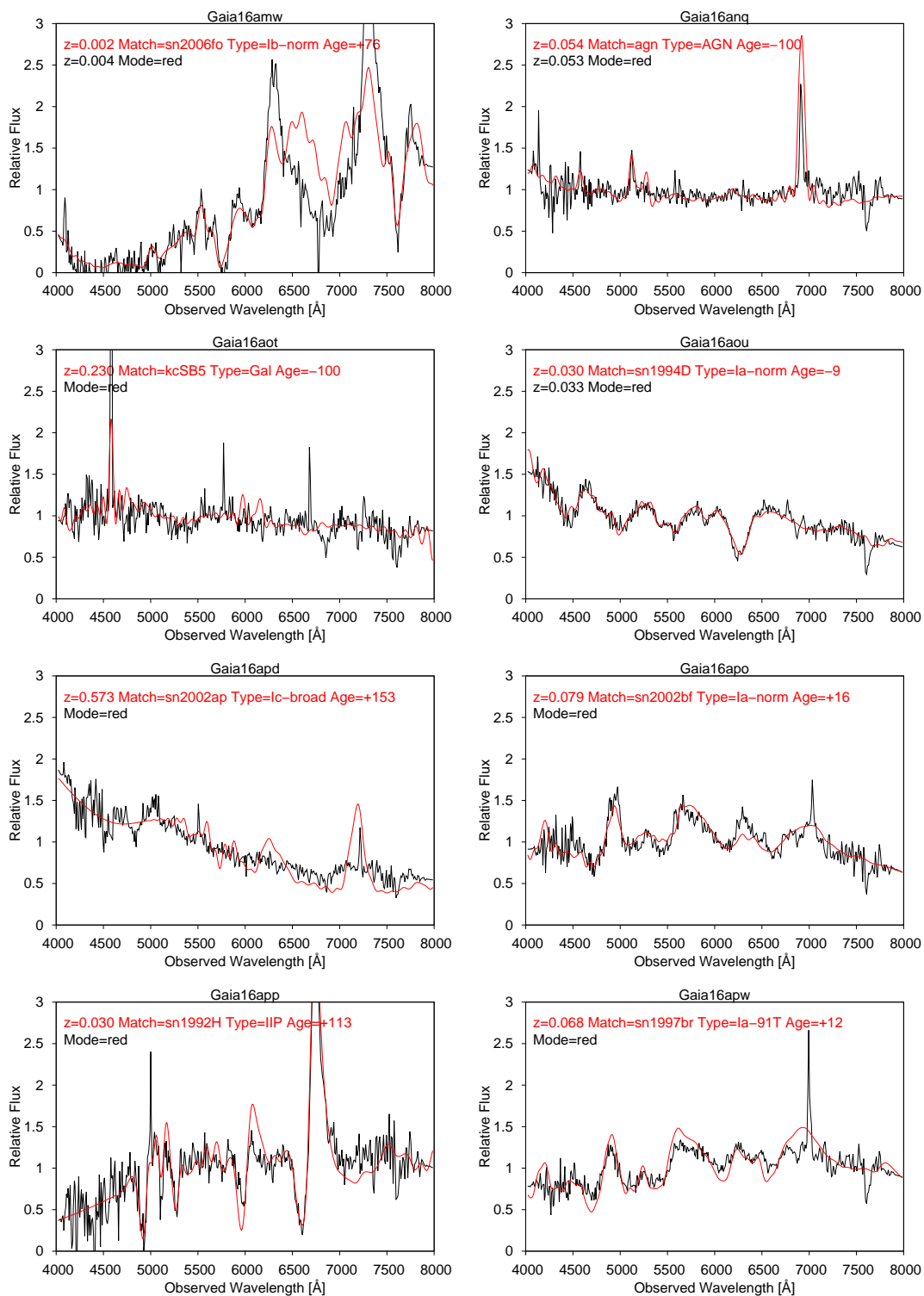


Figure A.13: Gaia - 4

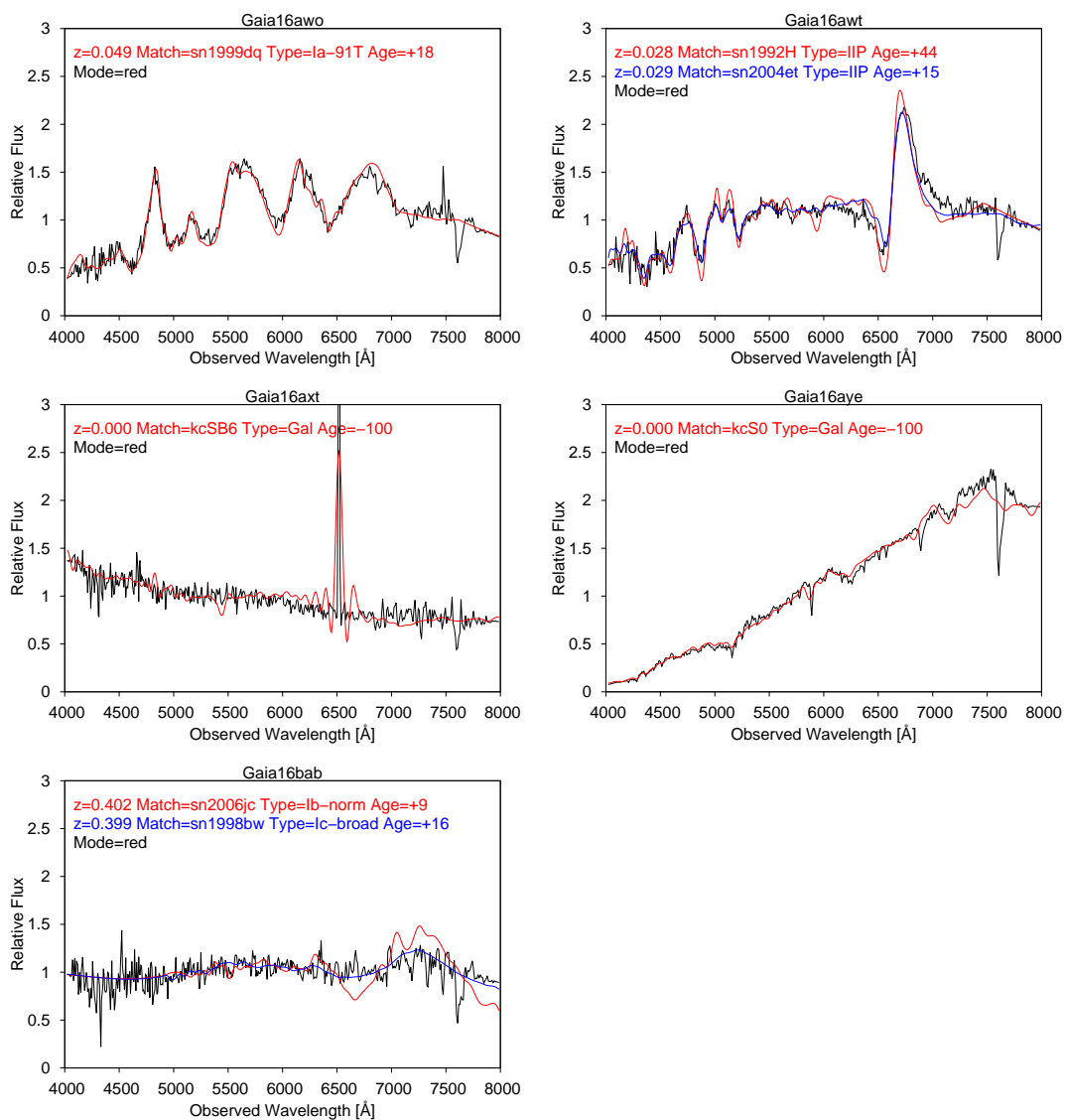


Figure A.14: Gaia - 5

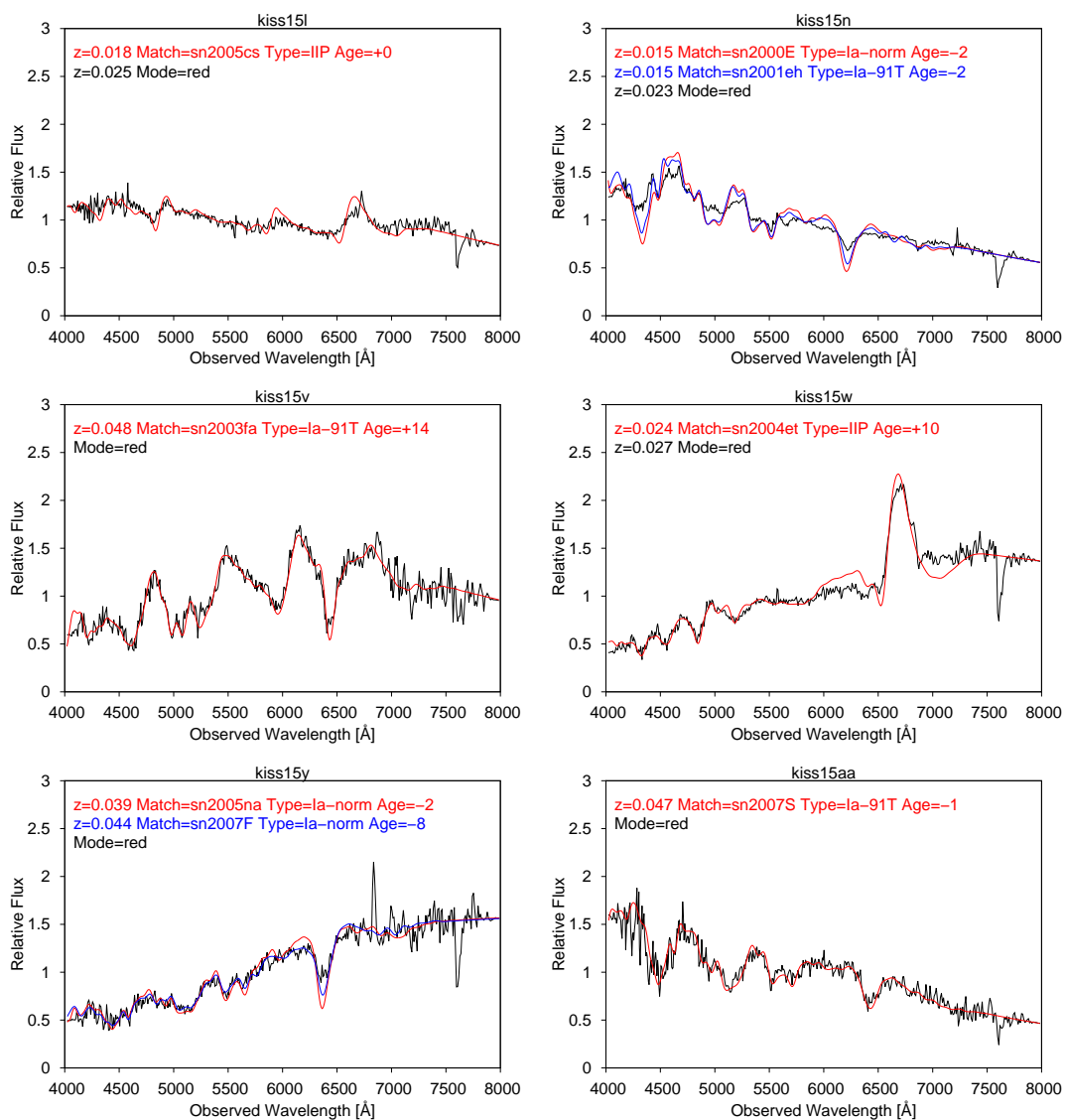


Figure A.15: KISS

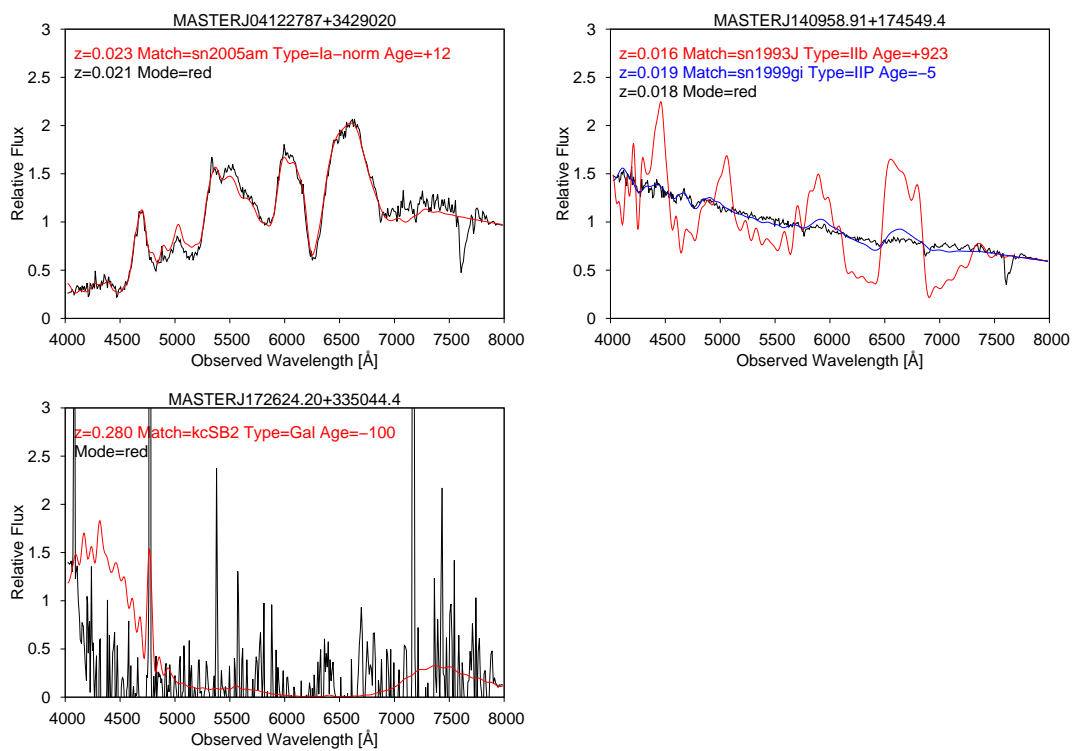


Figure A.16: MASTER

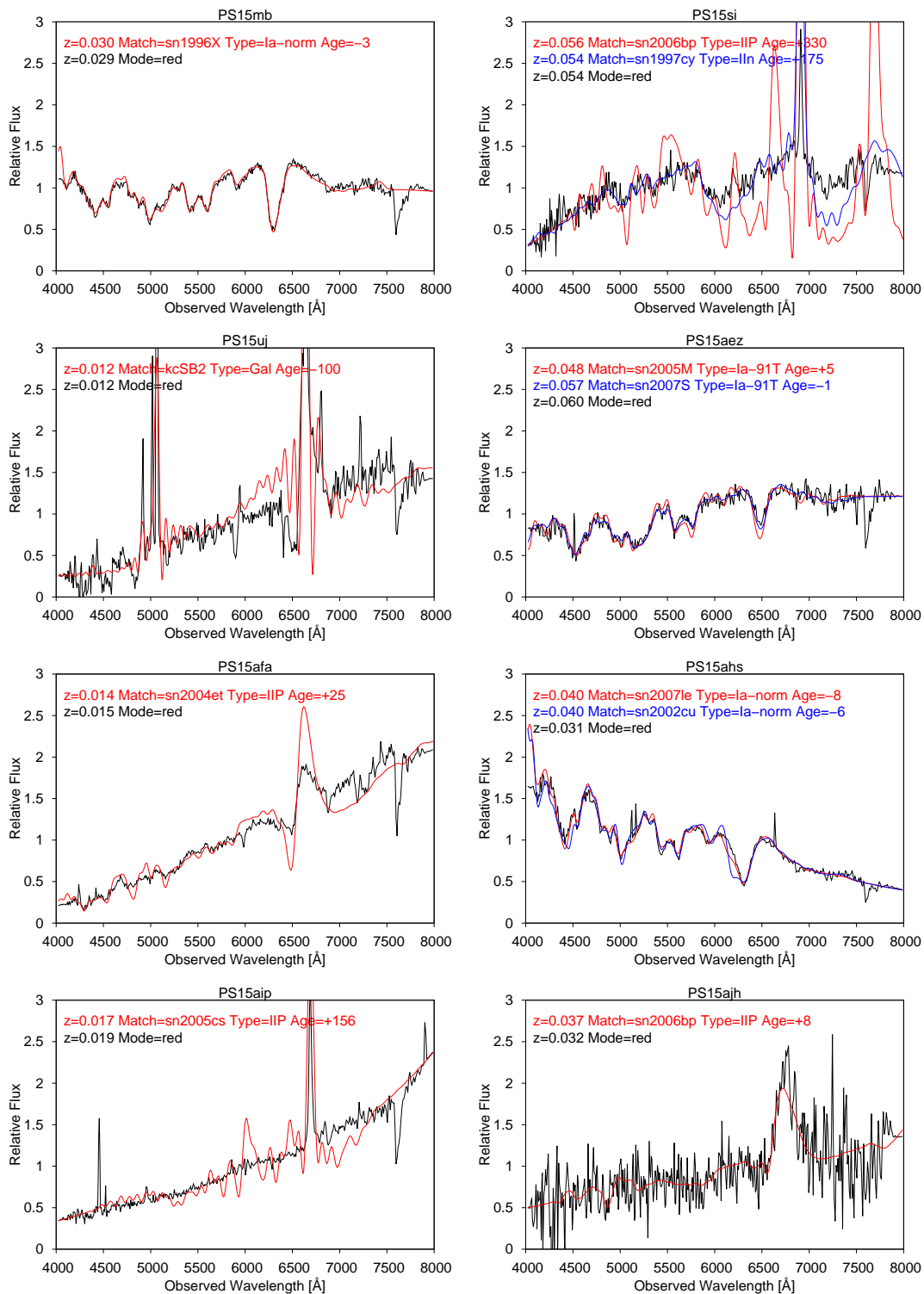


Figure A.17: PanSTARRS - 1

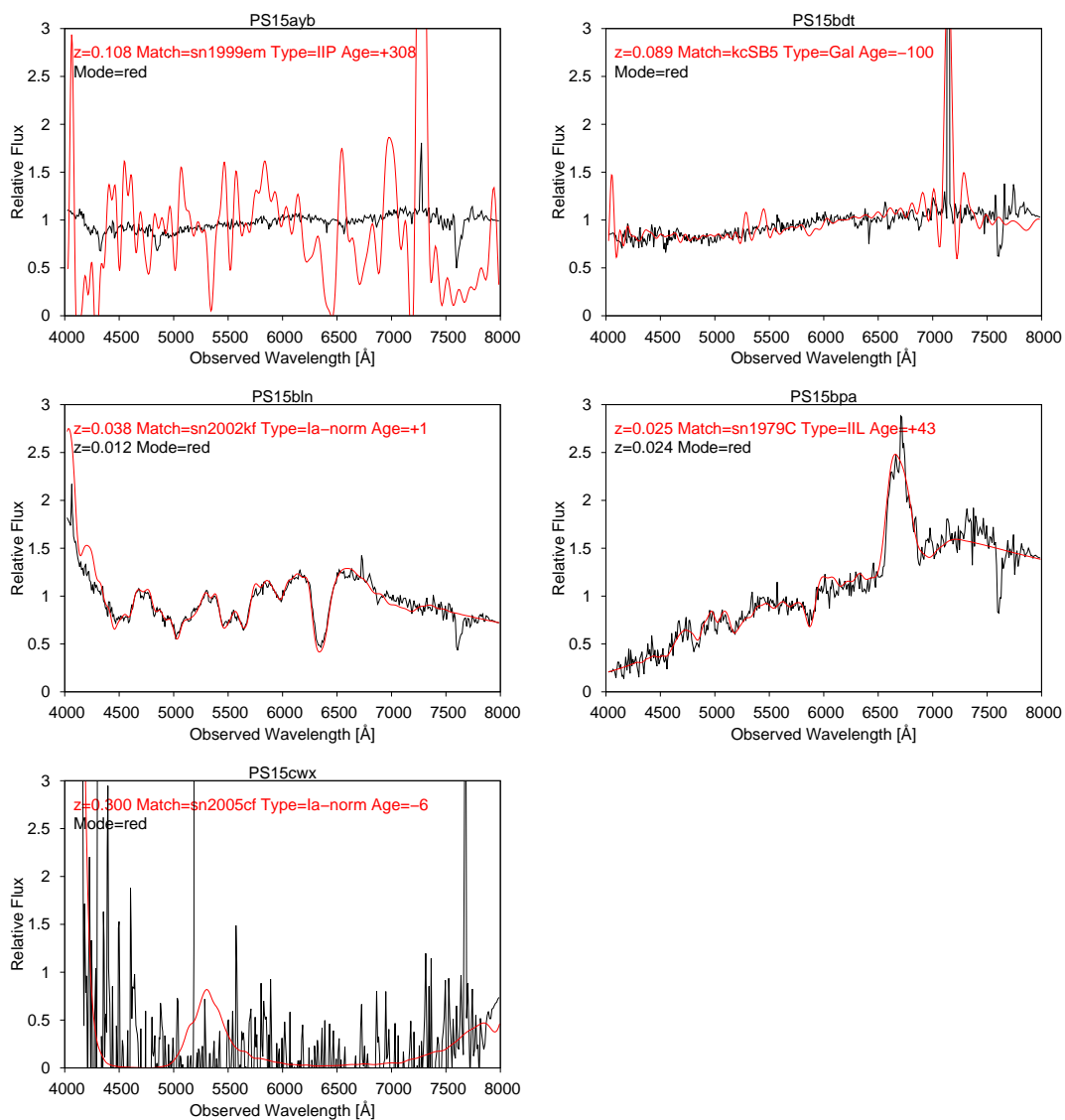


Figure A.18: PanSTARRS - 2

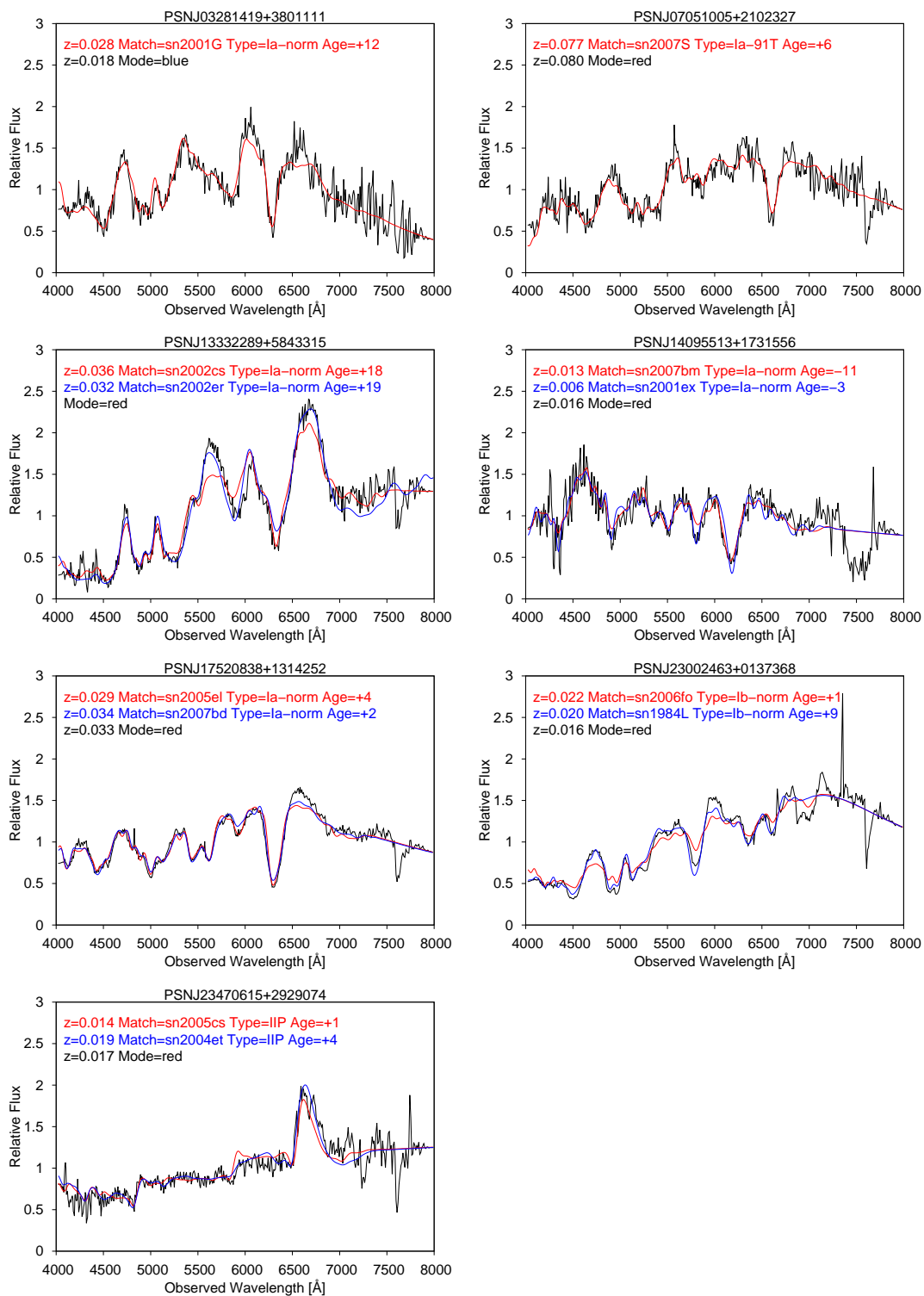


Figure A.19: CBAT

Appendix B

Supplemental Observations

Supplemental spectra were provided from the observing programme of Dr. David Bersier from LJMU. These were obtained using the SPRAT spectrograph on the LT using a single exposure for each object. Several of these are duplicate observation of objects in Appendix A A as listed here.

asassn-15az

asassn-15mj

asassn-15od

asassn-15ua

asassn-15uv

asassn-15ua

PSNJ14095513+1731556

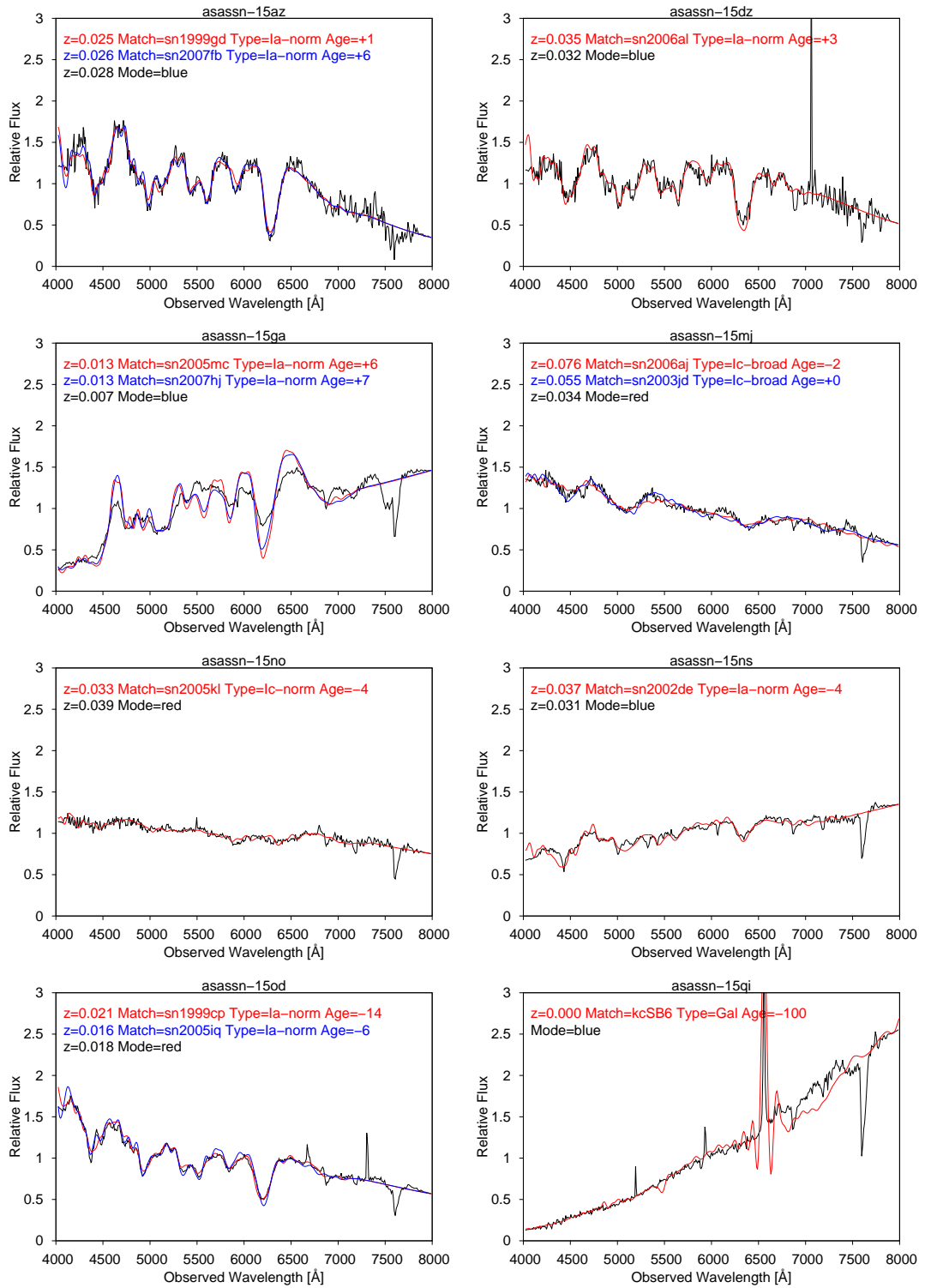


Figure B.1: Bersier Obs. - 1

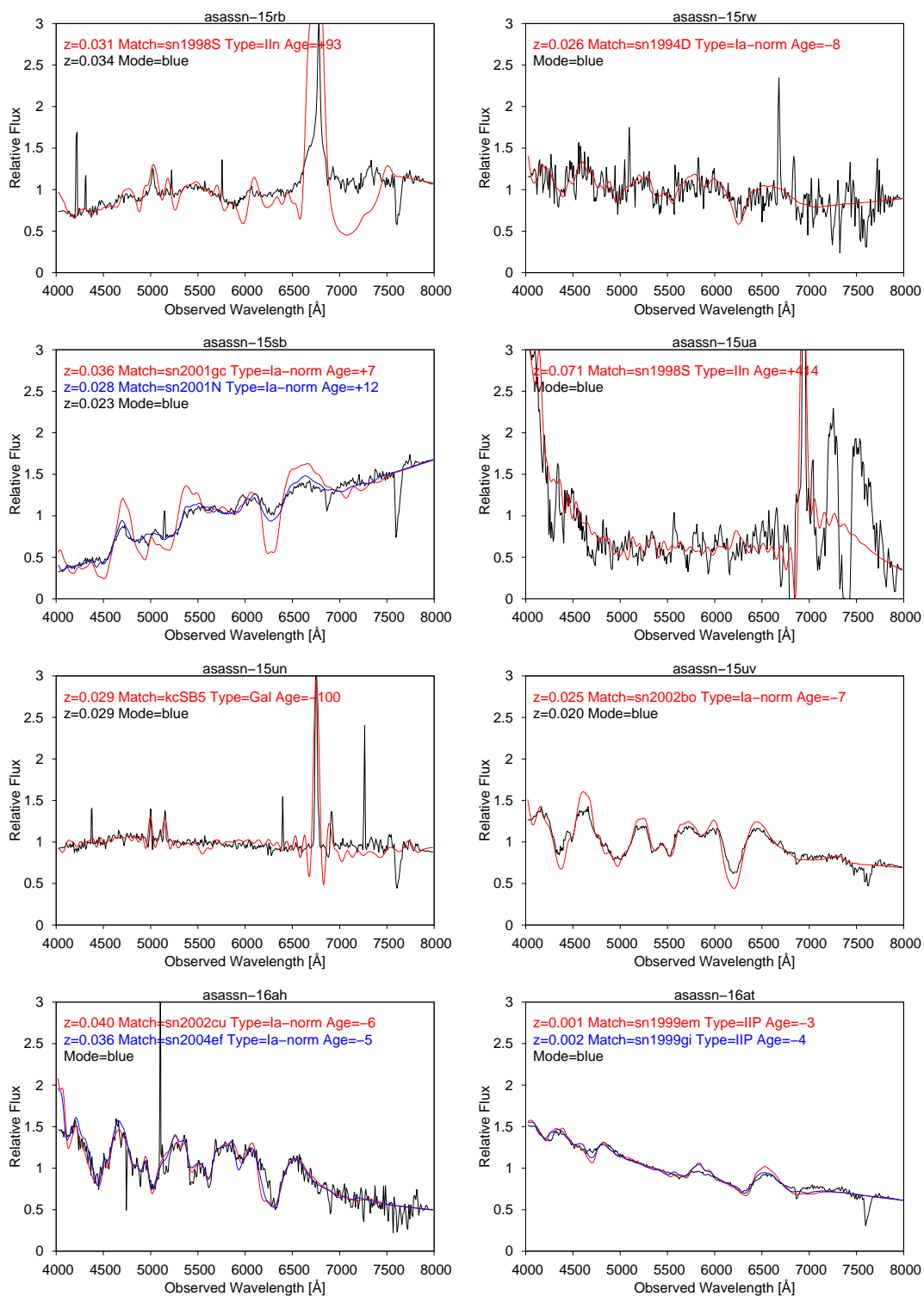


Figure B.2: Bersier Obs. - 2

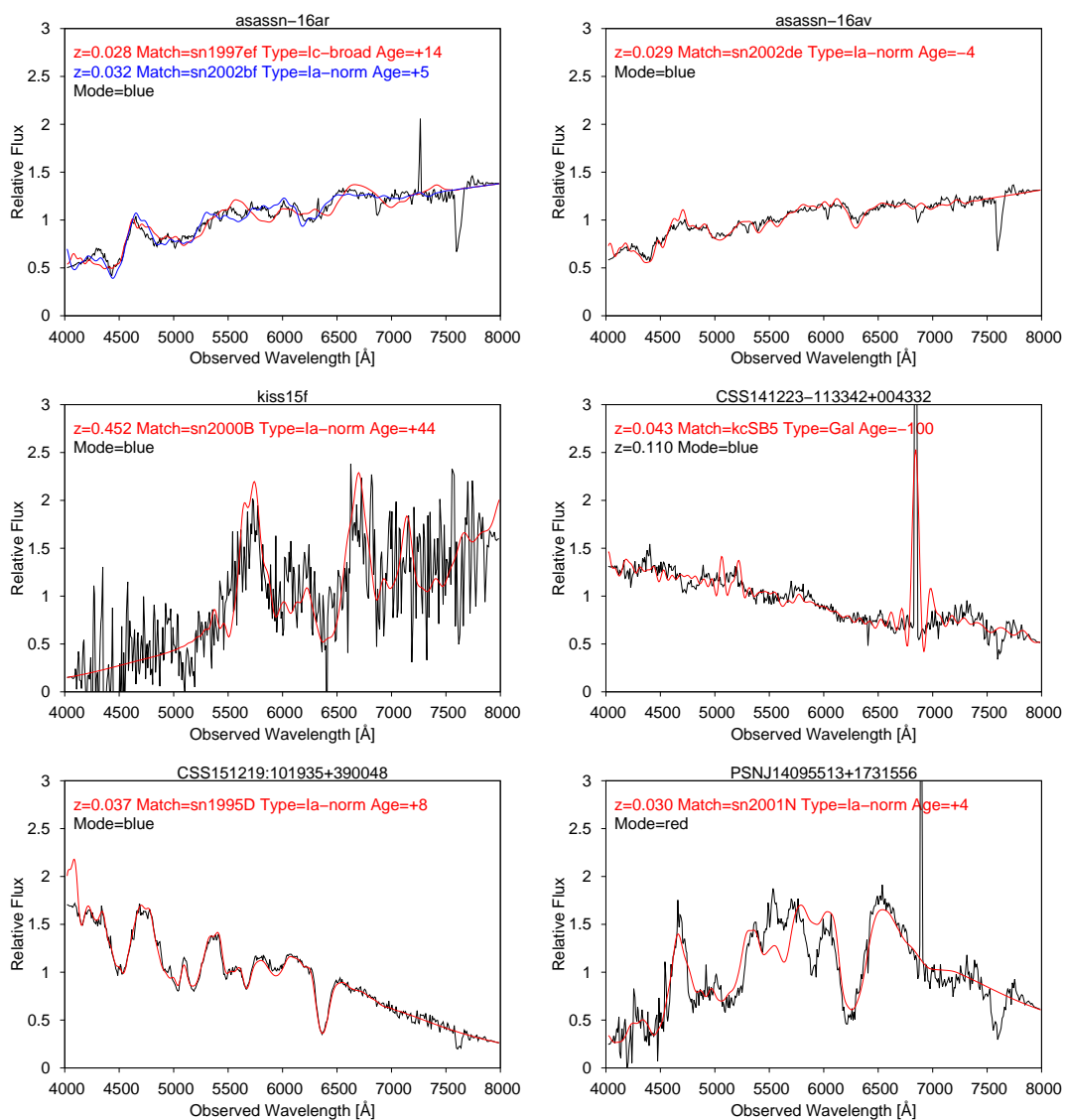


Figure B.3: Bersier Obs. - 3

Appendix C

Gravity Wave Observations

These spectra were analysed to classify potential optical counterparts to gravitation wave alerts issued by aLIGO

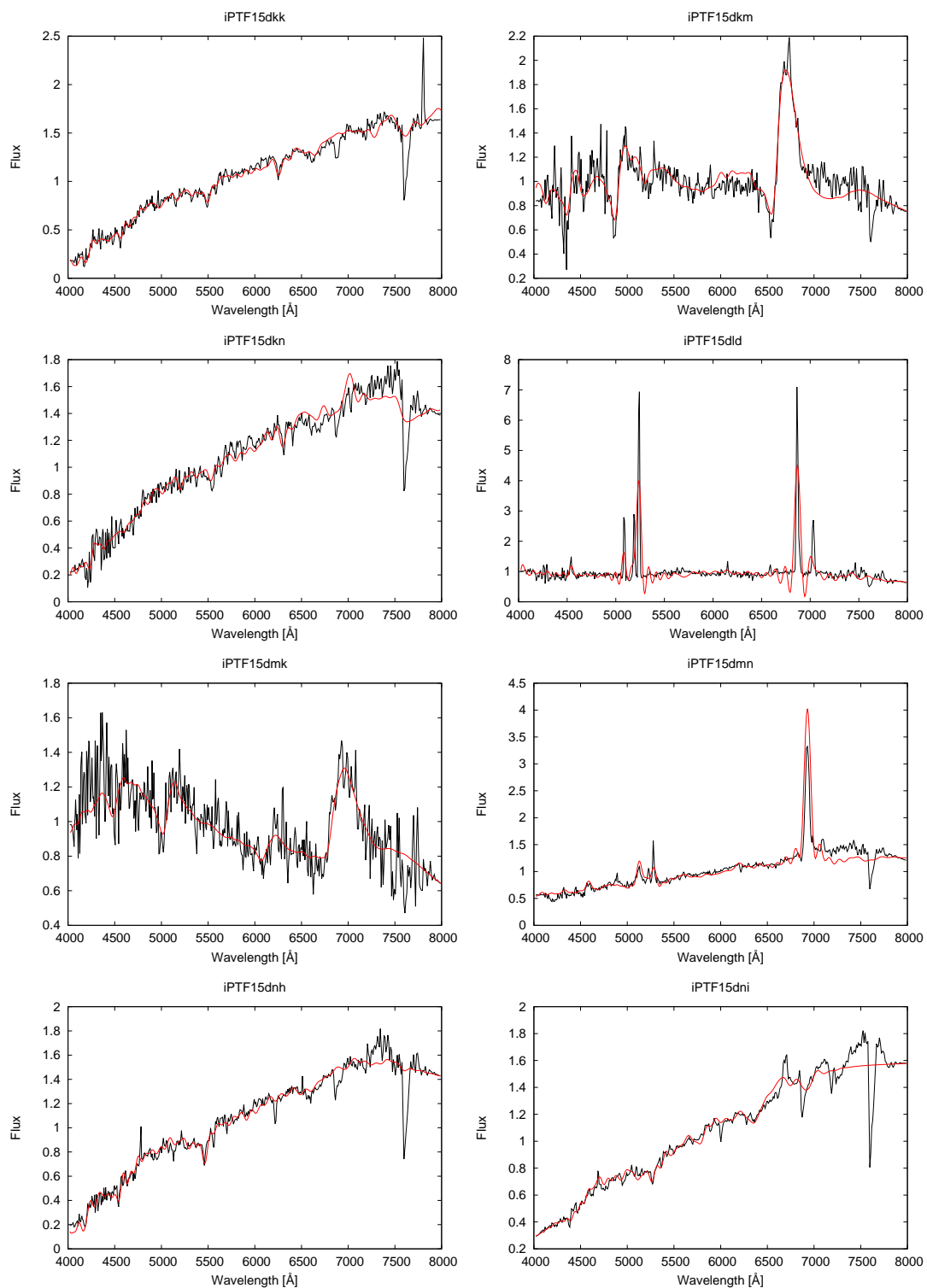


Figure C.1: GW Event G194575

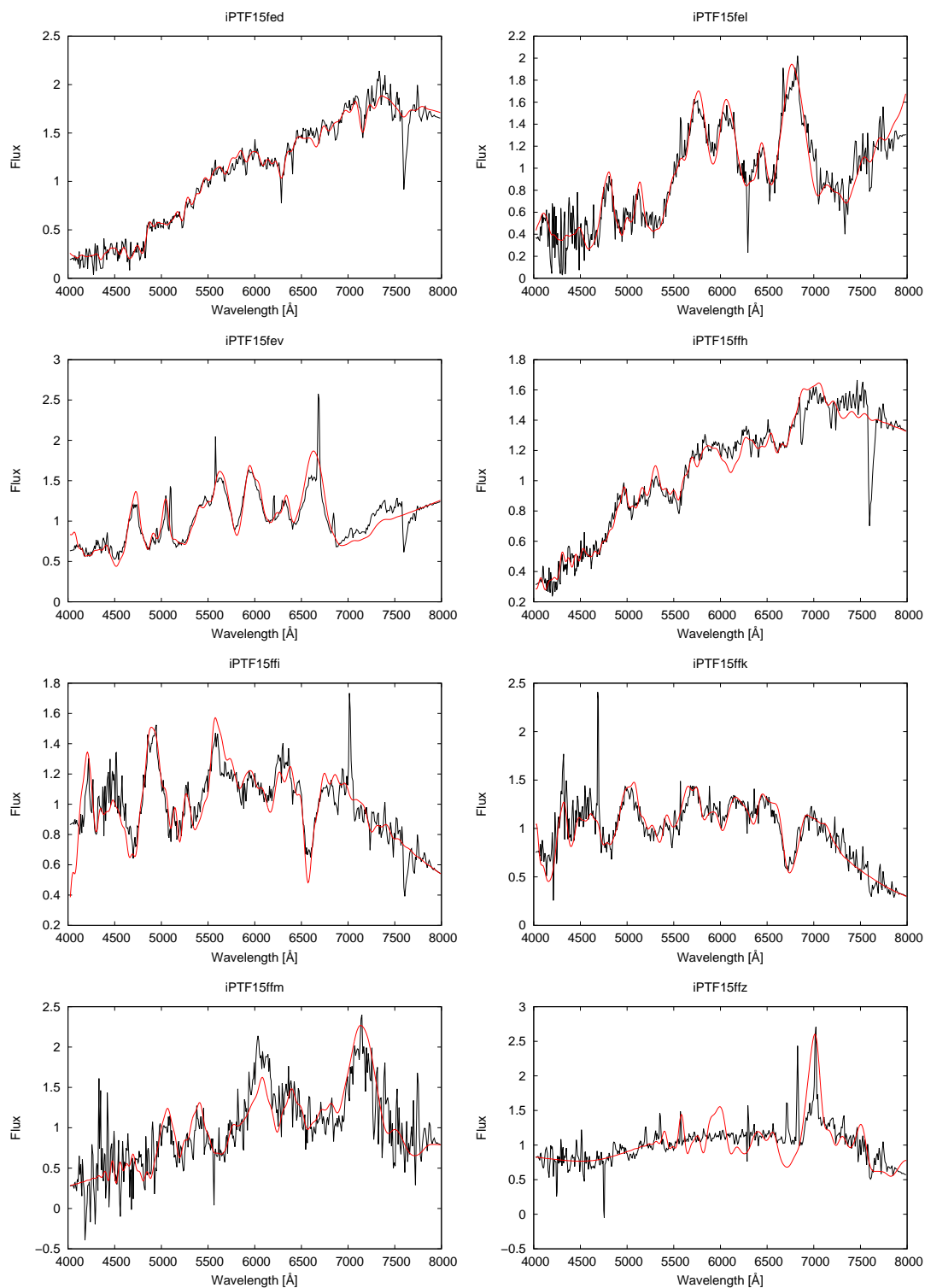


Figure C.2: GW Event GW151225 - 1

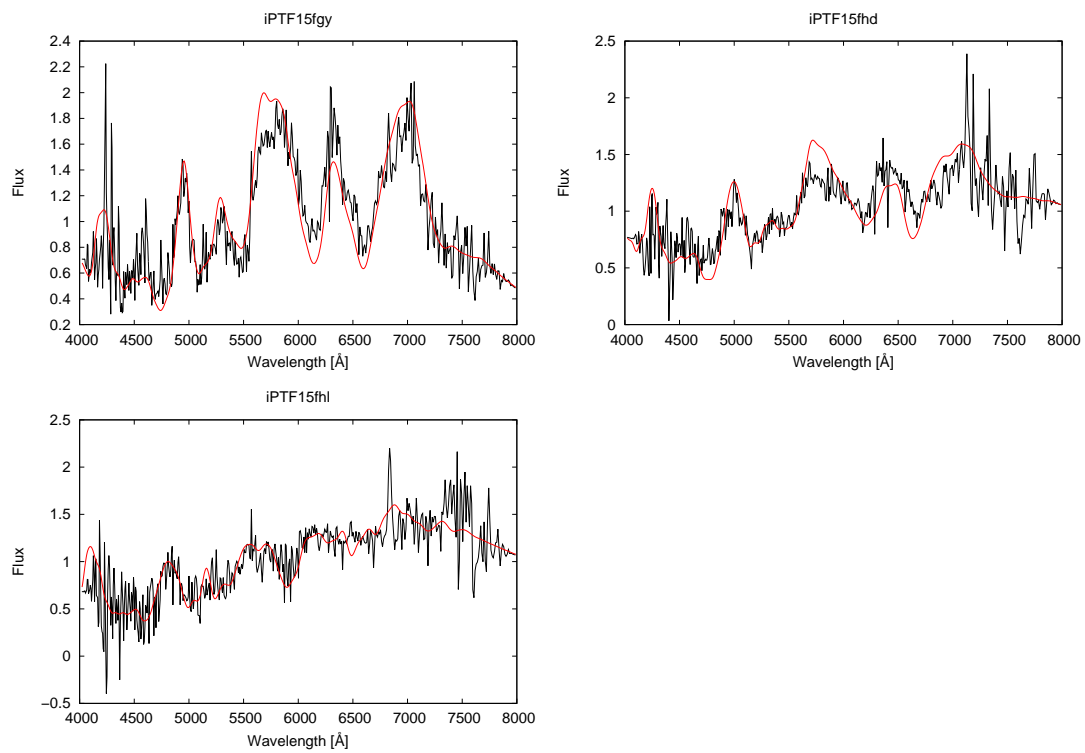


Figure C.3: GW Event GW51226 - 2

Appendix D

Xe Arc Calibration Lines

The values of emission lines wavelengths for the Xe calibration arc were primarily from Oriel Instruments arc lamp data sheet (Oriel-Instruments, 2008) with supplemental lines added from the NIST web-site, (physics.nist.gov, 2013). The 'Used' column identifies the sub-set of 19 lines included in calculating the polynomial to correct for the non-linear x-axis to wavelength mapping of a Xe arc image.

Wavelength [Å]	NIST relative intensity	Source	Used
4193.5	150	NIST	
4383.9	100	NIST	Yes
4501.0	500	Oriel	Yes
4524.7	400	Oriel	
4582.8	300	Oriel	Yes
4624.3	1000	Oriel	Yes
4671.2	2000	Oriel	Yes
4697.0	300	Oriel	
4734.2	600	Oriel	Yes
4807.0	500	Oriel	Yes
4829.7	400	Oriel	
4843.3	300	Oriel	
4919.9 ¹	500	Oriel	Yes
5028.28	200	Oriel	Yes
5392.80	100	NIST	
5823.89	300	NIST	Yes
6182.42	300	Oriel	
6318.06	500	Oriel	Yes
6469.7	300	Oriel	
6668.92	150	Oriel	Yes
6728.01	200	Oriel	Yes
6827.3	200	Oriel	
6882.16	300	Oriel	
6976.18	100	NIST	Yes
7119.60	500	Oriel	Yes
7285.30	60	Oriel	Yes
7584.68	200	Oriel	Yes
7642.02	500	Oriel	
7887.40	300	NIST	Yes
7967.34	500	NIST	Yes
8231.6	10000	Oriel	
8280.117	7000	Oriel	
8346.823	2000	Oriel	
8409.2	2000	Oriel	

¹The mean of blended lines 4916.5 Å & 4923.2 Å.

Appendix E

Experiments with Flat Fielding

Methods

In this Appendix are described experiments as part of an analysis into optimising flat fielding and was presented by Smith et al. (2016).

Flat fielding of a spectral image is a more complex problem than for a simple imaging instrument. As well as correcting the standard small spatial scale “pixel to pixel” variations, there are larger scale, wavelength dependent variations of the detector sensitivity. The flat field is also required to correct for any spatially dependent variations in the sensitivity of the instrument due to the effect of the spectrograph optics. These variations will typically be on a much larger spatial scale than pixel to pixel variations. Overall we expect the flat field may be affected by:

- Non-uniform illumination of the slit generated by vignetting and mis-alignment within the telescope as well as small scale dust and other contaminants.
- Vignetting by the optics within the instrument itself.
- De-focused images of surface contamination on the optics.

- Surface features on the CCD created during manufacture (polishing marks).
- Variation in sensitivity between individual pixels.

In the following sections we will describe some experiments for deriving flat-fields that will correct the pixel-to-pixel variation, larger scale errors and the effect of slit illumination, including the effect of geometric distortions on the derived corrections. A “final” flat field can be constructed by the multiplication of the various individual corrections.

E.1 Measuring Pixel to Pixel Variation Without the Slit and Dispersing Elements.

In some spectrographs (e.g., SPRAT, but not LOTUS) it is possible to withdraw the slit and dispersing elements from the optical beam. This allows measurement of detector flat field effects using an undispersed twilight sky image. Figure E.1 shows an example SPRAT exposure taken in such a configuration and indeed is the flat-field used to correct data taken in imaging mode as described in Figure 3.33. A large scale vignetting (which does not affect data taken through the slit) is apparent. The effect of the large scale vignetting can be removed by applying a 2D Gaussian smoothing function to the bias-subtracted image, I_{sub} producing a smoothed image, I_{smo} . The effect of this is to remove the pixel-to-pixel variations on spatial scales approximately less than the Gaussian full width half maximum (FWHM). I_{smo} is then divided into I_{sub} to produce a normalized pixel-scale flat field, F_{pix} (Equation E.1)

$$F_{\text{pix}} = \frac{I_{\text{smo}}}{I_{\text{sub}}} \quad (\text{E.1})$$

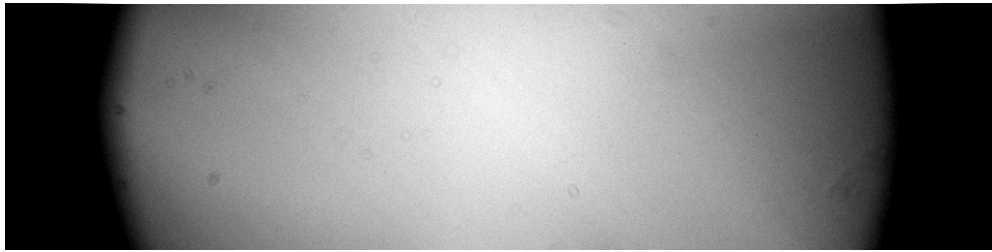


Figure E.1: SPRAT sky flat in imaging mode with slit and dispersing elements removed from the beam. The image shows some of the features requiring correction. A large scale vignetting is evident across the field. This vignetting is caused by the size of the field lens, and does not affect spectral data where the slit restricts the field size to the region of the focal plane corresponding to the centre of the image. De-focused dust produces small circular features. Manufacturing polishing marks on the CCD chip surface create faint 45° diagonal features.

The effect of different levels of smoothing on the standard deviation (s.d.) of F_{pix} is shown in Fig. E.2, with a knee at FWHM ~ 2 pixels and flattening at FWHM ~ 3.5 pixels. Larger scale smoothing FWHM (>5 pixels), causes a bleed effect from large features, particular evident at the image edges. For SPRAT a smoothing with FWHM = 3.5 pixels smoothing was chosen. Similar values are likely to be appropriate for most systems. The objective is simply to select a smoothing length that captures all the pixel-scale signal intrinsic to the detector whilst rejecting the larger scale features caused primarily in the optical beam.

E.2 The Effect of Geometric Distortions

Geometric distortions of the instrument focal plane are a common feature of long slit spectrographs. Care is usually taken to align the rotations of the slit, grating and detector such that “on average” the spatial and dispersion directions are orthogonal and aligned with the CCD detector edges. In the discussion that follows we will assume that the spectrum is oriented on the detector such that the x -axis (roughly) corresponds to the dispersion (wavelength) direction and the y -axis (roughly) to the spatial (slit) direction. We will also assume we are always working with bias subtracted images.

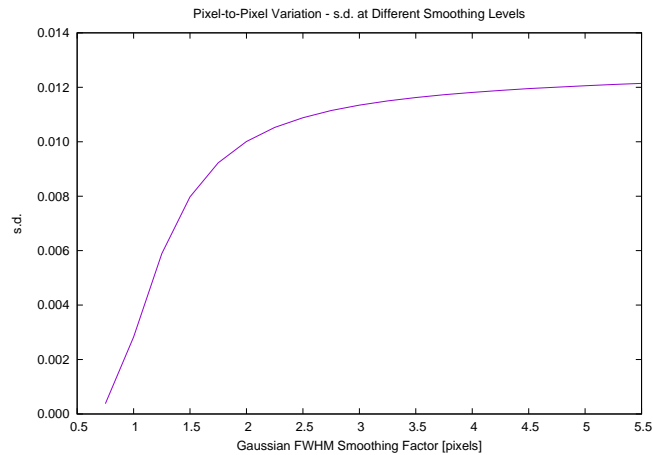


Figure E.2: Flat field pixel value standard deviation vs Gaussian FWHM smoothing applied. In this graph, we aim to maximize the measured standard deviation (indicating we have captured the full pixel-to-pixel variation) whilst keeping the length scale smaller than, and thus ignoring, features which are not intrinsic to the detector. We selected FWHM=3.5 pixels.

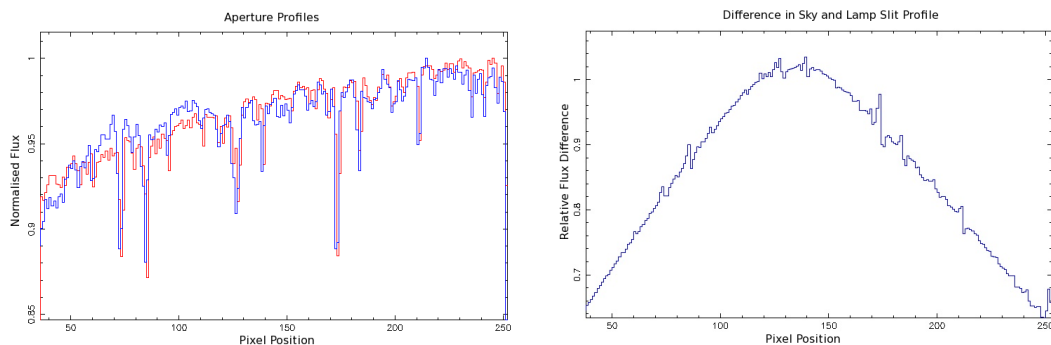


Figure E.3: Left panel: Slit profiles extracted from 30 pixel wide sections at the red and blue ends of a SPRAT twilight sky spectrum. The 1-3 pixel wide decreases in flux are caused by dust particle contamination on the slit. The relative shift of these features is indicative of misalignment and distortion. The overall slope of the line shows a brightening of the slit from top to bottom caused by either non-uniformity of the slit width or illumination. Right panel: Ratio of collapsed lamp and sky illumination profiles of the SPRAT slit. The overall flux distribution incident on the slit from the flat lamp does not match that from the sky via the telescope, producing the large scale variation across the image. The smaller peaks show that dust line positions are not co-incident indicating probable illumination angle differences between the two flat sources.

In this scenario the tilts and curvatures of the local spatial and dispersion vectors with respect to the overall focal plane mean that (for example) the projected traces of imperfections and dust in the slit will tend to curve slightly across the detector (Figures E.3 and E.4). To add further complication, the trace of an astronomical source across the image will have an additional curvature due to the effect of differential atmospheric

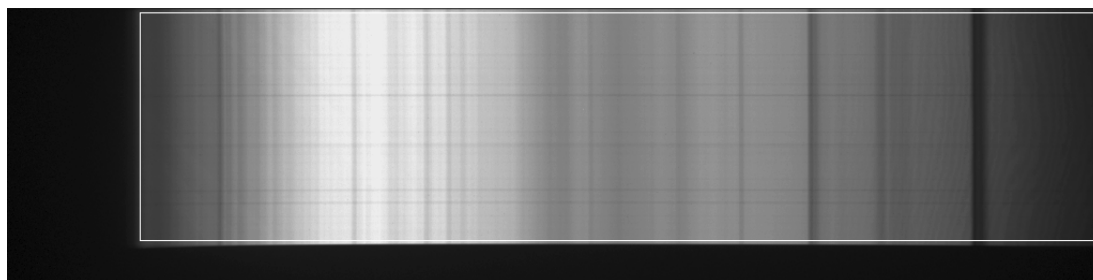


Figure E.4: A twilight sky flat spectrum observed using SPRAT. The 900×216 pixel region used in deriving a flat field is within the white rectangle. Solar Fraunhofer and telluric atmospheric lines are evident. The left black region marks the 4000 \AA high-pass filter cut-off wavelength and it is from this region that the bias level was estimated in Sec. 3.8. The lower black band is a mask on the slit. The horizontal dust lines and vertical absorption lines can be used to map geometric distortion (see Section E.5).

refractionFilippenko (1982). The combination of these effects can lead to subtle errors in the large scale photometric calibration of the spectrum as a function of wavelength as the spectrum “curves through” the dispersed slit profile. In a similar fashion the wavelength calibration (and hence location of sky emission lines) may curve slightly as a function of the spatial direction due to optical distortion. This can lead to errors in sky subtraction.

The most common type of flat field (which is essentially available to any spectrograph, including LOTUS and SPRAT) is a twilight “sky” flat taken through the slit and dispersive elements. Such sky flats are illuminated in a similar fashion to incoming stellar light, but contain various time-dependent emission and absorption lines and bands (Fig. E.4). Some spectrographs also provide the ability to illuminate the slit via an internal tungsten or similar incandescent bulb. Such “lamp” flats have the advantage of a smooth spectral energy distribution (SED) but the disadvantage that the illumination of the slit is usually not via the telescope optics, and therefore may be different to incoming stellar light (Fig. E.3). Such a tungsten lamp facility is available on SPRAT but not LOTUS.

E.3 Use of the Lamp Flat

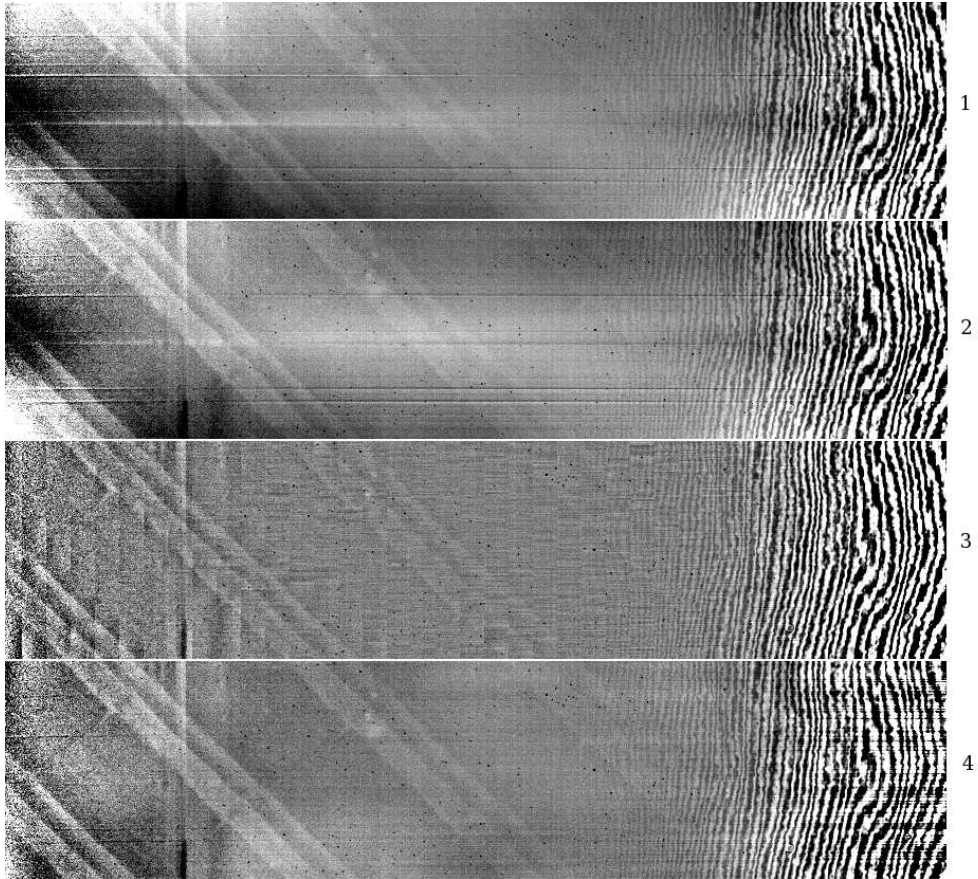


Figure E.5: Flat fields derived from lamp flat observations using methods 1–4 (top–bottom). Method 1 assumes a constant mean slit profile for all positions on the x -axis. Method 2 derives the slit profile as a function of position on the x -axis via a linear interpolation of the profiles on the left and right hands sides. Method 3 derives individual slit profiles in windows of length 23 pixels along the x -axis. Method 4 fits a polynomial to each row in the image to derive how individual rows of the slit profile change as a function of x . The grey scale represents between -5% (black) and $+5\%$ (white) deviations from the whole-image mean.

Nominally lacking emission lines and with a smooth SED, the lamp flat is well suited to the derivation of pixel and larger scale flat field features (e.g. CCD polishing marks). To do this we must remove the contaminating effect of the slit spatial profile, which as already discussed does not accurately reflect the illumination pattern for sources observed through the telescope. We have evaluated four methods for this process, all of which begin with a bias subtracted lamp flat $L(x, y)$ that has already been corrected for the effects of pixel to pixel variation using the flat field derived in Section E.1. Images

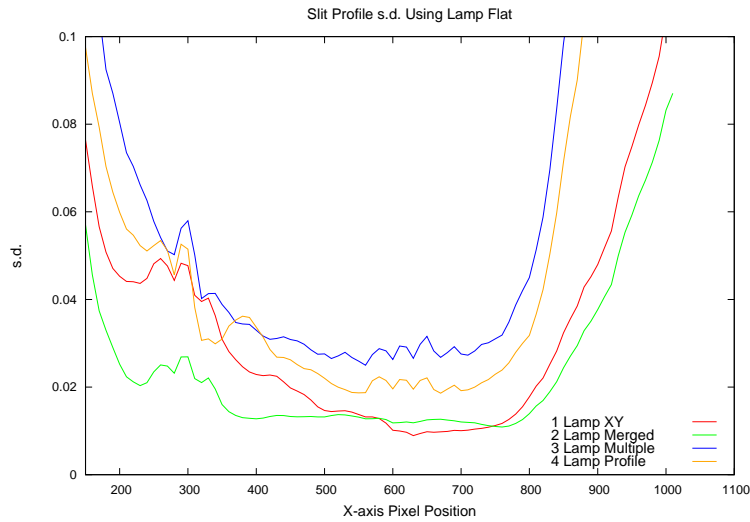


Figure E.6: Standard deviation as a function of x -axis position for the four methods. Standard deviations have been measured over a sliding window of width 20 pixel and the full height of the detector.

of the derived flats for all four methods are presented in Figure E.5. The fringing on the right of the images is an interference effect between the surfaces of the CCD silicon and, being an additive effect, is not correctable by flat fielding. Our methods are:

1. **Division by x - and y - axis profiles.** A simple flat fielding method is to rescale each axis with an average illumination profile using a sky flat spectrum. A slit (y -axis) illumination profile, P_y , is created by summing $L(x, y)$ along each row. Similarly, a wavelength (x -axis) illumination profile, P_x is created by summing $L(x, y)$ along columns. Dividing each column of $L(x, y)$ by P_x and each row by P_y then attempts to remove the spatial and wavelength dependent features, which following normalization to a mean pixel value of 1.0, forms the flat field $F(x, y)$. The outcome of this procedure is shown in Figure E.5 (top). As hoped for, the flat field shows the larger scale (e.g. polishing marks) features that we wished to characterize. However although the central region is well corrected for the effect of the slit profile there are obvious strong adjacent-row “positive-negative” slit residuals at the spectral extremes caused by geometric distortions.

2. **Application of a merged “left-right” profile.** Method 1 shows that application of single profile along an axis introduces errors if the image is distorted. This is particularly evident at the ends of dust and spectral lines. A method employing 2 merged slit profiles derived from each end of the slit was therefore investigated. This is identical to method 1 apart from the construction of P_y . The correction applied in the spectral direction (P_x) is the same in all four methods since we are investigating different methods of removing the slit illumination P_y . Two half image-width slit profiles were created, a left-hand side, P_{lhs} , and right-hand side, P_{rhs} profile. For an image of width W , the correction applied for a column at offset x is a linear proportion of the flux from the left and right profiles:

$$P_y(x) = \left(\frac{x}{W}\right)P_{lhs} + \left(1 - \frac{x}{W}\right)P_{rhs}. \quad (\text{E.2})$$

The outcome of this procedure is shown in Figure E.5 (second from top). Comparison with method 1 shows a improved correction of the slit profile, although residuals associated with it are still present.

3. **Multiple profiles.** In this method a number of local slit profiles are generated and applied sequentially across an image. The slit profile is generated by collapsing image subsections, each of width L pixels. These are then joined together to form $P_y(x)$ which is then applied as per methods 1 and 2. It can be seen as a potential improvement to method 2 in that it does not assume the contribution to a given pixel from a slit feature is a *linear* function of distance along the x -axis. The results of this approach are shown in Figure E.5 (third from top) for $L = 23$ pixels. The residuals associated with the slit features are very well suppressed at all x -axis positions using this method. Another obvious advantage compared to the other methods is the overall very large scale “flatness” of the image. We note however that horizontal correlated noise of length L can be seen in the images, as well as some weak vertical features.

4. **Polynomial fitting to each row.** In this method $L(x, y)$ is divided by P_x to remove the spectral lamp dependence. A fifth order polynomial is then fitted to each row in turn to model the slit response on a row by row basis. Row spectra generated from each polynomial are then multiplied by P_x to create an image which is then divided by $L(x, y)$ to create the flat field. The results from this procedure are shown in Fig. E.5 (bottom). The procedure is more effective than methods 1 and 2 (but not as effective as 3) in removing the residuals due to the slit profile variation.



Figure E.7: Division of a sky flat spectrum by X and Y profiles. Strong vertical features are apparent in the flattened image and result from optical distortion present in the raw sky flat image.

We now consider which of these methods is “best”. Overall the best flat field will be the one that accurately maps all defects affecting the image apart from any resulting from the slit profile. In Table E.1 we list standard deviations for a 50×50 pixel sub-region near the centre of the images which avoids any large scale features. Since we have already corrected our input image for pixel-to-pixel variations using the undispersed imaging flat, the *lowest* standard deviation within this small featureless region is therefore our target. This is assuming that any deviation present is caused by having imperfectly removed the slit illumination pattern. In this interpretation, the order of method preference (best to worst) is 1–2–4–3.

Looking to the large scales you can argue that we prefer a flat field that has the *largest* standard deviation, based on an interpretation that this is one that is capturing the maximum amount of information about image structures. On this assumption (Tab. E.1 (figures in parentheses)) the order of preference derived from “whole image” standard

Table E.1: Standard Deviations of a 50×50 pixel “featureless” region and (in parentheses) the whole image (apart from the image edges and fringed areas). The “Lamp” results are based on measurements of the flat-field. The “Sky” results are based on measurements of the residuals in the sky flat divided by the original input image. In both cases the results are presented for using both the normal and distortion corrected flat-fields.

Method	Normal Lamp	Normal Sky	Corrected Lamp	Corrected Sky
1. Conventional (XY)	0.007 (0.043)	0.024 (0.079)	0.008 (0.050)	0.024 (0.078)
2. LR Merge	0.008 (0.032)	0.026 (0.079)	0.012 (0.046)	0.025 (0.077)
3. Multiple Regions	0.022 (0.127)	0.029 (0.079)	0.009 (0.049)	0.034 (0.089)
4. Row Polynomial Fit	0.014 (0.103)	0.012 (0.087)	0.009 (0.022)	0.031 (0.086)

deviations would be 3–4–1–2. This argument is obviously flawed though if applied naïvely, since the algorithm might have introduced erroneous features. However, in the example of SPRAT data tested here, the same sequence (3–4–1–2) would be chosen by visual inspection of the images to evaluate qualitatively how well line residuals are removed.

Finally we consider the “medium” scale. In Fig. E.6 we present the measured standard deviation as a function of x -axis position for the four methods. Standard deviations have been measured over a sliding window of width 20 pixels and full height of the detector. The low standard deviation for method 3 in this plot, especially at the extremes of the x -axis, demonstrates how well it removes the slit profile residuals.

Ultimately, the choice is best made through testing against simulated spectra rather than the simple, single parameter metrics discussed above, and this will be addressed in a future publication.

Overall the best choice appears to be method 3, with the caveat that this method appears to introduce additional small scale noise. The choice for any particular spectrograph will therefore depend on the relative importance of the slit profile and pixel to pixel noise to the overall flat field quality.

E.4 Use of the sky flat

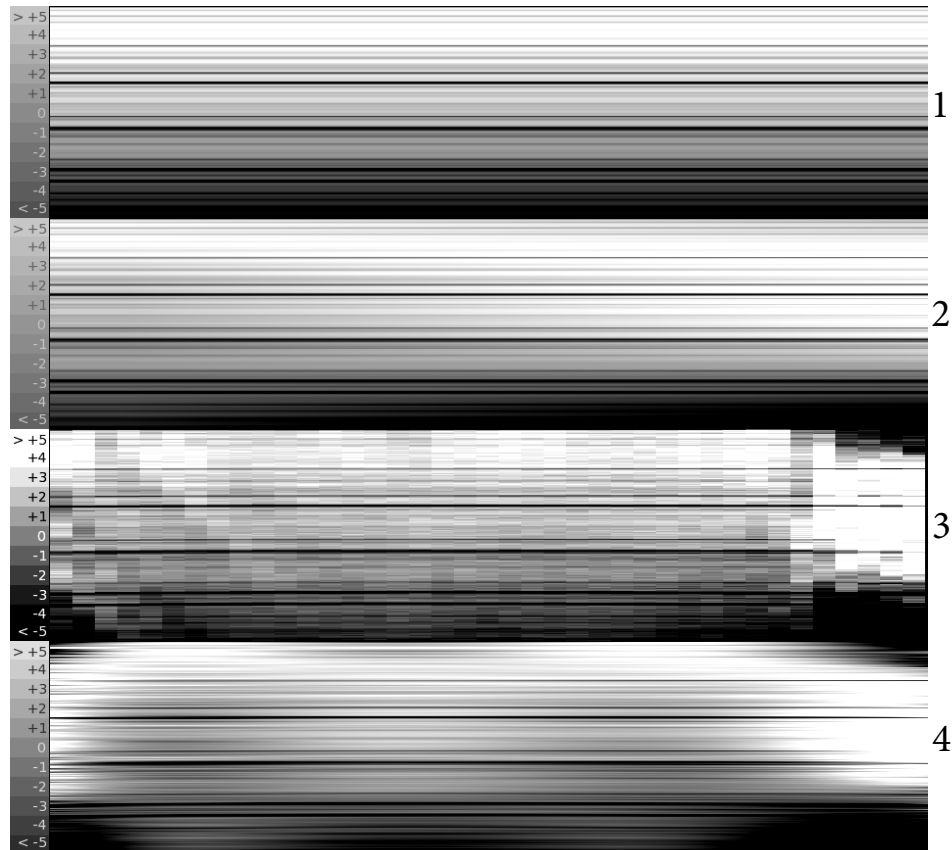


Figure E.8: Flat fields generated using sky flat images and the derived y -axis profiles in methods 1-4.

As described previously, the sky flat contains strong wavelength dependent features. It is however always available and does accurately reflect the slit profile on the recorded spectrum. Attempts to use our four methods on the sky flat in a similar fashion to the lamp flat do not succeed since the curvature of the vertical spectral features adds an additional component that generates strong vertical residuals. For example, the application of method 1 yields Figure E.7. We therefore have focused our attention on using the sky flat to create a correction only for the effect of the slit profile. We used the same four methods as for the lamp flat, however the input image was the bias subtracted sky-flat and the resulting product was the $P_y(x)$ images containing only the spatial contribution along the slit length. We do not include the contribution from

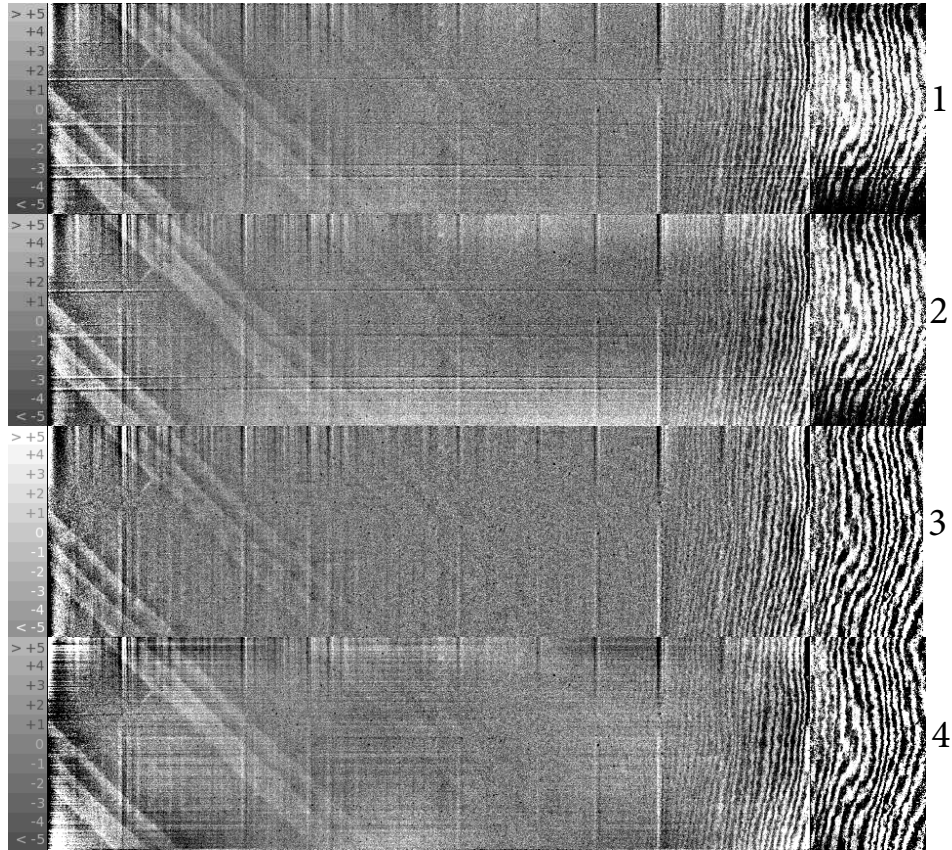


Figure E.9: Ratio of flat fields from Figure E.8 to raw sky flat field frame. The vertical features are expected residuals from the geometric distortion of sky features and this figure is intended only to assess the effectiveness of removing the slit illumination pattern by removing the horizontal features.

$P_x(y)$ along the spectral direction. These $P_y(x)$ images are shown in Fig, E.8.

To evaluate the performance of the four methods, we ratio the derived flat fields with the twilight sky flat. Such ratio images (Figure E.9) are contaminated by uncorrected vertical features associated with the wavelength dependence of the sky spectrum. These vertical features should be ignored in the comparison of the images. The standard deviations for methods 1–4 in the 50×50 pixel “featureless” and whole detector region are listed in Table E.1. The whole detector values are meaningless as they are dominated by the spurious vertical residuals. However for the 50×50 pixel regions there is an apparent preference for method 4 as that which adds the least additional pixel to pixel noise. Based on visual inspection of the images, method 3 seems

to be the most effective at deriving a flat field that can remove the slit profile, again at the cost of it being the noisier on a pixel-to-pixel level.

E.5 An Alternative Approach - Correcting Image Distortion

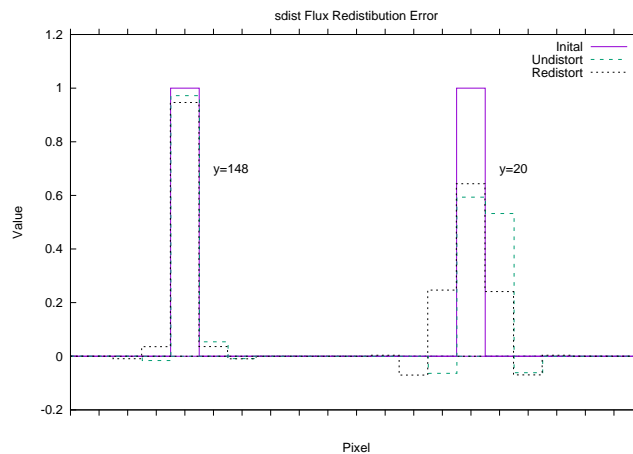


Figure E.10: The progressive effect of un-distorting and re-distorting for a vertical line in the simulated line field. Left shows broadening of a line near the centre at $y=148$, the overall amplitude is reduced by 3% and the width increase to ~ 3 pixels. Towards the lower edge of the image at $y=20$ the amplitude is reduced by 40% and broadened to 5 pixels with overcompensation indicated by the negative values.

Rather than trying to map the curved effect of the slit profile and remove it (for lamp flats) or use it (for sky flats), an alternative approach would be to apply a correction for the geometric distortion of the images to the data before using the conventional (method 1) approach. Either all data (science and calibration) could be corrected this way, or after deriving the flat field, it could then be “re-distorted” back to the original geometry before being applied to the science frames. This second approach would be computationally less intensive if processing a large number of science frames and prevents the need for resampling the science target pixel data which obviously risks degrading resolution. As we have already seen with a sky flat the diffraction grating disperses slit defects producing easily identifiable horizontal lines. Similarly, strong

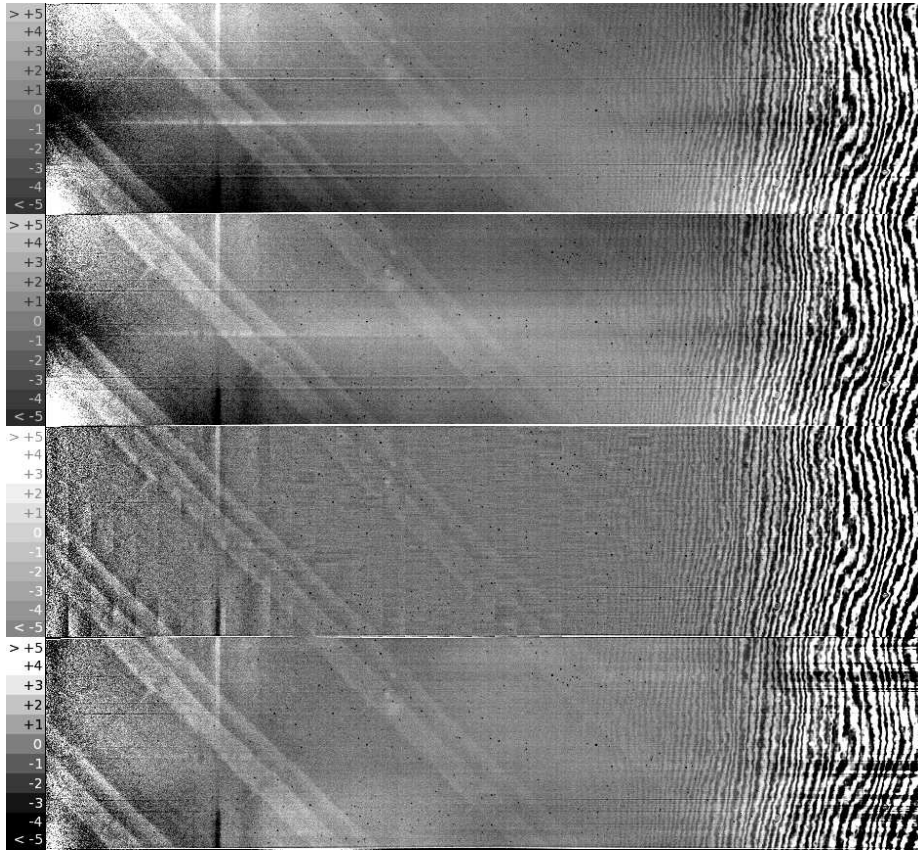


Figure E.11: Flat fields generated using geometrically undistorted versions of the lamp flat images and then re-distorted using methods 1–4. (Compare with Figure E.5)

spectral lines provide a dispersed, vertical image of the aperture, ~ 4 – 5 pixels wide, (Fig. E.4). These two sets of orthogonal lines extend across the image and their deviation from linear alignment with CCD pixels provides a measure of the distortion along the x - and y -axes (which also characterizes rotational skewing around the z -axis).

Using SPRAT data and various FIGARO routines we traced and corrected the horizontal and vertical lines in the sky flat sequentially. The correction used 5th order polynomials $f(x)$, $f(y)$ to characterize the distortion independently in each direction. We also wished to create the complement of the un-distort functions, $\overline{[f(x)]}$, $\overline{[f(y)]}$. This allows the finally derived flat-field to be re-distorted for use in the existing data pipe-line. Initially $\overline{[f(x)]}$, $\overline{[f(y)]}$ were derived from a line template with simulated straight dust and spectral lines. The template was distorted using $[f(x)]$ & $[f(y)]$ from

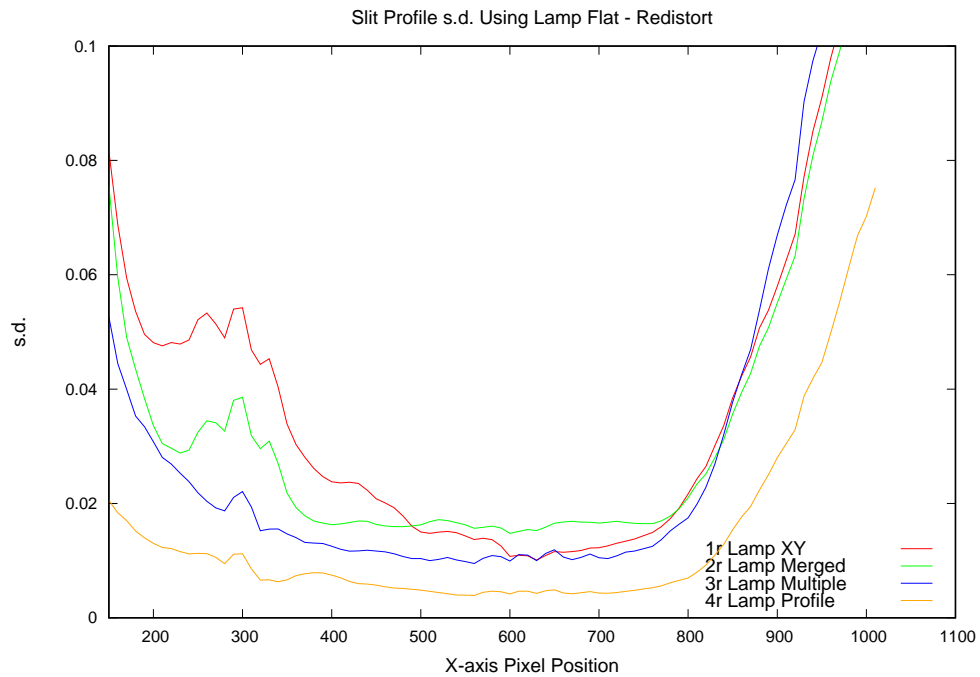


Figure E.12: As Fig. E.6 but for flat fields that have been undistorted and re-distorted as part of their construction.

a sky-flat to create a pre-distorted image. We then derived a second correction to the pre-distorted image to generate approximate inverse functions, $\overline{[f(x)]}$ & $\overline{[f(y)]}$. Having used Legendre polynomials to characterize the distortion, creation of the inverse transformations is trivial by simply negating the polynomials coefficients.

Since the geometric correction involves a redistribution of flux across pixels, we wished to investigate its effect on small scale features in the images and whether it was fully reversible. For a uniform blank field set to pixel value 1.0 the standard deviation increased from 0.0 to 0.004 as a result of the distortion and un-distortion of the image largely as a result of numerical rounding errors. For a field containing random values in the range 0.0–1.0 the standard deviation decreased from 0.280 to 0.226 illustrating there is some degree of smoothing. In a simulated one pixel wide line image it can be seen how flux redistribution results in a broadening of the line. The progressive change in cross-section for vertical line near the centre (where distortion is low) and edge (high distortion) of an image is shown in Figure E.10. Overall the flux re-distributions asso-

ciated with geometry corrections can be seen to distort pixel to pixel scale structures in an image. This is a natural consequence of the fact that a structure with a pixel scale of 1 pixel is by definition Nyquist under-sampled by a factor of 2. The effect on pixel to pixel scale flat fielding of geometric corrections is therefore potentially severe, in general resulting in an image smoothing. We note that it may be that an oversampling approach to flux redistribution would help alleviate this problem, and will be the subject of a future investigation.

With the above caveat in mind regarding the risks associated with flux re-distribution, we investigated the effect of correcting our lamp flat images for geometric distortions (with the distortion polynomials derived from our sky flats). The outcome of this investigation can be seen in Figure E.11. Comparison with the original analysis of the lamp flat shows that the horizontal residuals associated with the slit profile are indeed improved. The order of effectiveness of the different methods in slit profile removal is the same. The beneficial effect of the distortion on the correction of small scale variations can be seen in the increased apparent contrast of the dust features in this method. The standard deviations for the 50×50 pixel “featureless” regions are listed in Table E.1 and show lower noise than the normal methods, presumably due to the smoothing introduced by flux distribution. Standard deviation as a function of x -axis coordinate is plotted in Fig. E.12. Comparison with Fig. E.6 shows overall reduced standard deviations on the medium scale also.

In the specific case of SPRAT, this smoothing is not anticipated to be a problem and application of the geometrically distorted flat is potentially useful. The very first step of the procedure was removal of all the pixel-scale structure using the undispersed imaging flat. No genuine optical feature will be under-sampled at the detector due to the resolution of the grating, atmosphere and optics. Therefore any structure in the flat-field smaller than the Gaussian filter applied in Sec. E.1 must simply be noise and any slight smoothing caused by the distortion re-sampling is unlikely to be detrimental.

E.6 Summary

We have described some initial experiments and comparisons in the construction of flat-fields for a long slit spectrograph. While showing promise, a more thorough analysis on the effect of averaging multiple fields on the SNR in different regions is necessary.

Appendix F

List of Observations

The transient classification programme involved 180 observations generated from 155 transient alerts.

The white left columns contain discovery information from the alerting source.

The first column is the object name. Multiple LT observations of the same object are numbered sequentially.

The alert sources are identified in the SRC column.

- # NNNN = Astronomer Telegram (ATel)
- Gaia=Gaia Photometric Alert from web-site or Gaia marshall
- TNS=Transient Name Server
- CBAT=Central Bureau for Astronomical Telegrams

The RA and Dec are Right Ascension and Declination. Date UT is the discovery date/time UTC. Where only a date was provided by an alert, midday is assumed as the time. Mag. is reported discovery magnitude. The proposed host galaxy and redshift z are either from the alert or obtained from NED/SIMBAD.

The yellow coloured central section contain information about the SPRAT observation Date and time of the observation. N = the number of exposures taken. Exp. = the individual exposure time (total exposure = $N \times \text{Exp.}$) SNID classification: Closest match, Age and z are from the best fit manually selected from SNID suggested spectra.

Si Vel. = mean ejecta velocity obtained from 3 estimates of the centre of the SiII feature taken using the FIGARO `abline` and correcting for host galaxy radial velocity from its redshift. The mean s.d. using this method was $\sim 100 \text{ km s}^{-1}$.

LT Atel = An Astronomer Telegram submitted by the ARI

The white columns on the right contain information reported by other classification sources.

DISCOVERY Object	SRC	RA	Dec	Date UT	Mag.	Host Galaxy	Host z	OBSERVATION Date	N x	Exp s	SNID Class	SNID Age	SNID Match	SNID z	SI Vel. km/s	LT Atel	Other Atel	SI Vel. km/s	Type	Age d	
ASASSN-14li	#6777	12:46:15.23	+17:46:26.22	2014/11/22 15:07:12	16.50	PCC 043234	0.02600	2014/12/04 05:41:51	1	400	CV	6	sn1996E	0.021	10556		#6777		CV/AGN		
ASASSN-14lo	#6794	10:51:53.19	-21:35:31.03	2015/01/10 13:55:12	16.20	UGC 06837	0.01990	2014/12/18 06:05:38	1	800	CV	6	sn1996E	0.021	10556		#6811		CV/AGN	0	
ASASSN-15al	#6894	10:57:49.63	-21:35:34.11	2015/01/10 17:55:12	16.89	GALEXASC 1045749.46-213526.3	Unk	2015/01/16 22:42:01	1	800	Fail						#6909		la	0	
ASASSN-15ar	#6915	02:28:20.36	+10:23:03.87	2015/01/13 11:02:24	17.00	CGCG 439-010	0.028820	2015/01/17 03:08:18	1	400	la	-4	sn1997E	0.030	12186		#6925		la	-5	
ASASSN-15az	#6921	11:08:37.60	-10:14:57.85	2015/01/14 11:02:24	16.70	2MASX J11083863-1014456	0.019998	2015/03/04 02:20:44	1	400	la	9	sn2006N	0.012	10095		#7086		la	-4	
ASASSN-15bb	#7078	15:46:58.69	+17:53:02.55	2015/02/15 13:55:12	15.19	NGC 5996	0.032216	2015/03/04 03:34:36	1	400	Fail						#7180		la	9	
ASASSN-15bd	#7145	16:41:20.87	+08:54:31.66	2015/03/01 14:09:36	17.00	CGCG 080-055	Unk	2015/03/27 20:55:04	1	500	Fail	57	sn1995F	0.139			#7219		lbn		
ASASSN-15be	#7163	16:46:25.16	+50:59:30.72	2015/03/01 14:09:36	17.10	PGC 059030	0.033430	2015/03/27 20:55:04	1	500	Fail						#7305		la	-2	
ASASSN-15bf	#7281	09:20:20.44	-07:38:26.78	2015/03/24 08:24:00	16.40	2MASX J09202045-0738229	0.017479	2015/04/01 02:09:35	1	800	Fail						#7323		II		
ASASSN-15bz	#7300	13:35:25.14	+01:24:33.00	2015/03/30 13:40:48	16.85	NGC 5227	0.006631	2015/04/01 01:48:17	1	800	la-91bg	-3	sn1999by	0.007	10166	#7333					
ASASSN-15ga	#7317	12:59:27.292	+14:10:15.79	2015/03/30 08:57:36	15.60	NGC 4866	0.034027	2015/04/16 00:24:08	1	600	la	0	sn1996X	0.035	11543		#7401		la	-2	
ASASSN-15gd	#7385	14:42:32.09	-13:27:35.90	2015/04/13 07:26:24	16.78	2MASX J14423254-1327294	0.030978	2015/04/20 21:00:56	1	600	la	9	sn2007ca	0.032	10420		#7411		la	0	
ASASSN-15gc	#7398	10:24:38.81	-02:59:07.70	2015/04/15 04:48:00	16.65	LRS B102206.7-024353	0.030978	2015/04/20 21:00:56	1	600	la	9	sn2007ca	0.032	10420		#7411		la	0	
ASASSN-15hd	#7426	09:09:23.89	-04:43:30.98	2015/04/19 01:26:24	16.90	2MASX J09092384-044327	Unk	2015/04/22 20:51:43	1	600	la	3	sn2005cf	0.042			#7432		la	3	
ASASSN-15hb	#7450	20:10:02.35	-00:44:21.31	2015/04/25 05:02:24	16.40	APMUKS(B) B222606.49-654315.6	Unk	2015/04/28 04:39:32	1	600	la-pec	-12	sn2006gz	0.030			#7452		la-pec	-14	
ASASSN-15hh	#7483	09:59:59.57	-02:53:16.36	2015/05/06 01:40:48	16.50	GALEXASC 095959.71-025322	0.019827	2015/05/10 20:57:24	1	600	Fail						#7531		12800	la	-6
ASASSN-15hi	#7491	15:57:08.15	-12:40:23.93	2015/05/11 07:26:24	16.70	2MASX J15570808-1240252	0.023316	2015/05/14 00:47:48	2	800	la	-3	sn2006S	0.022	9713		#7497		la	-5	
ASASSN-15hj	#7507	11:20:06.399	+34:07:43.00	2015/05/13 08:52:48	17.20	2MASX J11200680-3407396	0.035660	2015/05/16 23:15:50	2	800	la	5	sn2007au	0.038	10040		#7510		10980	la	2
ASASSN-15jm (1)	#7550	17:21:09.189	+25:34:55.50	2015/05/19 09:50:24	17.10	2MASX J17210913-2534558	Unk	2015/05/21 00:33:11	4	400	la-91T	-1	sn2006cm	0.047		#7550					
ASASSN-15jm (2)							Unk	2015/05/22 00:33:11	4	400	la-91T	-1	sn2006cm	0.047							
ASASSN-15ke	#7568	15:25:44.81	+59:21:10.09	2015/05/26 08:24:00	17.00	2MASX J15254441+5921091	0.045359	2015/05/27 23:04:46	2	400	Fail						#7571		10200	la	9
ASASSN-15mf	#7775	14:14:22.80	-02:58:31.00	2015/07/07 07:40:48	16.80	UGC 09108 NED02	0.026000	2015/07/09 21:52:06	1	600	la	-2	sn2001ep	0.024	11207	#7781					
ASASSN-15mg	#7790	14:03:15.75	+41:36:14.36	2015/07/06 07:40:48	17.20	Mrk 0283a	0.034446	2015/07/15 21:29:43	1	600	la	-6	sn2008Z	0.039	10810		#7796		la-pec		
ASASSN-15mh	#7790	14:03:15.75	+41:36:14.36	2015/07/06 07:40:48	17.20	Mrk 0283a	0.034446	2015/07/15 21:29:43	1	600	la	-6	sn2008Z	0.039	10810		#7796		la-pec		
ASASSN-15mi	#7790	14:03:15.75	+41:36:14.36	2015/07/06 07:40:48	17.20	Mrk 0283a	0.034446	2015/07/15 21:29:43	1	600	la	-6	sn2008Z	0.039	10810		#7796		la-pec		
ASASSN-15mj	#7790	14:03:15.75	+41:36:14.36	2015/07/06 07:40:48	17.20	Mrk 0283a	0.034446	2015/07/15 21:29:43	1	600	la	-6	sn2008Z	0.039	10810		#7796		la-pec		
ASASSN-15mk	#7790	14:03:15.75	+41:36:14.36	2015/07/06 07:40:48	17.20	Mrk 0283a	0.034446	2015/07/15 21:29:43	1	600	la	-6	sn2008Z	0.039	10810		#7796		la-pec		
ASASSN-15ml	#7790	14:03:15.75	+41:36:14.36	2015/07/06 07:40:48	17.20	Mrk 0283a	0.034446	2015/07/15 21:29:43	1	600	la	-6	sn2008Z	0.039	10810		#7796		la-pec		
ASASSN-15mm	#7792	15:25:23.50	+29:10:24.50	2015/07/13 08:24:00	17.50	SDSS J152523.40+291018.8	0.021466	2015/07/14 21:28:49	2	400	II	-5	sn1999gl	0.021	9568	#7802					
ASASSN-15mp	#7808	00:58:45.265	+44:04:11.82	2015/07/17 08:28:48	16.70	2MASX J00584521-4404122	Unk	2015/07/19 04:30:00	2	400	la	3	sn2006cf	0.037	10400	#7817					
ASASSN-15mq	#7811	19:39:56.82	+50:55:28.49	2015/07/18 10:04:48	17.40	CGCG 257-002	0.026759	2015/07/20 00:47:49	2	400	Gal						#7877		AGN		
ASASSN-15mr	#7811	19:39:56.82	+50:55:28.49	2015/07/18 10:04:48	17.40	CGCG 257-002	0.026759	2015/07/20 00:47:49	2	400	Gal						#7877		AGN		
ASASSN-15ms	#7811	19:39:56.82	+50:55:28.49	2015/07/18 10:04:48	17.40	CGCG 257-002	0.026759	2015/07/20 00:47:49	2	400	Gal						#7877		AGN		
ASASSN-15mt	#7811	19:39:56.82	+50:55:28.49	2015/07/18 10:04:48	17.40	CGCG 257-002	0.026759	2015/07/20 00:47:49	2	400	Gal						#7877		AGN		
ASASSN-15mu	#7811	19:39:56.82	+50:55:28.49	2015/07/18 10:04:48	17.40	CGCG 257-002	0.026759	2015/07/20 00:47:49	2	400	Gal						#7877		AGN		
ASASSN-15mv	#7811	19:39:56.82	+50:55:28.49	2015/07/18 10:04:48	17.40	CGCG 257-002	0.026759	2015/07/20 00:47:49	2	400	Gal						#7877		AGN		
ASASSN-15mw	#7811	19:39:56.82	+50:55:28.49	2015/07/18 10:04:48	17.40	CGCG 257-002	0.026759	2015/07/20 00:47:49	2	400	Gal						#7877		AGN		
ASASSN-15mx	#7811	19:39:56.82	+50:55:28.49	2015/07/18 10:04:48	17.40	CGCG 257-002	0.026759	2015/07/20 00:47:49	2	400	Gal						#7877		AGN		
ASASSN-15my	#7811	19:39:56.82	+50:55:28.49	2015/07/18 10:04:48	17.40	CGCG 257-002	0.026759	2015/07/20 00:47:49	2	400	Gal						#7877		AGN		
ASASSN-15mz (1)	#7909	02:23:13.210	-04:31:02.05	2015/08/10 12:14:24	17.40	UGC 01332	0.022619	2015/08/02 01:26:56	2	100	la-91bg	8	sn2006H	0.021	9315		#7871		CV		
ASASSN-15mz (2)	#7911	22:30:41.977	+39:17:35.22	2015/08/14 10:04:48	16.50	MCG +06-49-027	0.016835	2015/08/17 23:40:22	3	400	la	-5	sn2004fu	0.022	12112		#7913		la	-7	
ASASSN-15na	#7917	16:36:36.156	+55:33:09.95	2015/08/16 05:02:24	16.60	SDSS J163636.15+553311.0	Unk	2015/08/17 21:10:26	2	400	Fail						#7924		la		
ASASSN-15nb	#8273	06:12:33.398	-14:15:26.94	2015/11/11 07:26:24	17.10	MCG -02-16-004	0.035558	2015/11/12 01:47:53	2	300	la	-1	sn2007F	0.037	10700	#8279					
ASASSN-15zc (1)	#8404	02:41:08.86	+43:40:48.80	2015/12/12 08:52:48	17.30	UGC 02164	0.022862	2015/12/16 19:58:25	3	400	la	-8	sn2002cu	0.035							
ASASSN-15zc (2)							0.022862	2015/12/19 22:11:23	3	400	la	-7	sn2004ef	0.033							
ASASSN-15zd (1)	#8408	13:34:54.473	+10:59:04.69	2015/12/12 15:07:12	16.90	SDSS J133454.38+105905.6	Unk	2015/12/15 06:35:32	2	300	AGN										
ASASSN-15zd (2)							Unk	2015/12/15 06:35:32	2	300	AGN										
ASASSN-15aa (1)	#8480	01:43:56.574	+17:03:34.44	2015/12/29 08:09:36	16.70	VV 790a	0.026795	2015/01/03 20:30:08	2	400	AGN						Simbud		Quasar		
ASASSN-15aa (2)							0.026795	2015/01/03 20:30:08	2	400	AGN						#8495		la	0	
ASASSN-15ab	#8488	06:27:08.174	+27:48:41.74	2015/12/31 09:07:12	16.40	2MASX J06270817+2748382	0.020330	2016/01/01 02:10:49	2	400	Gal						#8493		la	-3	
ASASSN-15ab	#8502	11:55:04.245	-01:43:06.77	2016/01/03 14:52:48	14.70	PGC 037392	0.004293	2016/01/04 02:36:24	2	400	II	-3	sn2004er	0.002		#8505		II			
ASASSN-15ac	#8556	04:45:21.278	+73:23:41.09	2016/01/15 08:38:24	17.40	CGCG 328-018	0.019524	2016/01/17 23:34:46	2	400	la	13	sn2002bn	0.023		#8560					
ASASSN-15ad	#9073	18:30:02.383	-39:57:54.31	2016/05/20 12:57:56	16.40	IC 1289	0.018313	2016/05/20 12:57:56	3	200	la	0	sn2003ch	0.016	11000		#9075		la	-4	
ASASSN-15ae	#9081	12:56:58.887	-15:32:10.51	2016/05/26 05:02:24	16.20	H-alpha	0.020120	2016/05/29 23:16:42	3	200	la	-7	sn2008Z	0.021	11350		#9118		la		
ASASSN-15af	#9081	12:56:58.887	-15:32:10.51	2016/05/26 05:02:24	16.20	H-alpha	0.020120	2016/05/29 23:16:42	3	200	la	-7	sn2008Z	0.021	11350		#9118		la		
ASASSN-15ag	#9114	14:47:06.98	+11:35:41.92	2016/06/03 10:19:12	16.80	2MASX J13323577-0516218	0.029610	2016/05/29 23:40:07	3	200	la-91T	-2									

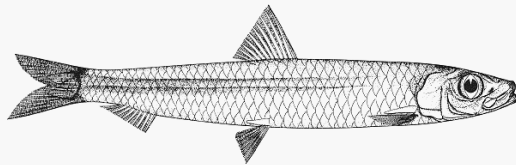
DISCOVERY Object	SRC	RA	Dec	Date UT	Mag.	Galaxy	Host z	OBSERVATION Date	N x	Exp s	SNID Class.	SNID Age	SNID Match	SNID z	Si Vel. km/s	LT Atel	Other Atel	Si Vel. km/s	Type	Age d
AT2016adl	#8652	11:51:56.24	-13:25:03.07	2016/02/08 05:02:24	17.00	GALEXASC J115155.69-132459.3	0.097000	2016/02/11 01:37:22	2	200	II	1	sn2004et	0.004	#8679		#8679	10600	II	4
AT2016adn	#8660	05:10:34.46	+04:16:10.80	2016/02/02 18:45:39	16.50	ZMASX J03103162+0416184	0.023000	2016/02/11 20:33:52	2	300	la	0	sn2003ch	0.022	#8672		#8672	10600	la	2
AT2016adp	#8666	14:06:44.37	+71:53:15.25	2016/02/09 14:22:40	16.20	CGCG 336-041	0.034194	2016/02/11 02:09:41	2	300	Fail								la	10
AT2016aew	#6685	14:11:26.49	+01:17:09.47	2016/02/12 12:28:40	17.30	IC 0986	0.025001	2016/02/14 05:25:25	2	300	la	-9	sn2007bm	0.020	#8694		#8694		la	0
AT2016aib	TNS	10:51:12.55	+19:21:45.03	2016/01/03 11:12:33	17.82	ZMASX J10511255+1921474	0.047912	2016/01/29 04:04:10	3	400	la	20	sn2006cf	0.050	#8524		#8524		la	0
AT2016azc	TNS	14:05:57.10	+43:53:02.20	2016/01/31 14:24:00	16.60	SDSS J140557.36+435257.2	0.034000	2016/02/04 05:36:30	2	300	la-91T	-2	sn2001eh	0.034	#8634		#8634	10500		
AT2016azd	#8628	12:05:25.83	-21:24:01.20	2016/02/02 06:43:12	17.00	ZMASX J12052488+2123572	0.031939	2016/02/04 03:21:58	2	400	la	-8	sn2006ax	0.033	#8634		#8634	11100		
AT2016aqk	#8775	15:19:26.89	-00:55:29.71	2016/03/04 09:07:12	17.00	ZMASX J15192684-0055256	0.029722	2016/03/08 04:58:32	2	200	la	1	sn2006X	0.031	#8794		#8794	15000		
AT2016aqr	#8796	15:13:54.326	-04:45:25.89	2016/03/06 09:50:24	17.20	SDSS J151354.30+044525.7	0.041934	2016/03/10 04:38:37	2	200	la-91T	-4	sn2007S	0.044	#8798		#8798	10000		
AT2016arf	#8801	13:45:00.521	+61:16:48.90	2016/03/10 13:55:12	16.80	CGCG 295-010	0.034811	2016/03/12 02:52:13	2	200	la	-2	sn2006nz	0.040	#8830		#8830	12600	la	-2
AT2016aui	TNS	11:20:59.02	+53:10:25.60	2016/03/13 23:22:34	17.80	NGC 3631	0.003856	2016/03/16 00:45:19	3	200	lb	-6	sn2004gq	0.004	#8818		#8818	16800	lb	-8.5
AT2016aue	TNS	07:19:27.39	+47:32:19.80	2016/03/11 07:55:12	17.43	None	Unk	2016/03/17 20:40:14	3	200	Gal									
AT2016aui	#8839	18:02:55.28	+69:15:29.70	2016/03/11 14:52:48	17.95	ZMASX J18025452+6915258	0.024000	2016/03/17 03:43:43	3	200	la	1	sn2005na	0.051	#8899		#8899	11000	la	-1
AT2016aui	TNS	14:09:40.49	-00:39:24.04	2016/03/31 17:37:10	17.40	CGCG 018-062	0.032641	2016/04/04 02:21:06	3	300	la	4	sn2005el	0.023	#8899		#8899	11000	la	-1
AT2016aui	#8892	14:59:42.13	+04:05:08.09	2016/03/31 11:17:00	16.80	SDSS J145942.12+040518.1	0.032641	2016/04/04 02:43:22	3	200	la	10	sn2008Z	0.033	#8896		#8896	11900	la	7
AT2016aui	#8915	13:03:10.74	-21:59:14.28	2016/04/06 05:45:36	16.80	ZMASX J13031054-2159149	0.032773	2016/04/09 00:45:57	3	200	la	3	sn2001gc	0.026	#8924		#8924	11800	la	0
AT2016aui	#8939	19:10:37.33	+37:39:17.02	2016/04/11 13:26:24	16.90	UGC 11409	0.028016	2016/04/14 03:48:41	3	200	la	6	sn2006ev	0.025	#8955		#8955	10400	la	-4
AT2016aui	TNS	12:05:14.48	+10:36:55.40	2016/04/16 12:46:49	17.40	NGC 4083	0.034000	2016/04/23 22:05:52	3	200	la-91lg	8	sn2006hb	0.034	#8985		#8985			
AT2016aui	#9001	11:50:54.530	+02:18:26.41	2016/04/27 09:21:36	16.90	DS J115054.45+021828.1	Unk	2016/04/28 21:24:03	3	200	la	1	sn2001ay	0.014	#9016		#9016	8800	la	3
AT2016aui	#9020	17:10:23.919	+26:23:47.89	2016/05/03 10:19:12	17.50	SDSS J171023.63+262350.3	Unk	2016/05/05 02:40:26	3	200	la-pec	-9	sn2006gz	0.040	#9023		#9023			
AT2016aui	TNS	17:35:37.80	+08:48:32.35	2016/05/03 18:31:40	17.80	ZMASX J17353788+0848387	0.037000	2016/05/05 02:23:52	3	200	la	-1	sn1999cc	0.041	#9023		#9023	10600	la	0
AT2016aui	TNS	17:29:21.83	+16:12:22.30	2016/05/13 17:27:11	17.60	NGC 6375	0.020201	2016/05/15 00:51:35	4	200	M-star									
AT2016aui	#9073	18:30:02.41	+39:57:55.84	2016/05/20 12:54:43	16.40	IC 1289	0.018313	2016/05/22 01:10:15	3	200	Fail									
AT2016aui	#9086	21:59:04.14	+18:11:10.46	2016/05/27 12:57:36	15.70	UGC 11868	0.003646	2016/05/28 04:42:53	3	200	lc-BL?	-1	sn2006al	0.240	#9090		#9090		lc	pre
AT2016aui	#9095	12:08:06.80	+65:10:38.24	2016/05/28 04:39:05	14.80	NGC4125	0.004483	2016/05/29 03:16:12	3	200	lc-BL	27	sn1998bw	0.052	#9090		#9090		lc	pre
AT2016aui	TNS	22:46:12.82	+10:33:33.31	2016/06/18 19:31:24	17.80	MCG +02-58-008	0.039000	2016/06/22 21:23:31	3	100	la	-5	sn2007au	0.005	#9095		#9095	15400	la	-6
AT2016aui	TNS	21:09:35.83	+15:07:31.80	2016/07/02 09:21:40	17.90	NGC 7033	0.030290	2016/07/05 04:04:02	4	400	la	-1	sn2007hj	0.043	#9173		#9173	11200	la	-3
AT2016aui	TNS	14:43:25.74	+79:11:59.21	2016/07/06 08:38:24	15.05		Unk	2016/07/07 22:08:02	3	100	Fail									
AT2016aui	#9223	13:59:04.46	+33:08:20.30	2016/07/07 07:26:24	17.40	ZMASX J13590394+3308172	0.050972	2016/07/09 00:19:22	3	300	la	-2	sn2005ma	0.050	#9237		#9237	10800	la-91T	0
AT2016aui	#9422	23:47:11.64	+10:04:59.56	2016/08/27 13:40:47	17.10	SDSS J234711.91+100459.8	0.034000	2016/08/29 03:33:06	3	300	la	-6	sn2007F	0.030	#9420		#9420	12600	la	pre
AT2016aui	TNS	22:45:29.96	-07:20:07.14	2016/08/27 16:00:50	17.50	APMUKS(B) B224253.45-073553.1	Unk	2016/08/29 00:10:08	3	300	la	-1	sn2000dh	0.046	#9426		#9426	12500	la	-7

TNS

DISCOVERY Object	SRC	RA	Dec	Date UT	Host Galaxy	Host z	OBSERVATION Date	N x s	Exp s	SNID Class	SNID Age	SNID Match	SNID z	SI Vel. km/s	L.T. Atel	Other Atel	SI Vel. km/s	Type	Age d	
KISS15aa	KISS	01:10:24.10	+23:21:27.00	Unk	SDSS J011024.07+011014.1	Unk	2015/11/13 21:24:55	2	200	la-91T	-1	sn2007S	0.047							
KISS15b	#7390	12:02:35.42	+20:24:39.40	2015/04/17 12:00:00	Unk	2MASS J120235.35+202439.8	0.024943	2015/04/17 23:26:43	1	1000	II	0	sn2006cs	0.018		#7552			II	34
KISS15n (1)	KISS	13:00:32.33	+27:58:41.00	2015/05/10 12:57:36	18.30 COMA1 J130032.301+275841.02	0.023287	2015/05/13 23:12:57	3	800	la-91T?	-2	sn2006cz	0.009							
KISS15n (2)	KISS	13:00:32.33	+27:58:41.00	2015/05/10 12:57:36	18.30 COMA1 J130032.301+275841.02	0.023287	2015/05/17 01:04:44	6	800	la-91T	-2	sn2001eh	0.015		#7532	Simbad			la-pec	
KISS15w (1)	KISS	22:04:02.75	+09:30:50.00	Unk	2MASX J220402.82+093028.6	0.027228	2015/11/15 19:13:16	2	300	la-91T	14	sn2001fa	0.048	10200						
KISS15w (2)	KISS	03:11:16.73	+01:13:35.10	Unk	KUG 0308+010	0.027228	2015/11/15 23:20:58	2	300	lc-BL?	13	sn2002ap	0.025						II	0
KISS15y	KISS	02:03:50.88	+19:41:01.88	Unk	None	Unk	2015/11/14 01:52:08	2	300	la	-8	sn2007F	0.044							
J041227.87+342902.0	#8128	04:12:27.87	+34:29:02.00	2015/10/06 01:07:21	16.25 PGC097035	0.021000	2015/10/07 02:52:17	2	300	la	12	sn2005am	0.023	10600	#8138					
J172624.20+335044.4	#7346	17:26:24.20	+33:50:44.40	2015/04/01 23:21:51	17.60 SDSS J172624.20+335044.3	Unk	2015/04/10 20:45:16	1	800	Fail										
J015359.85+485955.6	#8262	01:53:59.85	+48:59:55.60	2015/11/09 22:40:00	15.20 PGC212862	Unk	2015/11/09 22:40:15	2	200	Fail					#8265					
J140958.91+174549.4	#8984	14:09:58.91	+17:45:49.40	2016/04/24 01:36:52	16.00 PGC0983	0.018000	2016/04/26 23:49:30	3	100	II	-5	sn1999gt	0.019			#9013			II	0
PS15awz		11:00:09.77	+05:33:48.50	2015/04/22 12:00:00	17.69 SDSS J110009.83+053348.6	0.060000	2015/04/23 23:18:43	1	600	la-91T	-1	sn2007S	0.057	11521	#7440					
PS15afa		10:50:18.15	+12:06:28.10	2015/04/23 12:00:00	17.42 MCG 3404	0.015364	2015/04/24 21:00:16	1	800	II	25	sn2006et	0.015			#7452			II	15
PS15ahs (1)		17:59:29.77	+43:32:24.00	2015/05/02 12:00:00	17.82 MCG +07:37:01. SDSS DR12	0.031000	2015/05/06 00:57:23	2	800	la	-15	sn1999cp	0.032	11443	#7477					
PS15ahs (2)		17:59:29.77	+43:32:24.00	2015/05/02 12:00:00	17.82 MCG +07:37:01. SDSS DR12	0.031000	2015/05/14 01:41:31	2	800	la	-6	sn2002cu	0.040							
PS15aap	#7488	13:21:55.23	+35:21:32.00	2015/05/02 12:00:00	17.46 KUG J1319+356	0.019477	2015/05/10 21:27:44	3	800	II	156	sn2005cs	0.017			#7530			II n	30
PS15aah	#7488	15:38:29.86	+27:17:56.10	2015/05/08 12:00:00	18.06 SDSS J153829.54+271753.2	0.032280	2015/05/11 03:28:43	3	800	II	8	sn2006bp	0.037			#7611			II	14
PS15aaj	#7489	19:51:09.81	+36:41:31.10	2015/05/09 12:00:00	16.94 None	Unk	2015/05/14 02:52:58	2	800	Fail										
PS15aak	#7723	21:20:28.08	+31:11:09.80	2015/06/25 12:00:00	16.78 GALEXASC J212028.21+311109.7	Unk	2015/07/01 04:07:07	2	600	Fail										
PS15abv (1)		17:59:29.77	+43:32:24.00	2015/06/25 12:00:00	17.82 MCG +07:37:01. SDSS DR12	Unk	2015/07/03 03:07:53	2	600	Fail					#7757				CV	
PS15abv (2)		17:59:29.77	+43:32:24.00	2015/06/25 12:00:00	17.82 MCG +07:37:01. SDSS DR12	Unk	2015/07/10 02:52:26	2	600	Gal										
PS15abd	#7769	23:44:04.67	+44:00:34.20	2015/07/04 12:00:00	17.73 SDSS J234404.66+440034.2	0.012000	2015/08/01 22:01:48	2	400	la	1	sn2002kf	0.038	11000	#7867					
PS15ah	#7876	15:31:31.38	+33:06:04.80	2015/07/25 12:00:00	18.37 SDSS J153131.39+330604.3	0.023783	2015/08/06 22:11:16	2	200	II	43	sn1979C	0.025		#7884					
PS15aha	#7876	19:28:43.62	+56:41:21.70	2015/08/01 12:00:00	17.88 UGC 11445	Unk	2015/12/03 00:54:51	2	600	Fail										
PS15awx	#8299	05:14:47.80	+07:03:01.30	2015/11/17 12:00:00	17.07 MFGC 04279	0.028700	2015/03/13 22:59:17	1	600	la	-3	sn1996X	0.029	10640		#7219			la	0
PS15amb	#7212	06:59:40.13	+15:11:12.40	2015/03/10 12:00:00	17.07 SDSS J065940.13+151112.4	0.063900	2015/03/28 00:37:37	1	600	II n	175	sn1997cy	0.055			#7308			II n	20
PS15ame	#7280	11:10:22.93	-04:21:31.50	2015/03/23 12:00:00	17.16 GALEXASC J095359.89+21748.4	0.012140	2015/03/27 21:36:04	1	600	Gal										
PS15aj	#7295	10:19:21.35	-22:08:37.60	2015/03/25 12:00:00	17.61 CTS 1011	0.017600	2015/01/06 20:11:03	1	400	la	12	sn2001G	0.028	8581	#6845	8500		la	-3	
PSN0281419+380111	CBAT	03:28:14.26	+38:01:10.30	2014/12/27 08:09:36	16.68 PGC 213221	0.080000	2015/11/17 05:08:41	2	200	la-91T	6	sn2007S	0.077	11500	#8295	11500		la	0	
PSN07051005+2102327	CBAT	07:05:10.05	+21:02:32.70	2015/11/17 05:08:41	16.50 PGC 1641403	Unk	2015/12/31 02:28:57	2	400	Fail										
PSN012080010+1944267	CBAT	12:8:00.10	+19:44:26.70	2015/11/17 05:08:41	16.50 PGC 1641403	Unk	2015/04/16 01:24:24	1	600	la	19	sn2004er	0.032	9830	#7403					
PSN013332289+5843315	CBAT	13:33:22.89	+58:43:31.50	2015/04/01 12:00:00	16.90 None	0.016195	2015/02/17 05:38:11	1	400	la	-3	sn2001ex	0.006	9972		#7091			la	1
PSN014095513+1731556 (1)	CBAT	14:09:55.13	+17:31:55.60	2015/02/14 12:00:00	17.54 NGC 5490	0.016000	2015/03/01 06:25:29	2	400	la	4	sn2004gs	0.021							
PSN014095513+1731556 (2)		14:09:55.13	+17:31:55.60	2015/02/14 12:00:00	17.54 NGC 5490	0.016000	2015/03/04 01:52:44	1	800	la	19	sn2006bk	0.016							
PSN014095513+1731556 (3)		14:09:55.13	+17:31:55.60	2015/02/14 12:00:00	17.54 NGC 5490	0.016000	2015/03/06 02:38:57	1	800	la	24	sn2006af	0.019							
PSN014095513+1731556 (4)		14:09:55.13	+17:31:55.60	2015/02/14 12:00:00	17.54 NGC 5490	0.016000	2015/03/29 00:51:19	1	800	la	33	sn2003du	0.019							
PSN014095513+1731556 (5)		14:09:55.13	+17:31:55.60	2015/02/14 12:00:00	17.54 NGC 5490	0.016000	2015/04/01 04:48:13	1	800	la-91hg	33	sn1999by	0.017							
PSN014095513+1731556 (6)		14:09:55.13	+17:31:55.60	2015/02/14 12:00:00	17.54 NGC 5490	0.016000	2015/04/11 03:16:11	1	800	Fail										
PSN014095513+1731556 (7)		14:09:55.13	+17:31:55.60	2015/02/14 12:00:00	17.54 NGC 5490	0.016000	2015/04/20 00:06:16	1	800	Fail										
PSN014095513+1731556 (8)		14:09:55.13	+17:31:55.60	2015/02/14 12:00:00	17.54 NGC 5490	0.016000	2015/07/10 22:21:27	1	600	la	-1	sn2007hd	0.030	11815	#7794					
PSN017520838+1314252	CBAT	17:52:08.38	+13:14:25.22	2015/07/07 21:17:06	17.60 2MASX J175209.13+1314038	0.033200	2015/08/17 00:27:45	4	600	lb	9	sn1984L	0.020			#7896	6000		lb	
PSN023002463+0137368 (1)	#7886	23:00:24.63	+01:37:36.80	2015/08/06 21:17:12	15.90 UGC12295	0.016128	2015/08/17 00:27:45	4	600	lb	9	sn1984L	0.020			#7888	9000		II	
PSN023470615+2929074	CBAT	23:47:06.15	+29:29:07.40	2015/08/06 16:19:12	17.30 NGC 7763	0.017242	2015/08/09 23:27:13	2	300	II	4	sn2004et	0.019							

OTHER

ERGO NULLA PRESSURA



"Spratelloides Gracilis"

Bibliography

Aasi, J., Abadie, J., Abbott, B. P., et al. 2014, *ApJS*, 211, 7

—. 2015, *Classical and Quantum Gravity*, 32, 115012

Abbott, B. P., Abbott, R., Abbott, T. D., et al. 2016a, *Physical Review Letters*, 997

—. 2016b, *ApJL*, 826, L13

—. 2016c, *Physical Review Letters*, 116, 061102

—. 2016d, *Living Reviews in Relativity*, 19, 1

—. 2016e, *ApJS*, 225, 8

Allen, C. W. 1973, *Astrophysical quantities*

Allkofer, O. C., Carstensen, K., Dau, W. D., & Jokisch, H. 1975, *Journal of Physics G Nuclear Physics*, 1, L51

ANDOR. 2012, *CCD Performance of iDus DU420A-BV Camera s/n 14307*, ANDOR Technology Ltd.

Arnett, W. D. 1969, *Ap&SS*, 5, 180

Arnold, D. M., Steele, I. A., Bates, S. D., Mottram, C. J., & Smith, R. J. 2012, in *Society of Photo-Optical Instrumentation Engineers (SPIE) Conference Series*, Vol. 8446, *Society of Photo-Optical Instrumentation Engineers (SPIE) Conference Series*

- Baldry, I. K., Bland-Hawthorn, J., & Robertson, J. G. 2004, *PASP*, 116, 403
- Barden, S. C., Arns, J. A., & Colburn, W. S. 1998, in *Society of Photo-Optical Instrumentation Engineers (SPIE) Conference Series*, Vol. 3355, *Optical Astronomical Instrumentation*, ed. S. D'Odorico, 866–876
- Barnes, J., & Kasen, D. 2013, *ApJ*, 775, 18
- Barnsley, R. M., Jermak, H. E., Steele, I. A., et al. 2016, *Journal of Astronomical Telescopes, Instruments, and Systems*, 2, 015002
- Barnsley, R. M., Smith, R. J., & Steele, I. A. 2012, *Astronomische Nachrichten*, 333, 101
- Barnsley, R. M., Steele, I. A., Smith, R. J., & Mawson, N. R. 2014, in *SPIE*, Vol. 9152, *Software and Cyberinfrastructure for Astronomy III*, 91522L
- Bellm, E. 2014, in *The Third Hot-wiring the Transient Universe Workshop*, ed. P. R. Wozniak, M. J. Graham, A. A. Mahabal, & R. Seaman, 27–33
- Ben-Ami, S., Konidaris, N., Quimby, R., et al. 2012, in *Proc. SPIE*, Vol. 8446, *Ground-based and Airborne Instrumentation for Astronomy IV*, 844686
- Benetti, S., Tomasella, L., Cappellaro, E., et al. 2015, *GRB Coordinates Network*, 18563
- Berger, E. 2014, *ARA&A*, 52, 43
- Berger, E., Fong, W., & Chornock, R. 2013, *ApJL*, 774, L23
- Berry, C. P. L., Mandel, I., Middleton, H., et al. 2015, *ApJ*, 804, 114
- Blagorodnova, N., Kuposov, S. E., Wyrzykowski, Ł., Irwin, M., & Walton, N. A. 2014, *MNRAS*, 442, 327

- Bloemen, S., Groot, P., Nelemans, G., & Klein-Wolt, M. 2015, in *Astronomical Society of the Pacific Conference Series*, Vol. 496, *Living Together: Planets, Host Stars and Binaries*, ed. S. M. Rucinski, G. Torres, & M. Zejda, 254
- Blondin, S., & Tonry, J. L. 2007, *Astrophysical Journal*, 666, 1024
- Bloom, J. S., Richards, J. W., Nugent, P. E., et al. 2012, *PASP*, 124, 1175
- Born, M., & Wolf, E. 1999, *Principles of Optics*, 986
- Brown, E. B. 1965, *Modern Optics*
- Campana, S., Mangano, V., Blustin, A. J., et al. 2006, *Nature*, 442, 1008
- Cenko, S., Cao, Y., Ferretti, R., et al. 2015, *GRB Coordinates Network*, 18762
- Chandrasekhar, S. 1935, *MNRAS*, 95, 207
- Connaughton, V., Burns, E., Goldstein, A., et al. 2016, *ArXiv e-prints*, arXiv:1602.03920
- Copperwheat, C., & Steele, I. 2015a, *GRB Coordinates Network*, 18791
- . 2015b, *GRB Coordinates Network*, 18807
- . 2015c, *GRB Coordinates Network*, 18812
- Copperwheat, C., Steele, I., & Piascik, A. 2015a, *GRB Coordinates Network*, 18832
- Copperwheat, C. M., Steele, I. A., Barnsley, R. M., et al. 2015b, *Experimental Astronomy*, 39, 119
- Copperwheat, C. M., Steele, I. A., Piascik, A. S., et al. 2016, *MNRAS*, 462, 3528
- D'Avanzo, P., Melandri, A., Piranomonte, S., et al. 2015, *GRB Coordinates Network*, 18536

- D'Avanzo, P., Melandri, A., Piranomonte, S., et al. 2015, GRB Coordinates Network, 18775
- D'Avanzo, P., Melandri, A., Brocato, E., et al. 2015, GRB Coordinates Network, 18822
- Dong, S., Shappee, B. J., Prieto, J. L., et al. 2016, *Science*, 351, 257
- Drake, A. J., Djorgovski, S. G., Mahabal, A., et al. 2009, *ApJ*, 696, 870
- Evans, P., Kennea, J., Barthelmy, S., et al. 2015, GRB Coordinates Network, 18569
- Evans, P. A., Kennea, J. A., Palmer, D. M., et al. 2016, *MNRAS*, 462, 1591
- Eversberg, T., & Vollmann, K. 2015, *Spectroscopic Instrumentation: Fundamentals and Guidelines for Astronomers*
- Fawcett, T. 2006, *Pattern Recogn. Lett.*, 27, 861
- Filippenko, A. V. 1982, *Proc. Ast. Soc. Pacific*, 94, 715
- . 1988, *AJ*, 96, 1941
- Filippenko, A. V., Richmond, M. W., Branch, D., et al. 1992, *AJ*, 104, 1543
- Foley, R. J. 2013, *MNRAS*, 435, 273
- Gray, R. O., Napier, M. G., & Winkler, L. I. 2001, *Astronomical Journal*, 121, 2148
- Harmer, C. F. W. 1974, *Monthly Notes of the Royal Astronomical Society*, 167, 311
- Harutyunyan, A. H., Pfahler, P., Pastorello, A., et al. 2008, *A&A*, 488, 383
- Heger, A., Fryer, C. L., Woosley, S. E., Langer, N., & Hartmann, D. H. 2003, *ApJ*, 591, 288
- Hill, G. J., J., W. M., R., T. J., & C., S. E. 2003a, in *Specialized Optical Developments in Astronomy*

- Hill, G. J., Wolf, M. J., Tufts, J. R., & Smith, E. C. 2003b, in Society of Photo-Optical Instrumentation Engineers (SPIE) Conference Series, Vol. 4842, Specialized Optical Developments in Astronomy, ed. E. Atad-Ettinger & S. D'Odorico, 1–9
- Hodapp, K. W., Kaiser, N., Aussel, H., et al. 2004, *Astronomische Nachrichten*, 325, 636
- Horne, K. 1986, *PASP*, 98, 609
- Howell, D. A., Sullivan, M., Perrett, K., et al. 2005, *ApJ*, 634, 1190
- Howell, D. A., Sullivan, M., Nugent, P. E., et al. 2006, *Nature*, 443, 308
- Itoh, R., Kanda, Y., Yoshida, M., et al. 2015, GRB Coordinates Network, 18742
- Ivezic, Z., Tyson, J. A., Axelrod, T., et al. 2009, in Bulletin of the American Astronomical Society, Vol. 41, American Astronomical Society Meeting Abstracts #213, 366
- Jewitt, D. 2003, *Earth Moon and Planets*, 92, 465
- Kaiser, N., Burgett, W., Chambers, K., et al. 2010, in SPIE, Vol. 7733, Ground-based and Airborne Telescopes III, 77330E
- Kantor, J. 2014, in The Third Hot-wiring the Transient Universe Workshop, ed. P. R. Wozniak, M. J. Graham, A. A. Mahabal, & R. Seaman, 19–26
- Kasen, D., Fernández, R., & Metzger, B. D. 2015, *MNRAS*, 450, 1777
- Kasliwal, M. M., & Nissanke, S. 2014, *ApJL*, 789, L5
- Kasliwal, M. M., Cenko, S. B., Singer, L. P., et al. 2016, *ApJL*, 824, L24
- Keller, S. C., Schmidt, B. P., Bessell, M. S., et al. 2007, "Publications of the Astronomical Society of Australia", 24, 1

- King, D. 1985, RGO/La Palma technical note no 31
- Kirkpatrick, J. D., Reid, I. N., Liebert, J., et al. 1999, *Astrophysical Journal*, 519, 802
- Kisaka, S., Ioka, K., & Nakamura, T. 2015, *ApJL*, 809, L8
- Kitaura, F. S., Janka, H.-T., & Hillebrandt, W. 2006, *A&A*, 450, 345
- Knigge, C. 2011, in *Astronomical Society of the Pacific Conference Series*, Vol. 447, *Evolution of Compact Binaries*, ed. L. Schmidtobreick, M. R. Schreiber, & C. Tappert, 3
- Lamb, G. P., & Kobayashi, S. 2016, *ApJ*, 829, 112
- Law, N. M., Kulkarni, S. R., Dekany, R. G., et al. 2009a, *PASP*, 121, 1395
- . 2009b, *PASP*, 121, 1395
- Li, L.-X., & Paczyński, B. 1998, *ApJL*, 507, L59
- Li, W., Filippenko, A. V., Chornock, R., et al. 2003, *PASP*, 115, 453
- LIGO Scientific Collaboration and Virgo. 2015a, *GRB Coordinates Network*, 18442
- . 2015b, *GRB Coordinates Network*, 18626
- . 2015c, *GRB Coordinates Network*, 18728
- Lipunov, V., Gorbovskoy, E., Tyurina, N., et al. 2015, *GRB Coordinates Network*, 18729
- Lipunov, V. M., Krylov, A. V., Kornilov, V. G., et al. 2004, *Astronomische Nachrichten*, 325, 580
- LSST Science Collaboration, Abell, P. A., Allison, J., et al. 2009, *ArXiv e-prints* 0912.0201, arXiv:0912.0201
- Marsh, T. R. 1989, *PASP*, 101, 1032

- Martin, D., Perego, A., Arcones, A., et al. 2015, *ApJ*, 813, 2
- Mawson, N. R., Steele, I. A., & Smith, R. J. 2013, *Astronomische Nachrichten*, 334, 729
- Mazzali, P. A., Deng, J., Nomoto, K., et al. 2006, *Nature*, 442, 1018
- Metzger, B. D., Bauswein, A., Goriely, S., & Kasen, D. 2015, *MNRAS*, 446, 1115
- Metzger, B. D., & Berger, E. 2012, *ApJ*, 746, 48
- Mink, D. J. 1997, in *Astronomical Society of the Pacific Conference Series*, Vol. 125, *Astronomical Data Analysis Software and Systems VI*, ed. G. Hunt & H. Payne, 249
- Minkowski, R. 1941, *PASP*, 53, 224
- Miyaji, S., Nomoto, K., Yokoi, K., & Sugimoto, D. 1980, *PASJ*, 32, 303
- Modjaz, M., Blondin, S., Kirshner, R. P., et al. 2014, *AJ*, 147, 99
- Morales-Rueda, L., Carter, D., Steele, I. A., Charles, P. A., & Worswick, S. 2004, *Astronomische Nachrichten*, 325, 215
- Morgan, W. W., Keenan, P. C., & Kellman, E. 1943, *An atlas of stellar spectra, with an outline of spectral classification*
- Morokuma, T., Tominaga, N., Tanaka, M., et al. 2014, *PASJ*, 66, 114
- Mottram, C. J., Steele, I. A., & Morales, L. 2004, in *Society of Photo-Optical Instrumentation Engineers (SPIE) Conference Series*, Vol. 5492, *Ground-based Instrumentation for Astronomy*, ed. A. F. M. Moorwood & M. Iye, 677–688
- Mundell, C. G., Kopač, D., Arnold, D. M., et al. 2013, *Nature*, 504, 119
- Newton, I. 1704, *Opticks: Or a Treatise of the Reflexions, Refractions, Inflexions and Colours of Light* (Smith and Walford)

- Ngeow, C.-C., Konidakis, N., Quimby, R., et al. 2013, in IAU Symposium, Vol. 290, IAU Symposium, ed. C. M. Zhang, T. Belloni, M. Méndez, & S. N. Zhang, 281–282
- Nomoto, K., Thielemann, F.-K., & Wheeler, J. C. 1984, *ApJL*, 279, L23
- Ober, W. W., El Eid, M. F., & Fricke, K. J. 1983, *A&A*, 119, 61
- Oke, J. B. 1990, *AJ*, 99, 1621
- Oriel-Instruments. 2008, Typical Spectra of Oriel Instruments. Spectral Calibration Lamps
- Palliyaguru, N., & Corsi, A. 2015, GRB Coordinates Network, 18780
- Peterson, B. M. 2006, in Lecture Notes in Physics, Berlin Springer Verlag, Vol. 693, Physics of Active Galactic Nuclei at all Scales, ed. D. Alloin, 77
- Phillips, M. M. 1993, *ApJL*, 413, L105
- Phillips, M. M., Wells, L. A., Suntzeff, N. B., et al. 1992, *AJ*, 103, 1632
- physics.nist.gov. 2013, NIST ASD Output Lines
- Pian, E., Mazzali, P. A., Masetti, N., et al. 2006, *Nature*, 442, 1011
- Pian, E., Tomasella, L., Cappellaro, E., et al. 2017, *MNRAS*, 466, 1848
- Piasticik, A. S., & Steele, I. A. 2016, in SPIE, Vol. 9908, Ground-based and Airborne Instrumentation for Astronomy VI, 99083Z
- Piasticik, A. S., Steele, I. A., Bates, S. D., et al. 2014a, in Proc. SPIE, Vol. 9147, Ground-based and Airborne Instrumentation for Astronomy V, 91478H
- Piasticik, A. S., Steele, I. A., Bates, S. D., et al. 2014b, in SPIE, Vol. 9147, Ground-based and Airborne Instrumentation for Astronomy V, 91478H
- Piasticik, A. S. 2017, Phd Thesis, Liverpool John Moores University

- Pignata, G., Maza, J., Antezana, R., et al. 2009, in American Institute of Physics Conference Series, Vol. 1111, American Institute of Physics Conference Series, ed. G. Giobbi, A. Tornambe, G. Raimondo, M. Limongi, L. A. Antonelli, N. Menci, & E. Brocato, 551–554
- Porter, A. C., & Filippenko, A. V. 1987, *AJ*, 93, 1372
- Prusti, T. 2012, *Astronomische Nachrichten*, 333, 453
- Pskovskii, I. P. 1977, "Soviet Astronomy", 21, 675
- Rabinowitz, D., Baltay, C., Ellman, N., & Nugent, P. 2015, GRB Coordinates Network, 18759
- Radice, D., Galeazzi, F., Lippuner, J., et al. 2016, *MNRAS*, arXiv:1601.02426
- Rees, M. J. 1984, *ARA&A*, 22, 471
- Savchenko, V., Ferrigno, C., Mereghetti, S., et al. 2016, *ApJL*, 820, L36
- Schlegel, E. M. 1990, *MNRAS*, 244, 269
- Shalyapin, V. N., & Goicoechea, L. J. 2014, *Astronomische Nachrichten*, 335, 428
- Shappee, B. J., Prieto, J. L., Grupe, D., et al. 2014, *ApJ*, 788, 48
- Singer, L. 2015, GRB Coordinates Network, 18330
- Singer, L., Kasliwal, M., Ferretti, R., et al. 2015a, GRB Coordinates Network, 18497
- Singer, L. P., Cenko, S. B., Kasliwal, M. M., et al. 2013, *ApJL*, 776, L34
- Singer, L. P., Price, L. R., Farr, B., et al. 2014, *ApJ*, 795, 105
- Singer, L. P., Kasliwal, M. M., Cenko, S. B., et al. 2015b, *ApJ*, 806, 52
- Singer, L. P., Chen, H.-Y., Holz, D. E., et al. 2016, *ApJL*, 829, L15

- Smartt, S., Smith, K. W., Chambers, K., et al. 2015, GRB Coordinates Network, 18362
- Smartt, S. J., Chambers, K. C., Smith, K. W., et al. 2016, MNRAS, 462, 4094
- Smith, K., Smartt, S., Wright, D., et al. 2015, GRB Coordinates Network, 18786
- Smith, R. J., Piascik, A. S., Steele, I. A., & Barnsley, R. M. 2016, in SPIE, Vol. 9913, Software and Cyberinfrastructure for Astronomy IV, 991317
- Stanishev, V., Taubenberger, S., Blanc, G., et al. 2007, in American Institute of Physics Conference Series, Vol. 924, The Multicolored Landscape of Compact Objects and Their Explosive Origins, ed. T. di Salvo, G. L. Israel, L. Piersant, L. Burderi, G. Matt, A. Tornambe, & M. T. Menna, 336–341
- Steele, I., & Copperwheat, C. 2015, GRB Coordinates Network, 18782
- Steele, I., Copperwheat, C., & Piascik, A. 2015a, GRB Coordinates Network, 18370
- . 2015b, GRB Coordinates Network, 18371
- . 2015c, GRB Coordinates Network, 18549
- . 2015d, GRB Coordinates Network, 18553
- . 2015e, GRB Coordinates Network, 18573
- Steele, I. A., Copperwheat, C. M., & Piascik, A. S. 2017, in IAU Symposium, Vol. 324, IAU Symposium, 283–286
- Steele, I. A., Mottram, C. J., Smith, R. J., & Barnsley, R. M. 2014, in SPIE, Vol. 9154, High Energy, Optical, and Infrared Detectors for Astronomy VI, 915428
- Steele, I. A., Smith, R. J., Rees, P. C., et al. 2004a, in Society of Photo-Optical Instrumentation Engineers (SPIE) Conference Series, Vol. 5489, Ground-based Telescopes, ed. J. M. Oschmann, Jr., 679–692

- Steele, I. A., Smith, R. J., Rees, P. C., et al. 2004b, in SPIE, Vol. 5489, Ground-based Telescopes, ed. J. M. Oschmann, Jr., 679–692
- Steele, I. A., Bates, S. D., Carter, D., et al. 2006, in Society of Photo-Optical Instrumentation Engineers (SPIE) Conference Series, Vol. 6269, Society of Photo-Optical Instrumentation Engineers (SPIE) Conference Series
- Steele, I. A., Marchant, J. M., Jermak J. E. Barnsley, R. M., et al. 2016, MNRAS, 460, 4268
- Stone, R. P. S. 1977, ApJ, 218, 767
- Tanvir, N. R., Levan, A. J., Fruchter, A. S., et al. 2013, *Nature*, 500, 547
- Tomasella, L., Cappellaro, E., Brocato, E., et al. 2015, GRB Coordinates Network, 18561
- Tomasella, L., Cappellaro, E., D’Avanzo, P., et al. 2015, GRB Coordinates Network, 18566
- TTL. 2004, 2m Class Telescope Product Specification, Telescope Technologies Ltd.
- Udalski, A., Szymański, M. K., & Szymański, G. 2015, "Acta Astronomica", 65, 1
- Walker, E. S., Baltay, C., Campillay, A., et al. 2015, ApJS, 219, 13
- Wheeler, J. C., & Harkness, R. P. 1986, in NATO Advanced Science Institutes (ASI) Series C, Vol. 180, NATO Advanced Science Institutes (ASI) Series C, ed. B. F. Madore & R. B. Tully, 45–54
- Wosley, S. E. 2017, ApJ, 836, 244
- Yaron, O., & Gal-Yam, A. 2012, PASP, 124, 668
- Youden, W. J. 1950, Cancer, 3, 32

Zwicky, F. 1965, in *Stellar Structure - Stars and Stellar Systems*, ed. L. H. Aller & D. B. McLaughlin, Vol. 8, 367